

# Investigations into the membrane architecture of cyanobacterial thylakoid membranes and nanopatterning of cyanobacterial photosystems



**Craig MacGregor-Chatwin**

A thesis submitted for the degree of Doctor of Philosophy at the  
University of Sheffield

Department of Molecular Biology and Biotechnology

September 2014



U.S. DEPARTMENT OF  
**ENERGY**



Photosynthetic Antenna  
Research Center

## Summary

*Synechocystis* sp. PCC6803 is a cyanobacterium used as a model organism to study photosynthesis. Thylakoid membranes are specialised invaginated areas of membrane that are enriched in the light harvesting antenna complexes and reaction centres. Energy is directed towards PSI and PSII by the phycobilisome complexes to drive charge separation. The native organisation of the photosynthetic complexes in cyanobacterial thylakoid membranes is still relatively unclear.

Procedures were developed to isolate and treat thylakoid membranes from *Synechocystis* to make them suitable for AFM imaging. Methods to remove contaminating material from thylakoid membranes were trialled and assessed by EM and AFM. Different approaches were used to induce the fragmentation of thylakoid membranes to produce flat, single layered lipid bilayers that were ideal for AFM imaging.

To determine the supramolecular organisation of photosynthetic protein complexes in cyanobacterial thylakoid membranes; AFM was used to image the membrane fragments produced by the methods that have been developed in this study. It was possible to identify protein complexes present in thylakoid membrane fragments initially from *Synechocystis* and subsequently from *Thermosynechococcus elongatus*. In membrane fragments from both cyanobacteria it was possible to identify PSII complexes in addition to complexes with lower topology than PSII that had dimensions consistent with the cytochrome *b<sub>6</sub>f* complex. In membrane fragments from *T.elongatus* it was possible to image PSI; which was found in densely packed, highly ordered arrays which have not previously been reported. Membrane fragments from *T.elongatus* were also imaged which contained PSI in a more disordered organisation.

In light of recent advances in lithographic techniques; it is now possible to produce nanopatterns of immobilised photoactive protein complexes. Such nanopatterns can be used to investigate the functionality and the energy transfer properties of

immobilised protein complexes. When *Synechocystis* is grown in low iron conditions the PSI trimer forms a complex with 18 copies of the IsiA protein called the IsiA-PSI supercomplex. Methods for producing a highly purified preparation of this complex for the purposes of nanopatterning were developed and the purified IsiA-PSI supercomplex was analysed by EM and AFM. Purified IsiA-PSI supercomplexes from *Synechocystis* and PSII complexes from *Thermosynechococcus elongatus* were immobilised on nanopatterns produced using reverse nanoimprint lithography. The binding specificity of protein complexes to the nanopatterns was determined using AFM. The dimensions of the nanopatterns were assessed with fluorescence microscopy and the spectroscopic properties of the immobilised complexes were investigated using fluorescence emission spectroscopy and fluorescence lifetime imaging. The fluorescence emission spectrum and the measured fluorescence lifetime of immobilised PSII complexes was comparable to that of active PSII complexes in solution. The fluorescence emission spectrum of immobilised IsiA-PSI supercomplexes was consistent with that of IsiA-PSI supercomplexes in solution. The measured fluorescence lifetime of the immobilised supercomplex was however significantly longer than that of supercomplexes in solution.

## Acknowledgements

First and foremost I would like to thank my supervisor Professor Neil Hunter for his continued support, advice and patience over the last four years and for giving me the opportunity to work in his lab.

In relation to this work, my sincerest thanks go to Dr. Cvetelin Vasilev for his help with AFM, data modelling, protein purification, nanopatterns and fluorescence imaging in addition to his seemingly infinite levels of patience and knowledge. My thanks also go to Dr. Karim Maghlaoui for providing me with membrane samples and purified PSII complexes from *Thermosynechococcus elongatus*.

Thanks to all the members of the University of Sheffield past and present who have aided me in this work; Dr. John Olsen and Dr. Peter Adams for teaching me to use the AFM; Dr. Pu Qian for his help with EM and single particle analysis; Dr. Chris Marklew and Jack Chidgey for their help regarding all things HPLC related; Dr. Svetomir Tzokov for teaching me how to use the electron microscope and Dr Amanda Brindley and Elizabeth Martin for supplying me with all the materials I needed.

Thanks to all the friends I've made since coming to Sheffield who have made my time here such an enjoyable experience. Jack Chidgey for his funny, honest and frankly sometimes hurtful remarks in relation to chickens and aeroplanes. Dave Armstrong for his intriguing insights into the management of Porta Loos at the Edinburgh fireworks. All of the members of the Hunter and Kelly labs past and present who are always up for a night out. Aaron for getting me more heinously drunk and into more trouble than I thought was possible. Gabriel for his willingness to dance around with his shirt off after consuming vanishingly small quantities of alcohol. Luke Gledhill and Caroline "soon to be Gledhill I think" Taylor whose dance moves make even me look good on a Friday night. James Harris who has been a constant inspiration for me to never give up and always try my best as I don't want to end up as washed out and useless as he is. All of the members of 20 Ashgate Road past and present who have been so much fun to live with.

Last but by no means least I would like to thank my loving parents for their continued support and encouragement over the last four years and for inspiring me to pursue a PhD in science.

# Contents

Summary .....	ii
Acknowledgements.....	iv
Contents.....	v
List of Figures .....	x
List of Tables .....	xiv
List of Abbreviations .....	xv
Introduction .....	1
1.1 Photosynthesis.....	1
1.2 <i>Synechocystis</i> sp. PCC6803.....	2
1.3 Pigments in photosynthesis.....	2
1.3.1 Function of pigments .....	2
1.3.2 Chlorophylls .....	3
1.3.3 Chlorophyll <i>a</i> biosynthesis .....	5
1.3.4 Bilins.....	8
1.3.5 Bilin biosynthesis.....	9
1.3.6 Carotenoids.....	11
1.3.7 Carotenoids biosynthesis .....	12
1.4 Cyanobacterial lipids .....	13
1.5 Light-harvesting complexes in <i>Synechocystis</i> .....	16
1.5.1 Photosynthetic unit.....	16
1.5.2 Phycobilisomes .....	18
1.5.3 Photosystem II (PSII) structure and function.....	21
1.5.4 PSII Assembly .....	25
1.5.5 Photosystem I structure and function .....	26
1.5.6 Photosystem I assembly.....	33
1.5.7 Cytochrome <i>b<sub>6</sub>f</i> .....	33
1.5.8 The terminal electron acceptor and ATP synthesis .....	37
1.6 Ultrastructure of thylakoid membranes. ....	38
1.7 Electron microscopy of protein complexes in cyanobacterial thylakoid membranes....	43
1.7.1 Freeze-fracture EM .....	43
1.7.2 Negative stain EM .....	45
1.8 Atomic force microscopy .....	47
1.8.1 Instrumentation .....	49

1.8.2 Imaging modes.....	51
1.8.3 Advantages and limitations of AFM.....	53
1.8.4 Use of AFM to image membrane proteins in 2D crystals.....	54
1.8.5 Use of AFM to image membrane proteins in native membranes.....	56
1.9 Nano-lithography and nanopatterns.....	60
2. Materials and methods.....	63
2.1 Materials.....	63
2.2 Standard buffers, reagents and media.....	63
2.3 Cyanobacteria strains and growth conditions.....	63
2.4 Measuring sucrose concentration.....	64
2.5 Absorbance spectroscopy.....	64
2.6 Fluorescence emission spectroscopy.....	64
2.7 Calculation of chlorophyll concentration.....	65
2.8 Standard membrane preparation.....	65
2.9 Detergent treatments.....	66
2.9.1 $\beta$ -DDM treatment.....	66
2.9.2 Tween 20 treatment.....	66
2.9.3 Triton X-100 treatment.....	66
2.9.4 Digitonin treatment.....	67
2.10 Atomic Force Microscopy.....	67
2.10.1 Instrumentation.....	67
2.10.2 Sample preparation.....	67
2.10.3 Sample imaging.....	68
2.11 Electron Microscopy.....	68
2.12 Single particle analysis of IsiA-PSI supercomplex.....	69
2.13 Protein manipulation.....	69
2.13.1 SDS-polyacrylamide gel electrophoresis (SDS-PAGE).....	69
2.13.2 Silver staining of gels.....	69
2.13.3 Clear native polyacrylamide gel electrophoresis (CN-PAGE).....	70
2.13.4 Electroelution of protein complexes from polyacrylamide gels.....	70
2.14 Purification of thylakoid membranes from <i>Synechocystis</i> 6803 for protein purification.....	70
2.15 Purification of the IsiA-PSI supercomplex from <i>Synechocystis</i> 6803 thylakoid membrane.....	71
2.15.1 Solubilisation.....	71
2.15.2 Sucrose gradients.....	71

2.15.3 Anion exchange.....	72
2.15.4 Gel filtration.....	72
2.16 Production of protein nanolines.....	73
2.16.1 Master pattern template.....	73
2.16.2 Spin coating of master patterns with polystyrene.....	73
2.16.3 Preparation of protein nanolines with 150 nm line width.....	73
2.17 <i>In situ</i> fluorescence microscopy and spectroscopy.....	74
2.18 Fluorescence-lifetime imaging microscopy.....	75
2.19 Low temperature fluorescence emission spectroscopy.....	75
Chapter 3: Development of procedures for the production of large, flat photosynthetic membrane patches for the purposes of AFM analysis.....	76
3.1 Summary.....	76
3.2 Introduction.....	77
3.3 Results.....	79
3.3.1 Initial trials for cell breakage and membrane purification.....	79
3.3.2 Optimisation of the primary purification step.....	82
3.3.3 EM of thylakoid membranes from primary sucrose gradients:.....	83
3.3.4 Initial AFM.....	84
3.3.5 Additional purification of thylakoid membranes.....	85
3.3.6 High salt secondary sucrose gradients for removal of glycogen granules.....	87
3.3.7 EM of membranes purified on high salt secondary gradients.....	88
3.3.8 DCMU treatment of cells.....	90
3.3.9 Amylase treated membranes.....	91
3.3.10 AFM of amylase treated membranes.....	93
3.3.11 Imaging membranes under air.....	95
3.3.12 Rehydration of dried membrane samples.....	97
3.3.13 $\beta$ -DDM treatment of membranes.....	100
3.3.14 AFM of $\beta$ -DDM treated membrane fragments.....	101
3.3.15 Tween 20 treatment of membranes.....	107
3.3.16 AFM of Tween 20 treated membrane fragments.....	108
3.3.17 Triton X-100 treatment of membranes.....	111
3.3.18 AFM of Triton X-100 treated membrane fragments.....	112
3.3.19 Digitonin treatment of membranes.....	114
3.3.20 AFM of Digitonin treated membrane fragments.....	115
3.4 Discussion.....	118

3.4.1 Initial trials for purification of thylakoid membranes .....	118
3.4.2 Removing contaminating material from membranes .....	119
3.4.3 AFM of membrane patches .....	121
3.5 Conclusions .....	124
Chapter 4: EM and AFM analysis of protein complexes in cyanobacterial thylakoid membranes .....	125
4.1 Summary .....	125
4.2 Introduction .....	127
4.3 Results .....	130
4.3.1 EM of thylakoid membranes from <i>Synechocystis</i> .....	130
4.3.2 AFM of digitonin treated membranes .....	132
4.3.3 Height measurements of protein complexes in membrane patches from <i>Synechocystis</i> .....	135
4.3.4 Lateral measurements of protein complexes .....	139
4.3.5 The organisation of protein complexes in membrane patches from <i>Synechocystis</i> .....	141
4.3.6 Possible topological features that correspond to PSI complexes in membrane patches from <i>Synechocystis</i> .....	143
4.3.7 AFM of membrane patches from <i>Thermosynechococcus elongatus</i> .....	145
4.3.8 Height measurements from <i>T. elongatus</i> membrane patches .....	147
4.3.9 AFM of trimeric complexes in <i>T. elongatus</i> membrane patches .....	150
4.3.10 Room temperature absorption spectroscopy of digitonin treated thylakoid membranes from <i>Synechocystis</i> and <i>T.elongatus</i> .....	154
4.3.11 Molar ratios of PSI and PSII in digitonin treated thylakoid membranes from <i>Synechocystis</i> .....	156
4.3.12 Molar ratios of PSI and PSII in digitonin treated thylakoid membranes from <i>T.elongatus</i> .....	159
4.3.13 Low temperature emission spectroscopy of thylakoid membranes from <i>Synechocystis</i> and <i>T.elongatus</i> .....	162
4.4 Discussion .....	163
4.4.1 EM of <i>Synechocystis</i> membranes .....	163
4.4.2 Identification of complexes on the luminal face of the membrane .....	164
4.4.3 Identification of trimeric complexes in membrane patches from <i>T.elongatus</i> .....	167
4.4.4 PSI and PSII content in membrane patches from <i>Synechocystis</i> and <i>T.elongatus</i> .....	167
4.4.5 Supramolecular organisation of cyanobacterial thylakoid membranes .....	170
Chapter 5: Purification and imaging of the IsiA-PSI supercomplex and nanopatterning of cyanobacterial photosystems .....	176

5.1 Summary .....	176
5.2 Introduction .....	178
5.3 Results.....	182
5.3.1 Growth conditions .....	182
5.3.2 Purification of the IsiA-PSI supercomplex on sucrose gradients .....	183
5.3.3 Anion exchange of the IsiA-PSI supercomplex.....	185
5.3.4 Negative stain TEM and AFM of the anion exchange eluate.....	188
5.3.5 Gel filtration of the IsiA-PSI supercomplex .....	190
5.3.6 Negative stain TEM and AFM of the gel filtration eluate .....	191
5.3.7 SDS-PAGE of IsiA-PSI samples .....	195
5.3.8 Production of functionalised surfaces using RNIL.....	196
5.3.9 Immobilisation of IsiA-PSI supercomplexes on MPTMS nano-lines.....	197
5.3.10 AFM of IsiA-PSI nanopatterns .....	199
5.3.11 Fluorescence imaging of IsiA-PSI nanopatterns.....	202
5.3.12 Immobilisation of PSII complexes on MPTMS nano-lines.....	204
5.3.13 AFM of PSII nanopatterns .....	205
5.3.14 Fluorescence imaging of PSII nanopatterns.....	209
5.4 Discussion.....	211
References .....	217

## List of Figures

Figure 1.1 Chemical structures of chlorophyll <i>a</i> , <i>b</i> and <i>d</i> .....	4
Figure 1.2. Absorption spectrum of some of the pigments present in cyanobacteria...	5
Figure 1.3 Chlorophyll <i>a</i> biosynthesis .....	7
Figure 1.4. Chemical structures of phycocyanobilin and phycoerythrobilin .....	8
Figure 1.5. Schematic showing the synthesis of phycocyanin and phycoerythrobilin from biliverdin IX $\alpha$ .....	10
Figure 1.6. Final stages of carotenoid biosynthesis .....	12
Figure 1.7. Lipids in cyanobacteria.....	15
Figure 1.8. Proteins of the photosynthetic unit.....	17
Figure 1.9. Z-scheme .....	18
Figure 1.10. Single particle averaging of the phycobilisome complex and subcomplexes.....	19
Figure 1.11. Schematic of phycobilisomes structure .....	20
Figure 1.12. Crystal structure of PSII from <i>Thermosynechococcus vulcanus</i> at 1.9 Å ..	22
Figure 1.13. Electron transport cofactors and charge separation in PSII .....	24
Figure 1.14. Schematic for PSII assembly.....	26
Figure 1.15. Crystal structure of trimeric PSI from <i>Thermosynechococcus elongatus</i> .	28
Figure 1.16. Schematic for electron transport in PSI and the relevant cofactors .....	30
Figure 1.17. Single particle reconstruction of the IsiA-PSI supercomplex.....	32
Figure 1.18. Crystal structure of cytochrome <i>b<sub>6</sub>f</i> from <i>Mastigocladus laminosus</i> .....	34
Figure 1.20. TEM of thin sections from <i>Synechocystis</i> .....	38
Figure 1.21. Tomographic model of thin sections from <i>Synechocystis</i> .....	40
Figure 1.22. Tomographic models of thylakoid convergence points.....	41
Figure 1.23. TEM of thin sections from wild type and VIPP1 knockout mutant.....	42
Figure 1.24 Freeze-fracture electron micrographs of cyanobacterial thylakoid membrane.....	44
Figure 1.25 Negative stain EM of PSII in membrane fragments.....	46
Figure 1.26. Schematic for AFM .....	50
Figure 1.27. AFM topographs showing 2D crystals of RC-LH1 from <i>R. rubrum</i> .....	55
Figure 1.28. AFM of photosynthetic membranes from different purple bacteria .....	57

Figure 1.29. AFM topographs of grana membranes from spinach.....	59
Figure 1.30. AFM topographs of grana membranes showing the location of.....	59
Figure 1.31. Schematic for production of protein nanopatterns using NIL.....	62
Figure 3.1. Initial sucrose gradients .....	80
Figure 3.2. EM of cell lysates from bead beating .....	81
Figure 3.3. Lengths of membranes patches from bead beating cell lysates .....	81
Figure 3.4. Optimised primary gradient.....	82
Figure 3.5. Negative stain TEM of thylakoid membranes from the revised primary gradient .....	83
Figure 3.6. Initial AFM of thylakoid membranes.....	84
Figure 3.7. Secondary sucrose gradient.....	85
Figure 3.8. Comparison of thylakoid membranes from primary and secondary gradients.....	86
Figure 3.9. Secondary gradients from high salt trials .....	87
Figure 3.10. Comparison of membranes from high salt trials .....	89
Figure 3.11. Negative stain TEM of membranes from cells grown in DCMU supplemented medium.....	90
Figure 3.12: Negative stain TEM of membranes treated with $\alpha$ -amylase.....	92
Figure 3.13. AFM analysis of amylase treated membranes from secondary gradients.....	94
Figure 3.14. Thylakoid membranes imaged by AFM in air .....	96
Figure 3.15. Rehydrated thylakoid membranes imaged by AFM under liquid.....	98
Figure 3.16. AFM of a rehydrated membrane patch using a smaller scan size .....	99
Figure 3.17. Secondary sucrose gradients from $\beta$ -DDM trial.....	100
Figure 3.18. Schematic showing how membrane structures can be identified from their height and topology .....	101
Figure 3.19. AFM of $\beta$ -DDM treated membranes.....	103
Figure 3.20. AFM of protein-containing membrane patches from $\beta$ -DDM method of preparation .....	104
Figure 3.21. Structures and CMCs of detergents that were trialled to produce flat membrane patches .....	106
Figure 3.22. Secondary sucrose gradients from Tween 20 trial .....	107
Figure 3.23. AFM of Tween 20 treated membranes.....	109

Figure 3.24. AFM of protein-containing membrane patches from Tween 20 treated membranes .....	110
Figure 3.25. Secondary sucrose gradients from Triton X-100 trial .....	111
Figure 3.26. AFM of Triton X-100 treated membranes.....	113
Figure 3.27. Secondary sucrose gradients from digitonin trial.....	115
Figure 3.28. AFM of protein-containing membrane patches from digitonin treated membranes .....	116
Figure 3.29. High resolution AFM of protein complexes in digitonin treated membranes .....	117
Figure 4.1. Negative stain EM of thylakoid membranes from primary sucrose gradients.....	131
Figure 4.2. AFM of digitonin treated membrane patches from <i>Synechocystis</i> .....	133
Figure 4.3. Sections of membrane patches produced by digitonin treatment .....	134
Figure 4.4. Height measurements of protein complexes in flat membrane patches from <i>Synechocystis</i> .....	137
Figure 4.5. Crystal structures of PSII, cytochrome <i>b<sub>6</sub>f</i> and PSI .....	138
Figure 4.6. Lateral measurements of putative PSII dimers.....	140
Figure 4.7. Organisation of PSII complexes into linear arrays .....	142
Figure 4.8. PSI compatibility of membrane patches from <i>Synechocystis</i> .....	144
Figure 4.9. Crystal structure of PSI.....	144
Figure 4.10. AFM of digitonin treated membrane fragments from <i>T.elongatus</i> .....	146
Figure 4.11. Height measurements of protein complexes in flat membrane patches from <i>T.elongatus</i> .....	148
Figure 4.12. PSI compatibility of membrane patches from <i>T.elongatus</i> .....	149
Figure 4.13. AFM imaging and height analysis of a digitonin treated membrane patch from <i>T.elongatus</i> that contains trimeric complexes in ordered arrays.....	152
Figure 4.14. AFM imaging and height analysis of a digitonin treated membrane patch from <i>T.elongatus</i> that contains trimeric complexes in a disordered arrangement. ..	153
Figure 4.15. Absorption spectra of thylakoid membranes from <i>Synechocystis</i> and <i>T.elongatus</i> .....	155
Figure 4.16. Digitonin containing sucrose gradients.....	157
Figure 4.17. CN-PAGE of solubilised <i>Synechocystis</i> thylakoid membranes from digitonin gradients. ....	158

Figure 4.18. CN-PAGE of solubilised <i>T.elongatus</i> thylakoid membranes from digitonin gradients.....	161
Figure 4.19. Low temperature emission spectra of thylakoid membranes from <i>Synechocystis</i> and <i>T.elongatus</i> .....	162
Figure 4.20. Model for the organisation of PSI, PSII, the cytochrome <i>b<sub>6</sub>f</i> complex and ATP synthase in <i>Synechocystis</i> thylakoid membranes based on AFM data .....	172
Figure 4.21. Model for the organisation of PSI, PSII, the cytochrome <i>b<sub>6</sub>f</i> complex and ATP synthase in <i>T.elongatus</i> membranes based on AFM data.....	175
Figure 5.1. Room temperature absorption spectra .....	183
Figure 5.2. (a) Sucrose gradients and (b) room temperature absorption spectra .....	184
Figure 5.3. Anion exchange of IsiA-PSI supercomplex.....	186
Figure 5.4. Room temperature absorption spectra of anion exchange fractions .....	187
Figure 5.5. AFM and negative stain TEM of IsiA-PSI complexes after anion exchange .....	189
Figure 5.6. Gel filtration of the IsiA-PSI supercomplex.....	191
Figure 5.7. Negative stain TEM of IsiA-PSI complexes after gel filtration.....	193
Figure 5.8. AFM of IsiA-PSI complexes after gel filtration .....	194
Figure 5.9. (a) Coomassie stained and (b) silver stained SDS-PAGE of samples from all purification steps.....	195
Figure 5.10. Dimensions of the master pattern.....	197
Figure 5.11. Schematic for producing nano-lines of immobilised protein complexes using RNIL.....	198
Figure 5.12. AFM of IsiA-PSI nano-lines .....	200
Figure 5.13. AFM of individual IsiA-PSI .....	201
Figure 5.14. Fluorescence microscopy, room temperature emission spectra and fluorescence lifetime imaging of IsiA-PSI nanopatterns.....	203
Figure 5.15. Coomassie stained SDS-PAGE of purified PSII complexes .....	204
Figure 5.16. AFM of PSII nano-lines .....	206
Figure 5.17. AFM of a single PSII nano-line.....	207
Figure 5.18. AFM of potential PSII dimers immobilised on MPTMS nano-lines.....	208
Figure 5.19. Fluorescence microscopy, room temperature emission spectra and fluorescence lifetime imaging of PSII nanopatterns.....	210

## List of Tables

Table 4.1. Measurements made on the membrane patches in Figure 4.2.....	135
Table 4.2. The table shows measurements made on the membrane patches in figure 4.10.....	146
Table 4.3. PSI:PSII ratios for samples harvested from gradients in Figure 4.16. ....	159
Table 4.3. PSI:PSII ratios for <i>T.elongatus</i> samples harvested from 0.0 % and 1.0 % digitonin sucrose gradients. ....	161
Table 5.1. Spectroscopic properties of anion exchange fractions.....	186
Table 5.2. Dimensions of IsiA-PSI supercomplexes.....	201
Table 5.3. Measurements of complexes in Figure 5.18 .....	208

## List of Abbreviations

$\beta$ -DDM	n-Dodecyl $\beta$ -D-maltoside
$\tau$	Fluorescence lifetime
2-D	Two-dimensional
3-D	Three-dimensional
AU	Absorbance units
ADP	Adenosine diphosphate
AFM	Atomic force microscopy
ALA	5-Aminolevulinic acid
ATP	Adenosine triphosphate
<i>Blc.</i>	<i>Blastochloris</i>
Chl	Chlorophyll
CM-AFM	Contact mode AFM
Da/kDa	Dalton/kilodalton
DCMU	3-3,4-dichlorophenyl-1,1-dimethylurea
DOC	Deoxycholate
FNR	Ferredoxin-NADP <sup>+</sup> reductase
Hz/KHz/MHz	hertz/kilohertz/megahertz
HMB	Hydroxymethylbilane
LH2	Light harvesting complex 2
LHC2	Light harvesting complex II
MPTMS	(3-mercaptopropyl)trimethoxysilane
M/mM	Molar/millimolar
ml/ $\mu$ l	millilitre/microlitre
MW	Molecular weight
NADP <sup>+</sup>	Oxidised nicotinamide adenine dinucleotide phosphate
NADPH	Reduced nicotinamide adenine dinucleotide phosphate
nm/ $\mu$ m	Nanometre/Micrometre
ns	Nanosecond
OEC	Oxygen evolving complex
OD <sub>x</sub>	Optical density at x nm

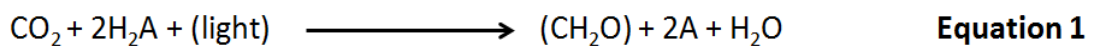
P680	Reduced special pair of chlorophyll in PSII
P680 <sup>+</sup>	Oxidised special pair of chlorophyll in PSII
P700	Reduced special pair of chlorophyll in PSI
P700 <sup>+</sup>	Oxidised special pair of chlorophyll in PSII
PcyA	Phycocyanobilin:ferredoxin oxidoreductase
PDM	PratA-defined membrane
PebA	15,16-dihydrobiliverdin:ferredoxin oxidoreductase
PebB	Phycoerythrobilin:ferredoxin oxidoreductase
PEG	silane 2-[methoxy(polyethyleneoxy)propyl]trimethoxysilane
PMT	Photomultiplier tube
PF-QNM	Peak Force Quantitative Nanomechanical Mapping
PFT	Peak force tapping
PGB	Porphobilinogen
PQH <sub>2</sub>	Reduced plastoquinone
PQ	Oxidised plastoquinone
PSI	Photosystem I
PSII	Photosystem II
pN	piconewtons
ps	picoseconds
<i>Rb.</i>	<i>Rhodobacter</i>
RC	Reaction centre
rpm	revolutions per minute
<i>Rps.</i>	<i>Rhodopseudomonas</i>
<i>Rsp.</i>	<i>Rhodospirillum</i>
SAM	Self assembled monolayer
SDS-PAGE	Sodium dodecyl sulfate polyacrylamide gel electrophoresis
SMCC	Succinimidyl-4-(n-maleimidomethyl)cyclohexane-1-carboxylate
TEM	Transmission electron microscopy
TM-AFM	Tapping mode atomic force microscopy
V	volts
WT	wild type

# Introduction

## 1.1 Photosynthesis

Photosynthesis is the biochemical mechanism through which light energy is harvested and converted into biochemical energy. Photosynthetic organisms such as plants, algae and certain bacteria contain pigment-protein complexes that facilitate photosynthesis and act as the primary energy source for the vast majority of life on Earth (Nelson and Ben-Shem, 2004). All photosynthetic organisms use the energy captured by these pigment-protein complexes to drive a variety of electron transport chains that are coupled to the translocation of protons through cellular membranes. The resultant proton gradient is then utilised for the synthesis of ATP which is in turn used drive further chemical reactions required to sustain downstream metabolism (Nelson and Ben-Shem, 2004).

Although the protein assemblies that facilitate photosynthesis in different types of organism vary significantly, photosynthesis is a redox reaction that can be described by **equation 1**.  $H_2A$  can be any compound that donates electrons and hydrogen ions for the reduction of  $CO_2$  into  $CH_2O$  (carbohydrate). In plants, algae and cyanobacteria  $H_2O$  is used to reduce  $CO_2$  which results in the generation of  $O_2$  as the oxidation product. Oxygenic photosynthesis is essential for maintaining the level of oxygen in the atmosphere required for aerobic respiration (Nelson and Ben-Shem, 2004).



Photosynthetic prokaryotes are able to use a variety of different compounds such as  $H_2S$ ,  $H_2$ , acetate as well as many others as electron donors in place of  $H_2O$  for the reduction of  $CO_2$ .

## **1.2 *Synechocystis* sp. PCC6803**

*Synechocystis* sp. PCC6803 is the subject of extensive research and is the primary focus of this thesis. This unicellular, Gram-negative cyanobacterium performs oxygenic photosynthesis using H<sub>2</sub>O to reduce CO<sub>2</sub> and is able to grow phototrophically when exposed to light and heterotrophically when supplied with a carbon source such as glucose (Anderson and McIntosh, 1991).

There are many aspects of *Synechocystis* that make it a useful model organism for photosynthesis. One of the most significant factors is the similarities between the photosynthetic mechanism of *Synechocystis* and that of plants and algae with a high level of homology between many of the photosynthetic protein complexes. *Synechocystis* was the first photosynthetic organism to have its genome fully sequenced (Kaneko and Tabata, 1997) and there are many established mutants of this bacterium that are already in existence. Furthermore it is naturally competent, allowing for the uptake and incorporation of foreign DNA into its genome by homologous recombination (Grigorieva and Shestakov, 1982). This, combined the ability to grow photoheterotrophically makes genetic manipulation of essential photosynthetic protein complexes from this organism relatively simple in comparison to its eukaryotic counterparts.

## **1.3 Pigments in photosynthesis**

### **1.3.1 Function of pigments**

There are many different types of pigment cofactors in light harvesting proteins which play a variety of different roles in photosynthesis. The most important function of pigments is to absorb light energy and transfer it to neighbouring pigments via excitation transfer in order to deliver the energy to a reaction centre where it drives charge separation. The light harvesting complexes in *Synechocystis* contain three different types of pigment; chlorophylls, carotenoids and bilins.

### 1.3.2 Chlorophylls

There are six types chlorophyll that are currently known to exist, named sequentially from chlorophyll *a* to chlorophyll *f* (Chen *et al.*, 2010). *Synechocystis* exclusively contains chlorophyll *a* whereas plants contain both chlorophyll *a* and chlorophyll *b*. Chlorophyll is essential for photosynthesis and whilst there are several different types of chlorophyll they share a number of common traits. Chlorophylls are planar molecules that are roughly square in shape and have a width of approximately 10 Å. They are modified cyclic tetrapyrroles in which a magnesium atom is co-ordinated to the nitrogen atoms at the centre of the macrocycle (see **Figure 1.1**). Chlorophyll molecules also contain a 5th ring in one corner of the macrocycle with each of the 5 rings designated A-E. Another feature common to all chlorophyll molecules is the presence of a C<sub>20</sub> hydrocarbon chain covalently bound to ring D of the tetrapyrrole. This hydrophobic phytol tail is important for the assembly and stability of light harvesting protein complexes (Bollivar *et al.*, 1994; Adlesee and Hunter, 1999).

The  $\pi$  bonds in the chlorophylls 5-membered ring structure form an extensive delocalised electron system over the majority of the molecule. The function of this system is to allow for the delocalisation of energy when it is transferred to the molecule either by absorption of light or excitation transfer. Chlorophylls absorb light in two different parts of the visible spectrum; the blue region (Soret band) and the red region (Q<sub>y</sub> transition) (**Figure 1.2**). These absorption bands arise from excitation of the delocalised  $\pi$ -electrons; the maxima of the absorption peaks change according to the chemical groups that are attached to the macrocycle. This leads to different types of chlorophyll molecules having different absorption spectra.

Different cyanobacterial species utilise different combinations of pigments, allowing them to absorb the varying wavelengths of light available in different ecological niches. *Acaryochloris marina* contains chlorophyll *d* as the main pigment in its light harvesting complexes which facilitates the absorption of far-red light that is unavailable to organisms that exclusively contain chlorophyll *a* (Miyashita *et al.*, 2003). *Prochlorococcus* is a genus of cyanobacteria that contains chlorophyll *b* in

addition to chlorophyll *a* which allows for absorption of a greater range of wavelengths to drive photosynthesis (Partensky *et al.*, 1999).

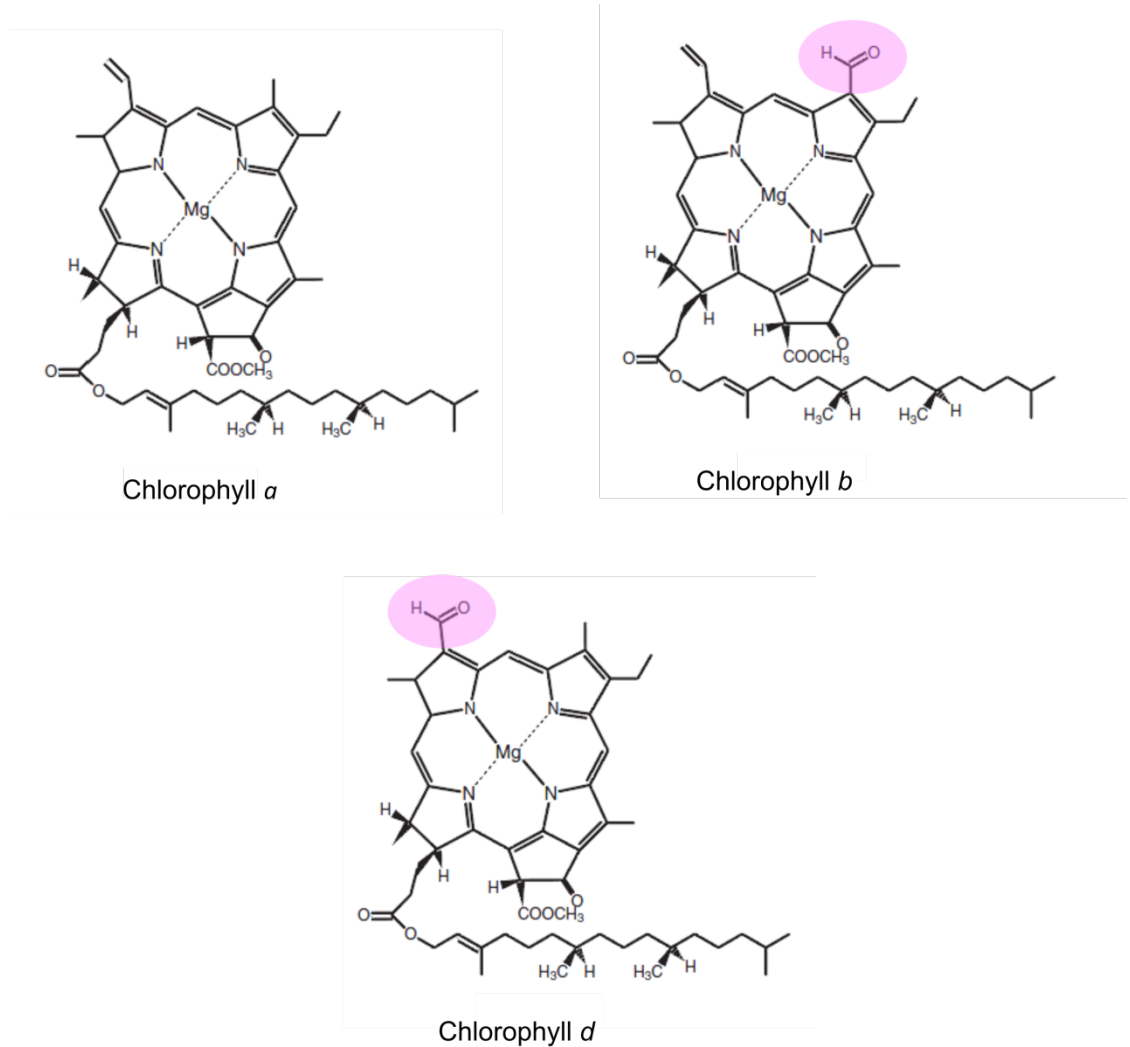


**Figure 1.1 Chemical structures of chlorophyll *a*, *b* and *d*.** Chlorophyll *a* is the only type of chlorophyll present in *Synechocystis*. The other forms of chlorophyll have slightly different chemical structures and thus have different absorption spectra; the chemical groups that differ from chlorophyll *a* are highlighted in pink in the chlorophyll *b* and chlorophyll *d* structures.

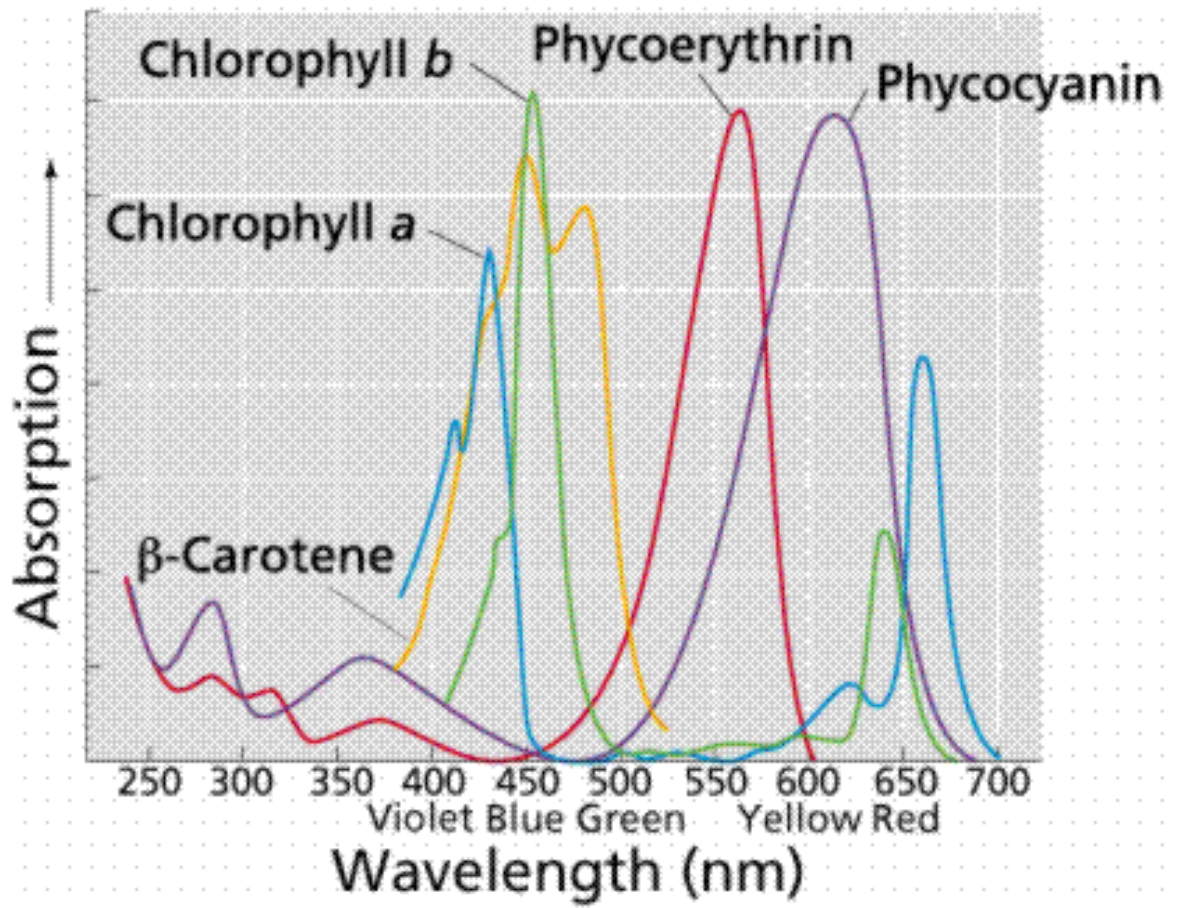


**Figure 1.2.** Absorption spectrum of some of the pigments present in cyanobacteria. Different pigments have absorption maxima in different regions of the spectrum; chlorophyll pigments absorb light in the blue and red regions of the spectrum whereas phycoerythrin and phycocyanin absorb light in the green and yellow regions. By utilising multiple pigments cyanobacteria are able to harvest a greater range of wavelengths to drive photosynthesis. (<http://www.ledflowergrowlights.eu/illuminate.html>).

### 1.3.3 Chlorophyll *a* biosynthesis

Chlorophyll biosynthesis is a complicated metabolic pathway that consists of 17 enzyme catalysed reactions (see **Figure 1.3**) the first of which is the production of 5-aminolevulinic acid (ALA), considered to be the first committed step in the synthesis of tetrapyrroles (Rieble and Beale, 1991). In *Synechocystis* ALA is synthesised via the  $C_5$  pathway from glutamic acid (Rieble and Beale, 1991), then two ALA molecules are utilised for a condensation reaction catalysed by porphobilinogen synthase to

produce porphobilinogen (PGB) (Jordan, 1991). The next step in chlorophyll biosynthesis requires 4 molecules of PGB which are converted into the linear tetrapyrrole hydroxymethylbilane (HMB) by a series of 4 deamination reactions catalysed by porphobilinogen deaminase (Battersby *et al.*, 1983). HMB is subsequently converted into uroporphyrinogen III by uroporphyrinogen III synthase (Crockett *et al.*, 1991). Uroporphyrinogen III is the first cyclic tetrapyrrole in the chlorophyll biosynthesis pathway and through the action of *HemE*, *HemF* and *HemG* uroporphyrinogen III is converted to protoporphyrin IX (Luo and Lim, 1993; Smith *et al.*, 1993; Kato *et al.*, 2010). The synthesis of protoporphyrin IX is a branch point in the tetrapyrrole biosynthesis pathway as either  $\text{Fe}^{2+}$  or  $\text{Mg}^{2+}$  can be inserted into the centre of the macrocycle, committing the pathway to the biogenesis of haem or chlorophyll, respectively. Magnesium chelatase inserts  $\text{Mg}^{2+}$  into protoporphyrin IX to produce magnesium protoporphyrin IX (Reid and Hunter, 2004), which then undergoes 11 more enzyme catalysed reactions, with the penultimate and ultimate steps being the addition of a geranylgeranyl tail and its subsequent reduction to phytol to produce chlorophyll *a* (Blankenship, 2002).

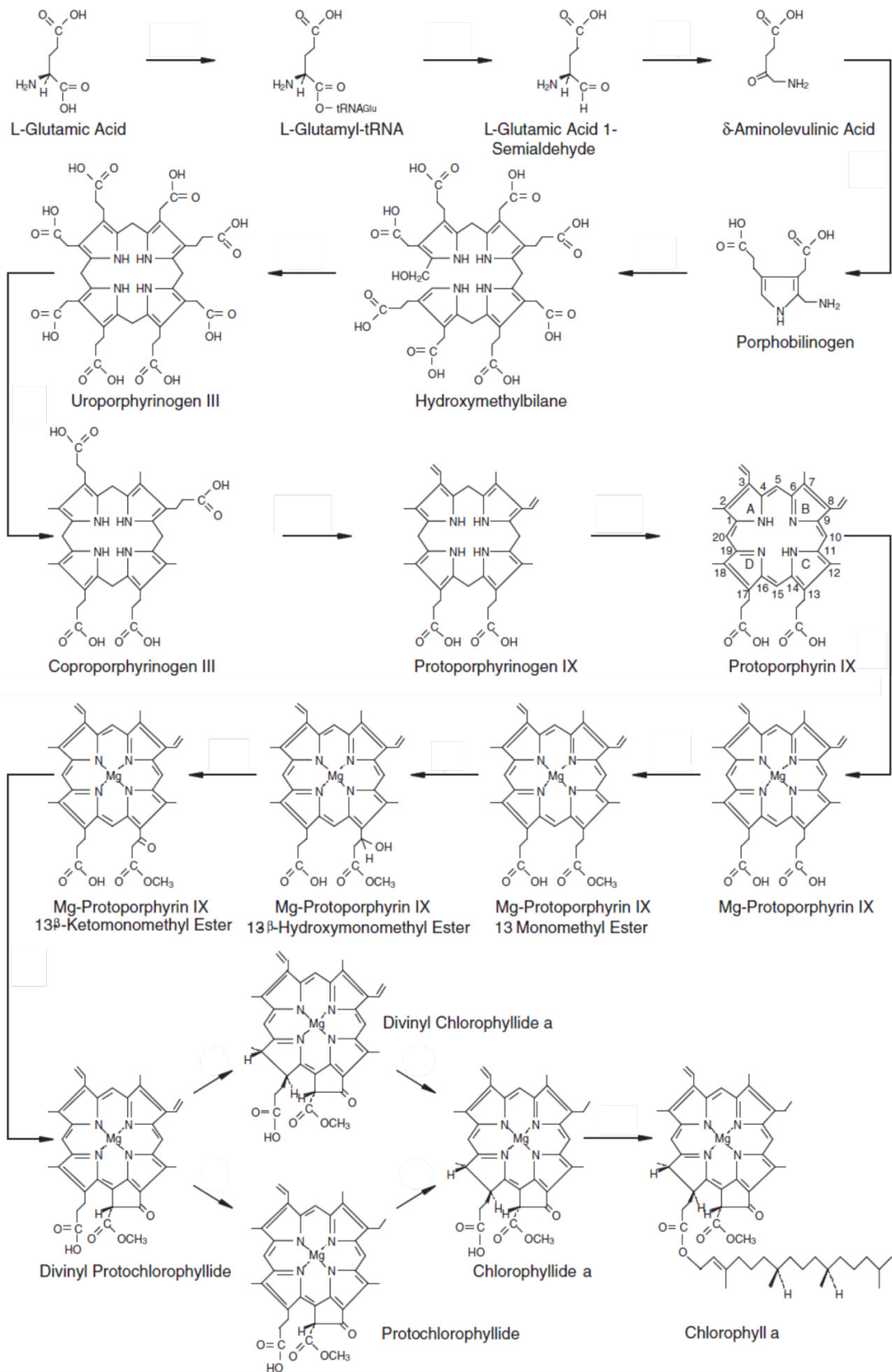


**Figure 1.3 Chlorophyll *a* biosynthesis.** This schematic outlines the 17 reactions for the production of chlorophyll *a*. From Blankenship, (2002)

### 1.3.4 Bilins

Bilins are linear tetrapyrroles that absorb between 550-650 nm and are found in phycobiliproteins where they are covalently bound to cysteine residues in the protein through either one or two thioester bonds (Brown *et al.*, 1990; Beale, 1993). Phycobiliproteins are assembled into phycobilisomes (see 1.4.2) which sit on the surface of the cyanobacterial thylakoid membranes where their main function is to harvest light energy and channel it toward the reaction centres (Arteni *et al.*, 2009). The two most common bilins are phycocyanobilin and phycoerythrobilin both of which contain extended conjugated double bonds systems that enable them to absorb light (Figure 1.4).

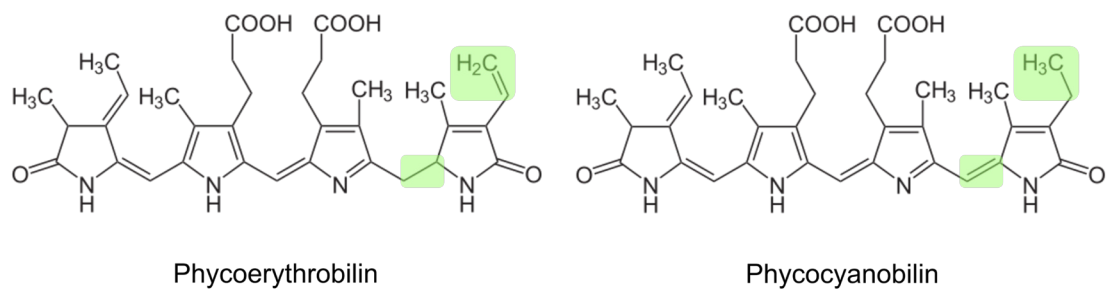


**Figure 1.4. Chemical structures of phycocyanobilin and phycoerythrobilin.** The chemical structures of the two bilin pigments in *Synechocystis* are very similar; the chemical groups that differ between the two structures are highlighted in green.

### 1.3.5 Bilin biosynthesis

Bilins are synthesised from protohaem which is converted to biliverdin IX $\alpha$  in a multi-step reaction driven by the catalytic action of haem oxygenase (Beale, 1993). Phycocyanobilin is synthesised from biliverdin IX $\alpha$  through two consecutive reduction reactions, both of which are catalysed by phycocyanobilin:ferredoxin oxidoreductase (PcyA) (**Figure 1.5**). Each reduction reaction requires two electrons which are donated by ferredoxin (Hagiwara *et al.*, 2006). Phycoerythrobilin is also synthesised from biliverdin IX $\alpha$  in a two step reaction process; the first reaction is catalysed by 15,16-dihydrobiliverdin:ferredoxin oxidoreductase (PebA) which reduces the 15, 16 -double bond in biliverdin IX $\alpha$  to produce 15, 16-dihydrobiliverdin (DHBV). The second step is catalysed by phycoerythrobilin:ferredoxin oxidoreductase (PebB) which reduces DHBV to produce phycoerythrobilin. In both steps ferredoxin provides the electrons required to reduce the substrate (Dammeyer and Frankenberg-Dinkel, 2006).

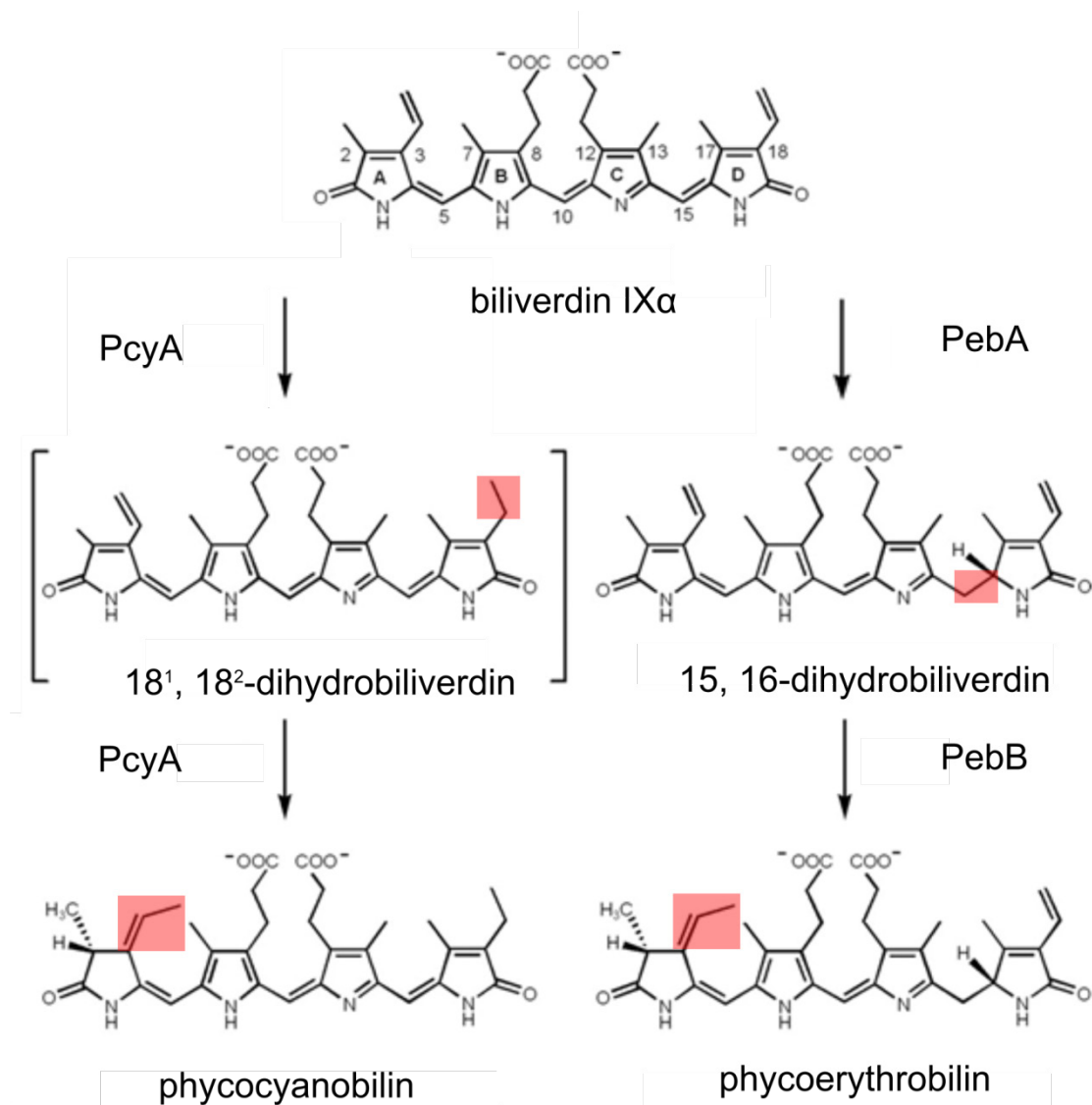


**Figure 1.5. Schematic showing the synthesis of phycocyanin and phycoerythrobilin from biliverdin IX $\alpha$ .** Phycocyanobilin is synthesised from biliverdin IX $\alpha$  in a two step process catalysed by phycocyanobilin:ferredoxin oxidoreductase (PcyA). Phycoerythrobilin is synthesised from biliverdin IX $\alpha$  by the action of 15,16-dihydrobiliverdin:ferredoxin oxidoreductase (PebA) and phycoerythrobilin:ferredoxin oxidoreductase (PebB). Adapted from Dammeyer and Frankenberg-Dinkel, (2006)

### 1.3.6 Carotenoids

Carotenoids are present in many light harvesting complexes and there is great chemical and structural variability in this class of pigments, so only the carotenoids relevant to *Synechocystis* will be discussed here. The major carotenoids commonly found in cyanobacteria are  $\beta$ -carotene, echinenone, myxoxanthophyll and zeaxanthin (**Figure 1.6**). These pigments are structurally similar and all contain extended conjugated double bond systems that facilitate the delocalisation of electrons and consequently allow for the absorption of light energy (Armstrong, 1994; Armstrong, 1997). These pigment molecules are relatively hydrophobic and are incorporated into the light harvesting pigment-protein complexes in cyanobacterial thylakoid membranes. Carotenoids also contribute to the structural stability of the protein complexes in which they reside (Armstrong, 1994; Armstrong, 1997).

Carotenoids serve multiple functions in cyanobacteria one of which is to act as accessory light harvesting pigments; they absorb light energy in the 450-570 nm region of the spectrum and transfer it to neighbouring chlorophyll molecules (Cogdell and Frank, 1987). Chlorophylls have very low absorption within this wavelength range, therefore carotenoids increase the proportion of the spectrum that can be utilised to drive photosynthesis in organisms that use chlorophyll as their primary photosynthetic pigment. Another function of carotenoids is to prevent photo-oxidative damage; under high light conditions excited chlorophyll molecules are unable to pass on their excitation energy as their neighbouring chlorophyll pigments are already in an excited state. When this happens chlorophyll can enter a long lived triplet state ( $^3\text{Chl}^*$ ) and in this state chlorophyll can react with oxygen to produce singlet oxygen ( $^1\text{O}_2^*$ ) which is a highly reactive and potentially damaging species. Carotenoids prevent photo-oxidative damage by rapidly quenching both ( $^3\text{Chl}^*$ ) (Cogdell and Frank, 1987) and ( $^1\text{O}_2^*$ ) (Foote, 1976) then releasing the energy as heat through internal conversion.

### 1.3.7 Carotenoids biosynthesis

The synthesis of  $\beta$ -carotene, echinenone, myxoxanthophyll and zeaxanthin begins with successive condensation reactions of the 5-carbon isoprene units which ultimately produces the 40-carbon phytoene (Armstrong, 1997). The next steps involve multiple desaturation reactions that introduce double bonds into the hydrocarbon chain; the end product from these desaturation reactions is lycopene which has an extensive conjugated double bond system (Armstrong, 1997). Through cyclisation of lycopene and subsequent modifications to ends of the hydrocarbon chain all four of the major carotenoids can be derived as shown in **Figure 1.6**, although the precise details of these biosynthetic pathways are not fully understood (Armstrong, 1997).

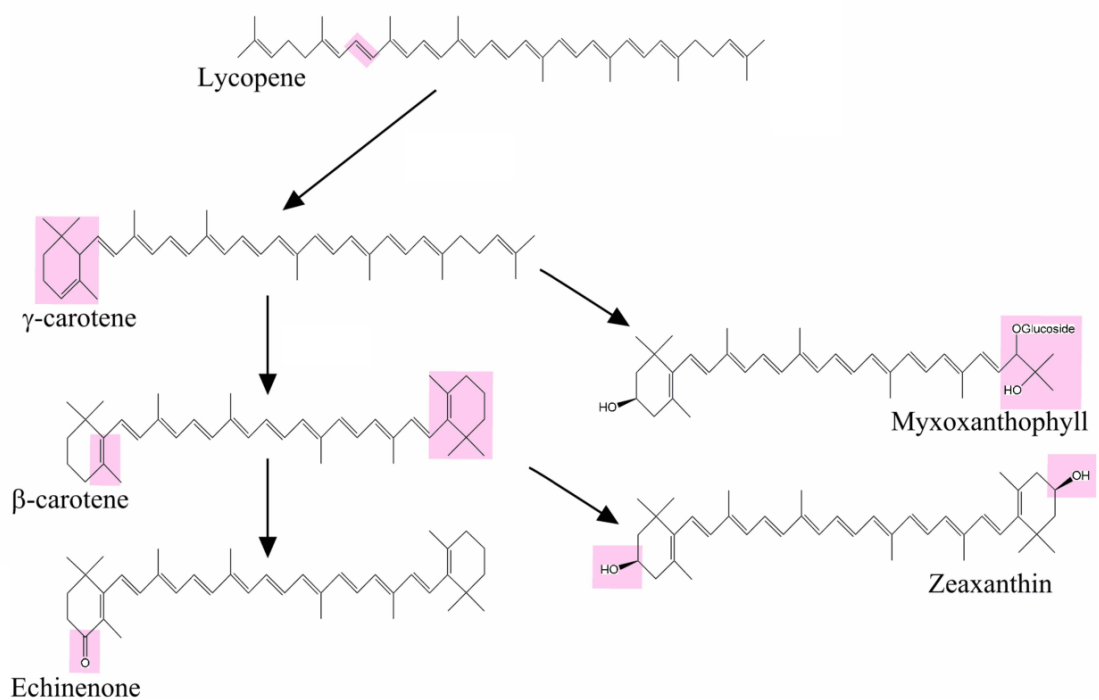


**Figure 1.6. Final stages of carotenoid biosynthesis.** Lycopene is a precursor for the four major carotenoids in cyanobacteria;  $\beta$ -carotene, zeaxanthin, myxoxanthophyll and echinenon. Chemical modifications are shown in pink.

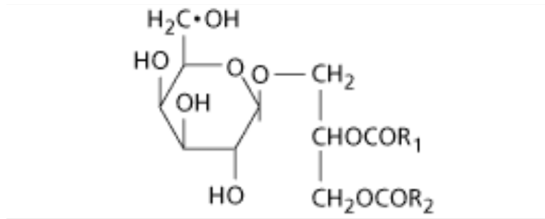
## 1.4 Cyanobacterial lipids

There are four major types of lipid found in cyanobacterial thylakoid membranes (**figure 1.7**); monogalactosyldiacylglycerol (MGDG), digalactosyldiacylglycerol (DGDG), sulfoquinovosyldiacylglycerol (SQDG) and phosphatidylglycerol (PG); the abundance of MGDG, DGDG, SQDG and PG has been measured in *Synechocystis* at 37 %, 20 %, 29 % and 14 % respectively (Wada and Murata, 2007). The lipid composition is similar to that of eukaryotic plants and different to that of most bacteria, as bacteria mainly contain phospholipids as opposed to glycolipids (Stanier and Bazine, 1977). The crystal structure of PSII (Umena *et al.*, 2011) has revealed the presence of 20 lipid molecules associated with the PSII complex; six molecules of MGDG, five molecules of DGDG, 4 molecules of SQDG and five molecules of PG. The majority of these lipids are found close to the D1/D2 reaction centre and are believed to facilitate the removal of damaged D1 during PSII repair (Umena *et al.*, 2011). With the exception of one molecule of MGDG, all of the MGDG and DGDG molecules were located on the luminal face of the complex whereas all of the SQDG and PG molecules were associated with the stromal face of the membrane (Umena *et al.*, 2011). It has been suggested that the hydrophilic head groups of SQDG and PG are unable to traverse the lipid bilayer, explaining their presence on the stromal face of the membrane. It is also believed that the relatively hydrophobic glycolipids MGDG and DGDG are able to cross the membrane to occupy its luminal face (Umena *et al.*, 2011). The crystal structure of PSI (Jordan *et al.*, 2001) has shown there to be one molecule of MGDG and three molecules of PG present on the stromal side of the membrane. Lipids have also been found to associate with cytochrome  $b_6f$ ; one molecule of SQDG and two molecules of MGDG were found to crystallise with cytochrome  $b_6f$  by Stroebel *et al* (2003) and two molecules of PG were found in the cytochrome  $b_6f$  complex by Kurisu *et al* (2003).

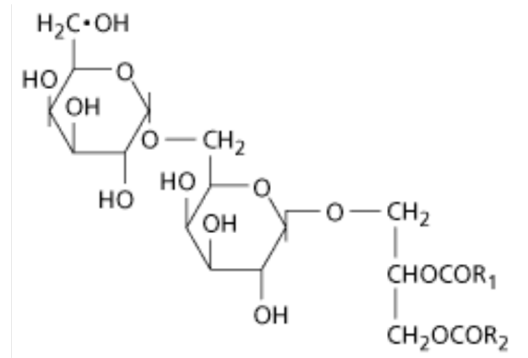
In *Synechocystis* the fatty acid groups in the lipids tend to be C16 and C18 carbon chains, where the level of desaturation is partially dependent on the temperature at which the cyanobacteria are grown at (Wada and Murata, 2007). The major fatty acid is palmitic acid (16:0) (Wada and Murata, 1990) which accounts for roughly half of the

fatty acid content regardless of growth temperature and does not undergo desaturation in response to lower temperature growth conditions. The other major fatty acids in *Synechocystis* are; 18:1, 18:2 and  $\gamma$ -18:3 which account for 30-40 % of the fatty acid content of the cell (Wada and Murata, 1990). The amount of  $\gamma$ -18:3 acid is seen to increase and the levels of 18:1 and 18:2 acids are seen to decrease as the growth temperature decreases, indicating that the latter fatty acids are undergoing desaturation in response to the decreased temperature (Wada and Murata, 1990). This increase in the level of tri-unsaturated fatty acids is presumably to counteract the effects of decreased lipid fluidity at lower temperatures. Interestingly the  $\alpha$ -18:3 fatty acid, which could not be detected at higher growth temperatures of 38 °C and 34 °C, was found to account for 10 % of lipid content in *Synechocystis* when the growth temperature was 22 °C.

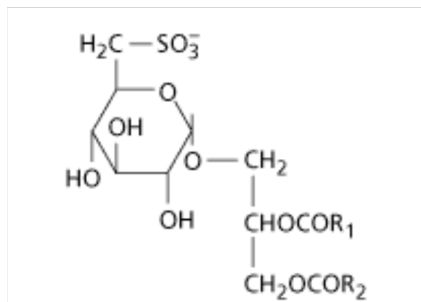
The fatty acid composition of thermophilic cyanobacteria is similar to that of *Synechocystis* in that the major fatty acid is palmitic acid (16:0) however polyunsaturated fatty acids tend to be present at a significantly lower level or are often completely absent (Maslova *et al.*, 2004). In response to lower temperatures the levels of 18:3 acids are not seen to increase as they do in *Synechocystis*; instead the levels of the 18:1 acid are increased and the levels of 16:0 are decreased (Maslova *et al.*, 2004). The increased ratio of unsaturated fatty acids to saturated fatty acids is believed to counter the effects of the decreased membrane fluidity induced by lower temperatures.



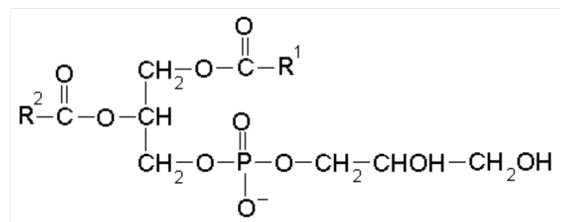
Monogalactosyldiacylglycerol



Digalactosyldiacylglycerol



Sulfoquinovosyldiacylglycerol



Phosphatidylglycerol

**Figure 1.7. Lipids in cyanobacteria.** The four major lipids in cyanobacteria are monogalactosyldiacylglycerol, digalactosyldiacylglycerol, sulfoquinovosyldiacylglycerol and phosphatidylglycerol. The fatty acids chains attached to the glycerol molecule in these lipids vary between species of cyanobacteria. Adapted from <http://5e.plantphys.net/article.php?ch=t&id=20>

## 1.5 Light-harvesting complexes in *Synechocystis*

### 1.5.1 Photosynthetic unit

Three types of pigment-containing protein complexes are responsible for the absorption and transfer of light energy in *Synechocystis*, two of which also utilise the energy for the purposes of driving charge separation. Phycobilisomes are large assemblies of bilin-containing proteins (phycobiliproteins) that are attached to the cytoplasmic surface of the thylakoid membrane (Mullineaux, 2008) (**Figure 1.8**); they are responsible for absorbing light energy and transferring it to the photosystem I (PSI) and photosystem II (PSII) complexes (Mullineaux, 2008). The phycobiliproteins that are present in phycobilisomes are; allophycocyanin, phycocyanin and phycoerythrin which contain; 2, 3 and 5 bilin pigments respectively (MacColl, 1998). Phycobilisomes do not have a fixed size and can be composed of hundreds of phycobiliproteins (MacColl, 1998) and hence they can contain hundreds of bilin pigments. PSI is a membrane bound chlorophyll-containing protein complex that typically exists in a trimeric configuration (Jordan *et al.*, 2001). Trimeric PSI contains 288 molecules of chlorophyll *a* which allows for the absorption of light energy to drive charge separation in its special pair of chlorophyll molecules (P700) (Jordan *et al.*, 2001). PSII is a membrane-bound chlorophyll-containing protein complex that typically exists in a dimeric state and absorbs light energy to drive charge separation; dimeric PSII contains 70 molecules of chlorophyll *a* (Umena *et al.*, 2011). By using H<sub>2</sub>O as an electron donor, O<sub>2</sub> is liberated as a result of the redox photochemistry of PSII (Popelkova and Yocum, 2011). This is of obvious importance as the global output of PSII is responsible for maintaining atmospheric levels of O<sub>2</sub> that allow aerobic life to survive. The cytochrome *b<sub>6</sub>f* complex is the other protein complex in the photosynthetic unit; it typically exists in a dimeric state and links electron transport between PSII and PSI at the same time as mediating the transport of H<sup>+</sup> ions across the thylakoid membrane (Kurusu *et al.*, 2003). The electron transport chain of the photosynthetic unit is summarised in **Figure 1.9**.

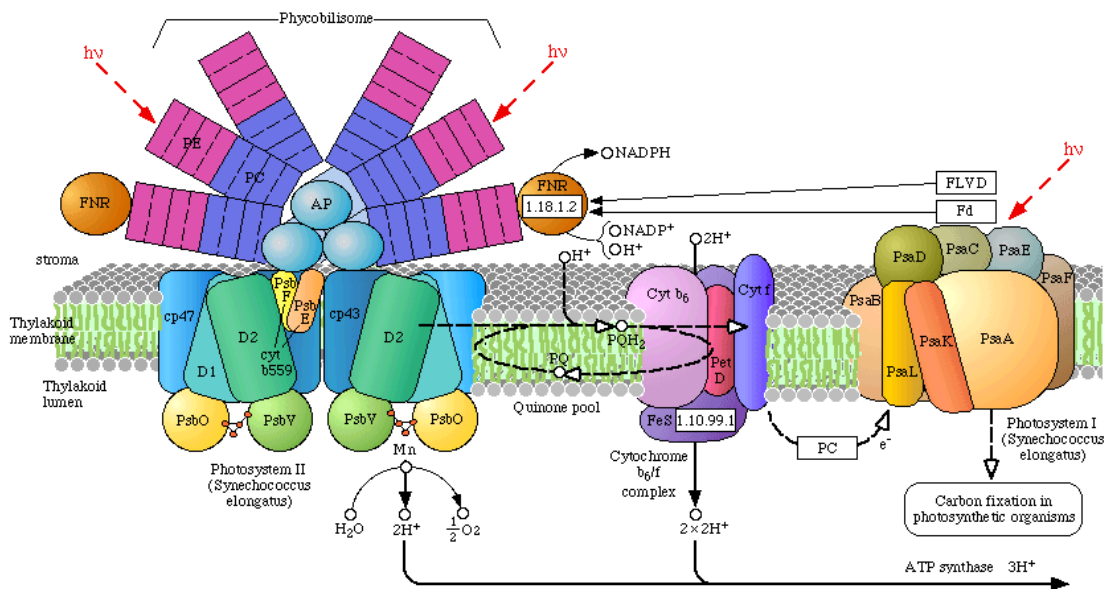


**Figure 1.8. Proteins of the photosynthetic unit.** Phycobilisomes are antenna complexes that channel light energy into the reaction centres; mainly to PSII. PSII accepts electrons from  $H_2O$  and reduces plastoquinone which diffuses through the internal structure of the membrane bilayer to donate electrons to the cytochrome  $b_6f$  complex. The cytochrome  $b_6f$  complex in turn reduces plastocyanin or cytochrome  $C_6$  which diffuses through the thylakoid lumen to donate electrons to PSI. PSI then reduces ferredoxin which goes on to interact with ferredoxin-NADP<sup>+</sup> reductase (FNR) which uses ferredoxin to reduce NADP<sup>+</sup> to NADPH. The electron transport chain is coupled to the translocation of  $H^+$  ions from the cytoplasm into the thylakoid lumen to produce a proton gradient; this proton gradient is then utilised to drive ATP synthesis. (<http://www.chm.bris.ac.uk/motm/oec/images/phyco.gif>)

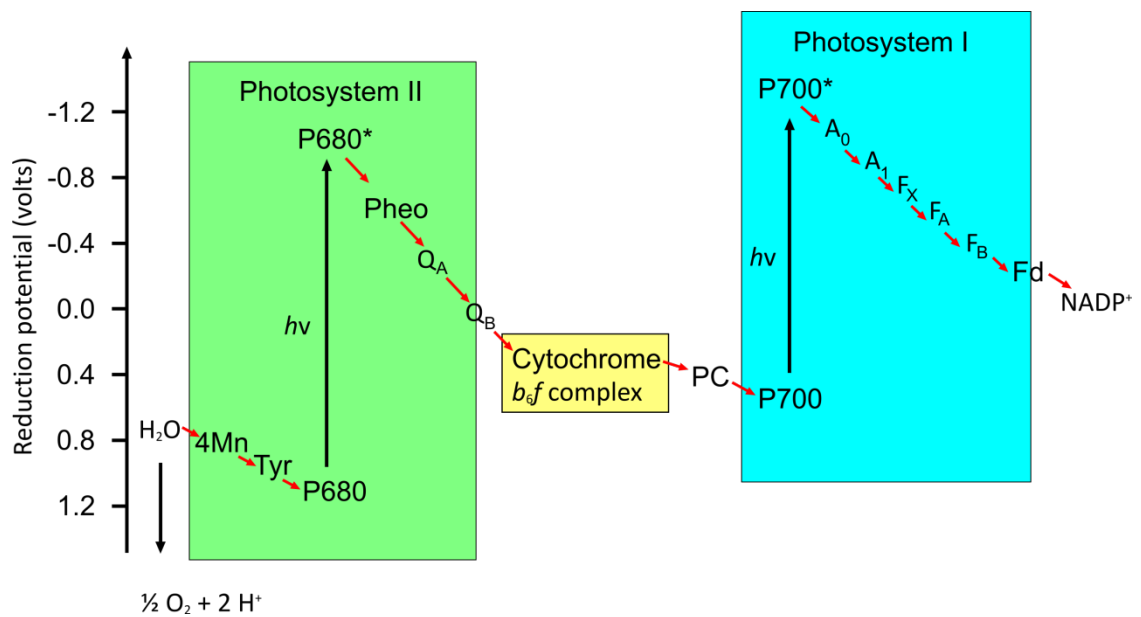


**Figure 1.9. Z-scheme.** This schematic shows the electron transport pathway from the initial electron donor, H<sub>2</sub>O, to the final electron acceptor, NADP<sup>+</sup>. The various electron transport cofactors associated with PSII are highlighted in green and the cofactors associated with PSI are highlighted in blue. Red arrows indicate electron transport. The values for reduction potential are approximate.

### 1.5.2 Phycobilisomes

Phycobilisomes are large pigment-protein assemblies that are associated with the cytoplasmic face of the thylakoid membrane and act as an antenna for the reaction centres (Mullineaux, 2008). The pigment-containing proteins that make up the phycobilisome are phycoerythrin, phycocyanin and allophycocyanin which are heterodimers of  $\alpha$  and  $\beta$  subunits (Arteni *et al.*, 2009). These proteins are termed biliproteins as they have bilin pigments covalently attached to them and absorb light in the 500–650 nm range (Liu *et al.*, 2005). Negative stain TEM of phycobilisome complexes has been used for single particle reconstruction to show the structure of the phycobilisome (**Figure 1.10**) (Arteni *et al.*, 2009). They reveal an allophycocyanin core with six rod-like structures composed of phycoerythrin and phycocyanin. Phycoerythrin is situated at the ends of the rods with phycocyanin situated at the “start” of the rods where it is attached to the allophycocyanin core. The core is made up of three cylinders, each comprising a stack of four allophycocyanin trimeric discs

(Arteni *et al.*, 2009). In addition the core also contains the ApcC and ApcE proteins which are believed to be involved with attaching the phycobilisome to the membrane and PSII (Liu *et al.*, 2005). Phycoerythrin contains the phycoerythrobilin pigment whereas phycocyanin and allophycocyanin contain phycocyanobilin. Phycoerythrin absorbs light at the shortest wavelengths with phycocyanin then allophycocyanin absorbing light at longer wavelengths. This allows energy to be funnelled from the periphery of the phycobilisome to its core before transfer to PSI and PSII (see **Figure 1.11**).

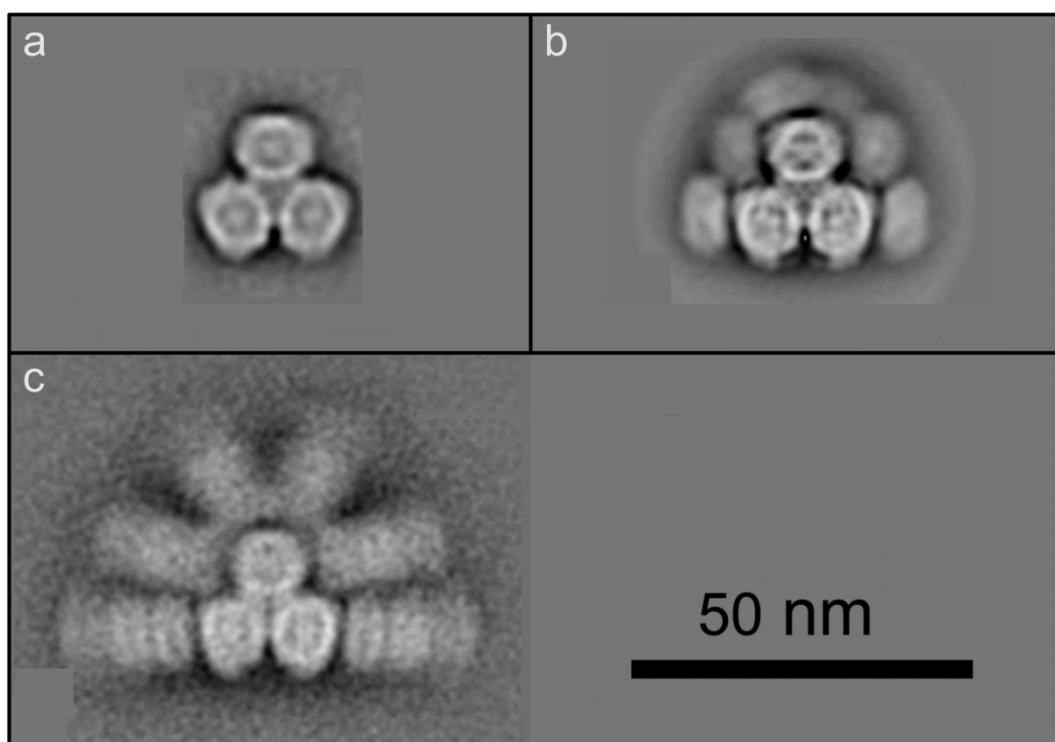


**Figure 1.10. Single particle averaging of the phycobilisome complex and subcomplexes.** The structure of the phycobilisome has been resolved through single particle analysis of negative stain TEM images. **(a)** The allophycocyanin core, **(b)** six phycocyanin subunits attached to the allophycocyanin core, **(c)** whole phycobilisome complex with six phycocyanin/phycoerythrin rods attached to the allophycocyanin core. Adapted from Arteni *et al.*, (2009).

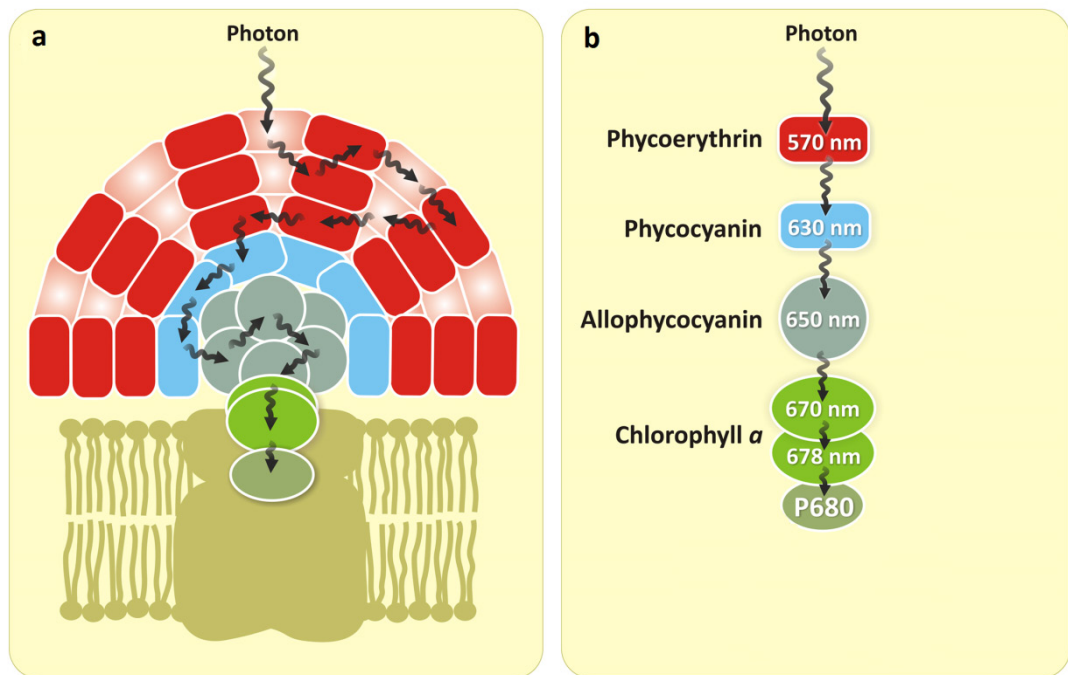


**Figure 1.11. Schematic of phycobilisomes structure.** This schematic shows the structure of the phycobilisome and the flow of energy inside the complex. **(a)** The phycobilisome has an allophycocyanin core to which phycocyanin is attached. There are 6 tubes of phycoerythrin that attach to the phycocyanin subunits. Light energy is absorbed at the periphery of the phycobilisome and funnelled to the core before being transferred to PSII. **(b)** The wavelength at which the phycobilisome subunits absorb light energy increases the closer they are to the centre of the complex enabling light energy to be funnelled to the centre of the complex. (adhttp://www.frontiersin.org/files/Articles/11696/fpls-02-00028-HTML/image\_m/fpls-02-00028-g002.jpg)

### 1.5.3 Photosystem II (PSII) structure and function

The 3D crystal structure has been solved for the PSII complex from *Thermosynechococcus elongatus* initially at 3.8 Å and then 3.0 Å (Zouni *et al.*, 2001; Loll *et al.*, 2005); the highest resolution structure to date is of the PSII complex from *Thermosynechococcus vulcanus* at 1.9 Å (Umena *et al.*, 2011). PSII has 20 constituent polypeptides, representing 35 transmembrane helices and it forms a homodimer (**Figure 1.12**). There is however evidence that suggests the presence of additional polypeptides in the native structure that cannot be seen in the crystal structures (Roose *et al.*, 2007). Not all of the constituent proteins have a clear function as it is possible to remove several of them and still retain primary photochemical activity. There are several cofactors bound to this complex that are necessary to harvest light, drive charge separation, reduce a plastoquinone acceptor and to oxidise H<sub>2</sub>O to molecular oxygen (Umena *et al.*, 2011); the overall reaction carried out by PSII can be seen in **equation 2**. The core of PSII is formed by the D1 (PsbA) and D2 (PsbD) proteins which contain the following cofactors; six chlorophyll *a* molecules, two pheophytin molecules, two plastoquinones (designated Q<sub>a</sub> and Q<sub>b</sub>) and a MnCaO<sub>5</sub> cluster (Umena *et al.*, 2011). The redox chemistry of these cofactors is essential for the oxidation of H<sub>2</sub>O. CP43 (PsbC) and CP47 (PsbB) bind 13 and 16 molecules of chlorophyll *a* respectively, these two subunits sit either side of the D1/D2 reaction centre where their chlorophyll molecules pass energy to the P680 special pair via excitation transfer (Renger and Schlodder, 2011). The PsbE and PsbF proteins form cytochrome *b*<sub>559</sub> which binds a molecule of haem and is located next to the D1/D2 reaction centre where it is important for the assembly of the reaction centre and the stability of the mature PSII complex (Umena *et al.*, 2011). It has been shown that this haem not needed for PSII mediated oxygen evolution and instead appears to play a role in photoprotection of the complex (Morais *et al.*, 2001). The PsbO, PsbU and PsbV proteins bound to the luminal face of cyanobacterial PSII are important for stabilising the oxygen evolving complex. PsbU and PsbV are not found in PSII from plants, and are replaced by the PsbP and PsbQ proteins; interestingly PsbQ has been detected in cyanobacterial PSII despite its absence in the crystal structure (Roose *et al.*, 2007). The rest of the subunits are small polypeptides many of which consist of a single

transmembrane helix; most of them are involved in stability and also play a role in the assembly of mature PSII.

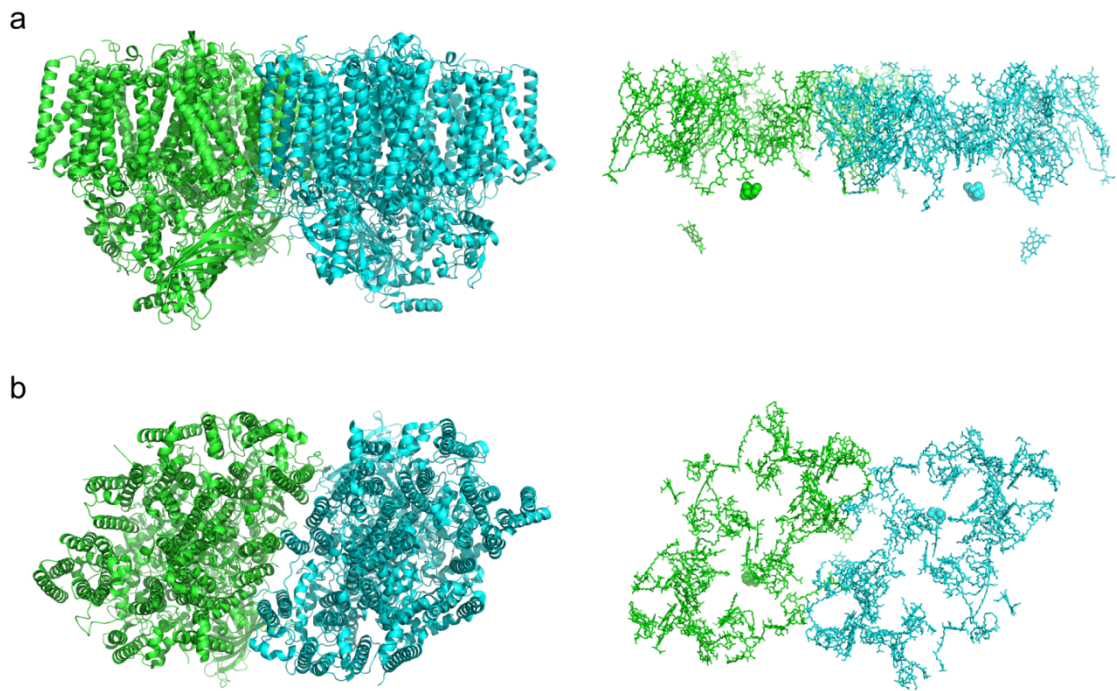
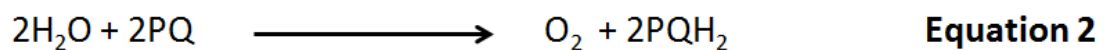


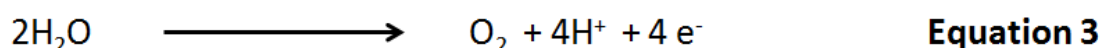
**Figure 1.12. Crystal structure of PSII from *Thermosynechococcus vulcanus* at 1.9 Å. (a)** Ribbon diagram of the protein backbone of the PSII dimer side-by-side with its associated cofactors viewed through the plane of the membrane bilayer. **(b)** The PSII complex side-by-side with its associated cofactors viewed from the luminal side of the membrane bilayer. One of the PSII monomers and its associated cofactors are coloured green and the other monomer and cofactors are coloured blue. The dimeric PSII complex contains 70 chlorophyll *a* molecules and 22  $\beta$ -carotene molecules (Umeha *et al.*, 2011).



The location of the initial charge separation event in PSII is still somewhat unclear; there is evidence to suggest it can take place in both the  $\text{P}_{\text{D1}}$  chlorophyll in the P680 special pair (Acharya *et al.*, 2012) and also the adjacent  $\text{Chl}_{\text{D1}}$  chlorophyll

(Cardona *et al.*, 2012). Regardless of which cofactor acts the primary electron donor, once charge separation has taken place, an electron is donated from Chl<sub>D1</sub> to a neighbouring pheophytin molecule. Pheophytin has two H<sup>+</sup> ions in place of the Mg<sup>2+</sup>; when this molecule is reduced it is in turn able to reduce a strongly bound plastoquinone molecule at the Q<sub>A</sub> site. The reduced Q<sub>A</sub> plastoquinone then transfers an electron to the more loosely bound plastoquinone at the Q<sub>B</sub> site. Following a second excitation of PSII and after receiving 2 electrons from Q<sub>A</sub> and 2 H<sup>+</sup> from the cytoplasm, the fully reduced Q<sub>B</sub> plastoquinone (PQ<sub>B</sub>H<sub>2</sub>) is released from PSII, then it diffuses through the membrane to the cytochrome *b<sub>6</sub>f* complex (**Figure 1.13**).

After the P680 special pair has donated an electron to Chl<sub>D1</sub> it is left with a positive charge (P680<sup>+</sup>), which is a very strong oxidant with a redox potential +1.2 V (Cardona *et al.*, 2012). The OEC contains a Mn<sub>4</sub>CaO<sub>5</sub> cluster which utilises the oxidising power of P680<sup>+</sup> to split H<sub>2</sub>O providing the electrons required to reduce P680<sup>+</sup> (**Figure 1.13**). Three manganese atoms, four oxygen atoms and one calcium atom are in a cubane-like configuration with oxo bridges between the metal atoms (Umena *et al.*, 2011). The exact mechanism of how the OEC oxidises H<sub>2</sub>O to produce O<sub>2</sub> is still not fully understood despite the 1.9 Å structure however the overall reaction can be seen in **equation 3**. The reaction requires 4 charge separation events to produce 1 molecule of O<sub>2</sub> and release 4 H<sup>+</sup> ions into the lumen.



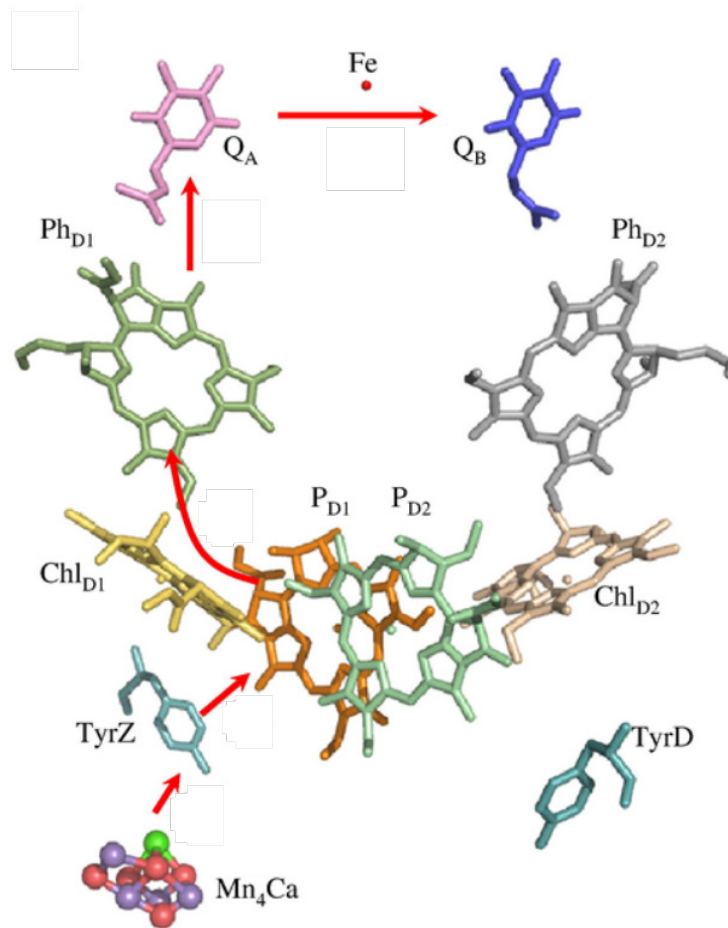


**Figure 1.13. Electron transport cofactors and charge separation in PSII.** A schematic showing the electron transport cofactors in a PSII monomer; red arrows indicate the transport of an electron between cofactors. The  $Mn_4$  containing oxygen evolving complex oxidises water and then transports electrons, one at a time to the P680 special pair via the TyrZ tyrosine residue. Either by direct absorption of light energy or by excitation transfer, charge separation takes place resulting in one electron being transferred to a molecule of pheophytin in the D1 subunit. The electron is then transferred via the  $Q_A$  plastoquinone to the  $Q_B$  plastoquinone which results in one  $H^+$  ion being taken up from the cytoplasm and the production of a semiquinone. The process is repeated and the  $Q_B$  plastoquinone gets fully reduced before being released into the quinone pool. Adapted from Cardona *et al*, (2012)

#### 1.5.4 PSII Assembly

As stated previously PSII is made up of 20 individual protein subunits and numerous cofactors which appear to be assembled in a modular fashion with the formation of PSII precomplexes which in turn are sequentially combined to form mature PSII (**Figure 1.14**). One PSII precomplex is formed by the association of unprocessed D1 protein (pD1) and PsbI (Dobáková *et al.*, 2007) (Komenda *et al.*, 2004) and another is comprised of cyt *b*<sub>559</sub> and D2 (Müller and Eichacker, 1999); these two precomplexes combine to form the reaction centre (RC) precomplex. CP43 and CP47 also form precomplexes prior to their insertion into PSII; CP47 binds associates with PsbH, PsbL and PsbT (Boehm *et al.*, 2011). This CP47 precomplex combines with the RC precomplex to form the RC47 complex (Komenda *et al.*, 2004). The CP43 precomplex is made up of CP43, PsbK, PsbZ and Psb30 (Boehm *et al.*, 2011) and then combines with RC47 (Komenda *et al.*, 2004). The Mn<sub>4</sub>CaO<sub>5</sub> is then assembled on the D1 subunit and the PsbO, PsbU and PsbV proteins are attached to the luminal face of the complex producing mature monomeric PSII which then undergoes dimerisation to create mature dimeric PSII.

There are also several proteins that are involved in the assembly of PSII that are not present in the mature complex. Psb27 has been observed to interact with CP43 and is believed to play a role in stabilising the complex as mutants in which this protein is not present have increased levels of degraded CP43 (Komenda *et al.*, 2012a). Another protein involved in PSII assembly is YFC48 which is known to bind to pD1 and has been shown to assist in the formation of the RC precomplex (Komenda *et al.*, 2008). The pD1 protein is also associated with the PrtA assembly factor which is involved in processing pD1 into mature D1. Interestingly a membrane fraction has been purified that contains pD1 bound PrtA that is not part of the thylakoid membrane or the plasma membrane (Schottkowski *et al.*, 2009). This membrane fraction has been termed the PrtA-defined membrane (PDM) and might be synonymous with thylakoid biogenesis centres (Nickelsen *et al.*, 2011). Mutants in which this protein is absent have increased levels of pD1 in these PDM fractions which suggests these areas of membrane could be the location of early PSII assembly (Nickelsen *et al.*, 2011).

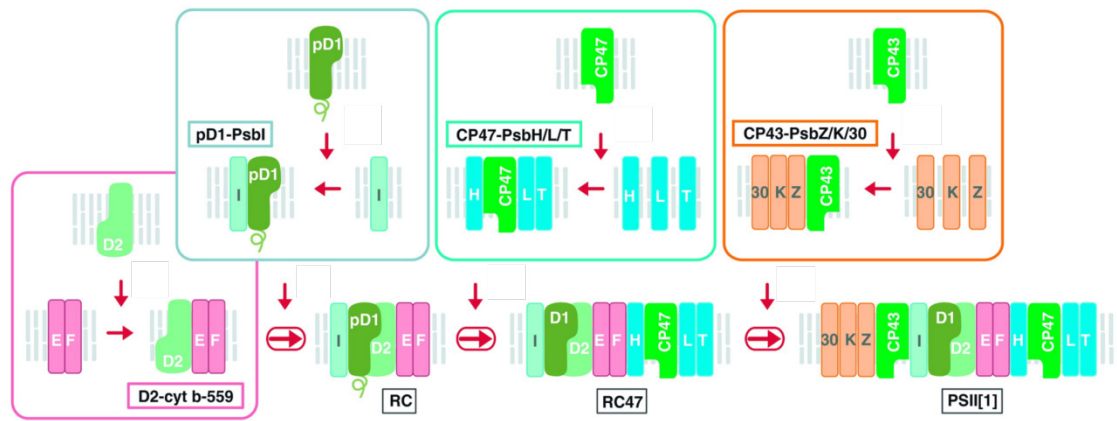


**Figure 1.14. Schematic for PSII assembly.** In this model of PSII assembly 4 precomplexes are formed and sequentially combined to yield monomeric PSII. The 4 precomplexes are; the cytochrome  $b_{559}$ /D2 precomplex, the pD1/PsbI precomplex, the CP47/PsbH/PsbL/PsbT precomplex and the CP43/PsbZ/PsbK/Psb30 precomplex. The first precomplexes to be combined are the cytochrome  $b_{559}$ /D2 precomplex and the pD1/PsbI precomplex which form the reaction centre (RC). The CP47/PsbH/PsbL/PsbT precomplex then docks with the RC to form the RC47 complex; the RC47 complex is then combined with the CP43/PsbZ/PsbK/Psb30 precomplex. Finally the  $Mn_4CaO_5$  cluster, PsbO, PsbU and PsbV of the oxygen evolving complex are assembled on the luminal face of the complex (not shown) to yield monomeric PSII. Adapted from Komenda *et al.*, (2012b)

### 1.5.5 Photosystem I structure and function

PSI is the other reaction centre in cyanobacteria and the crystal structure of PSI from *Thermosynechococcus elongatus* has been solved at 2.5 Å (Jordan *et al.*, 2001). PSI consists of 11 subunits and typically exists as a homotrimer in cyanobacteria (**Figure 1.15**). The PSI complex contains 96 chlorophyll *a* molecules and 22  $\beta$ -carotene molecules as well as a number of other cofactors that form an electron transport chain. The core complex of PSI consists of a heterodimer of the PsaA and PsaB proteins that contains most of the chlorophyll molecules including the P700 special pair, located close to the luminal side of this complex (Jordan *et al.*, 2001). Both PsaA and PsaB bind the electron transport cofactors, forming two symmetrical branches that each consist of; two chlorophyll *a* molecules and a phylloquinone ( $A_1$ ) (Jordan *et*

*al.*, 2001). These cofactors act as donors to a  $\text{Fe}_4\text{S}_4$  cluster ( $F_X$ ) which is located close to the stromal side of the complex. The PsaC protein is attached to the cytoplasmic face of the PsaA/PsaB heterodimer and contains two  $\text{Fe}_4\text{S}_4$  clusters that are designated  $F_A$  and  $F_B$ . PsaD and PsaE are located either side of PsaC on the cytoplasmic side of the complex and in combination with PsaC they provide the binding site for ferredoxin (Sétif *et al.*, 2002). PsaD is also involved in the assembly of PSI and is necessary for the insertion of PsaC, PsaE and PsaL into the complex (Xu *et al.*, 2001). The PsaL protein is important for the formation of the PSI trimer and is located in the centre of the homotrimer where it interacts with the PsaL proteins in the other two PSI complexes in the trimeric complex (Chitnis and Chitnis, 1993) (Karapetyan *et al.*, 1999). The PsaF protein is located on the opposite side of the PSI monomer to PsaL; the luminal face of this protein is involved in binding plastocyanin and cytochrome  $c_6$  (Farah *et al.*, 1995). The rest of the subunits; PsaI, PsaJ, PsaK and PsaM, are small polypeptides that are believed to be involved with stabilising the PSI; however, the loss of any one of these proteins does not significantly reduce the functionality of the protein (Schluchter *et al.*, 1996), (Xu *et al.*, 1994), (Naithani *et al.*, 2000),

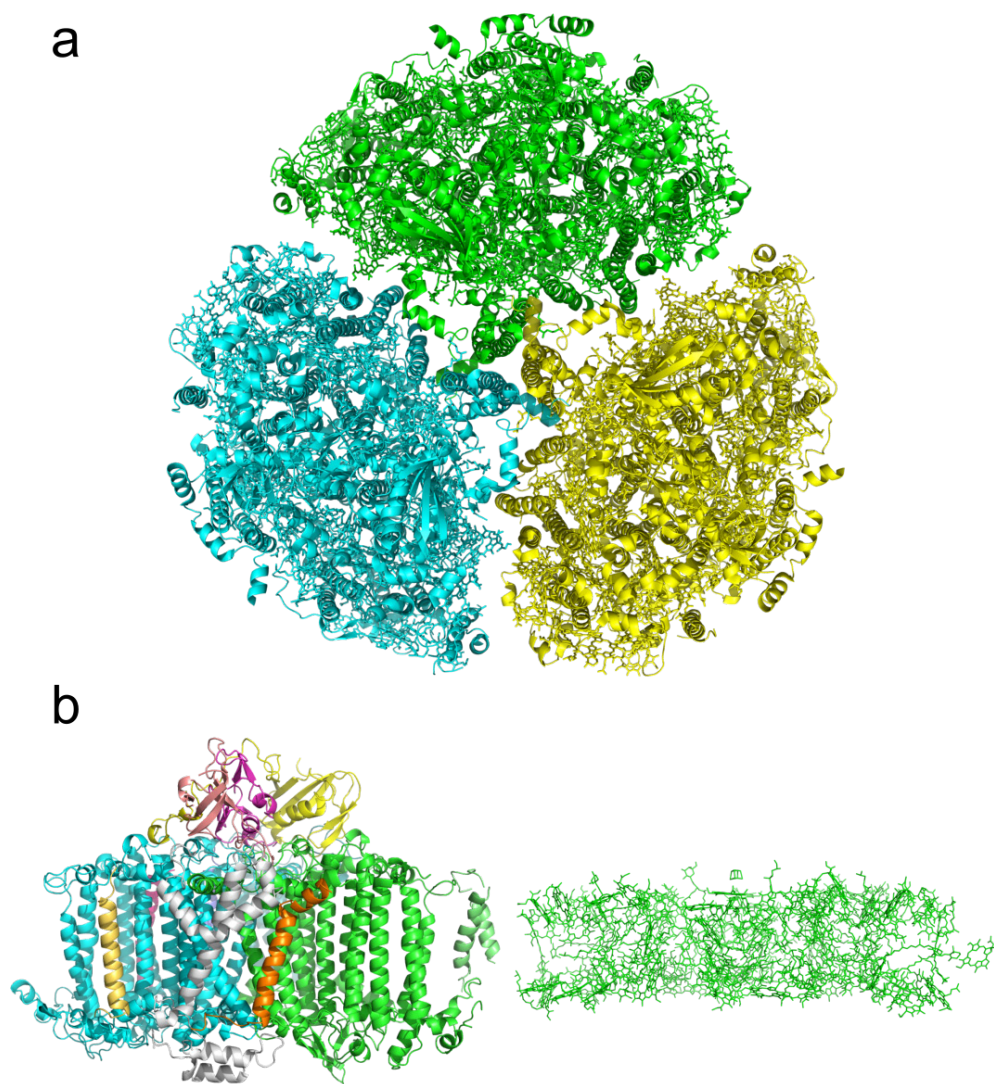


**Figure 1.15. Crystal structure of trimeric PSI from *Thermosynechococcus elongatus*.** (a) Shows the stromal face of the crystal structure of the PSI trimer with the individual monomers coloured blue, green and yellow. (b) The protein backbone of the PSI monomer is shown side-by-side with its associated cofactors as viewed through the plane of the membrane bilayer. The trimeric PSI complex contains 288 chlorophyll *a* molecules and 66  $\beta$ -carotene molecules (Jordan *et al.*, 2001). The monomeric ribbon diagram is coloured by subunit.

Following excitation transfer from one of the antenna chlorophylls in the complex, once in its excited state charge separation in the P700 special pair occurs and an electron is transferred to a neighbouring chlorophyll molecule in either the PsaA or PsaB protein (Nelson and Ben-Shem, 2004). The electron is then transferred via a chlorophyll molecule ( $A_0$ ) and a phylloquinone molecule ( $A_1$ ) to the  $F_x$  iron-sulphur cluster which is situated between the PsaA and PsaB subunits, close to the cytoplasmic side of the membrane (Nelson and Ben-Shem, 2004). The  $F_A$  iron sulphur cluster is then reduced by the  $F_x$  iron-sulphur cluster before passing the electron on to the  $F_B$  iron sulphur cluster.  $F_B$  can then donate an electron to ferredoxin, a soluble protein which is bound to the cytoplasmic side of PSI (**Figure 1.16**) (Nelson and Ben-Shem, 2004). After accepting an electron ferredoxin is released from PSI; the subsequent interactions of ferredoxin are discussed in **1.4.8**. The oxidised P700<sup>+</sup> that is produced as a result of charge separation is able to accept an electron from reduced plastocyanin which can dock to the lumenal side of PSI in order to donate an electron to the special pair (Nelson and Ben-Shem, 2004).

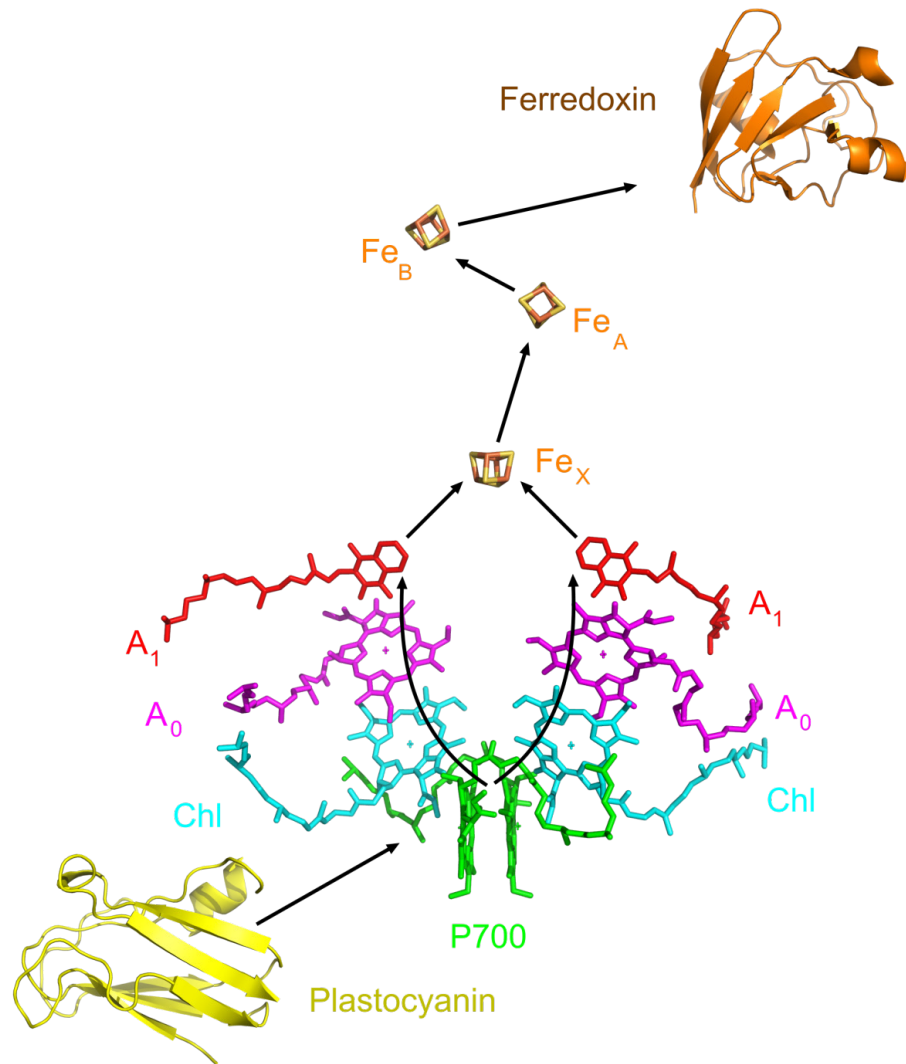


**Figure 1.16. Schematic for electron transport in PSI and the relevant cofactors.** After the excitation of P700, the special pair donates an electron to the iron sulphur cluster Fe<sub>X</sub> through an electron transport chain consisting of two chlorophyll molecules (Chl and A<sub>0</sub>) and a phylloquinone molecule (A<sub>0</sub>). There are two such electron transport chains in the PSI monomer and either can be used to transport the electron from P700 to Fe<sub>X</sub>. Fe<sub>X</sub> subsequently donates an electron to ferredoxin through the Fe<sub>A</sub> and Fe<sub>B</sub> iron sulphur clusters. Black arrows represent electron transport. Plastocyanin and ferredoxin are not to scale.

Another important aspect of the PSI complex is its incorporation into the IsiA-PSI supercomplex, comprising a PSI trimer surrounded by an 18-membered ring of the chlorophyll-containing IsiA protein (**Figure 1.17**). The IsiA-PSI supercomplex is synthesised by *Synechocystis* in response to low levels of iron in the environment (Bibby *et al.*, 2001; Boekema *et al.*, 2001; Melkozernov *et al.*, 2006). The function of the IsiA protein is still unclear although it is believed to be involved in photoprotection of PSI under low iron conditions in addition to increasing the number of pigments in the antenna system of PSI (Melkozernov *et al.*, 2003). The IsiA protein is believed to contain 16-17 molecules of chlorophyll *a* (Andrizhiyevskaya *et al.*, 2002) although the exact number is not known and there is currently no crystal structure available. The IsiA protein is also believed to contain; 2  $\beta$ -carotene molecules, 1 echinenone molecule and 1 zeaxanthin molecule (Ihalainen *et al.*, 2005). Assuming the IsiA protein contains 16 chlorophyll *a* molecules; an IsiA-PSI supercomplex consisting of a PSI trimer and an 18 membered IsiA ring would contain 576 chlorophyll *a* molecules, 102  $\beta$ -carotene molecules, 18 echinenone molecules and 18 zeaxanthin molecules. As a large proportion of the global cyanobacteria population is found in the ocean where the concentration of biologically available iron is very low this protein complex is extensively utilised.

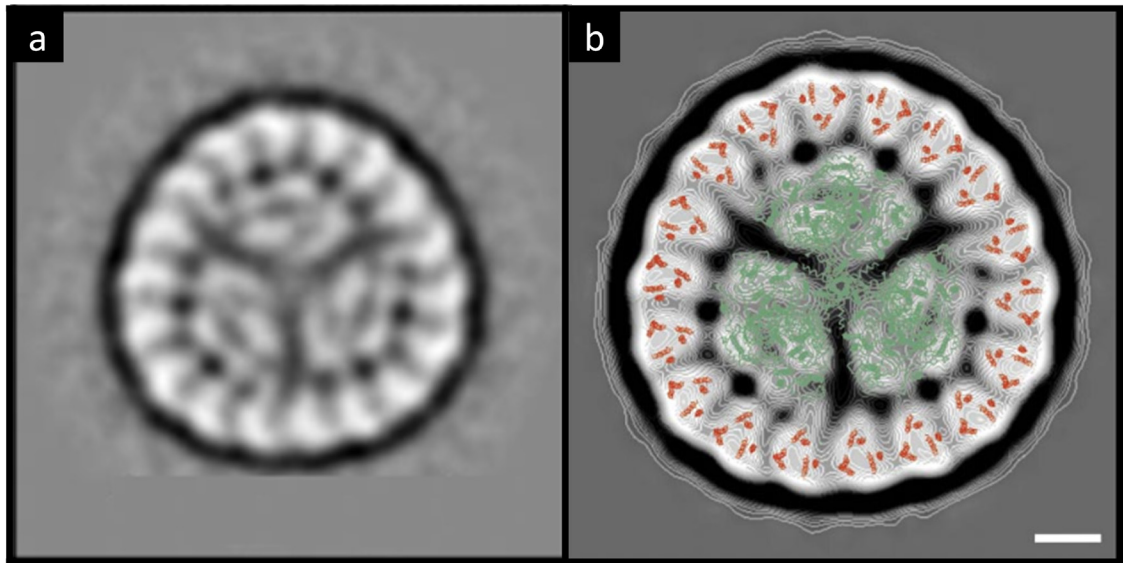


**Figure 1.17. Single particle reconstruction of the IsiA-PSI supercomplex.** TEM of IsiA-PSI supercomplexes has been used for single particle analysis to show its structure. **(a)** Reconstruction of IsiA-PSI supercomplex showing a trimeric PSI core with a ring of 18 IsiA proteins surrounding it. **(b)** Reconstruction of IsiA-PSI supercomplex with PSI and IsiA structures fitted to it. Scale bar 5 nm (Boekema *et al.*, 2001)

### 1.5.6 Photosystem I assembly

PSI assembly is less well characterised than PSII, however monomeric PSI complexes have been identified lacking PsaK (PSI\*) and both PsaK and PsaL (PSI\*\*) which are believed to represent the final stages of PSI assembly (Dühring *et al.*, 2007). A number of proteins have been identified such Ycf3, Ycf4 and Ycf37 which are suggested to play a role in the later stages of PSI assembly. In a *ycf4* knockout mutant fully assembled PSI complexes were present however at much lower levels relative to the wild type (WT) (Wilde *et al.*, 1995). The Ycf37 protein has been found to associate with the PSI monomer and the PSI\* monomer but not with the PSI trimer. A knockout mutant of the *ycf37* gene contains roughly 70% of PSI content seen in the WT and appears to completely lack the PSI\* complex. This suggests that the Ycf37 protein plays a role in forming the PSI trimer and also functions to preserve the PSI\* complex, however the mechanism through which Ycf37 functions is still unknown (Dühring *et al.*, 2006).

### 1.5.7 Cytochrome *b<sub>6</sub>f*

Cytochrome *b<sub>6</sub>f* is a multi-subunit protein complex that is found as a homodimer in cyanobacterial thylakoid membranes and is responsible for linking electron transport between PSII and PSI; the crystal structure of cytochrome *b<sub>6</sub>f* from *Mastigocladus laminosus* has been solved at 3.0 Å (Kurisu *et al.*, 2003) (**Figure 1.18**). The electron transport chain is made up of two *b*-type haems (*b<sub>p</sub>* and *b<sub>n</sub>*) that are associated with cytochrome-*b<sub>6</sub>*, an iron-sulphur cluster bound to the Rieske protein and a *c*-type haem covalently attached to cytochrome-*f*.

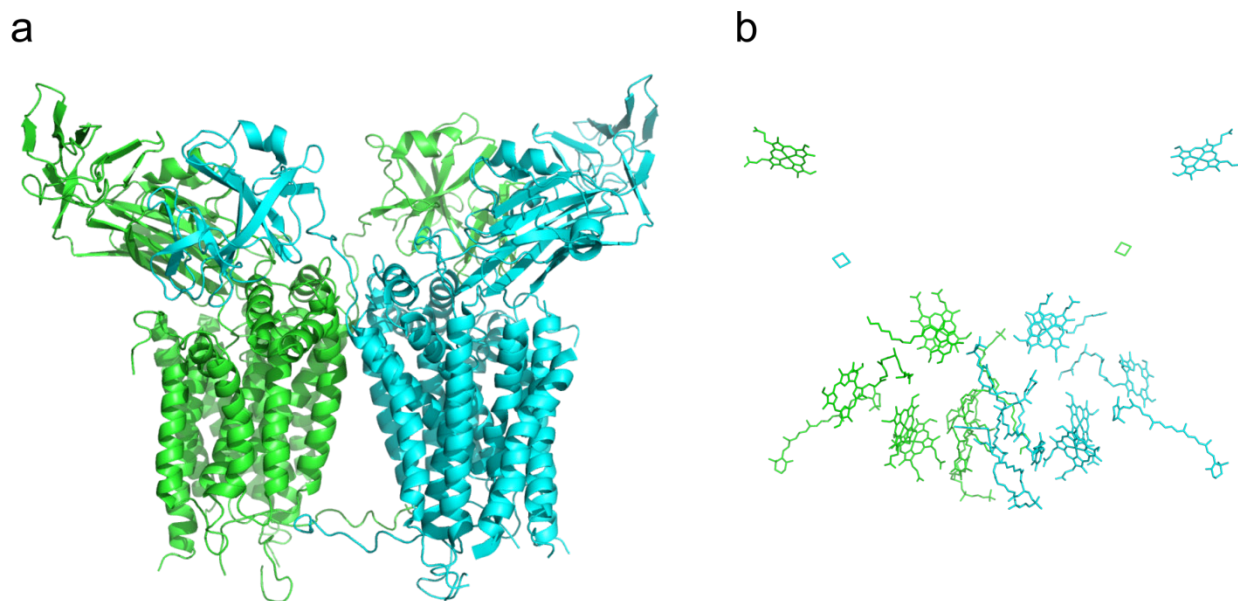


**Figure 1.18. Crystal structure of cytochrome  $b_6f$  from *Mastigocladus laminosus*.** (a) The protein backbone of the cytochrome  $b_6f$  complex with the individual monomers coloured in blue and green. (b) The cofactors associated with the cytochrome  $b_6f$  complex are coloured according to the monomer they belong to. (Kurusu *et al.*, 2003)

When a reduced plastoquinone molecule (from PSII) binds near the luminal face of the cytochrome  $b_6$  subunit it donates one electron to the iron-sulphur cluster on the Rieske protein and another to haem  $b_p$  on the cytochrome  $b_6$  subunit (Nelson and Ben-Shem, 2004) (**Figure 1.19**). This redox reaction also releases two protons from plastoquinone into the lumen of the thylakoid membrane. The electron that reduces the iron sulphur cluster in the Rieske protein is transferred to an oxidised plastocyanin protein via a *c*-type haem in the cytochrome *f* subunit (Nelson and Ben-Shem, 2004). The electron that reduces haem  $b_p$  is transferred to haem  $b_n$  and then goes on to reduce a bound oxidised plastoquinone leaving it in a semiquinone state (Nelson and Ben-Shem, 2004). A second reduced plastoquinone binds in the same place as the first and again releases two  $H^+$  ions into the lumen whilst donating an electron to the iron sulphur cluster and haem  $b_p$ . The electron donated to the iron-sulphur cluster goes on to reduce a second plastocyanin protein. The electron which is transferred to haem  $b_p$  goes on to reduce the bound semiquinone producing fully

reduced plastoquinone, this results in 2 H<sup>+</sup> ions being taken up from the cytoplasm to make the PQH<sub>2</sub> species (Nelson and Ben-Shem, 2004). The fully reduced plastoquinone is then released into the quinone pool and another fully oxidised plastoquinone molecule takes its place. The reduced plastocyanin protein goes on to interact with PSI where it reduces P700<sup>+</sup> providing the source of electrons for PSI. For every two reduced plastoquinone molecules that donate electrons to cytochrome *b<sub>6</sub>f* four H<sup>+</sup> ions are released into the thylakoid lumen and two H<sup>+</sup> ions are taken up from the cytoplasm which generates the proton motive force used to drive ATP synthesis (Nelson and Ben-Shem, 2004).

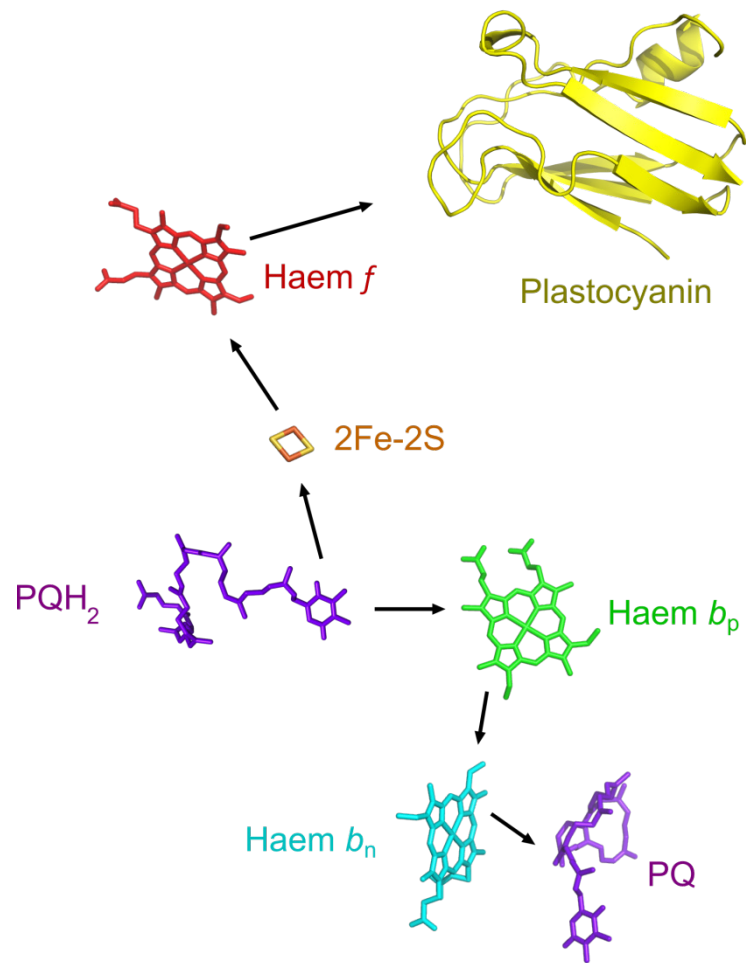
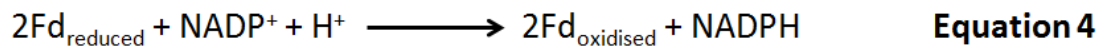


**Figure 1.19. Schematic showing electron transport in cytochrome  $b_6f$  and the relevant cofactors.** A molecule of reduced plastoquinone  $PQH_2$  donates one electron to haem  $b_p$  and one electron to the iron sulphur cluster ( $2Fe-2S$ ); the oxidation of the reduced plastoquinone molecule results in two  $H^+$  ion being released into the thylakoid lumen. The iron sulphur cluster then donates an electron to haem  $f$  which in turn donates an electron to plastocyanin which dissociates from the cytochrome  $b_6f$  complex. Haem  $b_p$  donates an electron to haem  $b_n$  which in turn reduces a bound oxidised plastoquinone molecule (PQ) to a semiquinone which results in one  $H^+$  ion being taken up from the stroma. A second reduced plastoquinone molecule donates one electron to the iron sulphur complex which is again used to reduce plastocyanin. The electron that is donated to haem  $b_p$  goes on to reduce the bound semiquinone to a fully reduced plastoquinone molecule through the uptake of one  $H^+$  ion from the stroma. The reduced plastoquinone is then released into the lipid bilayer and replaced by a molecule of oxidised plastoquinone. Black arrows indicate electron transfer. The location of  $PQH_2$  is approximate. Plastocyanin is not to scale.

### 1.5.8 The terminal electron acceptor and ATP synthesis

The reduced ferredoxin that is released from PSI goes on to interact with the membrane associated ferredoxin-NADP<sup>+</sup> reductase (FNR). The reaction that is carried out by FNR can be seen in **Equation 4** where a molecule of NADP<sup>+</sup> accepts two electrons from two molecules of reduced ferredoxin and one H<sup>+</sup> ion to produce NADPH. This means that NADP<sup>+</sup> is the terminal electron acceptor in the photosynthetic electron transport chain and is used by cyanobacteria for CO<sub>2</sub> fixation (Hermoso *et al.*, 2002).



The proton motive force that has been generated by oxidation of water and subsequent electron transport steps is utilised to drive the synthesis of ATP by the F<sub>0</sub>F<sub>1</sub> ATP synthase. The reaction that is carried out by the F<sub>0</sub>F<sub>1</sub> ATP synthase requires ADP and inorganic phosphate to synthesise ATP. ATP is used as a source of chemical energy to drive many of the metabolic processes in the bacterium. The F<sub>0</sub> complex is a membrane protein that mediates the translocation of H<sup>+</sup> ions across the membrane and the F<sub>1</sub> complex is the site of ATP synthesis (Nelson and Ben-Shem, 2004).

## 1.6 Ultrastructure of thylakoid membranes.

TEM of thin sections from *Synechocystis* cells in addition to electron tomography have made it possible to visualise thylakoid membranes. Thylakoid membranes exist as parallel invaginations of the plasma membrane known as cortical arrays that branch out from a common point of origin (**Figure 1.20**). In *Synechocystis* each invagination encloses a luminal space that is discontinuous with the periplasmic space (van de Meene *et al.*, 2006). These cortical arrays can consist of anywhere from one to approximately ten parallel invaginations of the thylakoid membrane where an individual thylakoid membrane can have a length of up to a couple of microns (van de Meene *et al.*, 2006). The arrays also tend to be located at the periphery of the cell in close proximity to the plasma membrane with the centre of the bacterium relatively free of thylakoids. The point of origin of the thylakoid membrane is believed to be a specialised area of the plasma membrane designated the thylakoid centre (Nickelsen *et al.*, 2011) however thylakoid biogenesis is still poorly understood.

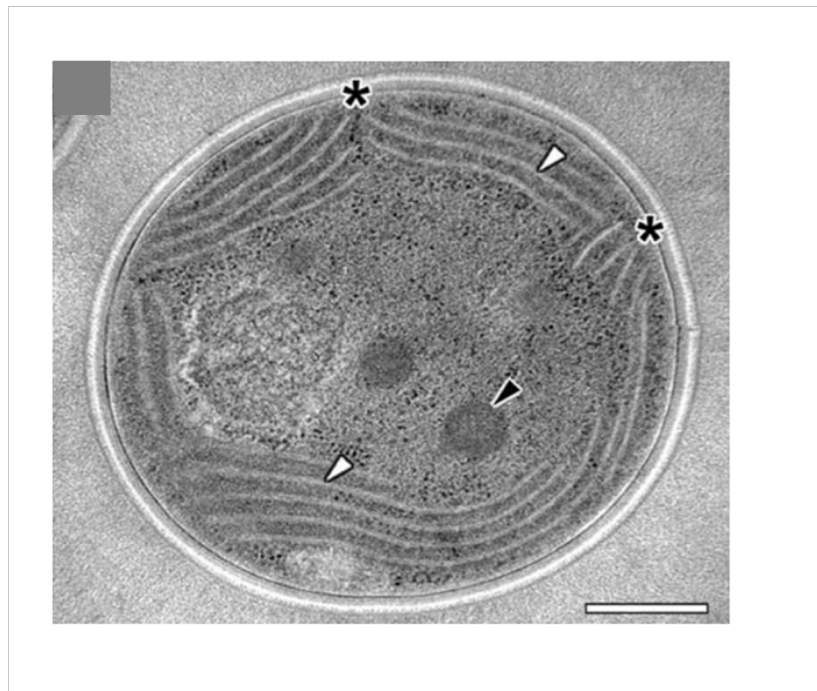


**Figure 1.20. TEM of thin sections from *Synechocystis*.** White arrowheads indicate thylakoid membranes, black arrowheads indicate carboxysomes, black asterisks indicate thylakoid convergence points. Scale bar is 200 nm. From van de Meene *et al.*, (2006)

Electron tomography of sectioned cells has been used to generate 3D reconstructions of the ultrastructure of *Synechocystis* (**Figure 1.21 and 1.22**) (van de Meene *et al.*, 2006). These tomographs show that each thylakoid invagination has an internal lumen with a width of 5-8 nm; the distance between adjacent thylakoid invaginations is roughly 30-50 nm. Electron tomographs also reveal the presence of large lipid bodies that adhere to the surface of the thylakoid and plasma membrane which are not observed in the cytoplasm, on average there were 20 of these bodies per cell. The appearance of the lipid bodies changes with the imaging angle indicating that they are made up of heterogeneous material. The location of these lipid bodies suggests they play a role in maintenance of thylakoid membranes however their exact function is unknown. The distribution of ribosomes in cyanobacterial cells can also be seen by electron tomography (van de Meene *et al.*, 2006). On average 70 % of ribosomes are present in the cytoplasm of the cell, 20 % are positioned between the plasma membrane the thylakoid membrane and 10 % are located between thylakoid membranes. The low levels of ribosomes between the thylakoid membranes suggests that proteins are likely to be synthesised in the plasma membrane or thylakoid centres before migrating to the thylakoid membrane. At some of the points where thylakoid membranes converge at the plasma membrane a cylindrical region of membrane can be seen that makes contact the sheets of thylakoid membrane (**Figure 1.22b**) (van de Meene *et al.*, 2006). This membrane cylinder is the thylakoid centre which has a diameter of 40-50 nm and can be up to 1000 nm in length; in many cases it appears to be continuous with the plasma membrane and periplasmic space. These thylakoid centres are believed to be required for biogenesis of thylakoid membranes in addition to maintaining the organisation of proteins and lipids in the thylakoid membranes (van de Meene *et al.*, 2006). At some points of thylakoid membrane convergence there is no thylakoid centre and the thylakoid membranes make contact with the plasma membrane (**Figure 1.22a**) (van de Meene *et al.*, 2006). In some cases the thylakoid membrane appears to be continuous with the plasma membrane and therefore the thylakoid lumen is continuous with the periplasmic space. The possible function of these connection points could be to allow the transport of proteins and lipids from the plasma membrane into the thylakoid membranes (van de Meene *et al.*, 2006).

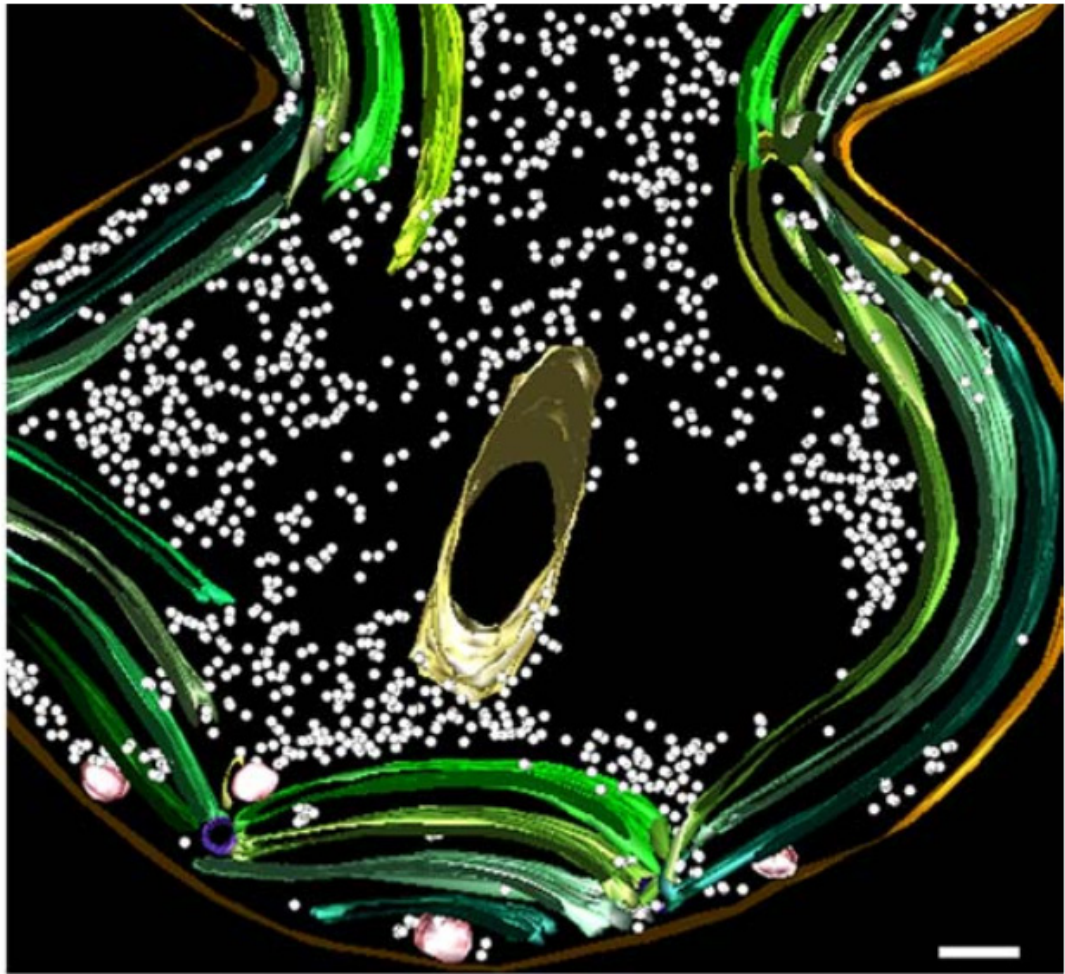


**Figure 1.21. Tomographic model of thin sections from *Synechocystis*.** The reconstruction shows the ultrastructure of *Synechocystis* in which many features can be observed; thylakoid membranes (green), plasma membrane (orange), thylakoid centres (purple), ribosomes (white), lipid bodies (pink) and a carboxysome (yellow). From van de Meene *et al.*, (2006)

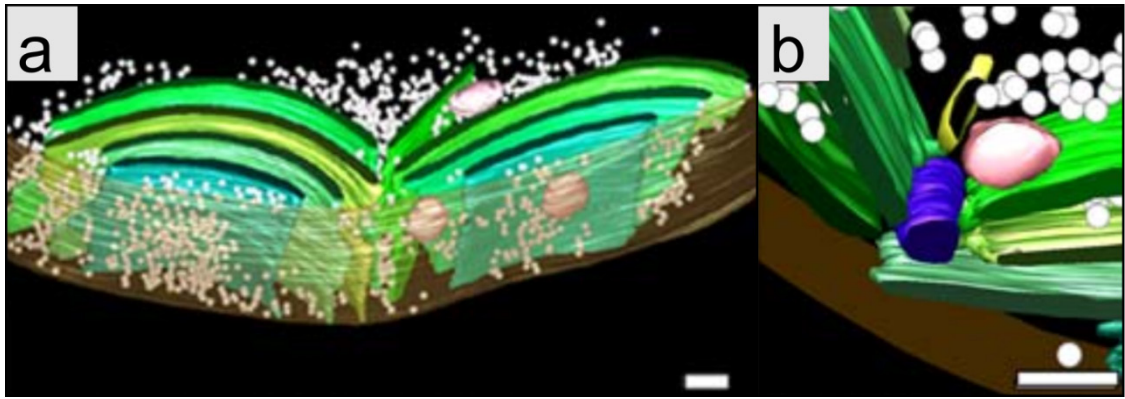


**Figure 1.22. Tomographic models of thylakoid convergence points. (a)** A reconstruction using tomography data showing a side on view of the parallel arrays of thylakoid membranes at a convergence point close to the plasma membrane. Scale bar is 50 nm. **(b)** A reconstruction using tomography data showing a thylakoid centre at high magnification. Scale bar is 50 nm. From van de Meene *et al.*, (2006)

The VIPP1 protein has been strongly implicated to have a role in thylakoid biogenesis as *vipp1* mutants are unable to produce mature thylakoids (Westphal *et al.*, 2001). VIPP1 was first identified in pea, then in *Arabidopsis thaliana*, where it is found is both in the chloroplast inner envelope and thylakoid membranes (Li *et al.*, 1994; Kroll *et al.*, 2001). Mutants in which *hcf155* (the gene that encodes VIPP1) was disrupted showed high levels of chlorophyll fluorescence which is indicative of a reduced capacity for photosynthesis. Ultrathin sections of this mutant revealed a thylakoid system remarkably different from WT with a complete absence of parallel thylakoid invaginations in addition to a complete absence of vesicles (Kroll *et al.*, 2001). In *Synechocystis* VIPP1 appears to be located exclusively in the plasma membrane (Westphal *et al.*, 2001). Disruption of the *sll0617* gene that encodes VIPP1 induces radical changes to internal cell structure in comparison to WT *Synechocystis* with a greatly elevated number of high-density carboxysomes and the complete loss of parallel thylakoid arrays at the cell periphery (**Figure 1.23**) (Westphal *et al.*, 2001). In the mutant, structures resembling membranes are distributed throughout the cell however these do not run parallel to each other and their organisation appears to be somewhat random. In addition, light-dependent oxygen evolution could not be detected in this mutant (Westphal *et al.*, 2001). While the precise function of VIPP1 is still unknown it is clearly plays an important role in thylakoid membrane biogenesis.

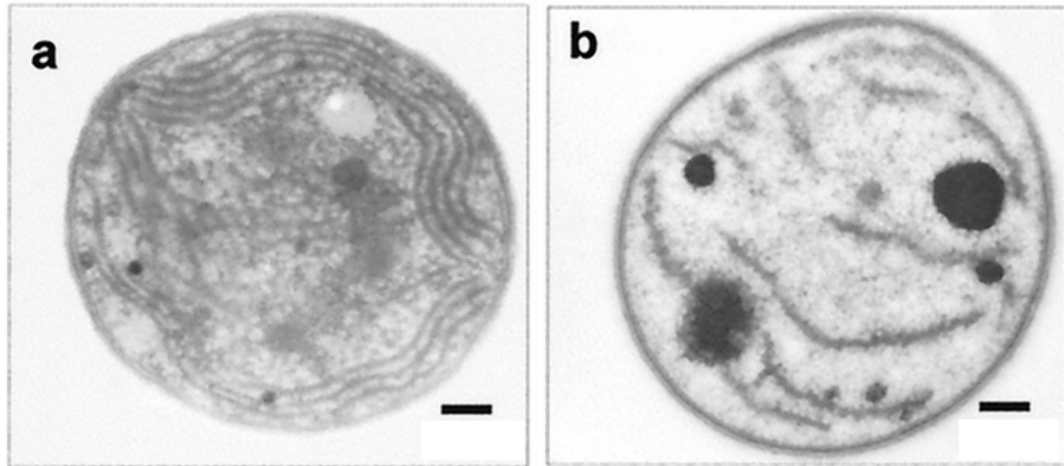


**Figure 1.23. TEM of thin sections from wild type and VIPP1 knockout mutant.** A comparison between WT *Synechocystis* and a mutant lacking the VIPP1 gene shows a remarkable difference in the ultrastructure of the two cyanobacteria. In the WT thylakoid membranes can be seen in parallel arrays around the periphery of the cell. The VIPP1 knockout mutant lacks these parallel arrays with only a few thylakoid membranes scattered throughout the cytoplasm. The VIPP1 knockout cell is also filled with carboxysomes giving it the bright white appearance. Scale bar is 100 nm. From Westphal *et al.*, (2001)

## 1.7 Electron microscopy of protein complexes in cyanobacterial thylakoid membranes

### 1.7.1 Freeze-fracture EM

Freeze-fracture EM has been used to image protein complexes in cyanobacterial thylakoid membranes and several studies have been able to identify PSII complexes which have been observed to form parallel rows with a regular spacing under certain conditions. The formation of PSII rows has been linked to state change; the rows are observed with a higher frequency in cells that are in state 1, whereas in state 2 PSII was observed in a more random distribution (Olive *et al.*, 1986; Vernotte *et al.*, 1990) (see **Figure 1.24**). The spacing and packing density of the PSII rows has been observed to change in phycobilisome mutants (see **Figure 1.24**); however the frequency with which rows are observed is not affected by the absence of phycobilisome complexes (Olive *et al.*, 1997). It has been suggested that the formation of PSII rows reduces the number of contacts between PSI and PSII and thus minimising the spill-over of excitation energy from PSII to PSI (Mullineaux, 1999). When PSII is in a more random distribution the number of contacts with PSI is greater thus increasing the spill-over of excitation energy from PSII to PSI (Mullineaux, 1999). By regulating the organisation of PSII, the bacterium is able to change the distribution of absorbed light energy between the two photosystems in response to changes in the redox state of the quinone pool (McConnell *et al.*, 2002).

The organisation of PSI and the cytochrome *b<sub>6</sub>f* complex in cyanobacterial thylakoid membranes is still poorly characterised and there are no studies where freeze-fracture EM has been used to identify PSI or cytochrome *b<sub>6</sub>f* particles in cyanobacterial thylakoid membranes.

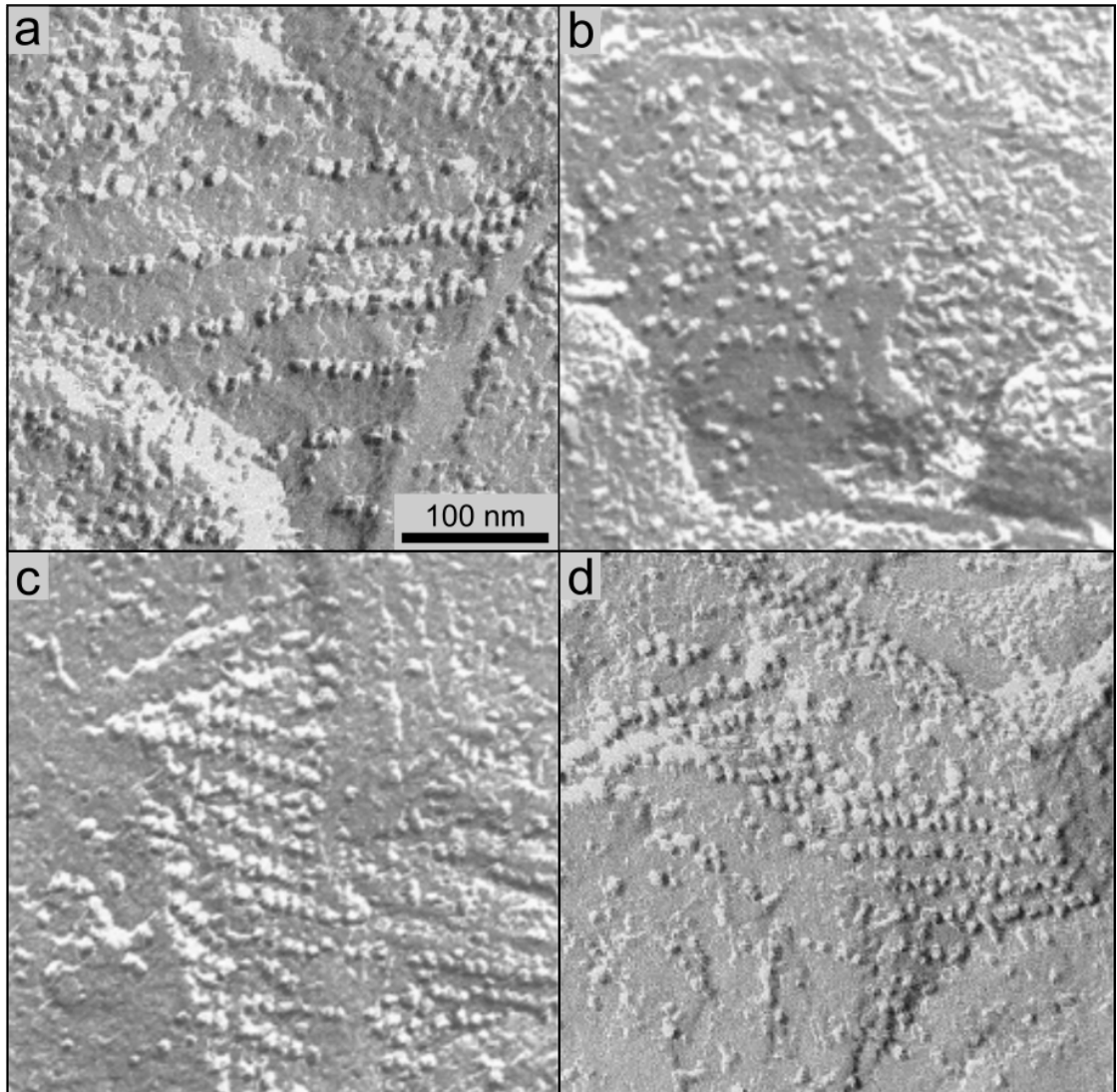


**Figure 1.24 Freeze-fracture electron micrographs of cyanobacterial thylakoid membranes.** (a) Rows of PSII can be seen in thylakoid membranes from WT *Synechocystis* cells in state 1. (b) PSII has a more random distribution in thylakoid membranes from *Synechocystis* cells in state 2. (c and d) When *Synechocystis* mutants that lack phycobilisomes are grown under conditions to induce state 1, PSII forms into rows that are closer together than in the WT. Adapted from Vernotte *et al.*, (1990) and Olive *et al.*, (1997).

### 1.7.2 Negative stain EM

Negative stain EM has been used to resolve PSII complexes in membrane fragments from detergent treated membranes; domains that exclusively contained PSII could be observed (see **Figure 1.25**) (Folea *et al.*, 2008a). These domains consisted of several adjacent rows of PSII and are an example of strict photosystem segregation in cyanobacterial thylakoid membranes (Folea *et al.*, 2008a). By image processing of membrane fragments it was possible to produce an average projection map to which the PSII crystal structure can be fitted to (see **Figure 1.25**) (Folea *et al.*, 2008a). Interestingly these PSII domains are similar to the PSII rows observed in *Synechocystis* mutants lacking phycobilisomes; however these negative stain EM images in **Figure 1.25** are of membrane fragments purified from WT *Synechocystis*. This implies that the more densely packed organisation of PSII rows seen in phycobilisome mutants can still occur in WT *Synechocystis* and that this arrangement is less easily degraded by the action of the detergent. Alternatively, it is possible that these arrays of PSII could in fact be an artefact of the detergent treatment or the dehydration that is required to image membrane samples by negative stain EM.

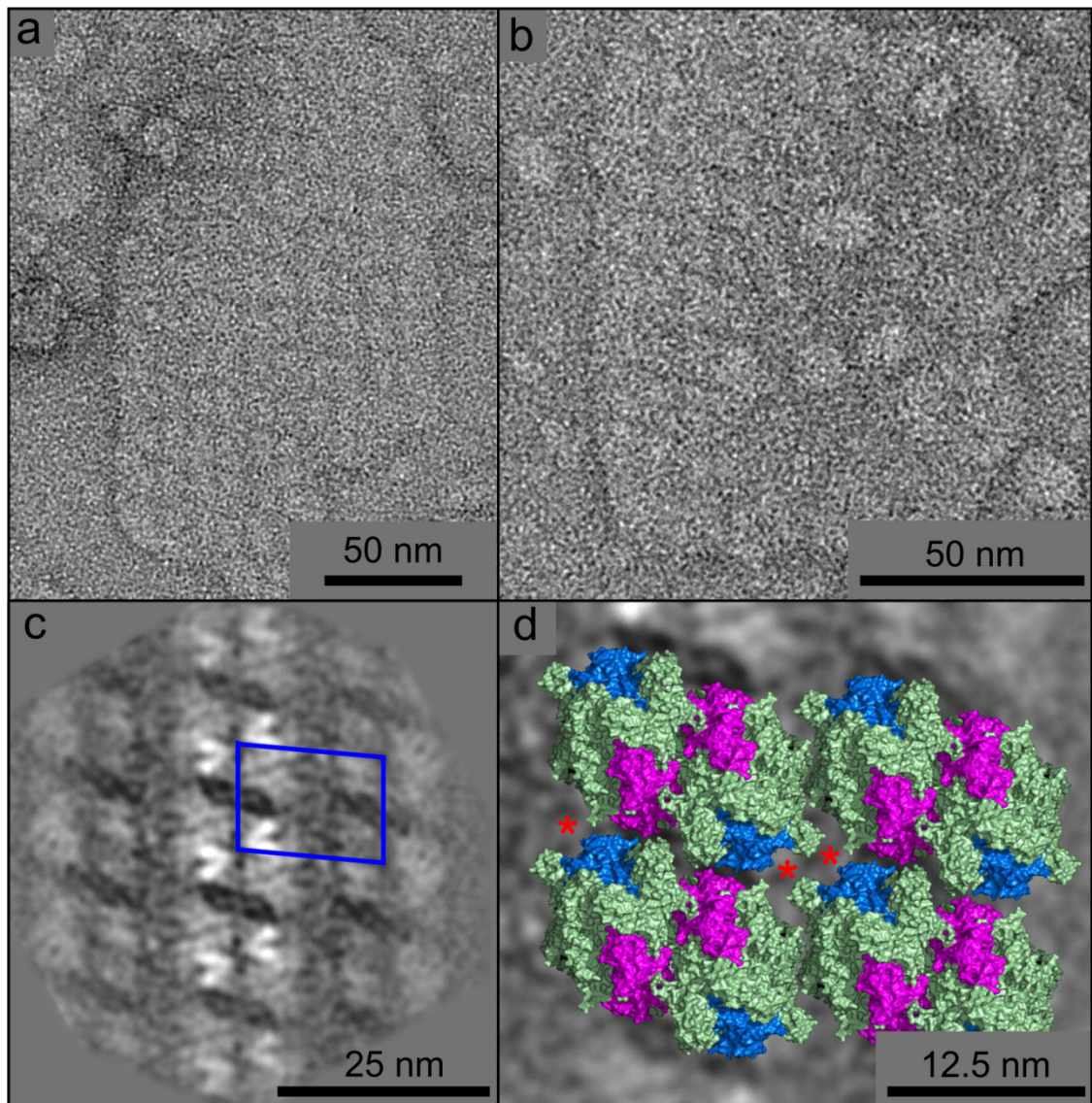


**Figure 1.25 Negative stain EM of PSII in membrane fragments.** (a and b) Membrane fragments from digitonin solubilised cyanobacterial thylakoid membranes which contain rows of PSII complexes. (c) 2D projection map of the averaged crystalline membrane fragments; the blue box shows lateral and vertical spacing of 16.7 and 12.2 nm respectively between the PSII dimers. (d) The PSII crystal structure was fitted to the reconstructed projection map; the red asterisks highlight unassigned electron density. Adapted from Folea *et al.*, (2008a).

## 1.8 Atomic force microscopy

Atomic force microscopy (AFM) is a form of scanning-probe microscopy in which the basic principle is to raster scan a probe that has an apex on the order of nanometres across the surface of a substrate and build a topological map of that surface. This instrument enables topological analysis of a wide variety of biological samples including whole cells, isolated membrane fragments and single proteins. This imaging method has several advantages over negative stain and freeze-fracture EM which have so far been the most successful techniques for imaging membrane proteins in cyanobacterial thylakoid membranes.

In freeze-fracture EM, membrane samples are rapidly frozen in the presence of a cryoprotectant before being broken using a microtome. This procedure splits cell membranes along the axis of the lipid bilayer and exposes the lipid faces of the luminal and cytoplasmic layers of the membrane. Integral membrane proteins such as PSI and PSII remain embedded in the membrane layers after the membrane is split. The surface of the membranes is then coated in an ultrathin layer of a heavy metal such as gold or platinum followed by a layer of carbon to stabilise the ultrathin heavy metal layer. The replica coats are formed by vapour deposition under vacuum meaning the frozen sample is exposed to vacuum during the procedure. The ultrathin layer of metal accurately reflects the shape of the membrane and areas corresponding to integral membrane proteins can be seen in the replica coat when it is imaged by TEM (see **Figure 1.24**). Negative stain EM sample preparation generally takes place at room temperature and requires the sample to be incubated with a heavy metal stain such as uranyl acetate before it is washed and then dehydrated. The stain adsorbs to the sample and can be visualised through TEM; areas of the sample that are heavily stained appear darker whereas areas in which there is only limited staining appear lighter (see **Figure 1.25**). As TEM is performed under vacuum the sample is exposed to vacuum during the imaging procedure.

One of the major advantages of AFM over freeze-fracture and negative stain EM is that the sample can be imaged under atmospheric conditions and at no point is the

sample exposed to vacuum during either the sample preparation or during the imaging procedure. In the case of thylakoid membranes, the vacuum could induce changes in the structure of the membrane or the organisation of the photosynthetic protein complexes. When investigating the native organisation of the photosynthetic apparatus it is an obvious benefit when using AFM that the sample is not exposed to harsh conditions that may alter its structure.

In the case of freeze-fracture EM there is the potential for disruption of the protein organisation when sample is frozen and when the membrane is split by the microtome. In AFM neither of these procedures is required; sample preparation takes place between 4-30 °C and mechanical breakage of membranes is generally not performed. The dehydration of samples that are negatively stained also a factor that could potentially alter the native organisation of protein complexes in the membrane. AFM imaging of biological samples is usually conducted under liquid in buffer conditions that are similar to the samples native environment and therefore avoids any of the potential problems that arise from dehydrating the sample. For these reasons it is clear that AFM has a number of advantages of EM based techniques for determining the native organisation of protein complexes in membranes. AFM is not without its own drawbacks; when looking at membrane samples it is often necessary to use detergents in order to produce flat membrane patches that are amenable to AFM. Such detergent treatments have to the potential to alter the structure of the membrane and the native protein organisation. AFM and EM should therefore be viewed as complementary techniques, rather than one being superior to the other, with both imaging techniques able to provide useful information on the organisation of proteins in membranes.

### 1.8.1 Instrumentation

An AFM probe consists of a small rectangular chip with a flexible cantilever protruding from one end which has a tip with a “point” that is roughly 1-10 nm in diameter. When the tip makes contact with a surface it is then raster-scanned across that surface and when it comes in contact with a topological feature the cantilever is deflected as the probe tracks over the feature. A laser is reflected off the “top” side of the cantilever into a position sensitive photo-diode that monitors the movement of the cantilever and allows the software to build up a topograph of the substrate as the probe scans over it line by line (see **Figure 1.26**).

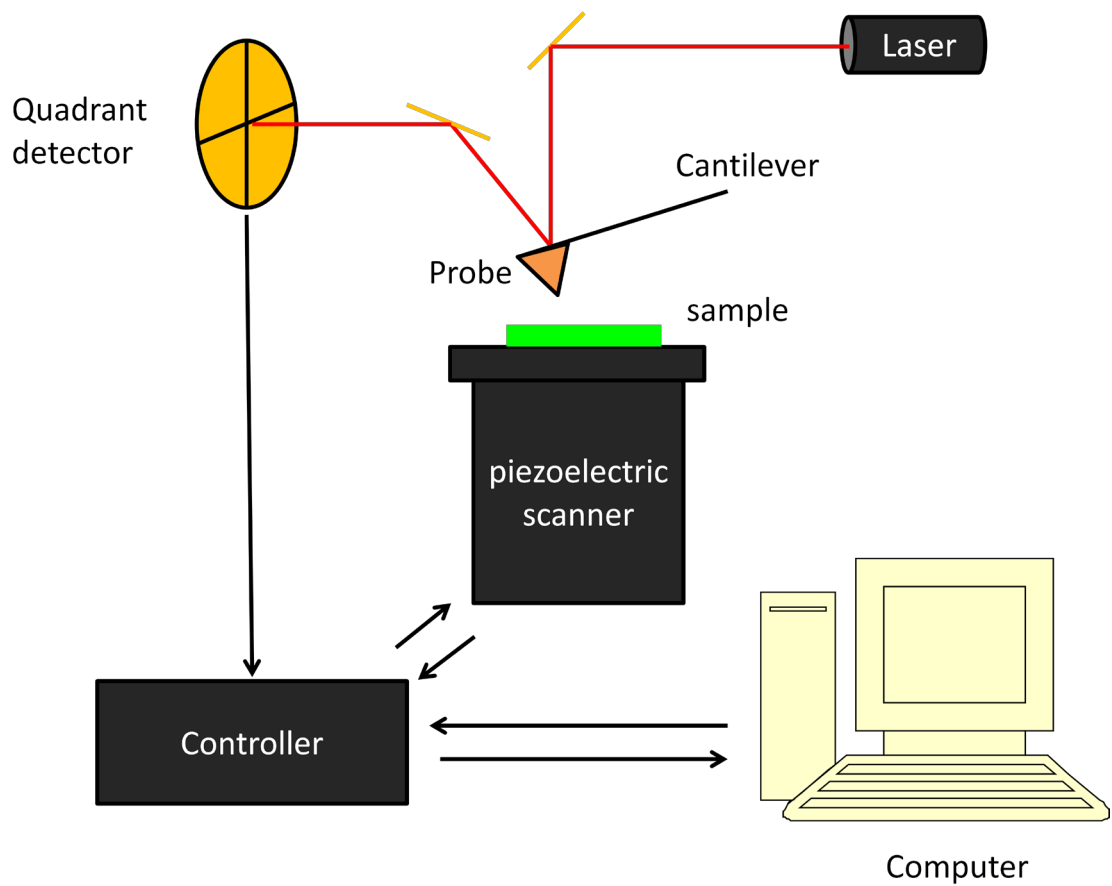


**Figure 1.26. Schematic for AFM.** This schematic shows how the components of the AFM relate to each other. The laser is focused onto the end of a gold coated cantilever which reflects the beam onto a quadrant detector. As the cantilever scans across the surface of the sample it is deflected which changes the position of the laser on the quadrant detector. The quadrant detector relays this information to the controller which manipulates the piezoelectric scanner to adjust the position of the sample relative the AFM probe to maintain the interaction with the sample. The user is able to change various imaging parameters through a computer which interfaces with the controller.

Mica often used as a substrate for adsorbing biological samples because it is atomically flat and therefore shows no significant topography when imaged by AFM. This means when biological samples are adsorbed to the mica all of the topological features that are seen can be confidently assigned to the sample and not the mica surface. The mica surface is mounted onto the top of a piezoelectric scanning stage to allow for precise movement of the sample in the x, y and z axes. Piezoelectric materials can be manipulated by applying an electric current to them causing them to expand or contract. The computer controller applies specific voltages to the piezoelectric scanner which is designed to allow for nanometre precision when moving through the x, y and z axes. The scanner moves the sample through x and y to allow the probe to scan the surface. The movement through the z-axis is regulated by a computer-controlled feedback system which ensures the probe maintains contact with the sample to provide accurate tracking across its surface.

### **1.8.2 Imaging modes**

AFM can be used for analysis of samples that have either been dried to the mica and imaged in air using an air cell or to analyse samples that are under liquid using a fluid cell. For the majority of biological samples it is preferable to image under liquid as buffer conditions that are similar to the native environment of the sample can be used.

The AFM can be run in two different modes; contact mode and tapping mode. In contact mode the probe is kept in constant contact with the sample when scanning its surface and the deflection of the cantilever can be measured. When the probe scans over a feature it causes further deflection of the cantilever; the feedback system then adjusts the height of the sample to return the deflection of the cantilever to its original position. From movement of the sample due to the feedback system the software is able to build a height profile for each scan-line over the sample. Contact mode applies a substantial amount of force to the sample which can result in the removal of structures that protrude from its surface; it can even cause the entire

sample to be swept away if it is not strongly adhered to the mica surface (Zhong *et al.*, 1993).

In tapping mode the cantilever is oscillated in the plane perpendicular to the sample so that it transiently interacts with the sample, this greatly reduces the forces applied to the sample, which is desirable when looking at biological membranes (Möller *et al.*, 1999). Different cantilevers have different resonant frequencies and the AFM can be tuned to oscillate the cantilever at the appropriate frequency.

In the case of tapping mode it is the amplitude of the resonance of the tip that is measured, and when the tip comes in contact with the sample the amplitude of the probe is reduced. The AFM feedback system will then move the sample away from the tip to return the amplitude to the defined value. The software can then build up a height profile of the sample based on its movement by the feedback system as the probe scans over it line by line

A specialised type of tapping mode is “Peak Force Tapping” (PFT) (trademark, Bruker Nano Surfaces Business) in which a force curve is measured every time the probe comes in contact with the surface of the sample. As the probe moves towards the sample it is deflected away from the surface owing to long range repulsive forces, as the probe moves closer to the sample the cantilever is pulled towards the sample owing to the short-range attractive forces. The movement of the laser that is reflected off the top of the cantilever is measured by the photo-diode. This records the magnitude of the deflection and the software is able to calculate the forces acting on the cantilever as it approaches the surface allowing it to generate the force curve (a force curve is also generated as the probe retracts from the surface of the sample). In order for these measurements to be taken the probe is oscillated a much lower frequency than in traditional tapping mode, typically 2 Hz. At this frequency the AFM is able to measure a force curve every time the probe comes in contact with the sample. By analysing the force curve it is also possible to measure a number of different properties of the sample such as the adhesion between the probe and the sample and the deformation of the sample caused by the probe. This mode therefore

gives a lot more information about the sample in addition to the height data that is not provided in standard tapping mode.

Contact mode AFM (CM-AFM) is generally accepted to have the potential for higher resolution than tapping mode AFM (TM-AFM) however the forces applied to the sample can be high enough to damage it or remove smaller pieces of membrane from the surface of the mica. It has been shown that high resolution TM-AFM can be performed on biological membranes and that individual protein complexes can be observed in these membranes (Bahatyrova *et al.*, 2004; Olsen *et al.*, 2008; Adams and Hunter, 2012). PFT allows the user to control the force that is being applied to the sample by the AFM probe with a high degree of precision. For these reasons the PFT system was the preferred mode for imaging biological samples.

### **1.8.3 Advantages and limitations of AFM**

Using AFM as an imaging technique has several advantages over traditional imaging techniques such as transmission electron microscopy (TEM). One such advantage is the facility to image samples at atmospheric pressure and under liquid in near-native buffer conditions, so the imaging procedure should have a minimal effect on the sample. By contrast TEM has to be conducted under vacuum using a heavy metal stain to visualise the sample. This procedure could be very damaging to the sample particularly in the case of cell membranes as it could disrupt the supramolecular organisation of protein complexes. AFM can also be used for very high resolution imaging with a potential lateral resolution of 0.1 nm and a potential vertical resolution of 0.01 nm. The vertical precision is of particular importance as much of the work in this study is performed on identifying integral membrane proteins from their membrane protrusions. By comparing the extremely accurate height data from the AFM with protein crystal structures it is possible to classify complexes and identify their organisation within the membrane. AFM also has a high signal to noise ratio allowing for direct imaging of single proteins in membrane patches without the need for any computational averaging or filtering that is required by other imaging methods. The topograph that is generated by imaging a sample is also a 3D model as

opposed to a 2D projection which yields more accurate information about the overall dimensions of the sample.

Whilst there are many benefits to using AFM there are also a number of drawbacks. The major factor in determining the lateral resolution is the “sharpness” of the AFM probe that is used. The process for manufacturing the AFM probes does not routinely produce probes that are sharp enough to distinguish individual proteins in a membrane patch. There can also be defects in the probes such as the presence of a second apex (known as a “double tip”) which can result in the AFM recording the same feature twice. This can require the user to test multiple probes before finding one of sufficient quality to provide high resolution images. The sample itself can also provide some challenges for the AFM as it has to be absorbed quite firmly to the surface of the mica or else the AFM probe can remove it. In addition a sample that has a lot of curvature can be problematic as the side of the probe can potentially interact with it before the apex does. This greatly diminishes the resolution of the AFM and that is why one of the main aims of the sample preparation is to make the sample as flat as possible when it is absorbed to the mica surface.

#### **1.8.4 Use of AFM to image membrane proteins in 2D crystals**

AFM has been used to image many types of biological samples; one of the first samples to be imaged at high resolution were 2D protein crystals as they have several properties that make them ideal for AFM analysis. 2D crystals are large flat arrays of highly ordered proteins that therefore adsorb easily and firmly to the mica surface. The “flatness” of the 2D crystal also allows for the AFM probe to freely scan over the sample and accurately track the protein structures that protrude from the crystal, these properties have enabled high resolution imaging of many membrane proteins that have been incorporated into 2D crystals (Schabert *et al.*, 1995; Seelert *et al.*, 2000; Scheuring *et al.*, 2002; Pogoryelov *et al.*, 2005). One example of a photosynthetic membrane protein being incorporated into a 2D crystal and imaged by AFM is that of RC-LH1 core complex from the purple bacterium *Rhodospirillum rubrum* (Fotiadis *et al.*, 2004). The AFM data shows the H-subunit of

the RC complex surrounded by an LH1 ring, both of which protrude from the surface of the lipid bilayer of the 2D crystal (see **Figure 1.27**). These topographs demonstrate how AFM can be used to identify proteins when they are imaged to high enough resolution and can be compared to their crystal structures. It also demonstrates how AFM can reveal any large-scale order in biological assemblies.

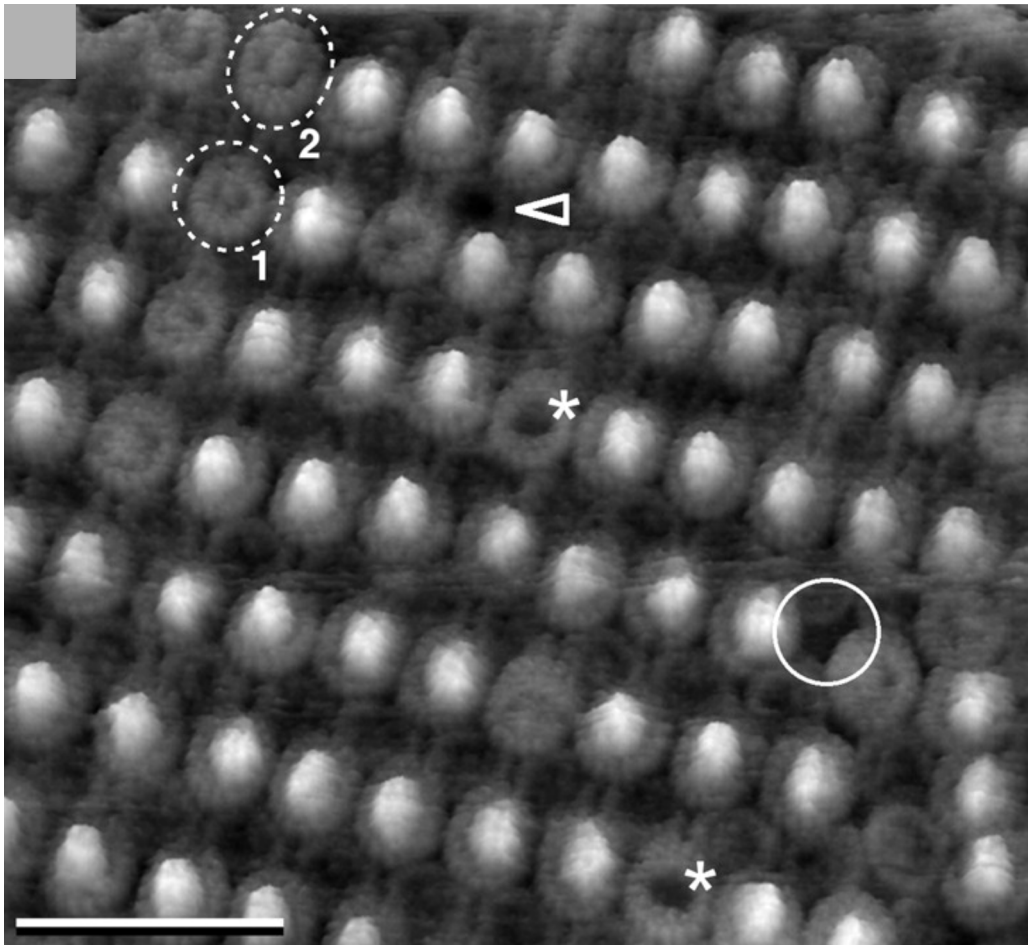


**Figure 1.27. AFM topographs showing 2D crystals of RC-LH1 from *R. rubrum*.** (a) High resolution AFM shows rows of RC-LH1 complexes in 2D crystals alternating in the up (bright rows) and down position (dark rows). The dotted circle (1) and eclipse (2) highlight RC-LH1 complexes that are missing the H-subunit of the reaction centre. Asterisks show the cytoplasmic face of LH1 rings missing the RC complex entirely; the empty arrowhead shows the periplasmic face of an LH1 complex lacking the RC complex. The solid circle highlights the lipid region of the 2D crystal. Scale bar is 40 nm. Adapted from Fotiadis *et al.*, 2004.

### 1.8.5 Use of AFM to image membrane proteins in native membranes

The potential of AFM to image the native protein architecture of cellular membranes is of particular interest for studies of photosynthetic membranes as one of the main functions of these membranes is to channel energy to reaction centres so charge separation can take place (Şener *et al.*, 2007). The organisation of the proteins in the membrane is integral to this process and as many of the crystal structures of chlorophyll and bacteriochlorophyll containing membrane proteins have been solved they can be identified from their membrane protrusions by AFM. Generally speaking membranes are not as easy to image with AFM as 2D crystals, as membranes tend to have some degree of curvature which can prevent high resolution imaging. In addition membranes have to be purified from cell lysates and contamination of the samples can interfere with the interaction between the probe and the sample. Despite these difficulties there have been several significant studies of photosynthetic membranes using AFM.

The photosynthetic membranes from many species of purple bacteria have been imaged using AFM; **Figure 1.28** shows photosynthetic membranes from several purple bacteria (Scheuring, 2006). The light absorbing proteins in these organisms assemble into ring structures in the membrane which can be resolved by AFM. Membranes can be imaged to high enough resolution for individual subunits of the ring structures to be seen.

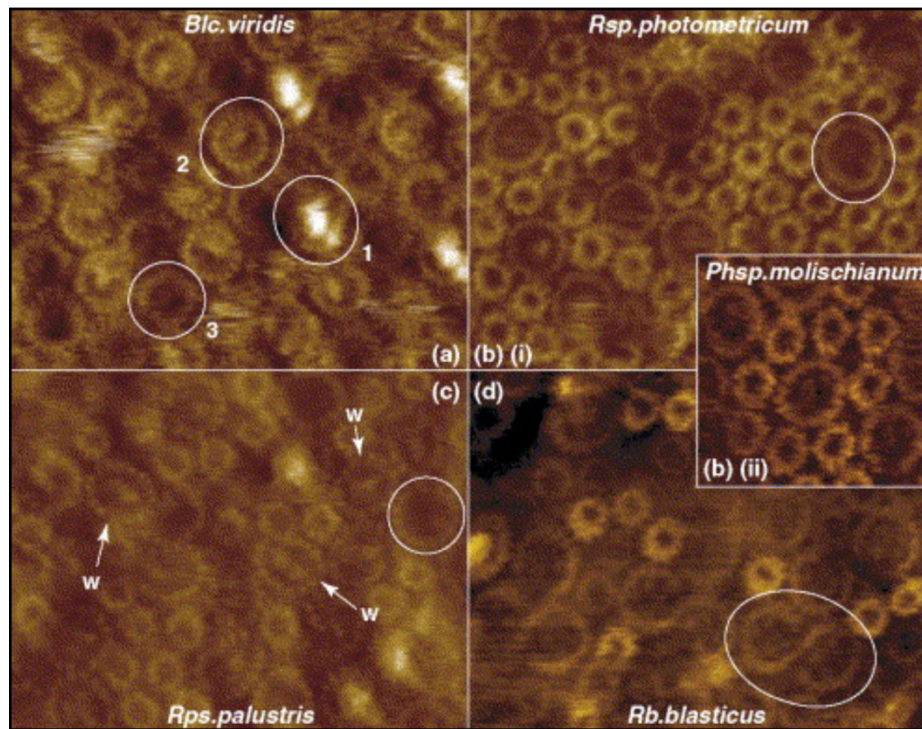


**Figure 1.28. AFM of photosynthetic membranes from different purple bacteria** (a) An AFM topograph of *Blc. viridis* membranes showing (1) an RC-LH1 complex, (2) an RC-LH1 complex lacking the tetrahaem cytochrome subunit and (3) an LH1 ring completely lacking the RC complex. (b) AFM topographs of (i) *Rsp. photometricum* and (ii) *Rsp. photometricum* membranes showing RC-LH1 complexes surrounded by LH2 antenna complexes. (c) An AFM topograph of *Rps. palustris* membranes showing RC complexes surrounded by an ellipsis of 15 LH1 subunits (white arrows). (d) An AFM topograph of *Rb. blasticus* membranes showing dimeric RC-LH1 complexes surrounded by LH1 subunits in an “S-shape” configuration. Adapted from (Scheuring, 2006).

Grana membranes from spinach have also been imaged via AFM (Sznee *et al.*, 2011; Johnson *et al.*, 2014), which is of particular interest as many of the proteins in cyanobacterial thylakoid membranes have homologues in plants. In grana stacks PSI and PSII are spatially segregated with PSI only present in the ends of the grana stack and PSII present within the grana stack. In Sznee *et al.*, (2011) grana stacks were treated to produce “inside-out” grana membrane fragments which have their luminal surface exposed; these patches were then purified and imaged via AFM. Areas of membrane that were densely packed with PSII could be identified though

AFM analysis as the oxygen evolving complex (OEC) of PSII protrudes by 5 nm from the surface of the luminal face of the membrane. By comparing the dimensions of the crystal structure with the dimensions of the membrane protrusions (**Figure 1.29**) it was possible to identify PSII. When membranes were imaged at room temperature the areas containing PSII had a relatively disordered configuration. However when the membrane fragments were incubated overnight at 4 °C there was a rearrangement of the PSII enriched domains which were seen to form numerous linear rows of PSII. As there are no reports of high resolution AFM of cyanobacterial thylakoid membranes it will be of great interest to see if the supramolecular organisation of PSII is similar to that of plants.

The cytochrome *b<sub>6</sub>f* complex has also been identified in “inside-out” grana membrane fragments where it found in nanodomains with PSII (Johnson *et al.*, 2014). By imaging the membrane fragments with an AFM probe that was functionalised with plastocyanin it was possible to measure the interaction between the cytochrome *b<sub>6</sub>f* complex and plastocyanin that was immobilised on the AFM probe. As plastocyanin does not specifically interact with PSII, this allowed for the identification of the cytochrome *b<sub>6</sub>f* complex which was previously been impossible owing to the similarity in luminal topology of the cytochrome *b<sub>6</sub>f* complex and PSII (**Figure 1.30**). Repeating this experiment in cyanobacteria would also be of great interest to determine if the same organisation of PSII and the cytochrome *b<sub>6</sub>f* complex was present.

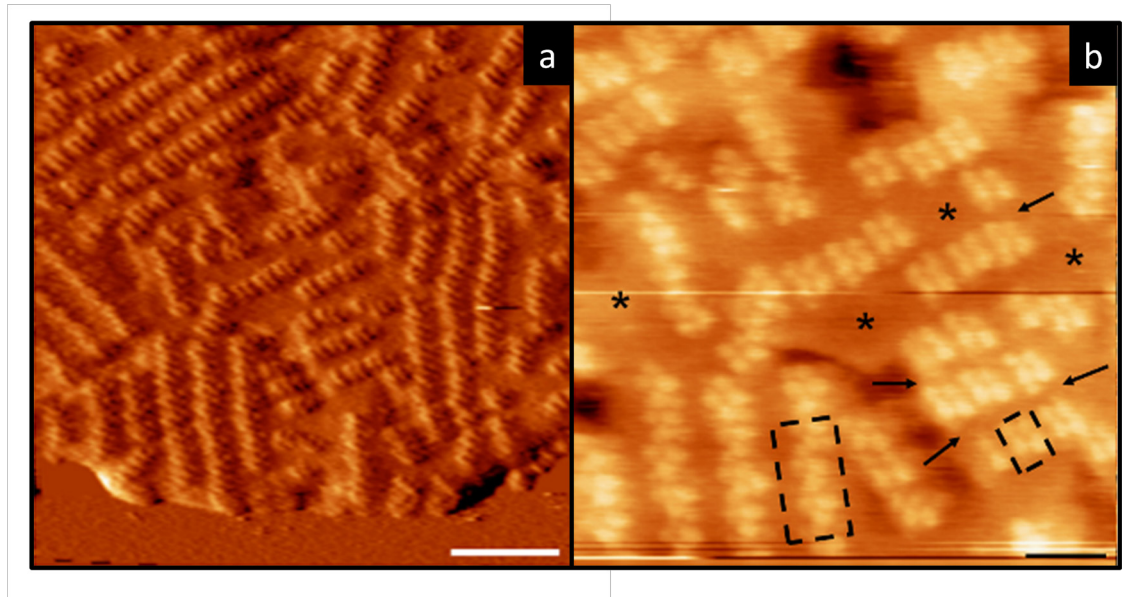


**Figure 1.29. AFM topographs of grana membranes from spinach. (a)** A lower resolution AFM topograph showing PSII complexes forming ordered arrays within the granal membrane. **(b)** A higher resolution AFM topograph in which individual PSII complexes can be identified from their protruding subunits. From Sznee *et al.*, (2011).

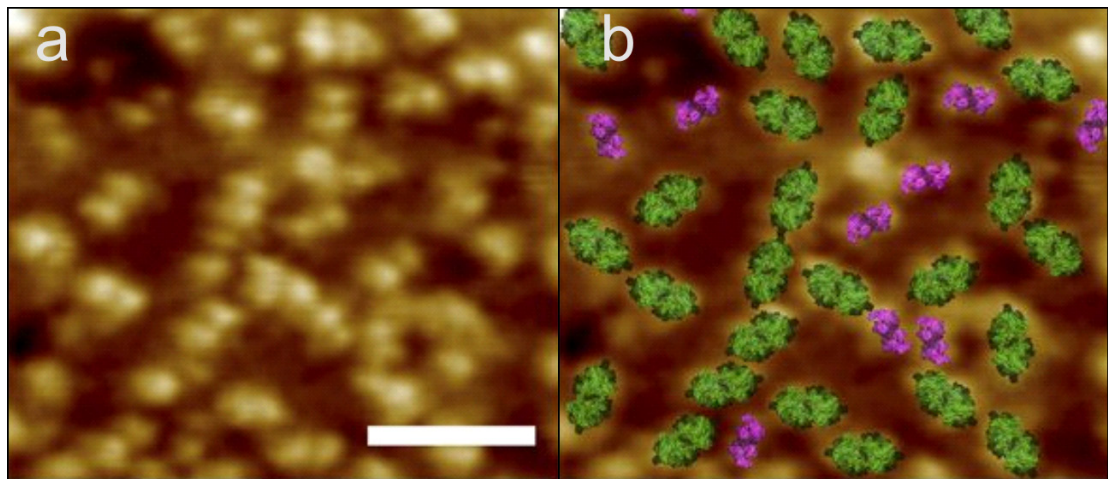


**Figure 1.30. AFM topographs of grana membranes showing the location of cytochrome  $b_6f$  complex and PSII.** Through the use of AFM probes functionalised with plastocyanin it is possible to locate the cytochrome  $b_6f$  complex (pink) and PSII (green). **(a)** The topology map of protein complexes in an inside-out grana membrane fragment. **(b)** Protein complexes in the topology image have been assigned on the basis of their interaction with the plastocyanin functionalised AFM probe. Scale bar is 50 nm. From Johnson *et al.*, (2014).

## 1.9 Nano-lithography and nanopatterns

Photosynthetic complexes are able to absorb and transfer energy with very high efficiency; this property has made the fabrication of bio-inspired photovoltaic devices a major goal in the area of photosynthetic research. A fundamental step in producing such devices is assembling nanoscale arrays of light harvesting complexes in which the distribution of reaction centres and antenna complexes can be controlled. It is also necessary for the light harvesting-complexes to retain their biological activity when attached to a surface. Lithographic techniques such as photolithography and nanoimprint lithography have been used to fabricate nanopatterns of self-assembled monolayers (SAM) (Falconnet *et al.*, 2004; Reynolds *et al.*, 2007). Through the combination of SAMs that are resistant to protein adhesion and SAMs that proteins can absorb to it is possible to direct the attachment of proteins to a surface.

LH2 is a light-harvesting complex from *Rhodobacter sphaeroides* which has been patterned using photolithographic techniques (Reynolds *et al.*, 2007). The LH2 complexes in these nanopatterns were shown to retain their native spectroscopic properties after immobilisation (Reynolds *et al.*, 2007). Through nanopatterning of LH2 complexes it has also been possible to measure energy transfer in these complexes over greater distances than are seen *in vivo*. Excitation of LH2 nano-lines showed that excitation energy could be transferred in excess of 2  $\mu\text{m}$ ; significantly further than is required in biological membrane antenna assemblies (Escalante *et al.*, 2008). This example shows how nanopatterning of protein complexes can be used to study the energy transfer processes of these light harvesting proteins that cannot be observed in native photosynthetic membranes.

Recently it has been shown that immobilised LHCII complexes are able to switch between a highly fluorescent state and a weakly fluorescent state (Vasilev *et al.*, 2014); this feature of LHCII allows for the amount of energy that reaches the RCs to be controlled. It has been found that by modifying the detergent of concentration of the sample, the fluorescent state of the LHCII complexes can be controlled (Illoaia *et al.*, 2008). In the case of immobilised LHCII complexes, a threefold drop in the level of

fluorescence intensity was observed upon the removal of detergent. When the detergent level was then returned to the original level; the measured fluorescence intensity also returned to the original level (Vasilev *et al.*, 2014). The average fluorescence lifetime was also measured in these LHCII complexes; with and without detergent. The average fluorescence lifetime in the presence of detergent was 2.24 ns which decreased to 0.4 ns when the detergent was removed. The change in the fluorescence lifetime was reversible and returned to 2.24 ns when the detergent concentration was returned to its original level (Vasilev *et al.*, 2014). This change from a highly fluorescent state with a longer lifetime to a weakly fluorescent state with a shorter lifetime is due to conformational changes in the LHCII complex (Illoaia *et al.*, 2008). Vasilev *et al.*, (2014) have shown that LHCII complexes retain their function after immobilisation and are able to alter their conformation to switch between fluorescent states. Whilst there has been some work on adhering complexes from *Synechocystis* to surfaces (Vittadello *et al.*, 2010); there have been relatively few studies on nanopatterning of these complexes.

In this thesis Nanoimprint lithography (NIL) is used to construct of linear arrays of immobilised protein complexes. A polystyrene mask which has raised and lowered regions on the scale on nanometres (**Figure 1.31**) is utilised to construct parallel linear SAMs of functional organosilanes on glass surfaces. One SAM can be cross linked to protein complexes whereas the other SAM will prevent the absorption of protein complexes. In photosynthetic membranes such as cyanobacterial thylakoids energy transduction takes place over distances of up to 500 nm. Linear nanoarrays produced by NIL have a width of 150-400 nm, which provides an artificial system that approximates the dimensions of native photosynthetic membranes. Nanoarrays that are fabricated using NIL can be used to investigate whether light-harvesting complexes from *Synechocystis* retain their native spectroscopic properties when incorporated into nanopatterns that are on a similar scale to their native environment.

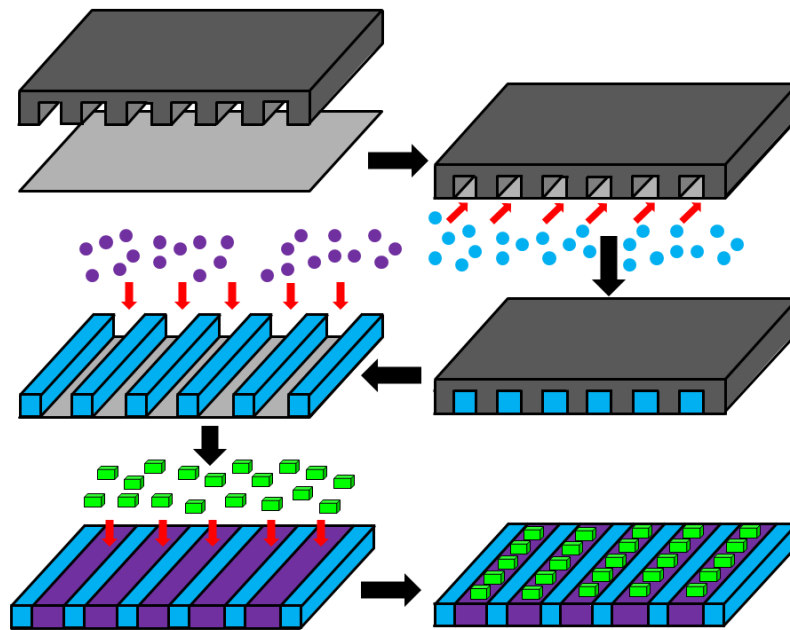


**Figure 1.31. Schematic for production of protein nanopatterns using NIL.** The mask (Dark grey) has raised areas which have a width of 100-400 nm and the lower areas have a width of 100-4000 nm depending on the spacing that is desired. The mask is then absorbed to a surface (light grey) which can be made of gold, silicon or glass depending on the type of self assembled monolayer that is required. The surface is then exposed to a compound (blue circles) in the gas phase that forms linear self assembled monolayers (SAM) where the surface is not in contact with the mask (blue cuboids). The compound that is used must form an SAM that resists protein adherence (for example an organosilane that has a terminal polyethylene glycol tail). The mask is then removed and the surface is exposed to a second compound (purple circles) that forms linear SAMs in the areas that were previously in contact with mask (purple cuboids). This time the compound must form an SAM to which the protein can either absorb to or be cross-linked to (for example (3-mercaptopropyl)-trimethoxysilane). If required a cross-linker is attached to the surface (not shown) before the protein (green cubes) is incubated on the surface. Using this method it is possible to fabricate parallel linear arrays of protein complexes where the width and spacing is defined by the dimensions of the mask that is used.

## 2. Materials and methods

### 2.1 Materials

All chemicals used were of analytical grade purity and purchased from Sigma Chemical Co unless otherwise stated.

### 2.2 Standard buffers, reagents and media

BG-11 medium was made up according to Rippka *et al.*, (1979) unless stated otherwise. Distilled water purified via the Milli-Q system was used to make up all media and solutions which were subsequently sterilised by either autoclaving or filtration using filters with a pore size of 0.2  $\mu\text{m}$ . Medium additives were added once the media had cooled to below 45°C as some additives were heat sensitive. All sucrose solutions were made up w/w in thylakoid buffer (25 mM potassium phosphate pH 7.4, 100 mM NaCl and 10 mM  $\text{MgCl}_2$ ) unless otherwise stated.

### 2.3 Cyanobacteria strains and growth conditions

The strains of cyanobacteria used were:

*Synechocystis* sp. PCC6803, grown in BG-11 supplemented with 5mM glucose and 10 mM TES pH 8.2. This strain is also known as the Nixon wild type

All strains were grown from DMSO stocks that had been stored at -80 °C. Initially the cyanobacteria were grown on agar plates which were made from the appropriate medium supplemented with 1.5 g/100 ml of bactoagar. Colonies from plates were then used to inoculate 100 ml starters of appropriate medium and incubated in a rotary shaker at 30 °C in 50  $\mu\text{mol m}^{-2} \text{s}^{-1}$  of light to allow for photosynthetic growth;

the shaker was run at 150 rpm. For low iron growth conditions 80 ml cultures of BG-11 medium were inoculated with a loop of cells and grown to an  $OD_{750}$  of approximately 1.0. A 720 ml culture of BG-11, in which no iron-containing compounds were present, was inoculated with the entire 80 ml culture giving a 1 in 10 dilution of the iron-containing compounds in the BG-11 medium of the original culture. The 800 ml culture was allowed to grow to an  $OD_{750}$  of approximately 1.0 before it was used to inoculate a flask containing 7.2 litres of iron-free BG-11. The culture was then left for three days before it was harvested.

## **2.4 Measuring sucrose concentration**

All sucrose concentrations were measured using a refractometer

## **2.5 Absorbance spectroscopy**

Absorbance spectra were taken of whole cells and membrane suspensions at room temperature using a Cary 50 spectrophotometer between the wavelengths of 250 nm and 800 nm. The Cary WinUV software package was used to display and analyse spectra that were taken of all cyanobacterial strains.

## **2.6 Fluorescence emission spectroscopy**

Room temperature emission spectra were recorded using a SPEX FluoroLog spectrofluorometer (SPEX Industries Inc.). A tungsten light source was used for excitation of the samples. Samples were excited at 435 nm and slit widths of 5 nm were used. All emission spectra were an average of 10 individual scans.

## 2.7 Calculation of chlorophyll concentration

The chlorophyll concentration of samples was measured by methanol extraction. 5  $\mu$ l of sample was incubated with 995  $\mu$ l of methanol and the absorbance was measured at 663 nm. The chlorophyll concentration was calculated using the extinction coefficient of  $82 \text{ mM}^{-1} \text{ cm}^{-1}$

## 2.8 Standard membrane preparation

Cells were harvested by centrifugation at 8000 rpm in a J-lite™ JLA-10.5 rotor for 25 minutes at 4 °C, the supernatant was discarded and the pellet was resuspended in thylakoid buffer (25 mM potassium phosphate pH 7.4, 100 mM NaCl and 10 mM  $\text{MgCl}_2$ ) to give a concentration of 1.5-2.0 mg/ml of chlorophyll. Resuspended cells were broken via use of the Mini-beadbeater (Biospec products). 3.5 ml of concentrated cell suspension, 3.5 ml of zirconium beads and 10 mg of  $\alpha$ -amylase were added to a 7 ml vessel which underwent 6 cycles of bead beating for 20 seconds with the vessels put on ice for 2 minutes for the interim period between cycles. The liquid fraction of the vessel was pipetted off the top of the solid bead fraction and centrifuged in a microcentrifuge for 1 minute at 3000 rpm in order to pellet any beads that were in solution.

1.5 ml of cell lysate was then loaded onto a continuous sucrose gradient which was made from solutions of 30 % w/w and 40 % w/w sucrose on top of 2 ml of 50 % w/w sucrose. The gradient was made in a SW41 centrifuge tube and once the membrane was loaded onto the top of the gradient it was centrifuged at 40000 rpm in an SW41 rotor for 2 hours at 4°C. The membrane band was then harvested using a peristaltic pump.

Much research went into finding the best procedure to isolate clean membrane patches and the “standard membrane preparation” underwent much development

before the procedure described here was developed; the development will be discussed in the chapter 3.

## **2.9 Detergent treatments**

### **2.9.1 $\beta$ -DDM treatment**

For the  $\beta$ -DDM treatment, membranes were prepared as in **2.8** and were loaded onto secondary sucrose gradients that contained  $\beta$ -DDM. Five 20-50 % w/w continuous sucrose gradients were prepared which contained 0.000 %, 0.001 %, 0.005 %, 0.01 % and 0.05 %  $\beta$ -DDM respectively. Each gradient was loaded with 1.5 ml of thylakoid membrane sample at a concentration of 0.2 mg/ml of chlorophyll. Gradients were centrifuged at 40,000 rpm in an SW41 rotor at 4 °C for 2 hours and the green thylakoid membrane containing bands were harvested.

### **2.9.2 Tween 20 treatment**

Membranes were prepared as in **2.8** and loaded onto secondary sucrose gradients which contained Tween 20. Five 20-50 % w/w continuous sucrose gradients were prepared which contained 0.000 %, 0.001 %, 0.005 %, 0.01 % and 0.05 % Tween 20 respectively. Each gradient was loaded with 1.5 ml of thylakoid membrane sample at a concentration of 0.2 mg/ml of chlorophyll. Gradients were centrifuged at 40,000 rpm in an SW41 rotor at 4 °C for 2 hours and the green thylakoid membrane containing bands were harvested.

### **2.9.3 Triton X-100 treatment**

Membranes were prepared as in **2.8** before being loaded onto secondary sucrose gradients that contained triton X-100. Five 20-50 % w/w continuous sucrose gradients were prepared which contained 0.000 %, 0.001 %, 0.005 %, 0.01 % and 0.05 %

triton X-100 respectively. Each gradient was loaded with 1.5 ml of thylakoid membrane sample at a concentration of 0.2 mg/ml of chlorophyll. Gradients were centrifuged at 40,000 rpm in an SW41 rotor at 4 °C for 2 hours and the green thylakoid membrane containing bands were harvested.

#### **2.9.4 Digitonin treatment**

Membranes prepared as in **2.8** were loaded onto secondary continuous gradient made up from solutions of 20 % w/w and 50 % w/w sucrose which contained digitonin. Three 20-50 % w/w continuous sucrose gradients were prepared that contained 0.00 %, 0.01 % and 0.1 % digitonin respectively. The gradients were made in a SW41 centrifuge tube which was centrifuged at 40,000 rpm in an SW41 rotor for 2 hours at 4°C. The membrane bands were then harvested via the use of a peristaltic pump.

### **2.10 Atomic Force Microscopy**

#### **2.10.1 Instrumentation**

A Multimode VIII AFM with Nanoscope 8.0 controller (Bruker Nano Surfaces Business) was used to image biological samples.

#### **2.10.2 Sample preparation**

Typically 5 µl of a sample that was at a suitable concentration was pipetted onto freshly cleaved mica followed by 45 µl of standard adsorption buffer (10 mM HEPES pH 7.5, 150 mM KCl and 25 mM MgCl<sub>2</sub>) and incubated for 1-2 hours. Prior to imaging, the buffer was changed to standard imaging buffer (10 mM HEPES pH 7.5 and 100 mM KCl). The adsorption buffer was pipetted off and discarded, then the mica

was washed four times with 50  $\mu$ l of imaging buffer with the final 50  $\mu$ l left on the surface for the sample to be imaged in. The sample was then mounted onto the piezoelectric scanner.

### **2.10.3 Sample imaging**

Samples were imaged in Peak Force Quantitative Nanomechanical Mapping™ mode (PF-QNM mode) under liquid with a Peak Force frequency of 2 kHz unless otherwise stated. When imaging under liquid the standard fluid cell was used to house the AFM probe and control it. Once the probe has been inserted into the fluid cell, the reservoirs were filled with standard imaging buffer and mounted on top of the sample where the laser was aligned with the probe. The Peak Force amplitude used during imaging was 10 nm and images were taken at 256 x 256 or 512 x 512 pixel arrays. The Peak Force set point was varied between 50-1000 pN and the scan rate was selected to be between 0.5-1.2 Hz. The probes used during imaging were SNL probes (Bruker) and all image processing was done in NanoScope Analysis v1.40r1

### **2.11 Electron Microscopy**

Membrane solutions were diluted to an appropriate concentration and 5  $\mu$ l was applied to glow discharged carbon grids for 2 minutes. The sample was then negatively stained with 0.75 % w/v uranyl formate and viewed in a Philips CM100 microscope that was outfitted with a Gatan Ultrascan 667 CCD camera. Images were taken between x 1,000 and x 52,000 magnification with image processing performed in Digital Micrograph (Gatan. Inc.).

## **2.12 Single particle analysis of IsiA-PSI supercomplex**

52 particles were selected from field of IsiA-PSI supercomplexes imaged by negative stain TEM. Image processing was performed using the IMAGIC-5 image processing system.

## **2.13 Protein manipulation**

### **2.13.1 SDS-polyacrylamide gel electrophoresis (SDS-PAGE)**

15  $\mu$ l of protein sample was incubated with 5  $\mu$ l of 4 x protein loading dye and placed in a heating block set to 100 °C for 10 minutes before being centrifuged for 2 minutes at 13,000 rpm in a microfuge. 15  $\mu$ l of protein sample was loaded onto a pre-cast 12 % Bis-Tris polyacrylamide gel (Invitrogen, NuPAGE™ system). 5  $\mu$ l of Precision Plus Protein™ Dual Color Standards (Bio-Rad) was loaded into each gel to estimate the mass of the proteins in the sample. Gels were run at 180 V for 50-70 minutes using the buffer system from Laemmli, (1970) and stained for 15 minutes with Coomassie Brilliant Blue R250. Gels were destained by 4 x 5 minutes of boiling in MilliQ water with 3 minute intervals.

### **2.13.2 Silver staining of gels**

After Coomassie stained gels had been destained they were fixed for 20 minutes in 50 ml of 50 % methanol, 10 % acetic acid and 10 % fixative enhancer (Bio-Rad) made up in MilliQ water. Gels were then washed twice for 20 minutes in 50 ml MilliQ. The development solution contained 5 % silver complex solution (Bio-Rad), 5 % reduction modulation solution (Bio-Rad), 5 % image development (Bio-Rad) and 50 % development accelerator solution (Bio-Rad) made up in MilliQ water. The second MilliQ wash was removed and the gel was incubated in 50 ml of development

solution for between 15-30 minutes. Once the gel had been stained to a sufficient degree the reaction was stopped by addition of 25 ml of 5 % acetic acid.

### **2.13.3 Clear native polyacrylamide gel electrophoresis (CN-PAGE)**

CN-PAGE was conducted using a 4-16 % gradient gel according to the protocol described in Wittig *et al.*, (2007). Gels were poured using 16 x 20 cm plates separated with 1 mm spacers. Typically 100 µl of sample was loaded per lane with a concentration of 0.1-0.2 mg/ml of chlorophyll. The temperature was maintained at 4 °C whilst the gel was running.

### **2.13.4 Electroelution of protein complexes from polyacrylamide gels**

Bands containing protein complexes were cut out of the gel before being sectioned into pieces with the approximate dimensions of 2 x 2 mm. The gel pieces were then placed the electro-eluter (Bio-Rad model 422 Electro-Eluter) which was run at a constant current of 10 mA. The elution buffer contained 500 mM Tricine, 150 mM Bis-Tris/HCl, pH 7.0, 0.5 % (w/v) DOC and 0.02 % (w/v) β-DDM.

## **2.14 Purification of thylakoid membranes from *Synechocystis* 6803 for protein purification**

An 8 L culture of *Synechocystis* in the logarithmic phase of growth (OD<sub>750</sub> 0.6) were pelleted by centrifugation at 8,000 rpm in a J-lite™ JLA-10.5 rotor for 10 minutes at 4 °C and resuspended in 50 ml of thylakoid buffer. Cells were then lysed by 8 x 1 minutes of bead beating with 5 minute intervals during which cells were left on ice. The cell lysate was then removed from the beads with a pipette and the beads were washed four times with thylakoid buffer with all the washes being pooled with the initial cell lysate to ensure high a high yield of thylakoid membranes. The thylakoid membranes were then pelleted by centrifugation at 23,500 rpm in a Beckman Coulter JA-25.5 rotor for 30 minutes at 4 °C. The supernatant was discarded

and the thylakoid membranes resuspended in thylakoid buffer to give a final concentration of  $\approx 1$  mg/ml chlorophyll  $\alpha$ .

## **2.15 Purification of the IsiA-PSI supercomplex from *Synechocystis* 6803 thylakoid membrane**

### **2.15.1 Solubilisation**

10 % n-dodecyl- $\beta$ -D-maltoside ( $\beta$ -DDM) was pipetted drop-wise into a solution of resuspended thylakoids with a chlorophyll concentration of  $\approx 1$  mg/ml (typically 20-30 ml of resuspended thylakoids were used) to give a final concentration of 1.5 %  $\beta$ -DDM. Solubilisation was carried out at 4 °C in the dark for 2 hours after which the suspension was centrifuged at 23,500 rpm in a Beckman Coulter JA-25.5 rotor for 30 minutes at 4 °C to pellet any unsolubilised material. The supernatant was decanted from the centrifuge tube and the pellet was discarded.

### **2.15.2 Sucrose gradients**

Sucrose gradients were prepared using buffer containing 50 mM MES-NaOH pH 6.0, 0.5 M glycine betaine, 0.5 M sucrose, 20 mM CaCl<sub>2</sub>, 5 mM MgCl<sub>2</sub> and 0.04 %  $\beta$ -DDM (gradient buffer). SW32 or SW41 centrifuged tubes were filled to 85 % capacity with gradient buffer and then left at -18 °C until frozen. Gradients were then thawed at 4 °C which induced the formation of a continuous sucrose gradient. Gradients were then filled to their full capacity with solubilised thylakoids and then centrifuged at 100,000 x g for 16 hours at 4 °C. IsiA-PSI supercomplexes were present in the lowest green band on the sucrose gradient and were harvested using a peristaltic pump; gradients were kept on ice and in the dark to prevent damage to the sample. If samples were not immediately used for further purification they were flash frozen in liquid nitrogen and stored at -80°C.

### **2.15.3 Anion exchange**

A self-packed anion exchange column was prepared using DEAE Sepharose in standard purification buffer (50 mM MES-NaOH pH 6.0, 0.5 M glycine betaine, 20 mM CaCl<sub>2</sub>, 5 mM MgCl<sub>2</sub> and 0.04 % β-DDM). IsiA-PSI complexes harvested from continuous sucrose gradients were concentrated using a concentrator with a 100000 MW cut off point (Sartorius Stedim Biotech) until they reached a volume of 5 ml. The concentrated suspension of IsiA-PSI complexes was applied to the anion exchange column and washed through with purification buffer. The IsiA-PSI complex was eluted by running a NaCl gradient from 0 mM to 600 mM. Fractions of IsiA-PSI complexes were assessed for purity using a spectrometer before being pooled and concentrated. If samples were not immediately used for further purification they were flash frozen in liquid nitrogen and stored at -80°C. All anion exchange was performed on an Akta FPLC (GE Healthcare)

### **2.15.4 Gel filtration**

IsiA-PSI complexes were further purified by gel filtration using an Agilent 1200 HPLC with a BioSeph-Sec-s3000 column (Phenomenex). 80 µl of concentrated anion exchange eluate was loaded onto the column which was run at 0.5 ml m<sup>-1</sup> with standard purification buffer. Elution of IsiA-PSI complexes was detected by monitoring the absorption at 674 nm. 1 ml fractions were collected with those containing IsiA-PSI complexes being concentrated, flash frozen in liquid nitrogen and stored at -80°C.

## **2.16 Production of protein nanolines**

### **2.16.1 Master pattern template**

The R100 template has a period of 4  $\mu\text{m}$  and line width of 150 nm. The templates were made by electron beam lithography on silicon wafers.

### **2.16.2 Spin coating of master patterns with polystyrene**

Silicon master patterns were placed in a spin coater that was set to 2000 rpm and 1-2 drops of 50-60 mg/ml polystyrene in toluene was pipetted onto the master pattern. The toluene typically evaporated within 5-10 seconds leaving a polystyrene film over the pattern with a thickness of 150-200 nm.

### **2.16.3 Preparation of protein nanolines with 150 nm line width**

R100 master patterns were spin-coated with polystyrene as described in **2.15.2**. MilliQ water was passed through a filter with pore size of 0.2  $\mu\text{m}$  and used to float the polystyrene mask off the master pattern and onto a small piece of piranha-cleaned silicon (dimensions of roughly 10 mm by 10 mm) which was left to dry in a desiccator under vacuum for 2 hours. Once dry, the silicon was removed from the desiccator and split along its axis so as to cleave the polystyrene mask adhered to its surface. The split was made in the direction perpendicular to the channels in the polystyrene mask; this ensured the channels were open at their ends to allow access for the chemicals used to make the monolayer.

The split polystyrene mask was floated of the surface of the silicon and onto a piranha-cleaned glass cover slip which was placed in a desiccator and left under high vacuum overnight to dry. Once dry, the vacuum was deteriorated and 25  $\mu\text{l}$  of (3-mercaptopropyl)trimethoxysilane (MPTMS) was pipetted into the lid of an

Eppendorf tube which was placed in the desiccator. The desiccator was flushed nitrogen gas for 5 minutes before being returned to vacuum and left overnight.

The glass cover slip was removed from the desiccator and the polystyrene mask was floated off its surface in the same way as previously described. The cover slip was then thoroughly dried under a constant stream of nitrogen and then placed in a solution of 15 mM 2-[methoxy(polyethyleneoxy)propyl]trimethoxysilane (PEG-silane) (ABCR GmbH & CO.) in toluene for 90 minutes.

### **2.16.3 Immobilisation of protein complexes on nanopatterns**

The glass cover slip was then removed from solution and washed with acetone. A solution of 10 mM Succinimidyl-4-(n-maleimidomethyl)cyclohexane-1-carboxylate (SMCC) in Dimethyl sulfoxide (DMSO) was made and 300  $\mu$ l was pipetted onto the cover slip which was left for 30 minutes. The cover slip was washed with MilliQ water then incubated with 300  $\mu$ l of the a solution of appropriate protein (either PSII or the IsiA-PSI supercomplex) for 10 minutes before being washed with thylakoid buffer and stored in the under buffer in the dark at 4°C. The solutions of protein complexes were used at a concentration of 5  $\mu$ g/ml of chlorophyll.

### **2.17 *In situ* fluorescence microscopy and spectroscopy**

Fluorescence microscopy and spectroscopy was performed on a home-built microscope system outfitted with an EMCCD camera (ProEM 512, Princeton Instruments) and a spectrometer (Acton 150, Princeton Instruments). Samples were excited by a collimated LED light source (M470L2, Thorlabs) and the subsequent fluorescence was detected by the EMCCD camera through the spectrometer. Fluorescence images and spectra were taken using a 470/40 nm band pass excitation filter with a 605 nm dichroic mirror and a 593 nm long pass emission filter. Spectra were taken with an 800  $\mu$ m slit width and a 150 line  $\text{mm}^{-1}$  grating at a central wavelength of 680 nm. To increase the signal to noise ratio, 15 individual frames were

captured and averaged to produce the spectra and fluorescent images; each frame was taken with a 150 ms exposure time and an electron multiplication gain of 90.

## **2.18 Fluorescence-lifetime imaging microscopy**

Fluorescence decay lifetimes for these complexes were recorded via illumination with a continuous spectrum laser (SC 480-10 Fianium) with a 470/40 nm band pass excitation filter pulsed at 80 MHz. The output was recorded with a photomultiplier tube synched with the laser via a Becker and Hickl TCSPC card. A single exponential decay function was fitted to the data in SigmaPlot.

## **2.19 Low temperature fluorescence emission spectroscopy**

Low temperature emission spectra were taken in a cryo-stable buffer containing 25 mM potassium phosphate, 100 mM NaCl, 10 mM MgCl<sub>2</sub> and 70 % glycerol (v/v). The samples were cooled to 77 K using an Optistat DN-V optical cryostat (Oxford Instruments). A SPEX FluoroLog spectrofluorometer (SPEX Industries Inc.) was used to record emission spectra. A tungsten light source was used for excitation of the samples. Samples were excited at 435 nm and slit widths of 5 nm were used. All emission spectra were an average of 10 individual scans.

# **Chapter 3: Development of procedures for the production of large, flat photosynthetic membrane patches for the purposes of AFM analysis**

## **3.1 Summary**

This chapter details the procedures that were developed to produce thylakoid membrane patches from *Synechocystis* that could be imaged by AFM for the purposes of investigating the organisation of the photosynthetic apparatus. Thylakoid membranes in *Synechocystis* exist as extensive invaginations of the inner cell membrane which contain an enclosed lumen. The ideal substrate for AFM is a flat, single membrane bilayer; to this end various protocols for membrane purification and treatment were explored.

The method of cell breakage found to be the most suitable was mild bead beating which produced large thylakoid membrane patches that could be easily purified by from the cell lysate through centrifugation of sucrose gradients. Centrifugation of a cell extract through a continuous 30-40 % w/w sucrose gradient on a 50 % sucrose step was routinely used to prepare large quantities of membrane; this type of gradient was also useful in removing most of the phycobilisomes from the stromal surface of the membrane. Initial EM analysis of purified membranes revealed the presence of a large number of small objects attached to the stromal face of the membrane which were ultimately identified to be glycogen granules. Several strategies were trialed to either remove or prevent the formation of these granules, the most successful of which was incubation of the membranes with amylase prior to purification on the primary sucrose gradient. It was found that a second purification step on a 20-50 % continuous sucrose gradient was required to remove the majority of contaminating material still present in the sample after the initial sucrose gradient. Initial AFM data revealed that the thylakoid membranes have a vesicular structure with an enclosed lumen when imaged under liquid. Numerous approaches were

trialled to produce flattened membrane patches for high resolution AFM and two protocols were established. One required membranes to be dried to a mica surface in order to burst the vesicular membranes, which were then rehydrated prior to imaging. The second protocol required the use of secondary gradients that contained low concentrations of digitonin to purify single layered membrane patches which were then adsorbed to a mica substrate for imaging

### **3.2 Introduction**

Atomic force microscopy had been used to investigate the native membrane architectures of photosynthetic bacteria (Bahatyrova *et al.*, 2004; Scheuring, 2006) and plants (Sznee *et al.*, 2011; Johnson *et al.*, 2014), however there are no reports of high resolution AFM imaging of *Synechocystis* thylakoid membranes. As no protocol currently exists for preparing cyanobacterial thylakoid membranes for AFM, a new protocol had to be developed. AFM uses a probe with an apex that has a diameter of the order of nanometres which allows for highly accurate measurement of membranes. One of the drawbacks to this imaging technique is the possibility that nano-scale debris such as soluble proteins and lipid bodies could adhere to the probe, preventing AFM imaging at high resolution. In the case of *Synechocystis* it is of particular concern that the thylakoid membranes have a large number of phycobilisome complexes attached to their surface which have the potential to adhere to the probe. It is therefore an important consideration when trying to produce membranes that are suitable for AFM analysis to use a purification procedure that keeps such contamination to a minimum. The ideal sample for AFM is a flat membrane that is adsorbed onto a mica surface; this allows the probe to track across its surface and record the protrusions of the proteins embedded in the membrane. As cyanobacterial thylakoid membranes are flattened vesicles with an enclosed lumen it was necessary to disrupt these structures to allow for single layered membrane patches to bind to the mica surface.

Current protocols used for preparing bacterial membranes for AFM involve the use of two sucrose gradient centrifugation steps (Cartron *et al.*, 2014). The first causes the dissociation of many smaller cellular bodies that are bound to the membrane in addition to pelleting the larger components of the cell lysate such as the cell wall. Once the membranes have been harvested from the first gradient they are loaded onto a secondary sucrose gradient that contains a low concentration of detergent. The primary purpose of the second gradient step is to “open out” vesicular membranes so they lie flat when applied to a mica surface; the gradient also provides a secondary purification step to remove contaminating material. Whilst this method could potentially be useful there is the risk of solubilising the membranes; therefore the development of a detergent-free protocol must also be considered.

As AFM is a very time consuming technique, the purity and AFM suitability of membrane preparations has to be investigated in combination with other methods. Negative stain TEM is very useful for assessing the effects that different treatments have on the thylakoid membranes as it is a relatively quick imaging technique with a resolution sufficient to visualise the shape and size of membrane patches. After membranes have been purified and treated, it is more efficient to image them initially using negative stain TEM to assess their suitability for AFM rather than to use AFM directly on every membrane sample.

The cell breakage procedure currently used in the Hunter lab for *Synechocystis* requires cells to be pelleted and resuspended in a small volume of buffer before they undergo bead beating. Although this technique is very efficient for breaking cells there is the possibility that it may be violent enough to damage the thylakoid membranes. It is not known what effect other breakage techniques such as French press and sonication will have on intact cells, however the potential for using a gentler breakage protocol must be investigated.

### 3.3 Results

#### 3.3.1 Initial trials for cell breakage and membrane purification

Three different methods for cell breakage were trialled; bead beating, French press and sonication. The standard bead beating procedure uses resuspended cells at a concentration of 1.5 mg/ml of chlorophyll; the cell suspension underwent 6 cycles of beating for 1 minute with the sample left on ice for 5 minutes between cycles. A gentler regime of bead beating was also trialled; this gentler method used 6 rounds of bead beating for 20 seconds with the sample left on ice for 5 minutes between cycles. The French press method of cell breakage required 10 ml of cell suspension at a concentration of 1.5 mg/ml of chlorophyll which was passed through the French press twice at a pressure of 18,000 psi. The sonication procedure requires 5 ml of cells at the concentration of 1.5 mg/ml of chlorophyll. The sample was sonicated for 30 seconds then left on ice for 30 seconds; this cycle was repeated for 10 minutes. For membrane purification 1.5 ml of cell lysate from each breakage procedure was loaded onto a 10-55% continuous sucrose gradient. The sucrose gradients were centrifuged at 40,000 rpm in an SW41 rotor at 4 °C for 2 hours; the gradients were photographed after centrifugation (**Figure 3.1**). A blue band can be seen at the top of every gradient; the blue colour comes from phycobilisome complexes which suggests that this band also contains water soluble components of the cells cytoplasm. The presence of this band indicates that all of these cell breakage techniques lyse cells effectively. The sucrose gradients on which cell lysate from the bead beater were loaded show a green band roughly two thirds of the way down the sucrose gradient that is not present in the other gradients. Cells that had undergone 6 x 1 minute of bead beating produced a stronger band in the sucrose gradient than cells that had undergone 6 x 20 seconds of bead beating. This indicated that cell breakage was more efficient under these conditions and allowed for the purification of greater quantities of thylakoid membrane. The green bands were harvested and the sucrose concentration of the membrane samples was measured to be 42 %. The sucrose concentration of the blue region of the gradient was measured at its lowest point and found to be 28 %.

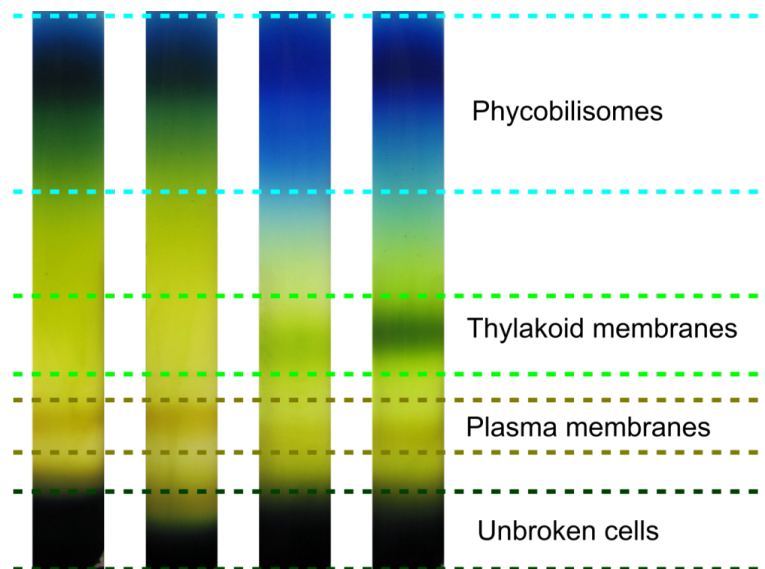


**Figure 3.1. Initial sucrose gradients.** Fractionation of cell lysates from different breakage procedures on 10-55 % continuous sucrose gradients. From left to right the breakage procedures were; sonication, French press, 6 x 20 seconds bead beating and 6 x 1 minute bead beating. The blue fraction (top) contains phycobilisomes; the light green fraction (second from top) contains thylakoid membranes; the yellow fraction (third from top) is believed to contain plasma membranes and the dark green fraction (bottom) contains unbroken cells and large debris such as the cell wall.

EM analysis of purified membranes revealed that 6 x 1 minute of bead beating produced significantly smaller membrane fragments than 6 x 20 seconds (**Figure 3.2**). Membrane patches from both breakage conditions were measured in their long axis and the data can be seen in **Figure 3.3**. It was found that the majority of membrane patches from cells that had undergone more extensive bead beating had a length of less than 400 nm. Cells that had undergone mild bead beating produced membrane patches that were far larger than those purified from the more extensive bead beating cell breakage procedure. When imaging with AFM it is desirable to have large membrane patches to ensure the probe tracks over the sample accurately and using a more gentle breakage procedure will also cause less damage to the sample. For these reasons it was decided that 6 x 20 seconds of bead beating was the optimum breakage procedure and was used in all subsequent experiments.

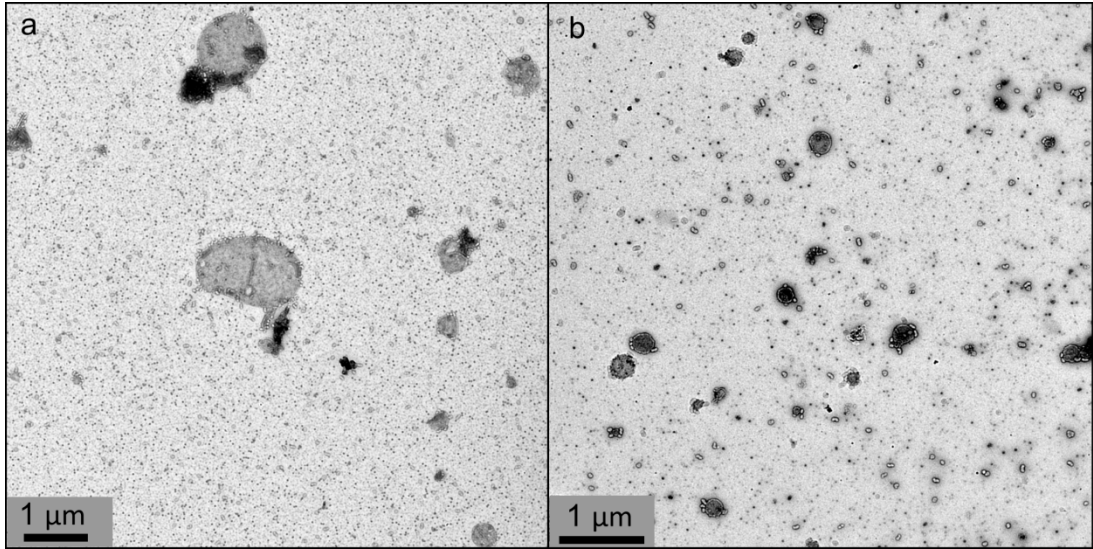


**Figure 3.2. EM of cell lysates from beat beating.** Negative stain TEM of thylakoid membrane containing bands from the initial sucrose gradients. (a) Membranes from 6 x 20 seconds bead beating. (b) Membranes from 6 x 1 minute bead beating.

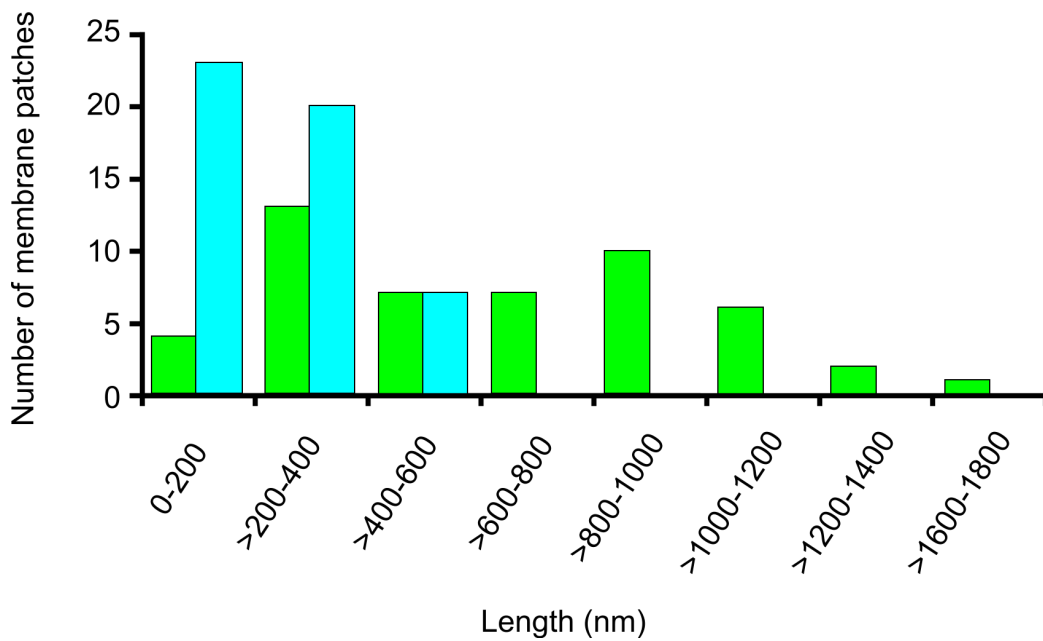


**Figure 3.3. Lengths of membranes patches from bead beating cell lysates.** Membranes from the two bead beating cell lysates were measured along their long axis; 6 x 20 seconds (green) and 6 x 1 minute (blue). 50 membrane patches were measured from each cell lysate.

### 3.3.2 Optimisation of the primary purification step

Whilst the gradients seen in **Figure 3.1** were successful in purifying thylakoid membranes, there was not much separation between the thylakoid membranes and the other bands in the gradient. To try and minimise contamination of the thylakoid membranes with other cellular components, the primary sucrose gradient protocol was altered. The cell lysate was centrifuged at 3000 x g to remove any unbroken cells and then diluted to a concentration of 0.2 mg/ml chlorophyll before 1.5 ml was loaded onto the gradient. The gradient itself was changed to a 30-40 % continuous sucrose gradient sitting on a 50 % sucrose step. The new sucrose gradient was used to increase the separation between the thylakoid membranes and the phycobilisomes in addition to concentrating the membranes against the 50 % sucrose step. As before the gradient was centrifuged at 40,000 rpm in an SW41 rotor at 4 °C for 2 hours; the resulting gradient was photographed (**Figure 3.4**).

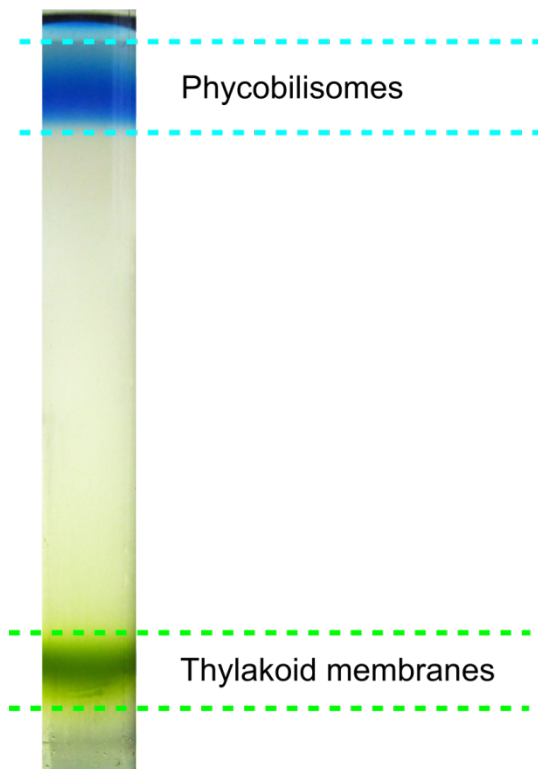


**Figure 3.4. Optimised primary gradient.**

The revised sucrose gradients consisted of a 30-40 % continuous gradient on a 50 % step. Blue phycobilisome fraction has been separated from the green fraction that contains thylakoid membranes.

### 3.3.3 EM of thylakoid membranes from primary sucrose gradients:

To assess how effective the new primary sucrose gradient was at purifying “clean” membranes the green band was harvested from the gradient and imaged using EM (**Figure 3.5**). The membranes harvested from the new primary gradient appear much cleaner than those purified by the 10-55 % sucrose gradient; however there was still a significant amount of contaminating material. There are small particles in the background of the image and adhered to the surface of the membrane that have an oval shape and a length of approximately 20-100 nm. These bodies have been previously identified as glycogen granules (Sherman and Sherman, 1983).

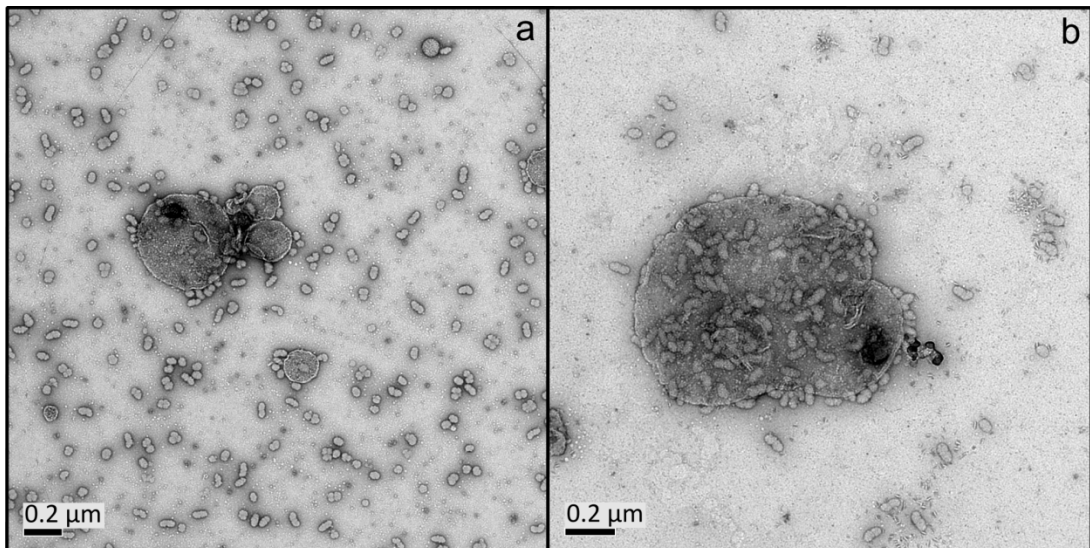


**Figure 3.5. Negative stain TEM of thylakoid membranes from the revised primary gradient.** (a) Negative stain TEM showing a thylakoid membrane and background glycogen granule contamination. (b) Negative stain TEM showing a thylakoid membrane coated in glycogen granules.

### 3.3.4 Initial AFM

Despite the presence of a significant amount of contaminating material, most notably in the form of glycogen granules, attempts were made to image the membranes by AFM. As expected there was significant contamination of the AFM probe; it was only possible to complete a few scans of the membrane patches without contamination preventing the imaging process altogether. Membrane patches were identified in the initial AFM (**Figure 3.6**) by their size and shape; however contamination of the probe led to large artefacts in the images such as those on the left hand side of **Figure 3.6**. It was clear that in order to image thylakoid membranes to the resolution of protein complexes samples would have to free of the contaminating bodies that can be seen in the EM images.

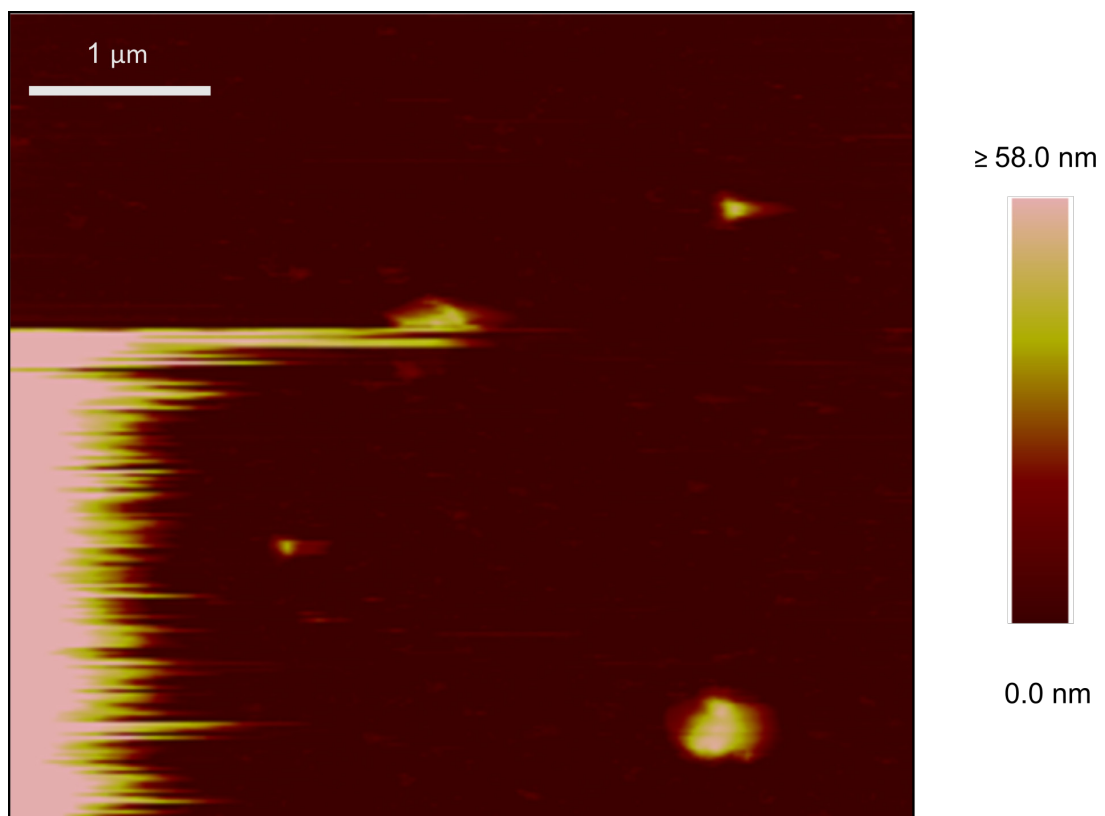


**Figure 3.6. Initial AFM of thylakoid membranes.** AFM of membranes harvested from revised primary sucrose gradients; the large feature on the left of the image is an image artefact caused by tip contamination. The smaller feature in the bottom right hand corner is believed to be a thylakoid membrane.

### 3.3.5 Additional purification of thylakoid membranes

To try and “clean up” the thylakoid membranes, samples harvested from the primary sucrose gradients were further purified on a secondary 20-50 % continuous sucrose gradient centrifuged at 40,000 rpm in an SW41 rotor at 4 °C for 2 hours; 1.5 ml of sample at a concentration of 0.2 mg/ml of chlorophyll were loaded. The resulting gradients (**Figure 3.7**) contained a diffuse green band towards the bottom of the centrifuge tube and a very pale blue band at the top. This indicated that the secondary gradients had removed phycobilisome complexes that the primary gradient had failed to separate from membranes. To see the extent to which the secondary sucrose gradient had removed contaminating cellular debris from the membrane fragments, the green band was harvested and imaged with EM (**Figure 3.8**). Much of the background contamination present in the primary gradients (**Figure 3.8a**) was absent in samples harvested from the secondary gradient (**Figure 3.8c**). However significant levels of contamination were still present on the surface of the membrane patches in the form of glycogen granules, indicating no improvement in this aspect of the purification (**Figure 3.8b and 3.8d**).

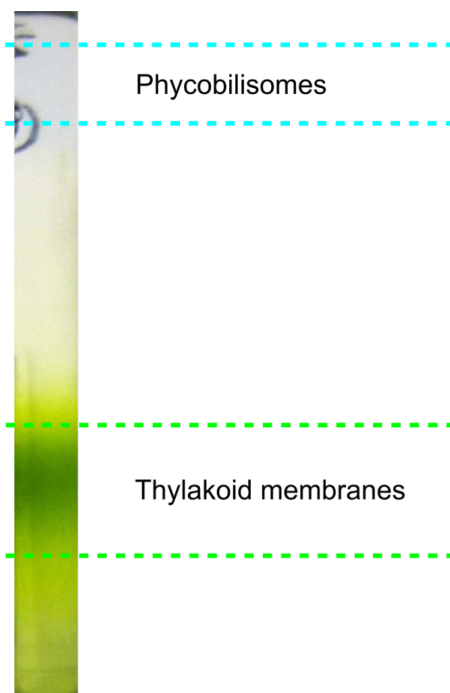


**Figure 3.7. Secondary sucrose gradient.** Membranes from primary gradients were further purified on a 20-50 % continuous gradient. A very pale blue fraction can be seen at the top of the gradient. A green fraction that contains thylakoid membranes is present close to the bottom of the gradient.

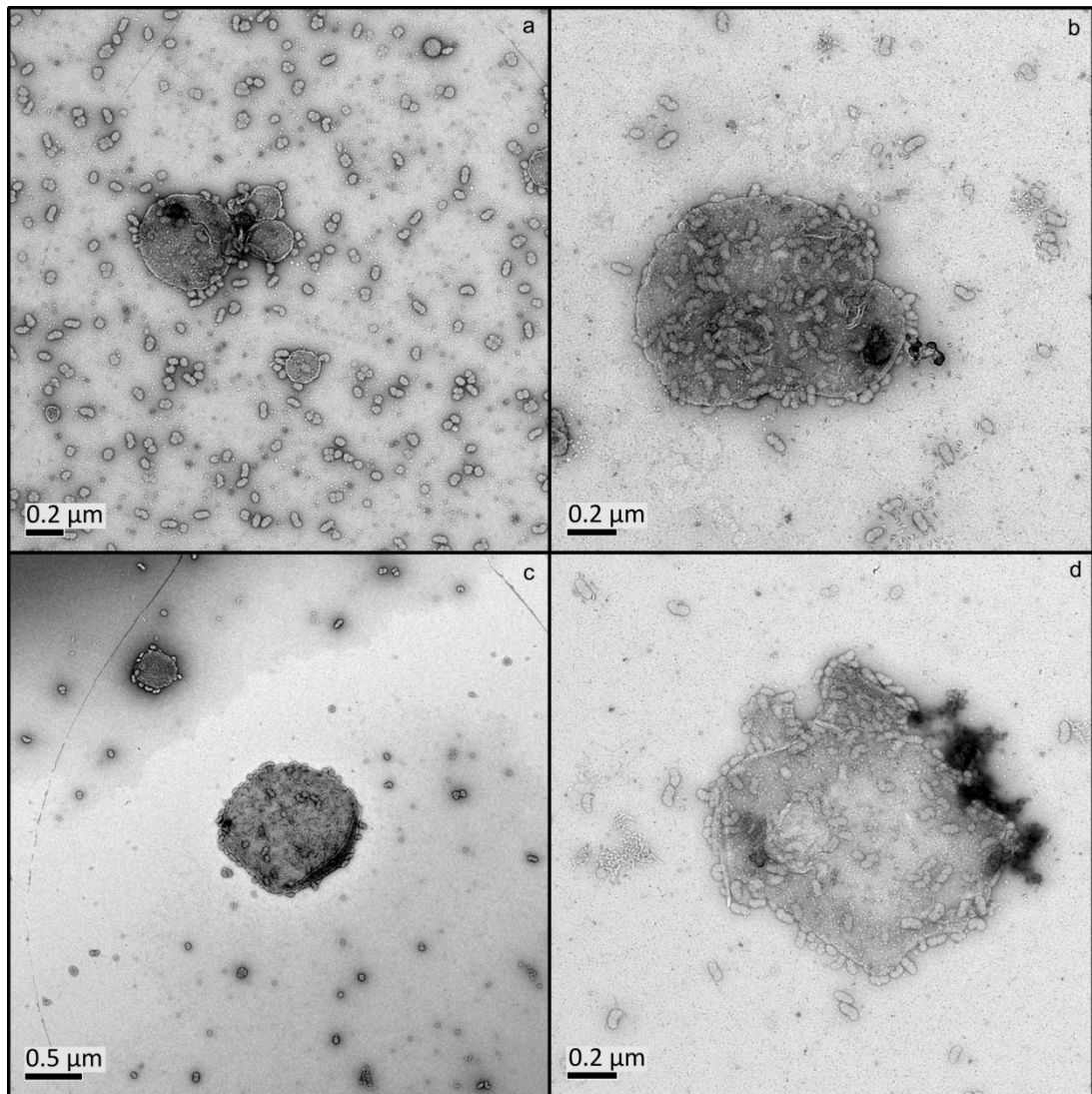


**Figure 3.8. Comparison of thylakoid membranes from primary and secondary gradients.** (a) Negative stain TEM of sample harvested from a primary gradient showing a thylakoid membrane and background glycogen granule contamination. (b) Negative stain TEM of sample harvested from a primary gradient showing a thylakoid membrane coated in glycogen granules. (c) Negative stain TEM of sample harvested from a secondary gradient showing a thylakoid membrane and reduced levels of glycogen granules in the background of the image. (d) Negative stain TEM of sample harvested from a secondary gradient showing a thylakoid membrane coated with a comparable number of glycogen granules to membranes harvested from primary gradients.

### 3.3.6 High salt secondary sucrose gradients for removal of glycogen granules

It was believed that purifying membranes on secondary sucrose gradients that contained a high concentration of NaCl would destabilise the interaction between the membrane and the glycogen granules. Three 20-50% continuous sucrose gradients were trialled that were made with buffer containing 300 mM, 600 mM and 1200mM NaCl respectively. Gradients were centrifuged at 40,000 rpm in an SW41 rotor at 4 °C for 2 hours; 1.5 ml of sample at a concentration of 0.2 mg/ml of chlorophyll was loaded. The post-centrifugation gradients can be seen in **Figure 3.9**.



**Figure 3.9. Secondary gradients from high salt trials.** NaCl concentration from left to right; 100 mM (NaCl concentration of standard thylakoid buffer), 300 mM, 600 mM, 1200 mM. The green thylakoid membrane containing fraction travels less distance through the gradient as the NaCl concentration increases. All of the green bands were harvested for EM analysis to find out what effect the increased NaCl concentration had on the granules that were adhered to the surface of the membranes.

The most noticeable effect of the increased concentration of salt is that the membranes travel a shorter distance through the gradient. In the 300 mM and 600 mM gradients there is still a clear separation between the membrane band and the phycobilisome band. In the 1200 mM gradient the membrane and phycobilisome bands have started to merge which could possibly cause contamination. Another difference in the high salt gradients is the presence of a much more visible phycobilisome band, indicating that the high salt treatment is disrupting the interaction between the membrane and the phycobilisomes. To determine whether the increased NaCl concentration has removed glycogen granules from the surface of the thylakoid membranes, the green band was harvested from the gradients and imaged via EM.

### **3.3.7 EM of membranes purified on high salt secondary gradients**

The EM of the membranes harvested from high salt gradients revealed that the increased salt concentration of the sucrose buffer was partially successful in removing glycogen granules from the surface of the membrane (**Figure 3.10**). Membranes harvested from the 300 mM and 600 mM gradients (**Figure 3.10b and 3.10c respectively**) have a number of glycogen granules attached to their surface similar to those of membranes purified using standard secondary gradients that contain 100 mM NaCl (**Figure 3.10a**). The levels of background glycogen granules in the 300 mM and 600 mM samples were also similar to those of standard secondary gradients. EM of membranes harvested from the secondary gradients containing 1200 mM NaCl (**Figure 3.10d**) show a significant reduction in glycogen granule contamination with few granules attached to the surface of the membrane. There is however a small number of granules in the background of the EM; so whilst this treatment seems fairly effective at removing the majority of the glycogen granules a different method had to be used to completely remove them.

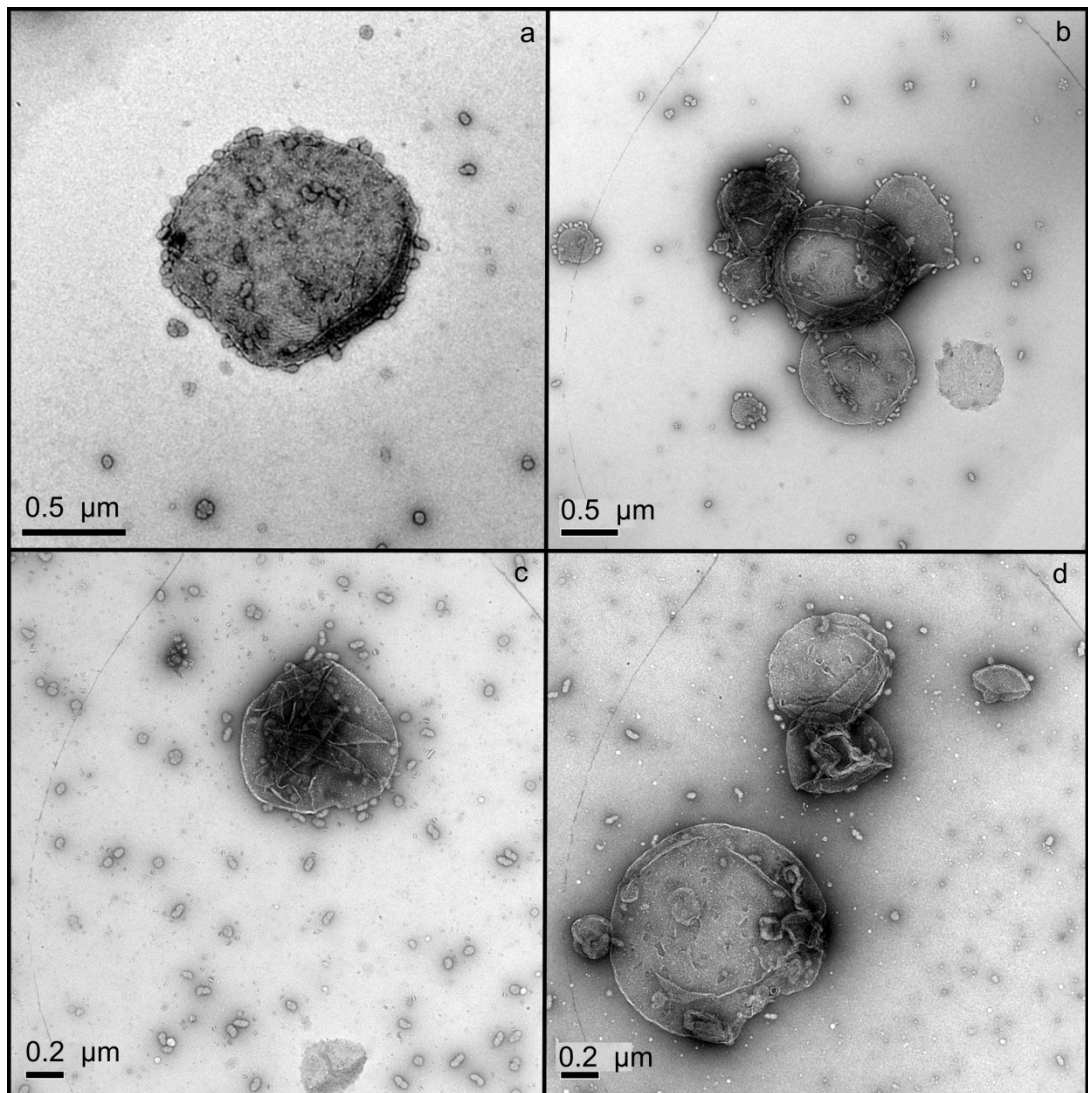


**Figure 3.10. Comparison of membranes from high salt trials.** (a) Negative stain TEM of membranes from 100 mM NaCl secondary gradients. (b) Negative stain TEM of membranes from 300 mM NaCl secondary gradients. (c) Negative stain TEM of membranes from 600 mM NaCl secondary gradients. (d) Negative stain TEM of membranes from 1200 mM NaCl secondary gradients. The number of glycogen granules on the surface of the membranes is seen to decrease with increasing concentrations of NaCl

### 3.3.8 DCMU treatment of cells

Another approach that was taken was to try and prevent glycogen synthesis in *Synechocystis*; 3-(3,4-dichlorophenyl)-1,1-dimethylurea (DCMU) is a PSII inhibitor which also has the effect of preventing glycogen synthesis in cyanobacteria (Lehmann and Wöber, 1976). 100 ml cultures were grown to an OD<sub>750</sub> of 0.2 (early log phase) before being transferred into 1 litre of BG-11 medium supplemented with 10 µM DCMU. The cells were grown under standard conditions to an OD<sub>750</sub> of approximately 1.0 before being harvested. Cells were then lysed under standard conditions and membranes purified by standard primary and secondary gradients; the membranes were then imaged via EM (Figure 3.11).

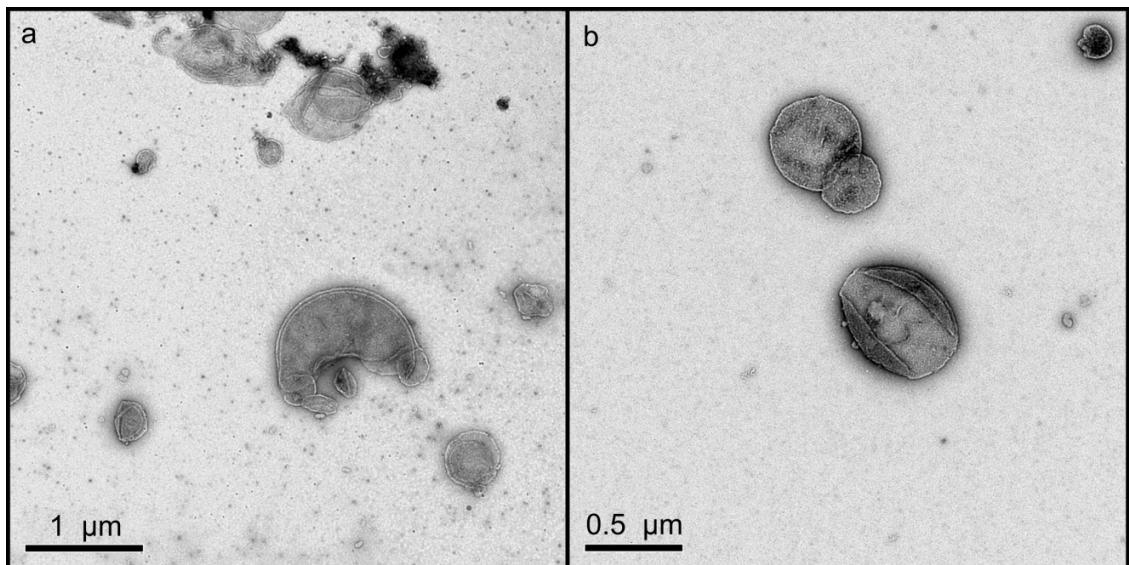


**Figure 3.11. Negative stain TEM of membranes from cells grown in DCMU supplemented medium. (a)** Sample harvested from primary gradients, **(b)** Sample harvested from secondary gradients. In both images the levels of glycogen granules are significantly reduced relative to membranes purified from cells grown in medium without DCMU.

The EMs of membranes harvested from the primary gradients (**Figure 3.11a**) show large membrane patches that are almost completely free of glycogen granules attached to the membrane. There is however a significant amount of cell debris in the background of this image, although granules are largely absent. In the EMs of the membranes purified on a secondary gradient (**Figure 3.11b**) most of the cell debris seen in the background of membranes from primary gradients (**Figure 3.11a**) is absent. These EM images show that growing *Synechocystis* in medium supplemented with 10  $\mu$ M DCMU is very effective for preventing the synthesis of glycogen granules.

### 3.3.9 Amylase treated membranes

Glycogen contains many  $\alpha$ ,1-4-glycosidic bonds which can be broken by  $\alpha$ -amylase; treating thylakoid membranes with  $\alpha$ -amylase should break down the glycogen granules attached to the surface of the membrane. Cells were broken using the standard cell breakage technique before incubation with 5  $\mu$ g/ml of  $\alpha$ -amylase (purified from *Aspergillus oryzae*, Sigma) for 1 hour. The cell lysate was then loaded onto a standard primary sucrose gradient to purify the thylakoid membranes. Membranes from this gradient were harvested and further purified on a standard secondary sucrose gradient; membranes from both gradients were imaged by EM (**Figure 3.12**).

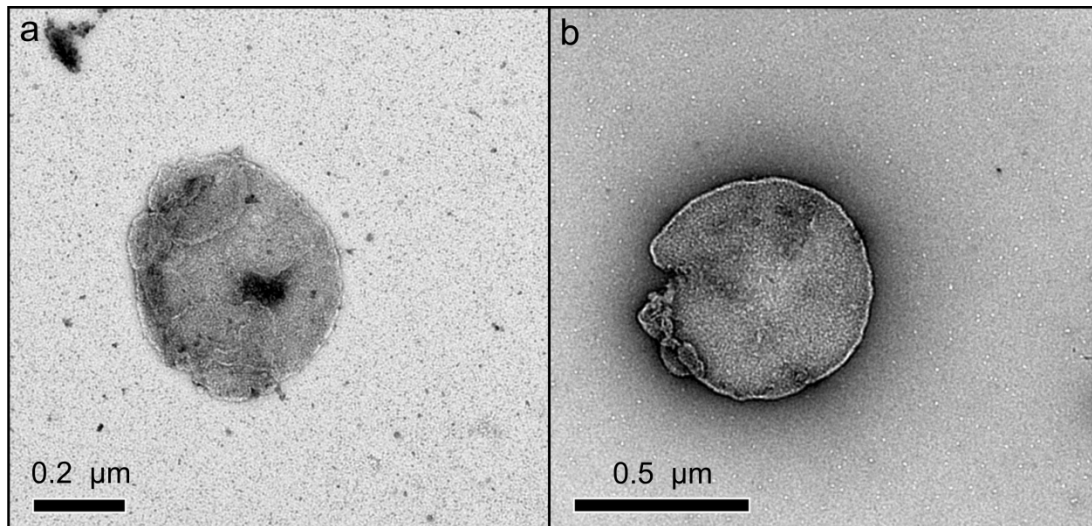


**Figure 3.12: Negative stain TEM of membranes treated with  $\alpha$ -amylase.** (a) Sample harvested from primary gradients, (b) sample harvested from secondary gradients. These EM images show  $\alpha$ -amylase treatment is very effective at removing granules.

From the EM images it can be seen that amylase treatment is able to remove close to 100% of glycogen granules from the surface of the thylakoid membranes and the background. In **Figure 3.12b** the combination of the amylase treatment and two sucrose gradient purification steps has been successful in producing membrane samples that are virtually free of any contaminating material. This method was the most effective in producing clean membrane patches of all those that were trialed. Therefore, in all subsequent membrane purifications cell lysates were treated with 5  $\mu\text{g/ml}$  amylase.

### **3.3.10 AFM of amylase treated membranes**

Samples prepared as described in **3.3.9** were imaged by AFM and membranes could be imaged without any problems arising from tip contamination (**Figure 3.13**). The sizes of the membrane patches were consistent with those observed in the EM data and the measured heights were between 50-200 nm, consistent with vesicular structures with a fluid filled lumen, and making them readily deformable when they come in contact with the AFM probe. This presents a significant challenge as the ideal sample for AFM is one that is flat and non-deformable, and it would be difficult to image the membrane fragments in their current state to a resolution high enough to observe single protein complexes. A procedure therefore had to be developed to alter the purified membrane fragments to make them more suitable for AFM.

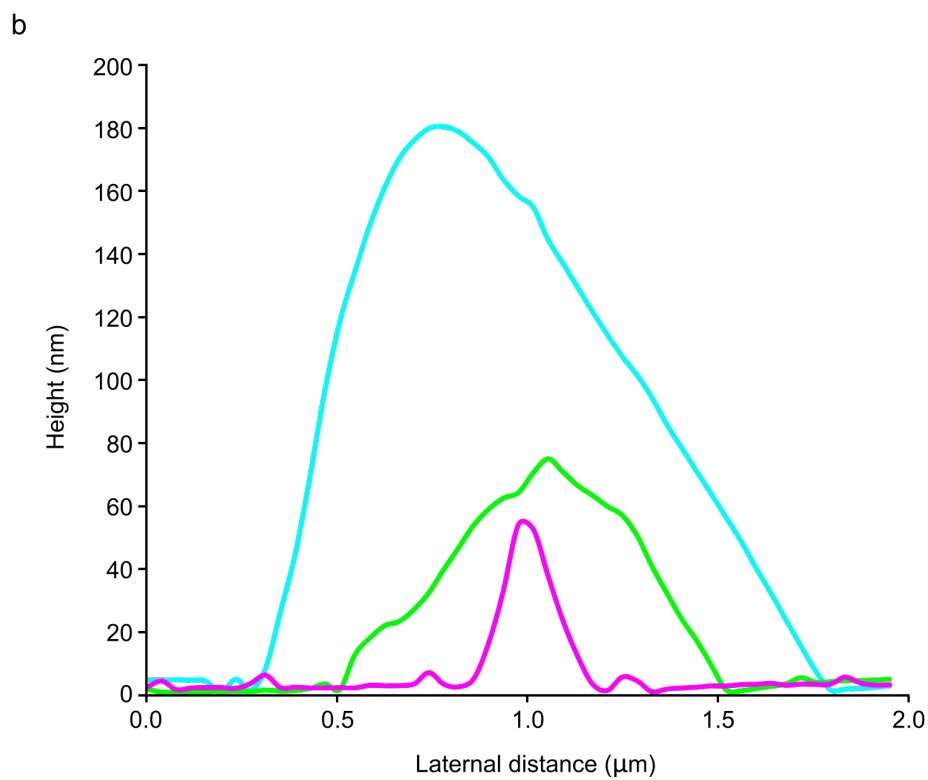
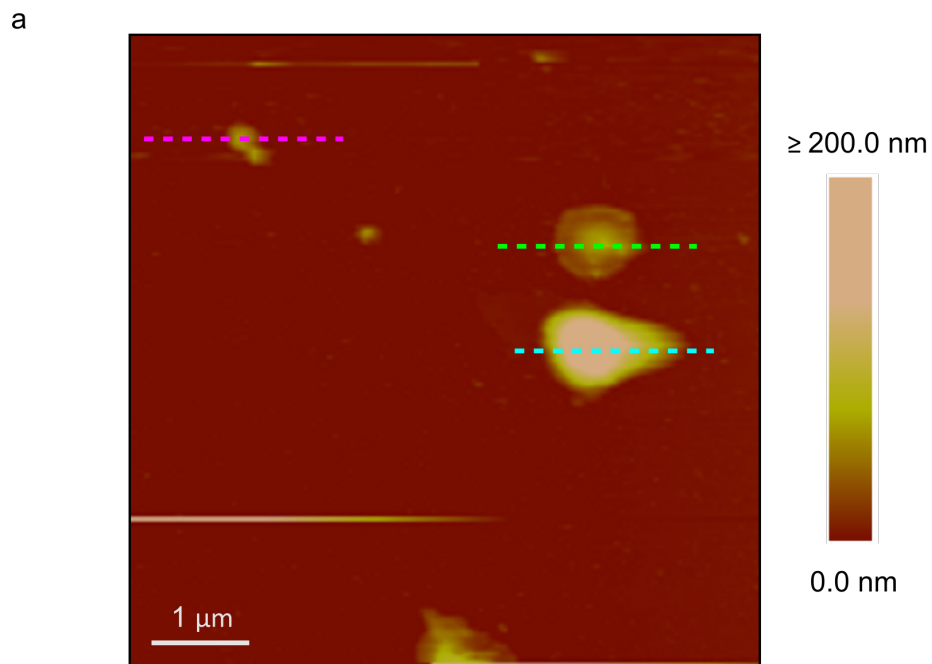
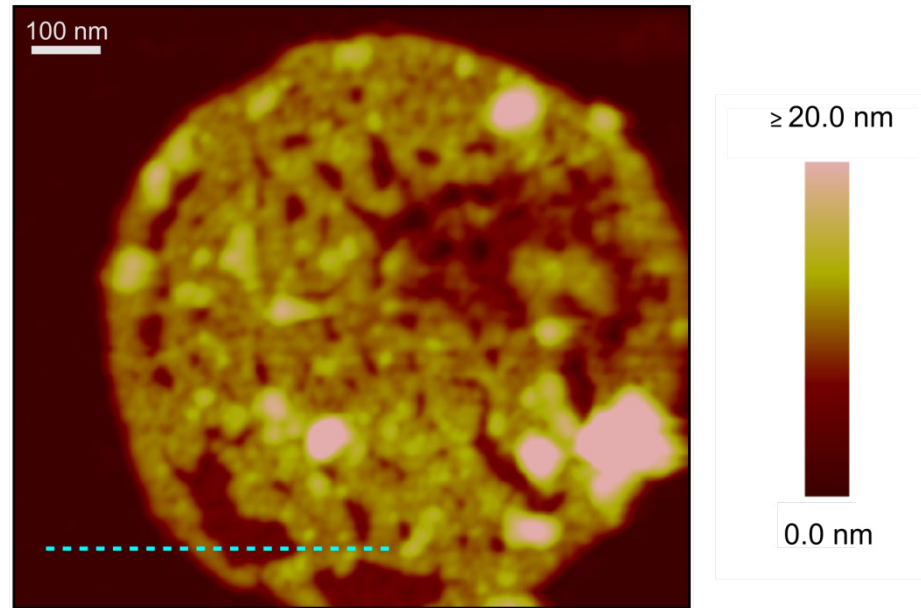


**Figure 3.13. AFM analysis of amylase treated membranes from secondary gradients. (a)** AFM scan showing several thylakoid membranes, **(b)** height profiles for selected membrane patches.

### 3.3.11 Imaging membranes under air

If the membranes were dried it was believed that its vesicular structure would collapse leaving two layers of appressed membrane which, when imaged under air would provide a flat, non-deformable sample that would be more suitable for AFM analysis. Membranes were harvested from standard secondary gradients and diluted to a concentration of 0.005 mg/ml of chlorophyll; 5  $\mu$ l of this sample was pipetted onto freshly cleaved mica followed by 45  $\mu$ l of absorption buffer. The membrane were then left to bind to the mica surface for 1 hour before being washed 10 times with 100  $\mu$ l of MilliQ water to remove any buffer salts before being dried under a constant stream of nitrogen; samples were then imaged in air by AFM (**Figure 3.14**). The AFM data show that the membrane sack does collapse when the sample is dried leaving a double layer of membrane with several perforations in the upper layer. In **Figure 3.14b** a cross-section of the membrane shows that the height of the upper layer is 10-12 nm and the lower layer is 5-6 nm. The absence of a liquid buffer leads to “crinkling” of the membrane which induces curvature on a nano-scale that can obscure the membrane topology of the integral protein complexes. High resolution imaging was difficult and protein complexes could not be observed in either the upper or the lower layer of membrane.

a



b

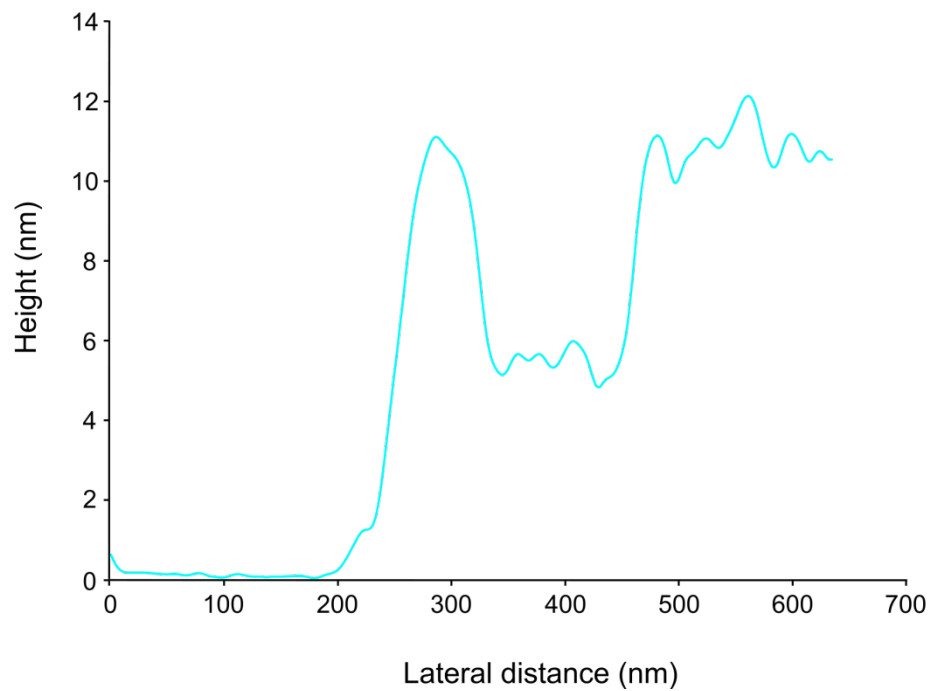


**Figure 3.14. Thylakoid membranes imaged by AFM in air. (a)** AFM scan showing a flattened thylakoid membrane, **(b)** height profile of the membrane patch; the upper layer of the membrane has a height of 10-12 nm and the lower membrane layer has a height of 5-6 nm.

### 3.3.12 Rehydration of dried membrane samples

In an attempt to try and address the issue of membrane shrinkage, samples were prepared in the same way as **3.3.11** however once the sample had been dried it was rehydrated with 50  $\mu$ l of standard imaging buffer and left for 1 hour. Due to the large perforations seen in many of the membrane fragments it was believed that upon rehydration the membranes would be unable to return to their original swollen vesicular conformation. Instead the two layers of the stacked membrane would remain flattened and in the presence of liquid buffer would “uncrinkle” to allow for AFM imaging of protein complexes. **Figure 3.15** shows a rehydrated membrane patch where a large area of the lower membrane layer is exposed. The cross-section shows a lower membrane layer with a height of 7-12 nm and an upper membrane layer with a height of 18-22 nm (**Figure 3.15b**); this would indicate that the membrane has expanded under liquid. In **Figure 3.16** the membrane patch from **Figure 3.15** has been imaged with a smaller scan size and does not appear to have the “crinkled” appearance seen in membrane patches imaged under air. Small protrusions in the luminal face of the lower membrane layer in **Figure 3.16a** have been circled in green; these protrusions are on the scale of single membrane complexes and are possibly from PSII or cytochrome *b<sub>6</sub>f*. In **Figure 3.16b** small protrusions on the stromal face of the upper membrane layer are circled in blue and could be from PSI; however the quality of the images is not high enough for assignment of protein complexes to the topology map. In **Figure 3.15** there are a number of smaller structures surrounding the membrane patch; these bodies are believed to be the contents of the thylakoid lumen and smaller fragments of membrane that have broken away from the main patch during the drying procedure. Unfortunately these smaller bodies appear to be causing contamination of the probe which made imaging difficult.

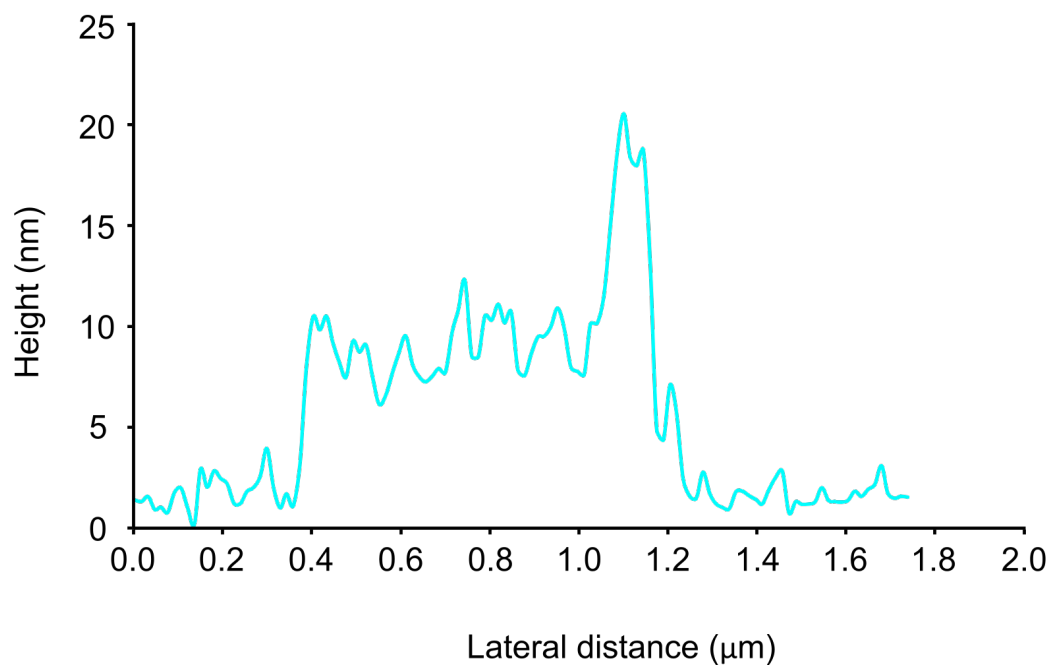
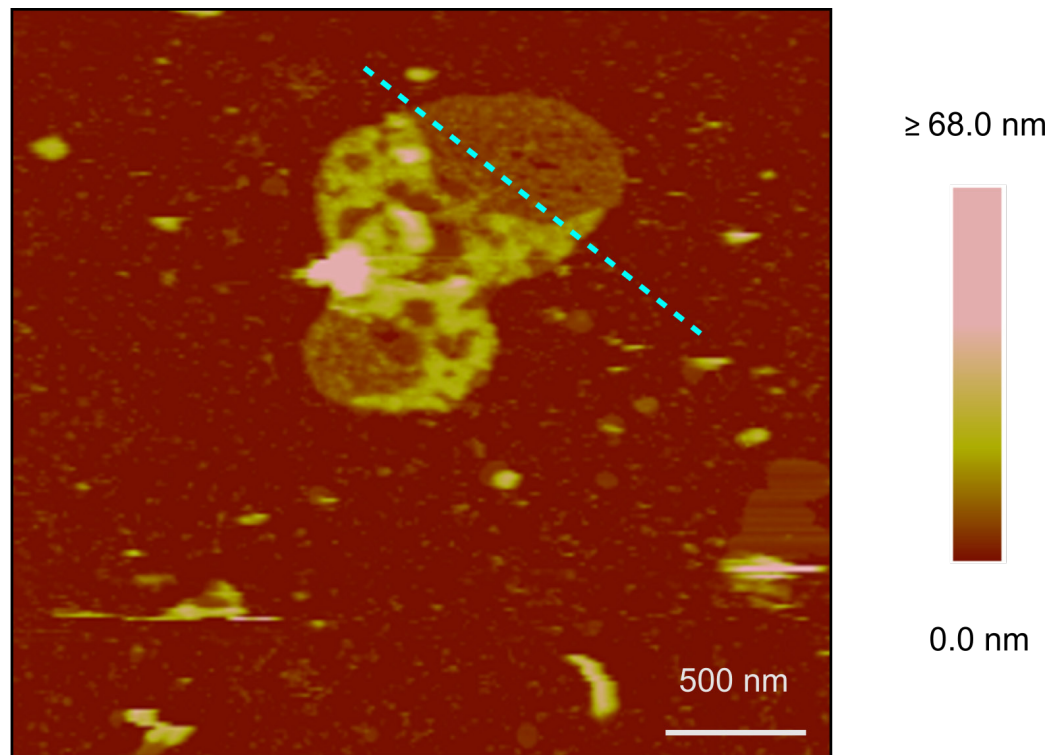


**Figure 3.15. Rehydrated thylakoid membranes imaged by AFM under liquid.** (a) AFM scan showing a rehydrated thylakoid membrane, (b) height profile of the membrane patch (left to right); the lower membrane layer has a height of 7-12 nm and the upper membrane layer has a height of 18-22 nm.

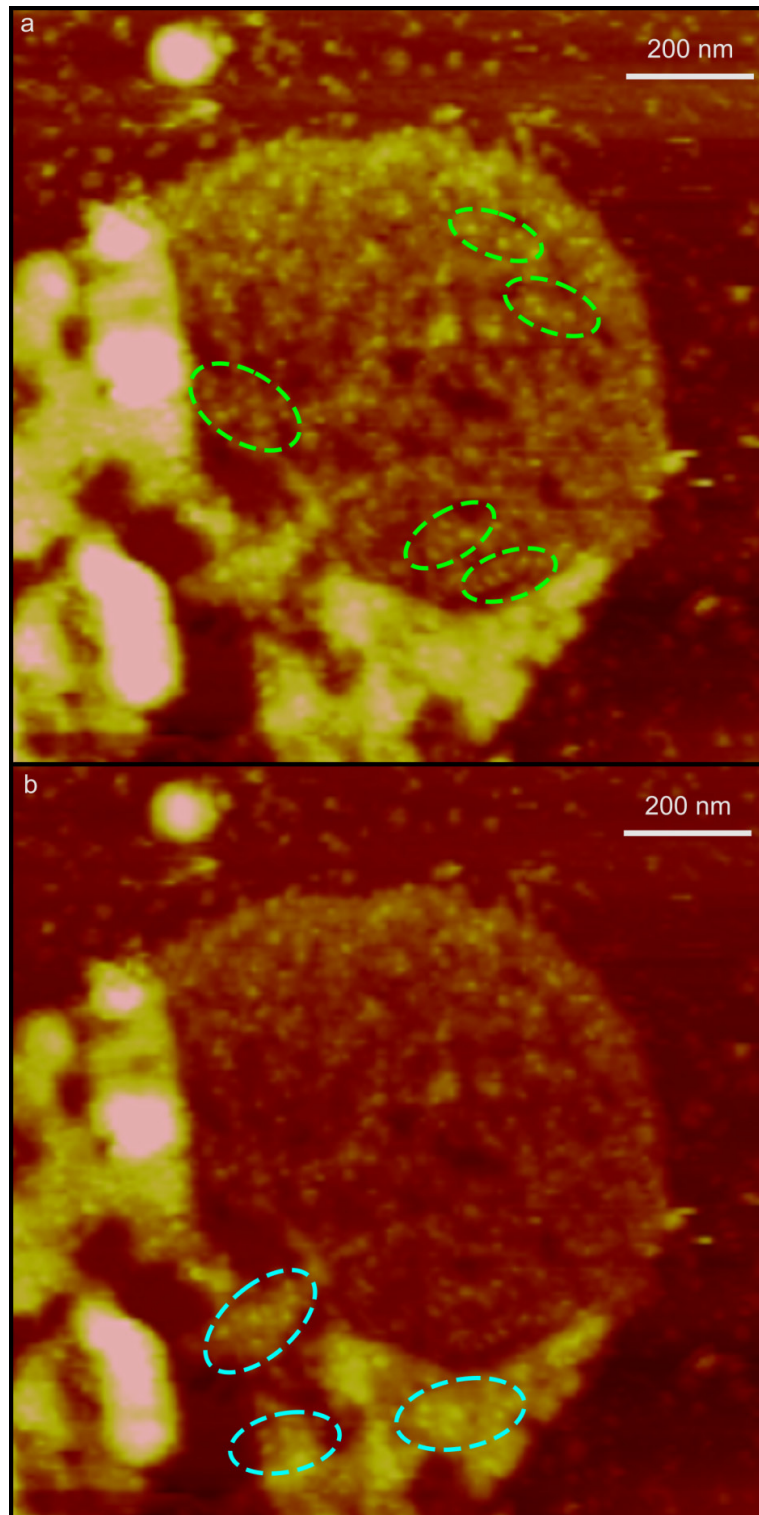


**Figure 3.16. AFM of a rehydrated membrane patch using a smaller scan size. (a)** AFM scan with potential proteins on the luminal face of the lower membrane layer circled in green. **(b)** AFM scan with potential proteins on the stromal face of the upper membrane layer circled in blue.

### 3.3.13 $\beta$ -DDM treatment of membranes

Previous protocols for producing flat membrane patches used very low concentrations of detergent to “open out” curved or vesicular membranes so that they would form flat layers that could be readily imaged via AFM. To try and replicate this effect, membranes harvested from a standard primary gradient were loaded onto a standard secondary sucrose gradient that contained n-Dodecyl-beta-D-Maltoside ( $\beta$ -DDM). Gradients containing 0.001%, 0.005%, 0.01% and 0.05%  $\beta$ -DDM in addition to a detergent-free control gradient were loaded with 1.5 ml of sample at a concentration of 0.2 mg/ml of chlorophyll. Gradients were centrifuged at 40,000 rpm in an SW41 rotor at 4 °C for 2 hours; the gradients were then photographed (**Figure 3.17**). The banding pattern seen in the detergent-containing secondary gradients shows a significant difference from the detergent-free control gradient. The green membrane containing band in the 0.001%, 0.005%, 0.01% and 0.05% gradients is significantly further up the gradient compared to the detergent-free gradient. This would indicate that the detergent in these gradients has broken the larger thylakoid membranes into smaller fragments that cannot travel as far through the gradient during centrifugation. With increased detergent concentration the green band travelled less distance through the gradient.



**Figure 3.17. Secondary sucrose gradients from  $\beta$ -DDM trial.** The concentrations of  $\beta$ -DDM in the gradients from left to right were; 0.000 % (control gradient), 0.001 %, 0.005 %, 0.01 % and 0.05 %. The green fraction travels less distance through the gradient as the detergent concentration increases indicating the size of the membrane fragments is decreasing

### 3.3.14 AFM of $\beta$ -DDM treated membrane fragments

The membrane bands from all the detergent-containing secondary gradients were harvested and absorbed to the mica under standard conditions before being imaged via AFM under liquid. It is generally possible to determine what type of structure the membrane has based on its height and topology; **Figure 3.18** details the different types of membrane structure including their respective heights and topologies.

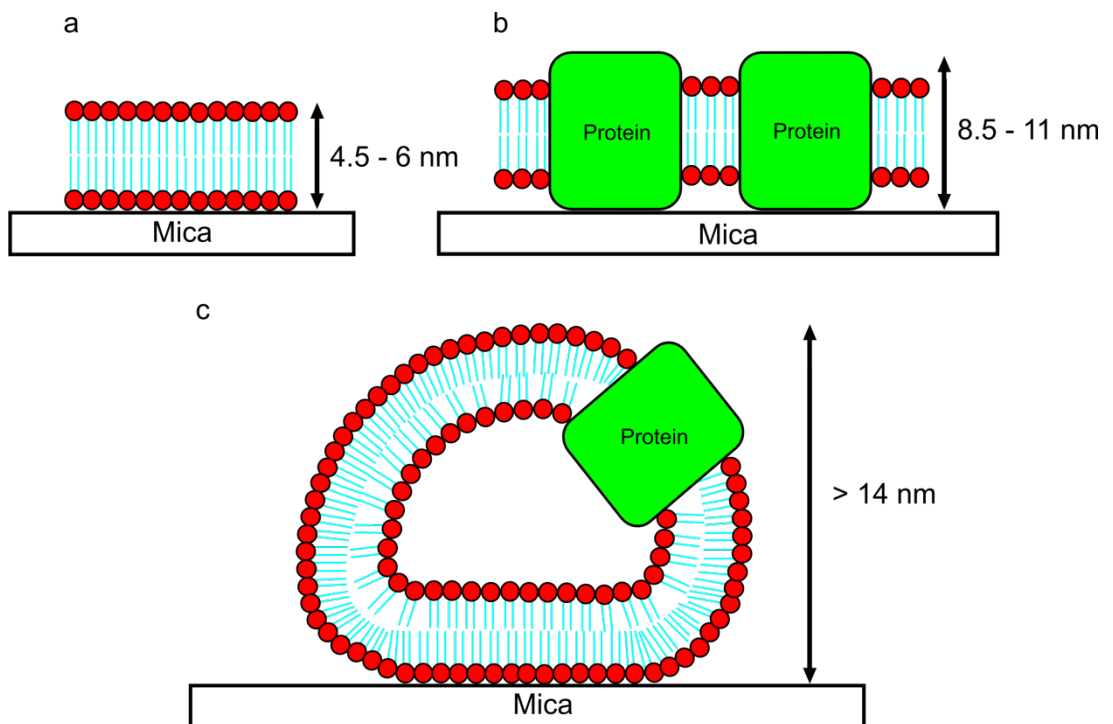


**Figure 3.18. Schematic showing how membrane structures can be identified from their height and topology. (a)** Membranes composed entirely of phospholipids have a height of 4.5-6 nm; when imaged with AFM they appear to have very little surface topology. **(b)** Membranes that contain proteins have a height of 8.5-11 nm; the surface of the membrane usually has significant topology. **(c)** Vesicular membranes have a curved topology and usually have a height greater than 14 nm, often significantly more.

AFM of the sample from the 0.05 %  $\beta$ -DDM gradient revealed only very small membrane patches which appeared to consist of lipid only. The samples from the 0.001, 0.005 and 0.01 %  $\beta$ -DDM gradients all contained membrane patches of similar shapes and sizes; **Figure 3.19** shows a field of membrane patches from the gradient containing 0.005 %  $\beta$ -DDM. There appeared to be three different types of membrane patch that could be imaged; vesicular patches, protein-containing single layered membrane patches and lipid-only single layered membrane patches. It was possible to image single protein complexes in some of the protein-containing single layered membrane patches (**Figure 3.20**) however this was rarely possible as these patches were observed at a low frequency and were relatively small.

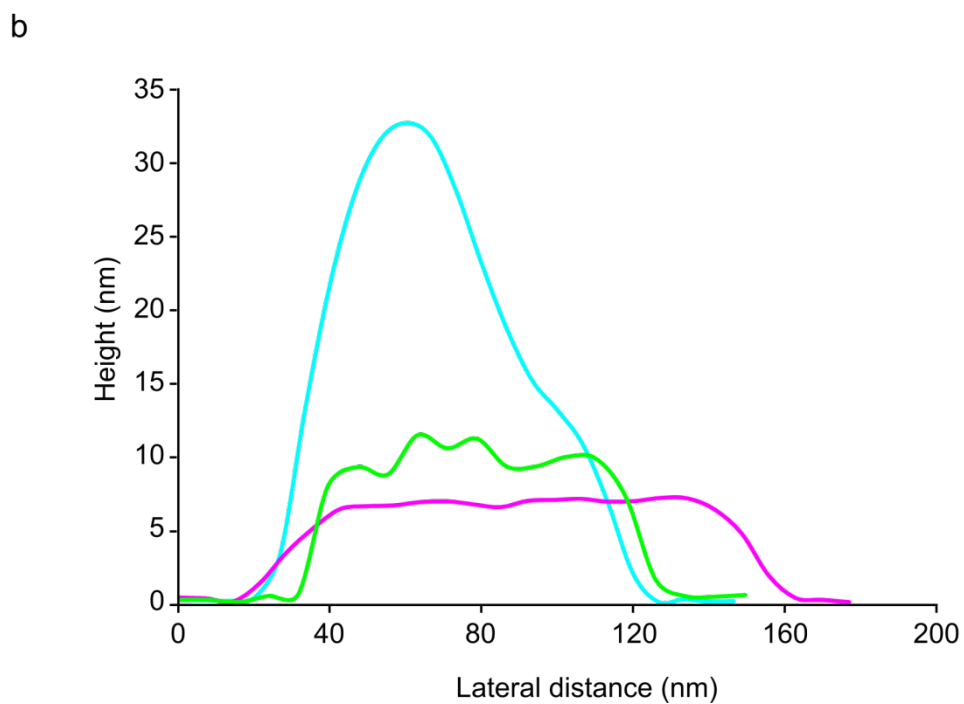
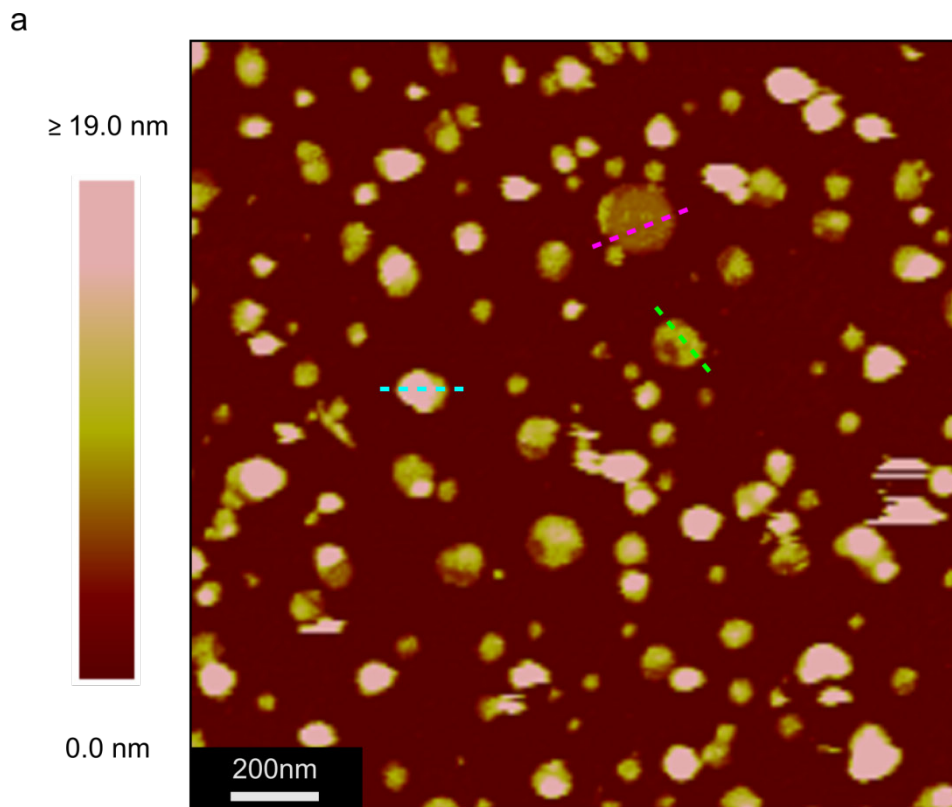


**Figure 3.19. AFM of  $\beta$ -DDM treated membranes.** (a) AFM scan of membranes harvested from a secondary gradient containing 0.005 %  $\beta$ -DDM. (b) Height profiles of vesicular (blue), protein-containing (green) and lipid-only (pink) membrane patches.

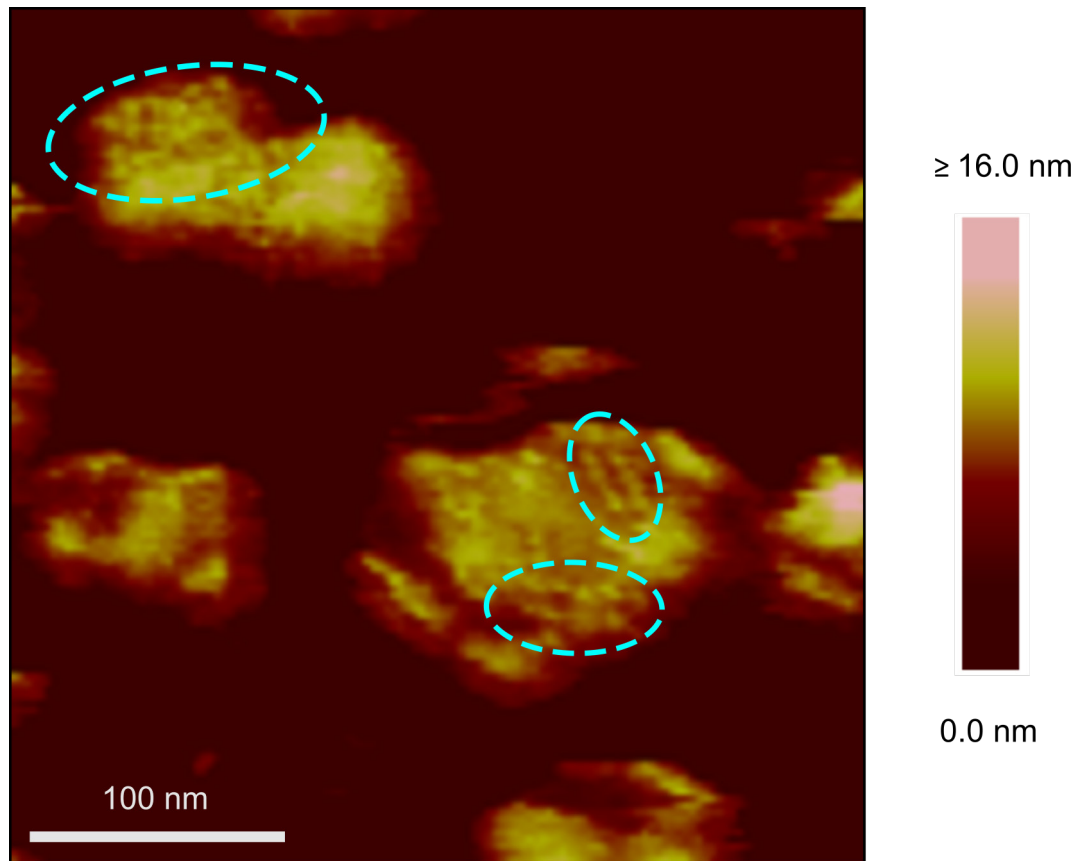


**Figure 3.20. AFM of protein-containing membrane patches from  $\beta$ -DDM method of preparation.** AFM scan of protein-containing membrane patches harvested from a secondary gradient containing 0.005 %  $\beta$ -DDM. Putative protein complexes have been circled in blue; the lower membrane patch appears to have a more ordered arrangement of protein complexes than the upper membrane patch.

As gradients containing  $\beta$ -DDM were not very efficient at producing protein-containing membranes patches, detergent trials were run to produce protein-containing membrane patches on a reproducible basis. Three different detergents were trialled; Tween 20, triton X-100 and digitonin (**Figure 3.21**). All of these detergents are non-ionic detergents which have non-charged hydrophilic head groups. These detergents typically do not denature protein complexes as is the case with some of the harsher ionic detergents such as SDS. All of these detergents have been used extensively to purify membrane proteins and it was believed that by using relatively low concentrations of these detergents it would be possible to produce protein-containing membrane patches that were amenable to AFM. In the case of digitonin, this detergent has previously been used to isolate PSII enriched domains from cyanobacterial thylakoid membranes (Folea *et al.*, 2008a) and chloroplast grana (Johnson *et al.*, 2014). It was hoped that this effect could be replicated to allow for such membrane patches to be imaged through AFM. Triton X-100 and Tween 20 are similar to  $\beta$ -DDM as both contain carbon chains which constitute the hydrophobic region of the detergent. Digitonin is different from the previously mentioned detergents as it contains a modified sterol ring as the hydrophobic region of the molecule. The critical micelle concentration (CMC) of  $\beta$ -DDM and triton X-100 is similar at around 0.2 mM at room temperature; the CMC of Tween 20 is lower at around 0.08 mM. It is unclear what the exact CMC of digitonin is, but it is believed to be below 0.4 mM.

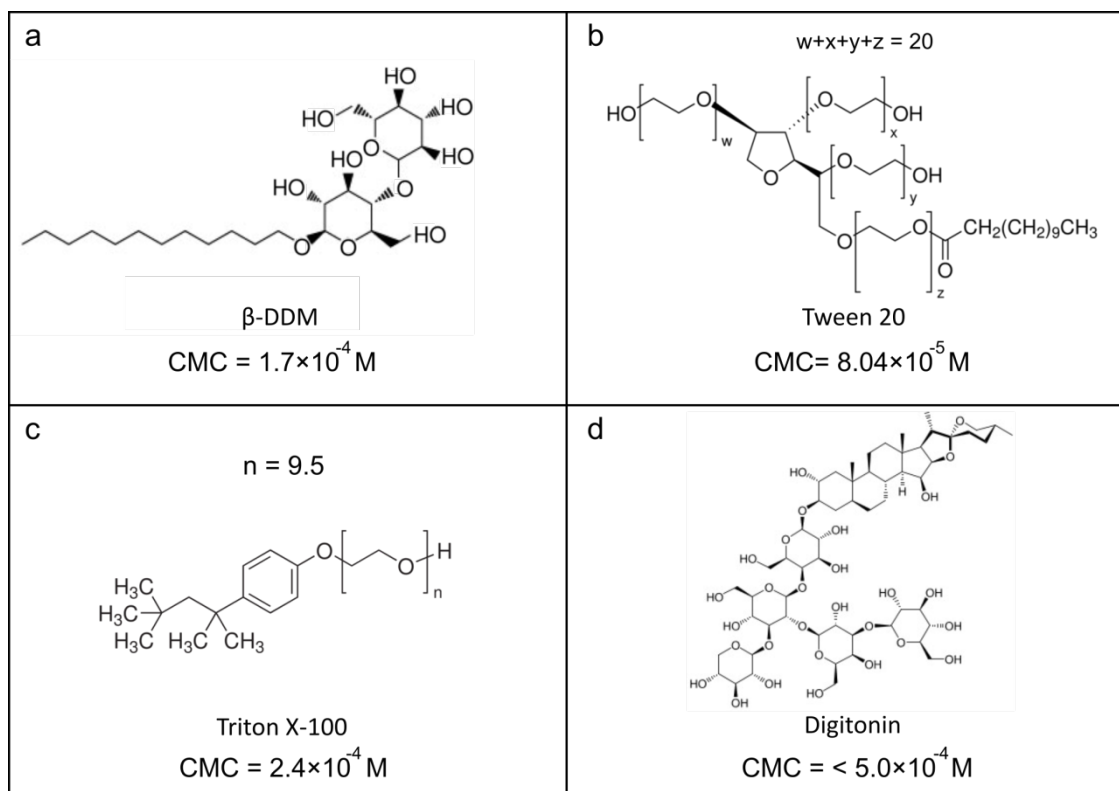


**Figure 3.21. Structures and CMCs of detergents that were trialed to produce flat membrane patches. (a)** The structure of  $\beta$ -DDM; **(b)** the structure of Tween 20; **(c)** the structure of triton X-100; **(d)** the structure of digitonin.

### 3.3.15 Tween 20 treatment of membranes

1.5 ml of membranes harvested from standard primary sucrose gradients at a concentration of 0.2 mg/ml chlorophyll were loaded onto standard secondary gradients that contained Tween 20, in addition to a detergent-free control gradient. The concentrations of Tween 20 used were 0.001 %, 0.005 %, 0.01 % and 0.05 %; the gradients were centrifuged at 40,000 rpm in an SW41 rotor at 4 °C for 2 hours and subsequently photographed (**Figure 3.22**). As with previous detergent-containing sucrose gradients the green membrane band did not travel as far through the gradient due to the reduced size of the membrane fragments. Interestingly the gradient containing 0.001 % Tween 20 is almost identical in appearance to the detergent-free gradient which suggests at this concentration the membranes had not been partially degraded. In the gradients containing 0.005 %, 0.01 % and 0.05 % Tween 20 the green band is at roughly the same place.

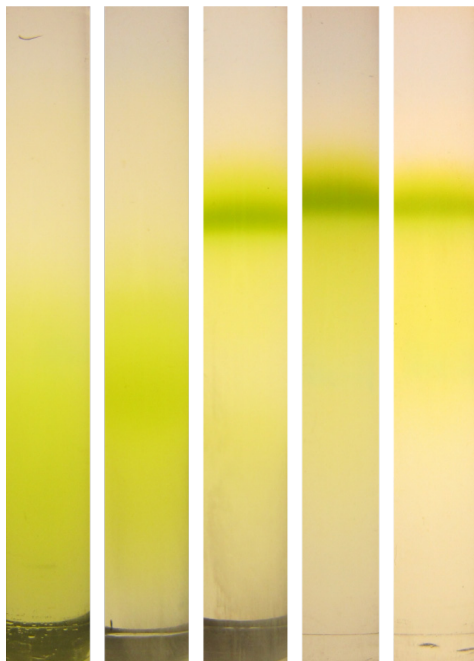


**Figure 3.22. Secondary sucrose gradients from Tween 20 trial.** The concentrations of Tween 20 in the gradients from left to right were; 0.000 % (control gradient), 0.001 %, 0.005 %, 0.01 % and 0.05 %. Increasing the detergent concentration reduces the distance travelled by the membranes through the gradient.

### 3.3.16 AFM of Tween 20 treated membrane fragments

Samples harvested from gradients containing Tween 20 were imaged by AFM; as expected the samples from the 0.001 % gradient looked similar to membranes from detergent-free gradients with no visible signs of membrane fragmentation. Membranes from the 0.005 %, 0.01 % and 0.05 % gradients had fragmented, as a consequence of the action of the detergent. AFM of membranes from the 0.005 % gradient (**Figure 3.23**) revealed vesicular membrane patches as well as lipid-only and protein-containing single layered membranes; however the latter was only present at a low frequency. Some of the protein-containing membrane patches were imaged at higher resolution (**Figure 3.24**); however, it was difficult to reproducibly image single protein complexes in membrane patches from samples prepared with Tween 20.

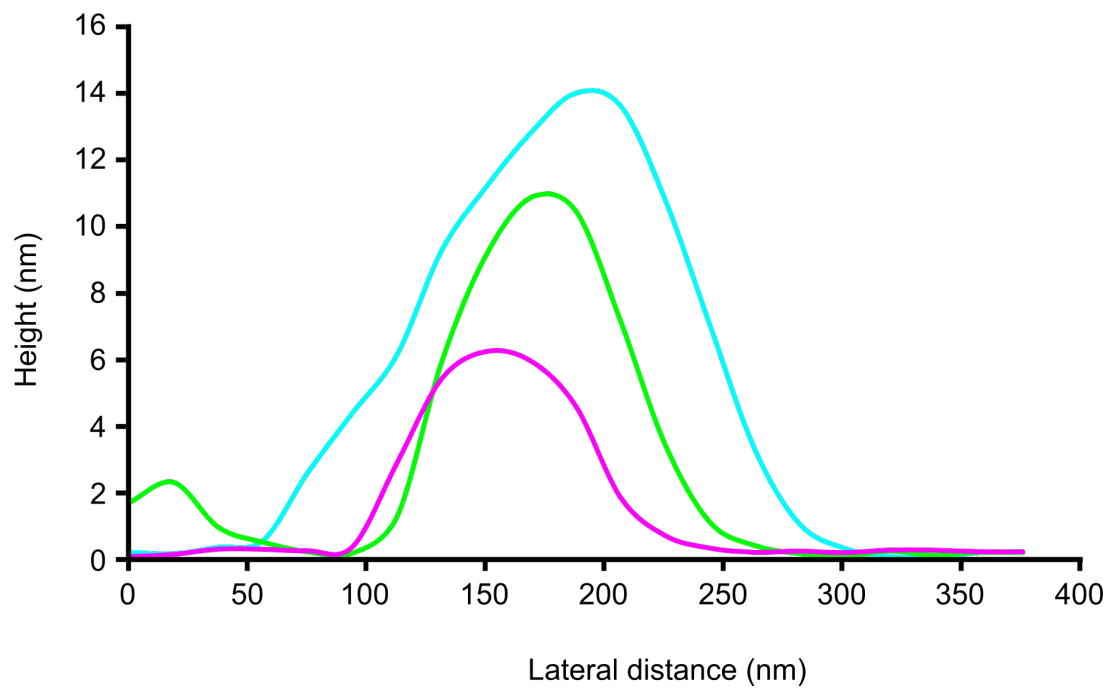
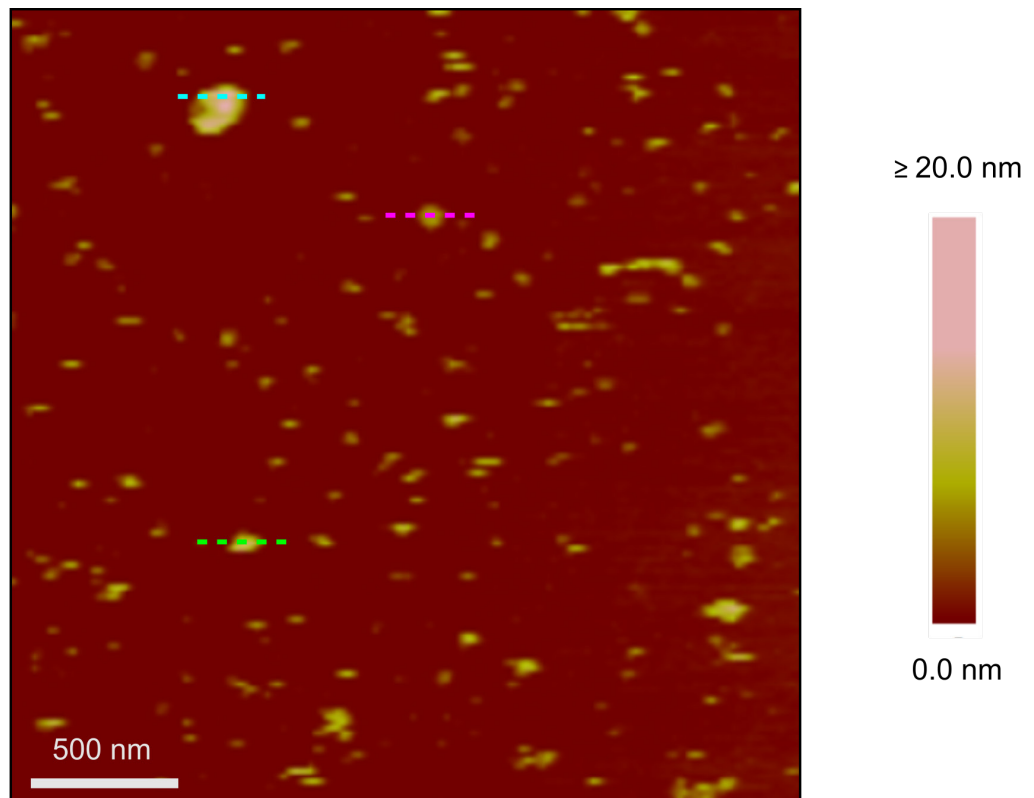


**Figure 3.23. AFM of Tween 20 treated membranes.** (a) Membranes harvested from a secondary gradient containing 0.005 % Tween 20 imaged by AFM. (b) Height profiles of vesicular (blue), protein-containing (green) and lipid-only (pink) membrane patches

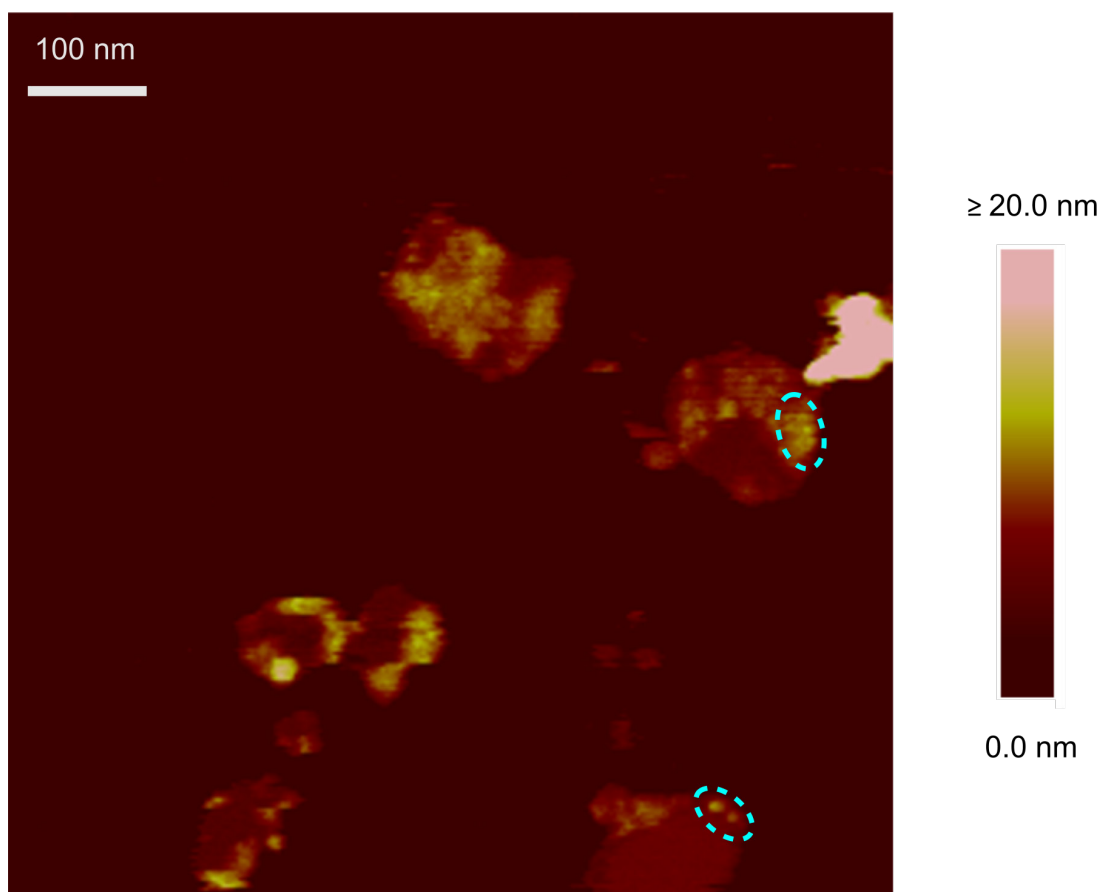


**Figure 3.24. AFM of protein-containing membrane patches from Tween 20 treated membranes.** AFM scan of protein-containing membrane patches harvested from a secondary gradient containing 0.005 % Tween 20. Putative protein complexes have been circled in blue.

### 3.3.17 Triton X-100 treatment of membranes

Thylakoid membranes purified on standard primary sucrose gradients were loaded onto standard secondary sucrose gradients containing 0.001%, 0.005%, 0.01% and 0.05% Triton X-100. 1.5 ml of membrane solution with a concentration of 0.2 mg/ml of chlorophyll was loaded onto each gradient and also loaded onto a detergent-free control gradient. The samples were then centrifuged at 40,000 rpm in an SW41 rotor at 4 °C for 2 hours and can be seen in **Figure 3.25**. In comparison to the detergent-free gradient, the green band in the Triton X-100 gradients had travelled less distance indicating the detergent had successfully fragmented the thylakoid membranes. The band in the gradient containing 0.01% Triton X-100 travels further through the gradient than in the gradient containing 0.005% Triton X-100. This was unexpected in the light of previous detergent trials. In the gradient containing 0.001% Triton X-100 the membrane band has travelled further with respect to the equivalent  $\beta$ -DDM gradient. The membrane band has also travelled further in the gradient containing 0.05% Triton X-100 with respect to the equivalent  $\beta$ -DDM gradient. Both these observations suggest that Triton X-100 is not solubilising the membrane to the same degree as  $\beta$ -DDM.

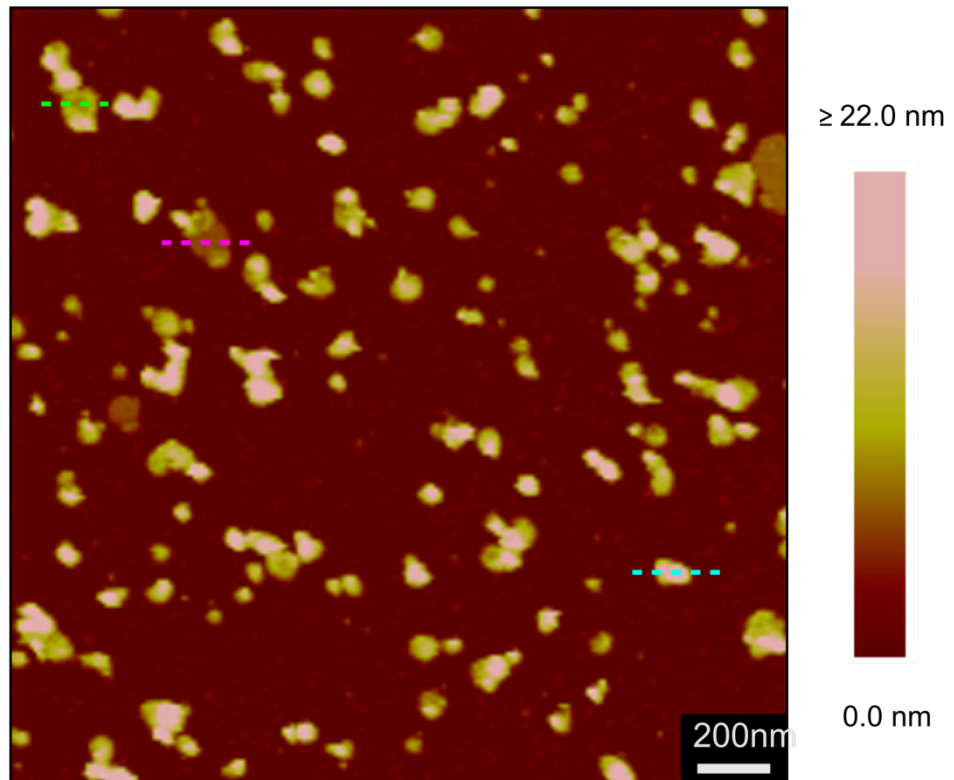


**Figure 3.25. Secondary sucrose gradients from Triton X-100 trial.** The concentrations of Triton X100 in the gradients from left to right were; 0.000 % (control gradient), 0.001 %, 0.005 %, 0.01 % and 0.05 %.

### **3.3.18 AFM of Triton X-100 treated membrane fragments**

AFM of membranes from the 0.001 % gradient (**Figure 3.26**) showed that the majority of the membrane fragments had a vesicular structure with a smaller number of lipid-only single layered fragments. Very occasionally protein-containing single layered membrane patches could be found however they were virtually absent in samples from Triton X-100 gradients. When protein-containing patches were imaged at high resolution no single protein complexes could be imaged; whether this was due to the “sharpness” of the AFM tip or if it was an effect of the detergent was unclear.

a



b

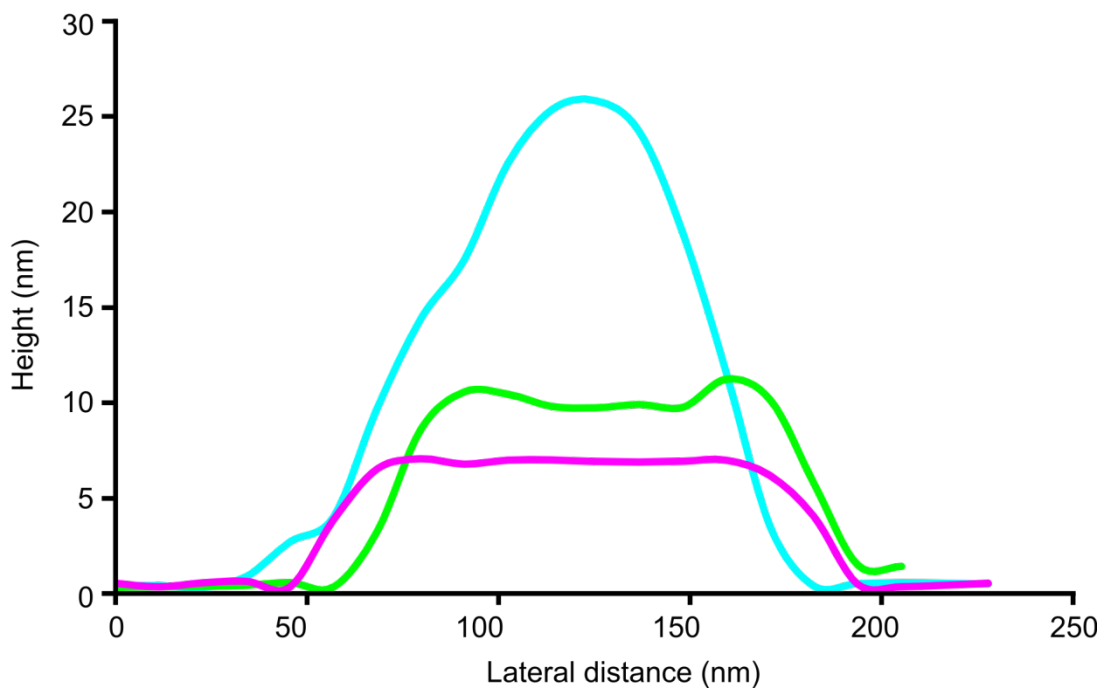


**Figure 3.26. AFM of Triton X-100 treated membranes.** (a) AFM scan of membranes harvested from a secondary gradient containing 0.001% Triton X-100. (b) Height profiles of vesicular (blue), protein-containing (green) and lipid-only (pink) membrane patches.

### 3.3.19 Digitonin treatment of membranes

Secondary sucrose gradients were poured that contained 0.1 % and 1.0 % digitonin in addition to a detergent-free control gradient. Digitonin was used at a higher concentration than previous detergents because it has a weaker effect on membranes than the other detergents (personal communication Dr. J. D. Olsen). 1.5 ml of membrane solution at a concentration of 0.2 mg/ml of chlorophyll was loaded onto each gradient. Gradients were centrifuged at 40,000 rpm in an SW41 rotor at 4 °C for 2 hours and were subsequently photographed (**Figure 3.27**). The gradients appear to show that digitonin is “weaker” than previously trialled detergents as a small proportion of membranes in the 1.0 % gradient have travelled almost as far as membranes in the detergent-free gradient. This suggests that at high concentrations of digitonin there are still membranes that are similar in size and shape to membranes in the detergent free gradient. The membranes in the digitonin gradients do not form distinct bands like those seen in **Figures 3.17, 3.22 and 3.25**, so the gradients were therefore fractionated. The 0.1 % gradient was fractionated into 3 parts; U1, M1 and L1 from which approximately 500 µl was harvested. The 1.0 % gradient was sectioned into 4 parts; U2, UM2, LM2 and L2 with approximately 500 µl being harvested from each.

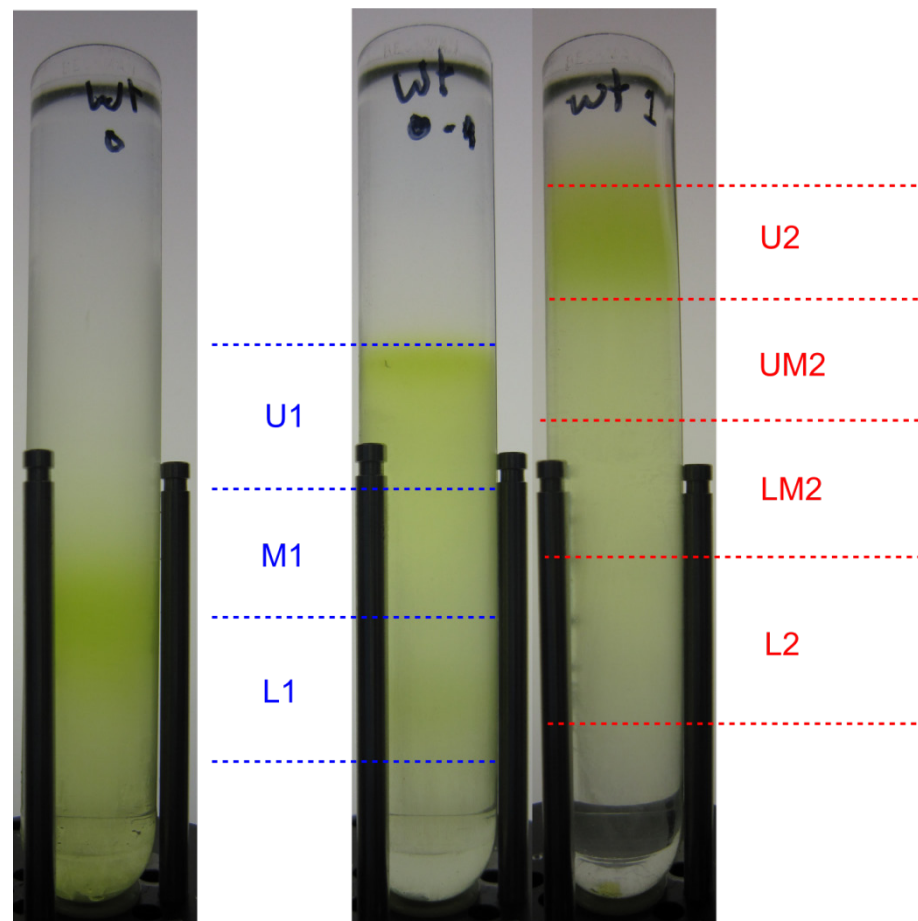


**Figure 3.27. Secondary sucrose gradients from digitonin trial.** The concentration of digitonin in the gradients from left to right: 0.0 % (control gradient), 0.1 % and 1.0 %.

### 3.3.20 AFM of Digitonin treated membrane fragments

AFM of the L1 and L2 fractions revealed mostly intact membranes although there were small numbers of lipid-only and protein-containing single membrane patches. The M1 and LM2 fractions contained large numbers of protein-containing single membrane patches in addition to vesicular membranes and lipid-only membrane patches. **Figure 3.28** is an AFM scan of membrane patches from the M1 fraction where single protein complexes can be observed in dozens of patches. The largest of the patches has a length and width of approximately 200 and 120 nm respectively and contains 60 protrusions on the scale of single protein complexes. Protein containing-membrane patches were also found in the U1, U2 and UM2 fraction, however these patches were relatively small with a maximum length of

approximately 100 nm. **Figure 3.29** shows an AFM topograph of a membrane patch from the U1 fraction in which the protein complexes appear to be dimers with a lateral spacing of between 11-14 nm and a height between 8-9 nm. The identification of these protein complexes is discussed in **Chapter 4**.

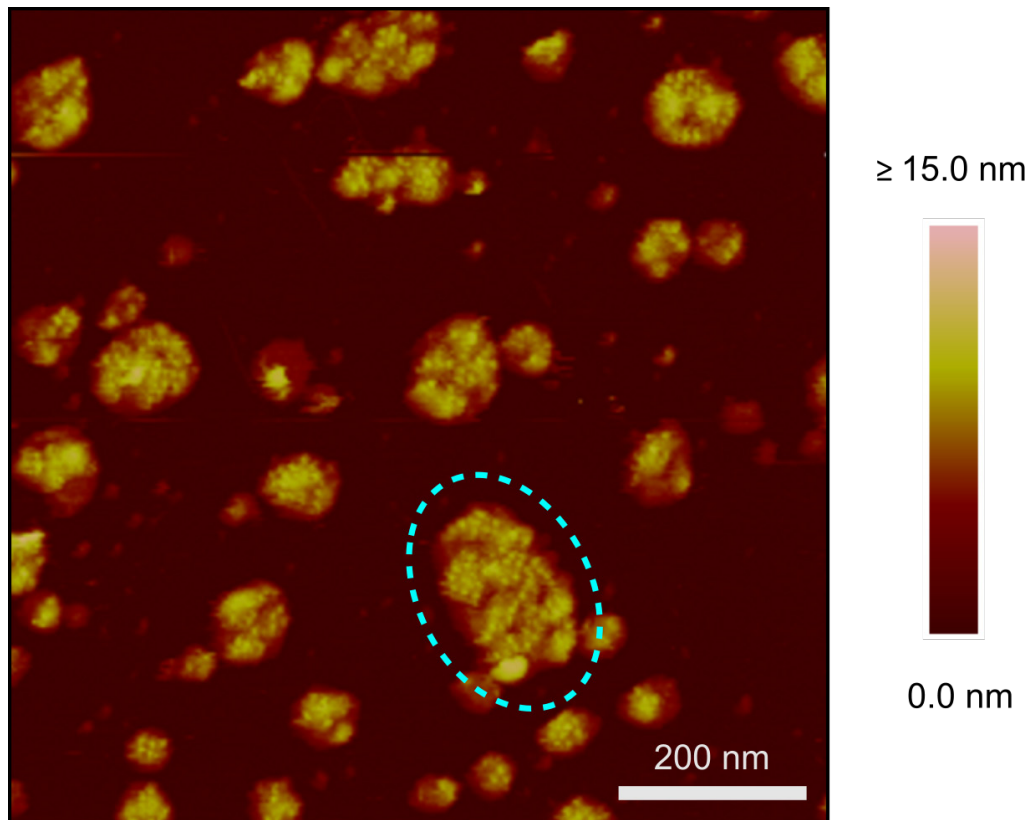
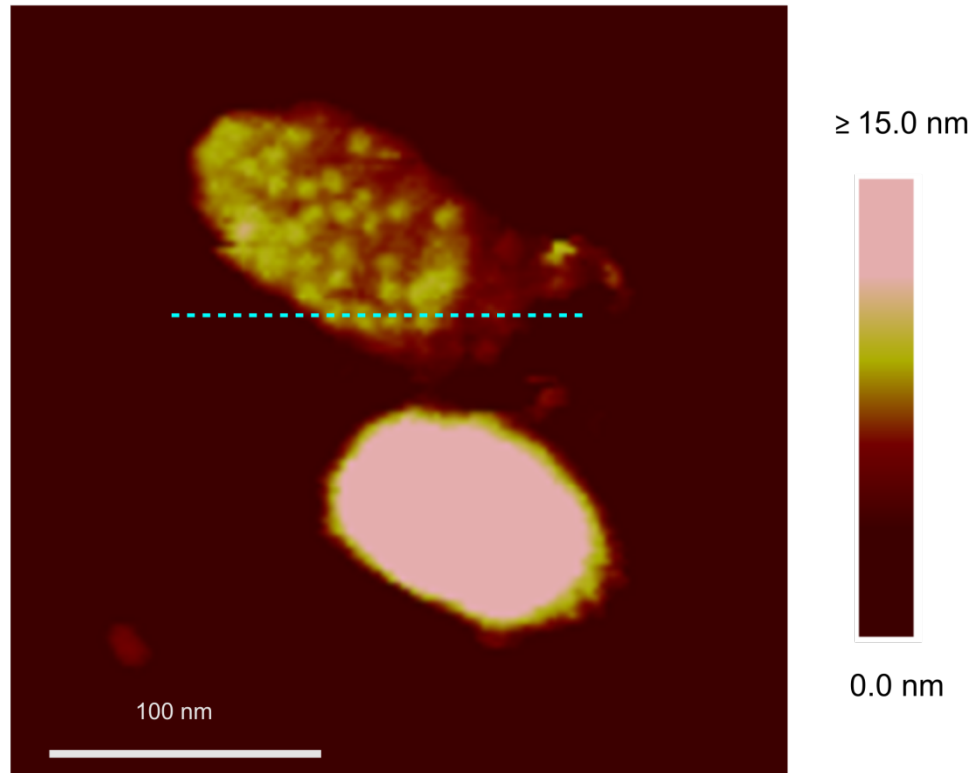


**Figure 3.28. AFM of protein-containing membrane patches from digitonin treated membranes.** AFM scan of a field of protein-containing membrane patches harvested from a secondary gradient containing 0.1 % digitonin. Individual protein complexes can be observed in several patches; the largest of these has been circled in blue.

a



b

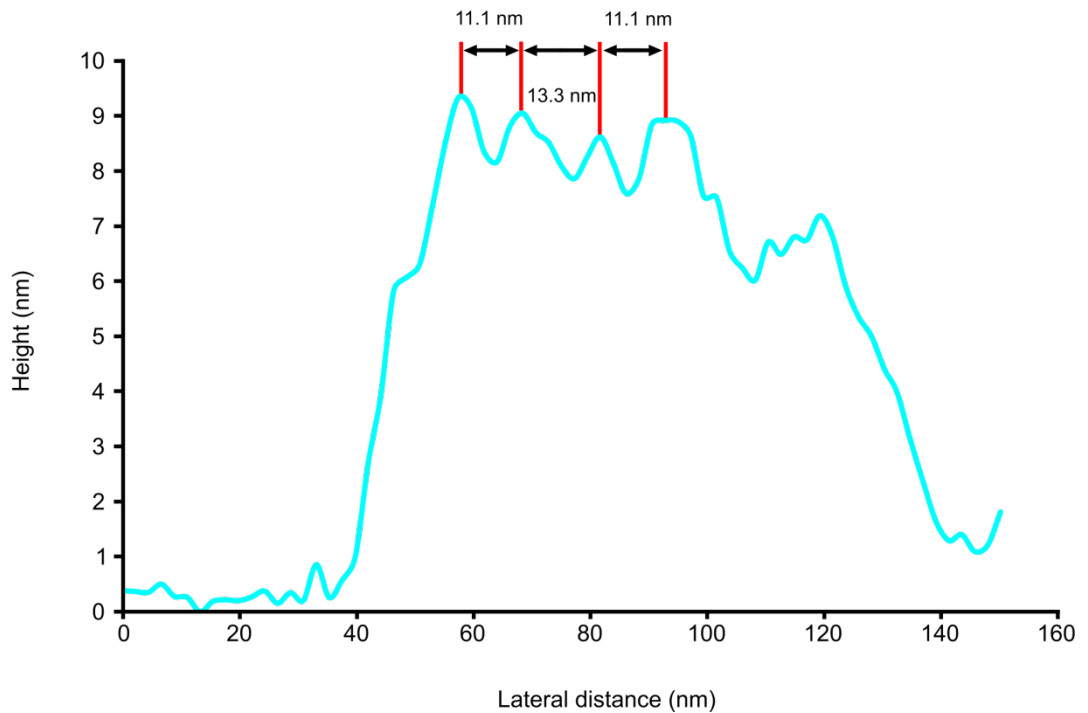


**Figure 3.29. High resolution AFM of protein complexes in digitonin treated membranes. (a)** AFM of a small membrane patch with clearly visible protein complexes. **(b)** Height profile showing the height and separation of the protein complexes in the membrane

### 3.4 Discussion

AFM has been used to investigate the organisation of light-harvesting complexes in membranes of several photosynthetic organisms; however there are no published data on high resolution AFM of cyanobacterial thylakoid membranes. In order to achieve an understanding of the native organisation of photosystems in cyanobacteria, it is essential to develop a method for producing thylakoid membranes that are amenable to AFM.

#### 3.4.1 Initial trials for purification of thylakoid membranes

Breakage trials found that mild bead beating was the most effective method for producing large thylakoid membranes that could be purified on sucrose gradients. Whilst French press and sonication were able to lyse *Synechocystis* cells there was no clear membrane-containing band in the sucrose gradients, so these cell breakage protocols were discounted. Using 6 x 1 minute and 6 x 20 seconds of bead beating both produced membrane-containing bands in the sucrose gradient with the former producing a much thicker band than the latter. EM analysis of samples from both gradients showed the increased length of time produced much smaller membranes. Despite the reduced quantity of thylakoid membranes produced by 6 x 20 seconds of bead beating, the increased size of the membrane patches was desirable and this procedure was used as the standard cell breakage method.

The initial primary sucrose gradients that were trialled did not provide very good separation between thylakoid membranes and the other cellular components and had to be altered to improve the purification of membrane samples. The sucrose concentration of the membrane sample harvested from the initial gradients was 42 % whereas the sucrose concentration of the blue fraction of the gradient was 28 % at its lowest point in the gradient. In order to separate these two fractions the revised primary sucrose gradient consisted of a 9 ml 30-40 % continuous gradient poured on top of 2 ml of 50 % sucrose. The reasoning for this gradient was that the membranes

would be able to enter the continuous gradient and the majority of the phycobilisomes would not. As the membranes travel through the continuous gradient larger contaminants should be removed and once the membranes reach the end of the gradient they will be concentrated against the 50 % sucrose step. Any large material such as the cell wall and unbroken cells should pass through the 50 % step and pellet at the bottom of the tube. Owing to the presence of a significant amount of material at the bottom of the initial primary gradients, the samples were centrifuged to remove the majority of unbroken cells and beads from the samples prior to loading. The gradient was successful in separating the phycobilisome and membrane fractions and there was a small pellet at the bottom of the centrifuge tube. The gradient was also successful in concentrating the membranes against the 50 % step as the green band is much stronger in **Figure 3.4** than in **Figure 3.1** which increased the quantity of thylakoid membranes that could be harvested. EM of these membranes from the revised primary gradients shows there was significant contamination in the samples. One particular problem with contamination was the presence of a large number of glycogen granules that appeared to coat the surface of the membranes. Initial attempts at imaging membranes from these samples with AFM proved to be very difficult. It is estimated that only 1 in 5 scans could be completed at a pixel density of 256 x 256 before contamination of the probes made imaging impossible. When imaging was not impeded by contamination membrane patches could be identified; however it was clear that further purification of the membranes was necessary to image single protein complexes.

#### **3.4.2 Removing contaminating material from membranes**

There were two types of contaminating material in the membrane samples; material that was in solution and material that adhered to the surface of the membrane. It was believed that the 50 % step in the primary gradient may be concentrating soluble contaminating material which is able to pass through the 30-40 % continuous gradient but not capable of entering the 50 % step. It was reasoned that if samples harvested from primary gradients were run on a second continuous sucrose gradient the contaminating material in solution would be able to separate from the membranes. It

was also hoped that a second sucrose gradient might help to dissociate the contaminating material from the surface of the membranes.

Imaging samples from secondary gradients by EM confirmed that the gradients were successful in removing much of the soluble contamination, although the majority of membranes still had a significant number of glycogen granules adhered to their surface. It became clear that a method for the targeted removal of glycogen granules or a change in growth conditions to prevent their synthesis had to be explored.

The first method that was investigated for the removal of glycogen granules was to increase the NaCl concentration of the secondary gradients. The approach had limited success as the number of glycogen granules associated with membrane patches was seen to decrease as the salt concentration increased; only at the maximum concentration of 1.2 M NaCl were the majority of the glycogen granules removed. It was thought that using even higher concentrations of salt in the buffer or running the samples on multiple high salt gradients could further reduce the levels of glycogen granule contamination. This line of investigation was not pursued as the effect of such high concentrations of salt on the membranes was unknown and could be potentially damaging to the photosynthetic protein complexes.

The PSII inhibitor DCMU has been shown to prevent glycogen synthesis in *Anacystis nidulans* when it is present at low concentrations in the growth medium (Lehmann and Wöber, 1976); DCMU binds to the Q<sub>b</sub> site on PSII and blocks electron transport in the protein complex (Lavergne, 1982). The exact mechanism of how PSII inhibition blocks glycogen synthesis is unclear, although glycogen synthesis is believed to occur only when cells are in a state of “energy excess” (Preiss, 1984) which is not the case when PSII function is inhibited. The presence of DCMU in the medium was highly successful at preventing the formation of glycogen granules on thylakoid membranes. EM confirmed that there were fewer glycogen granules on the surface of the membranes compared to the high salt trials. Although the levels of glycogen granules were very low in samples from the primary gradients, a significant amount of soluble contamination could still be observed. EM of samples harvested from secondary gradients shows significantly reduced levels of soluble contamination.

These EM images demonstrate the extent to which secondary sucrose gradients remove contaminating material and why they are useful for producing “clean” samples for AFM. The drawback to using these growth conditions is that the inhibition of PSII function could alter the native organisation of the photosynthetic proteins in the membrane. So whilst this is a very effective method of preventing the formation of glycogen granules it would be preferable not to interfere with the function of the proteins in the photosynthetic apparatus.

Glycogen is a polysaccharide composed of glucose monomers linked by  $\alpha$ -1, 4 glycosidic bonds and branched with  $\alpha$ -1, 6 glycosidic bonds;  $\alpha$ -amylase can cleave the  $\alpha$ -1, 4 glycosidic bonds allowing it to break down glycogen. The treatment of membrane samples with  $\alpha$ -amylase prior to purification on sucrose gradients was the most successful of all the procedures that were trialled to prevent glycogen granule contamination with close to 100 % removal of granules. There were no obvious drawbacks to treating membranes with amylase and the cell lysates for all further membrane purifications were incubated with amylase prior to purification.

### **3.4.3 AFM of membrane patches**

Whilst an effective method for purifying “clean” samples had been developed, the membranes themselves did not have a conformation that was amenable to high resolution AFM. For the AFM probe to track across the surface of the membrane the sample must be flat and not deform under the pressure from the probe; membranes purified on sucrose gradients had curved vesicular structures with a liquid-containing lumen. Dehydrating the sample and imaging the membranes in air was an effective method of flattening the membrane patches. The appearance of large holes in the membrane was useful as it allowed for the luminal face of the lower membrane layer to be imaged at the same time as the stromal face of the upper membrane. This feature could be advantageous as PSII and cytochrome *b<sub>6</sub>f* have significant topology on the luminal face of the membrane whereas PSI and the ATP synthase have significant topology on the stromal face (Jordan et al., 2001; Kurisu et al., 2003; Umena et al., 2011; Yoshida et al., 2001). Unfortunately the absence of buffer caused

the membrane to shrink which created creases in the membrane making it impossible to distinguish individual protein complexes. Another drawback is that one of the main advantages of AFM over other imaging techniques is its capacity to image membranes under buffer conditions similar to those in the native environment; imaging in air negates this advantage. For these reasons imaging membranes in air was discounted as an imaging technique. The presence of large holes in the membrane proved useful as membrane samples could be rehydrated with buffer and maintain their flat, double layered structure. Imaging rehydrated samples showed that membranes would uncrease when exposed to a liquid environment. Small protrusions on the scale of single protein complexes could be seen in both the luminal face of the lower membrane and the stromal face of the upper membrane.

Several studies have used low concentrations of  $\beta$ -DDM to produce flat membrane patches from vesicular membranes (Bahatyrova *et al.*, 2004; Olsen *et al.*, 2008; Adams and Hunter, 2012) and it was believed that this effect could be replicated with vesicular thylakoid membranes. Secondary gradients made with buffer containing low concentrations  $\beta$ -DDM were used to simultaneously purify and cause the fragmentation of membranes. Samples harvested from these gradients contained single layered protein-containing membrane patches and it was occasionally possible to image protein complexes in some of the membrane patches. The membrane patches produced by this treatment were relatively small with an observed maximum length of approximately 100 nm. The frequency of protein-containing membrane patches in the sample was low and most membrane patches were either vesicular or single layered. For these reasons further detergent trials were performed to find a detergent that could produce large single layered protein-containing membrane patches on a reproducible basis.

Secondary gradients containing three detergents were trialled; Tween 20, Triton X-100 and digitonin. The AFM analysis of samples from gradients containing either Tween 20 or Triton X-100 was similar to samples from  $\beta$ -DDM gradients as they contained a low frequency of protein-containing single layered membrane patches. Samples from digitonin gradients were able to consistently produce protein-containing single layered membrane patches that were of greater size than

those produced in any of the other detergent treated samples. Several membrane patches were imaged to high enough resolution to clearly identify single protein complexes. Secondary sucrose gradients were useful in separating membrane patches by size as larger patches were found further down the gradient. Digitonin treatment of thylakoid membranes was extensively used in this study and the identification of protein complexes in these membrane fragments is discussed in **Chapter 4**.

Whilst it is not clear why the digitonin treatment is more successful at producing single layered protein-containing membrane patches it should be noted that one of the major differences between digitonin and the other detergents that were trialled is the absence of a hydrocarbon tail. Digitonin contains a modified sterol which constitutes the hydrophobic region of the molecule. It is possible that this relatively large hydrophobic group does not insert as easily into the membrane as the smaller hydrocarbon tails in the other detergents due to steric hindrance; especially in the areas of membrane that are densely packed with protein. Digitonin also has a relatively large hydrophilic head group which may mean the number of digitonin molecules that are able to insert into the membrane is lower relative to detergents like triton X-100 and  $\beta$ -DDM which have smaller head groups. These factors could limit the degree to which digitonin is able to solubilise the thylakoid membrane which could in turn lead to the production of single layered protein-containing membrane patches.

### 3.5 Conclusions

A standard method was developed for producing cyanobacterial thylakoid membrane patches in which protein complexes can be imaged by AFM. Mild bead beating is the most effective cell breakage method for producing bulk amounts of large thylakoid membranes that can be purified on sucrose gradients. Treating the cell lysate with  $\alpha$ -amylase reduced the number of glycogen granules in the membrane sample to almost zero; eliminating one of the major sources of contamination. Purifying thylakoid membranes on two consecutive sucrose gradients yields clean membranes that can be imaged by AFM without significant contamination of the AFM probe. Two procedures were developed to produce flat thylakoid membranes for AFM imaging; the first procedure was to dehydrate membranes that were adhered to the mica then rehydrate the sample prior to imaging. The second procedure was to purify membranes on secondary sucrose gradients that contained low concentrations of digitonin. Both of these procedures produced flat membrane patches in which single protein complexes could be imaged with AFM.

## Chapter 4: EM and AFM analysis of protein complexes in cyanobacterial thylakoid membranes

### 4.1 Summary

Cyanobacteria are some of the most important and widely studied photosynthetic organisms. Despite the existence of crystal structures for the photosynthetic protein complexes of cyanobacteria there is still much to learn about the native organisation of these complexes in thylakoid membranes. EM and AFM are useful tools for investigating the protein organisation in biological membranes and towards this end these techniques were used to analyse highly purified thylakoid membranes.

EM of membranes from detergent-free primary gradients revealed the presence of large arrays of protein complexes which appeared to be parallel rows of PSII. These arrays were rarely observed and it was more common to find membrane patches in which no large scale organisation could be seen.

Membrane fragments from *Synechocystis* were purified on digitonin-containing secondary gradients and AFM was used to image the lumenal face of the membrane fragments to the level of single protein complexes. Two populations of protein complex could be identified from the height data; the complexes with high topology were identified as monomeric and dimeric PSII. The distances between these protein complexes that appeared to be in a dimeric configuration were measured and the heights of these complexes were comparable to the crystal structure of PSII. The complexes that protruded from the membrane to a lesser extent were tentatively assigned as cytochrome *b<sub>6</sub>f* and partially disassembled PSII; however further analysis of the membrane fragments will be required to confirm the identity of these topological features

The organisation of protein complexes in the membrane agreed with the EM data as complexes were generally observed to be in a disordered state. In some membrane patches parallel linear rows of PSII dimers could be imaged in areas that had a predominantly random distribution of complexes. It was also possible to image membrane fragments in which all of the protein complexes had formed into linear, parallel or close to parallel rows.

The density of identifiable protein complexes varied, with some membrane patches appearing to exclusively contain lumenally protruding complexes (PSII and cytochrome *b<sub>6</sub>f*); other membrane patches contained small domains of these complexes interspersed throughout otherwise featureless areas of flat membrane. The height of some areas of featureless membrane was consistent with the height of PSI although it was not possible to identify individual complexes, as PSI has minimal luminal topology.

Membrane fragments from *Thermosynechococcus elongatus* were purified on digitonin-containing gradients and subsequently imaged by AFM. Membrane fragments that were very similar to those purified from *Synechocystis* could be imaged to the level of single protein complexes. The heights of the protein complexes were consistent with those measured for protein complexes in *Synechocystis* membrane patches. It was possible to identify monomeric and dimeric PSII complexes in addition to assigning potential cytochrome *b<sub>6</sub>f* complexes. The major difference between membrane patches from *Synechocystis* and *T. elongatus* was a lower density of identifiable complexes in the latter. It was also possible to image PSI trimers in membrane patches from *T. elongatus* which were found to form larger ordered arrays; this organisation has not previously been reported and represents a strict segregation of PSI from all of the other protein complexes in the photosynthetic unit. Membrane patches from *T. elongatus* were also imaged that contained PSI which was not in large ordered arrays, but distributed randomly throughout the membrane fragment.

## 4.2 Introduction

PSI and PSII absorb light to drive photosynthesis and whilst the structure and function of these protein complexes has been extensively characterised in cyanobacteria (Jordan *et al.*, 2001; Umena *et al.*, 2011), the native organisation of photosystems in cyanobacterial thylakoid membranes is less well understood. Green plants contain homologues of the cyanobacterial photosystems; however the light harvesting antenna complexes in the two types of organism are very different. Green plants contain membrane bound complexes from the LHCII family (Horton *et al.*, 1996); whereas cyanobacteria utilise water soluble phycobilisome complexes that are attached to the cytoplasmic face of the thylakoid membrane (MacColl, 1998). The ultrastructure of chloroplasts also differs from that of cyanobacteria as it contains granal stacks of thylakoids that are connected by stromal lamellae (Albertsson, 2001). Cyanobacterial thylakoid membranes are not stacked due to the large phycobilisome complexes situated between thylakoid membranes. In chloroplasts PSI and PSII are segregated, with the latter located in the grana and the former situated in the outer most membranes of the grana stack and in the unstacked stromal lamellae (Albertsson, 2001).

Owing to the differences in membrane ultrastructure, cyanobacterial photosystems cannot be segregated in the same way as chloroplasts, although there is evidence to suggest some degree of spatial heterogeneity in cyanobacterial thylakoids. Hyperspectral fluorescence imaging of *Synechocystis* cells has shown the majority PSI fluorescence comes from thylakoid membranes in the centre of the cell; whereas the greatest levels of PSII fluorescence is detected in thylakoid membranes closer to the plasma membrane (Vermaas *et al.*, 2008). This indicates that linear electron transport between the two photosystems occurs primarily in the periphery of the cell and cyclic electron transport, which exclusively involves PSI, takes place in a more central location in the cell. Spatial heterogeneity in thylakoid membranes has also been observed in another species of cyanobacteria; immunogold labelled membranes from *Synechococcus* sp. PCC7942 were analysed by TEM which detected “radical asymmetry” in the distribution of the protein complexes from the photosynthetic apparatus (Sherman *et al.*, 1994). PSI and ATP synthase were primarily located in the

outermost thylakoid membranes that were closest to the plasma membrane whereas PSII and cytochrome *b<sub>6</sub>f* were found to be evenly distributed through the thylakoid membrane system. The consensus appears to be that in *Synechocystis* and *Synechococcus* PSI and PSII are spatially segregated in the thylakoid membrane to some degree.

Freeze fracture and negative stain EM have been used extensively to image protein complexes in thylakoid membranes. Most EM studies have focused on the identification of PSII complexes in the membrane. It has been found that PSII complexes can form into large ordered arrays consisting of parallel rows of PSII or have a more disordered, seemingly random, distribution depending on the growth conditions of the bacteria (discussed fully in **1.7**)

All of the techniques previously used to investigate the organisation of protein complexes in cyanobacterial thylakoid membranes have their merits and drawbacks. One advantage of hyperspectral fluorescent imaging is that it can be used on live cells allowing the native architecture of the thylakoid membrane to be investigated on the scale of whole cells. The resolution however is limited to approximately 200 nm which is not sufficient to image single protein complexes. Freeze fracture EM and negative stain EM have sufficient resolution to image single protein complexes; however the sample preparation and imaging procedures have the potential to disrupt the native structure of the thylakoid membrane. AFM has some advantages as it can be used to image single protein complexes in membranes that are in near-native buffer conditions causing minimal disruption to the membrane.

PSI, PSII, cytochrome *b<sub>6</sub>f* and ATP synthase span the membrane and have protrusions that extend past the surface of the membrane (Jordan *et al.*, 2001; Kurisu *et al.*, 2003; Umena *et al.*, 2011; Yoshida *et al.*, 2001). The extrinsic parts of PSI and ATP synthase protrude to the greatest degree from the cytoplasmic surface of the membrane, whereas PSII and cytochrome *b<sub>6</sub>f* protrude from the luminal surface of the membrane by 5 nm and 4 nm respectively. These features can be exploited by AFM as it has sub-nanometer resolution in the vertical axis allowing protein complexes to be identified from their height. Other distinguishing features include the trimeric

configuration of PSI and the dimers of PSII and cytochrome *b<sub>6</sub>f*. Thus, it is possible to identify individual protein complexes in oligomeric membrane assemblies, as long as the AFM analysis is performed with a sufficiently sharp AFM probe and a “clean” membrane patch is available

## 4.3 Results

### 4.3.1 EM of thylakoid membranes from *Synechocystis*

Through EM analysis of membranes harvested from primary sucrose gradients described in **3.3.2** it was sometimes possible to visualise single protein complexes (**Figure 4.1**). Typically proteins were disordered in the membrane (**Figure 4.1a**), although it was occasionally possible to see proteins adopt a more ordered configuration. In **Figures 4.1b, c and d** parallel rows of protein complexes can be seen in the membrane; similar domains have previously been purified from detergent treated membranes and imaged by negative stain EM. Through the use of single particle reconstruction the crystal structure of PSII was fitted to the EM projections (Folea *et al.*, 2008a). We have shown that these PSII domains are present in membranes that have not undergone any form of detergent treatment. Negative stain EM of membranes has the drawback that it takes place under vacuum and it cannot be ruled out that these ordered PSII arrays are artefacts of dehydration or the negative staining procedure. It is therefore still necessary to image thylakoid membranes by AFM, which is carried out at atmospheric pressure under liquid, to confirm if these arrays are present in the native structure of the thylakoid membrane.

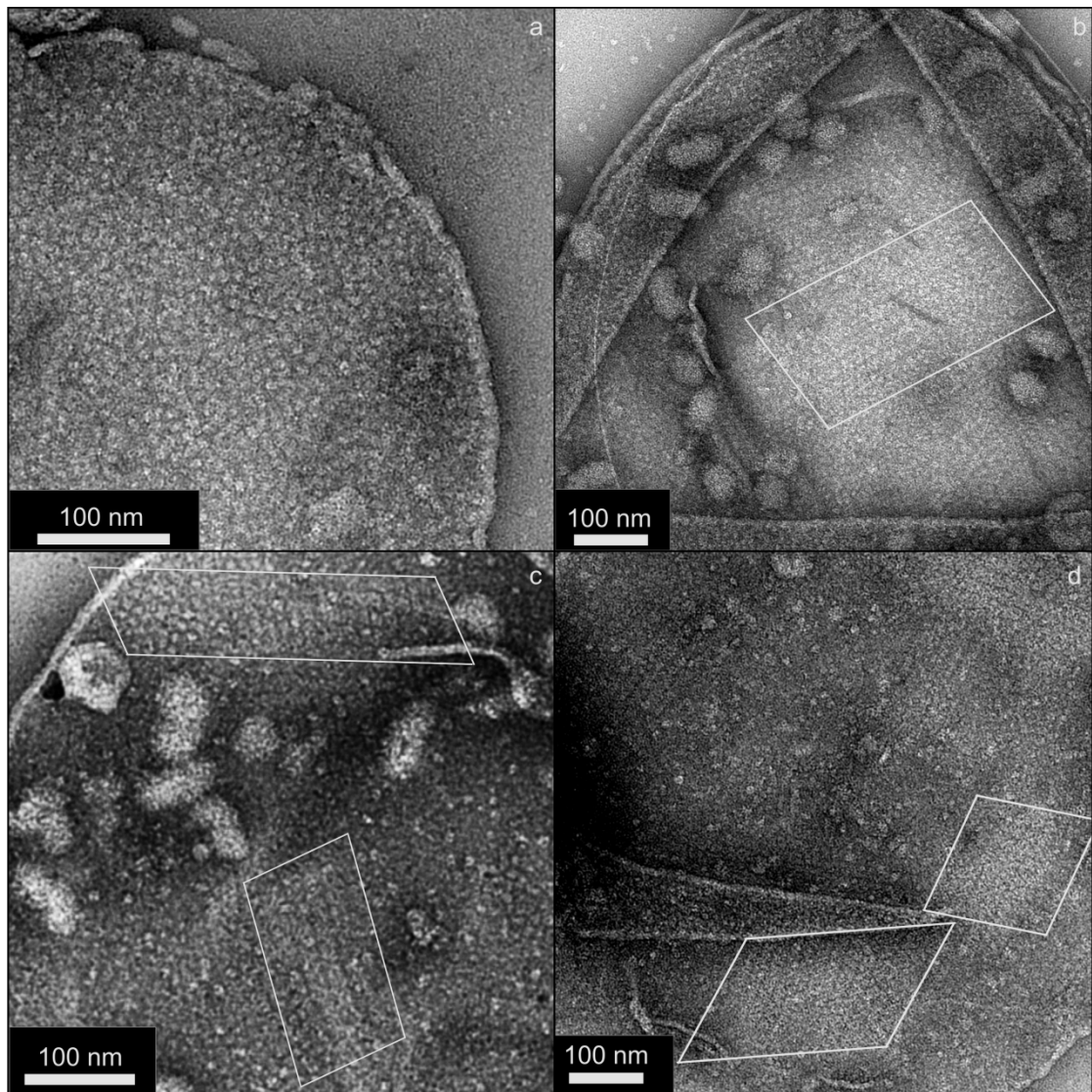


**Figure 4.1. Negative stain EM of thylakoid membranes from primary sucrose gradients. (a)** Occasionally the staining of thylakoid membranes was of high enough quality to visualise individual protein complexes which typically had a random organisation. **(b, c and d)** PSII complexes could sometimes be seen to organise into parallel linear arrays (outlined in white in **b, c and d**).

### 4.3.2 AFM of digitonin treated membranes

Membrane fragments from *Synechocystis* were purified on digitonin-containing sucrose gradients as described in 3.3.19 and were imaged by AFM. Owing to the difficulties associated with AFM imaging many membrane samples had to be prepared and imaged. In **Figure 4.2** there are several examples of membrane fragments in which single protein complexes have been imaged. With measured heights of approximately 8-14 nm it was possible to determine that these membrane fragments were single layered and contained protein complexes (**Figure 4.3**). The protein complexes appeared to be of similar size and shape in all membrane fragments and on initial inspection there appeared to be both monomeric and dimeric complexes present. The distribution of protein complexes appears to be random but there are areas in the membrane patches, most notably in **Figure 4.2a**, where protein complexes are organised into rows that are approximately parallel and reminiscent of those seen in freeze fracture EM (Vernotte *et al.*, 1990). The density of protein complexes in these patches varied; the lowest measured packing density was 2438.5 complexes per  $\mu\text{m}^2$  and the highest was 3431 complexes per  $\mu\text{m}^2$  (see **Table 1**). To determine the identity of the protein complexes that were present in the membrane fragments the vertical dimensions of the complexes were measured in the membrane patches seen in **Figures 4.2 c, d and e**. These membrane patches were chosen as the areas containing protein complexes were relatively flat. The cross sections of these membrane patches (**Figure 4.3 c, d and e**) show that the lipid bilayers had a relatively constant height with protein complexes protruding by a couple of nanometres. The heights of protein complexes in the membrane patches in **Figures 4.2 a, b and f** were not measured as the membrane patches themselves were not flat. Cross sections of these patches (**Figure 4.3 a, b and f**) shows the height of the lipid bilayer varies by a few nanometres due to membrane curvature. This curvature would obscure the height of the protein complexes as measured from the surface of the mica; therefore the height measurements of complexes in these patches were not taken. The lateral dimensions of a number of complexes in the membrane patches shown in **Figure 4.2b and c** were also measured to see if they were consistent with crystal structure of protein complexes in the photosynthetic apparatus.

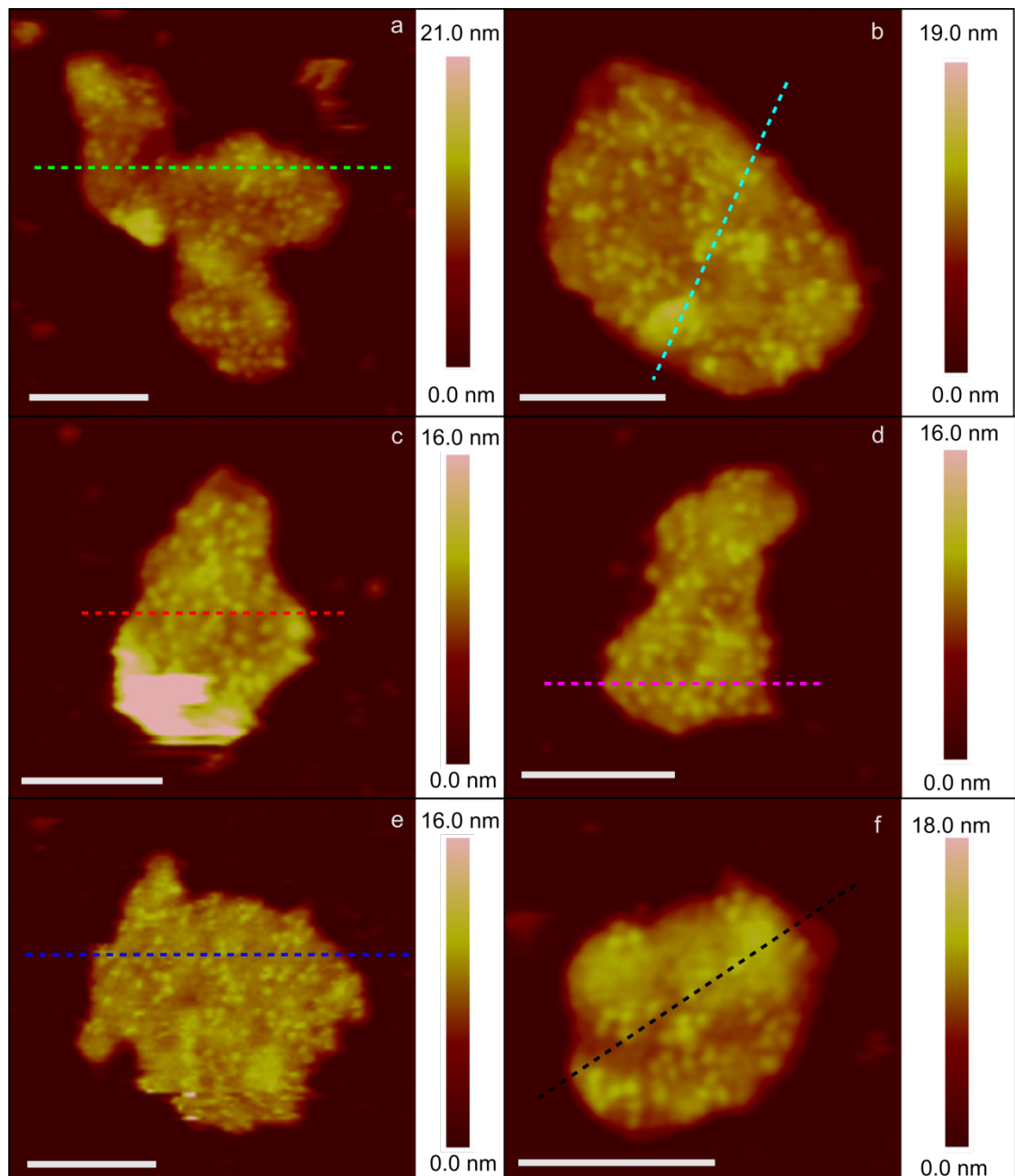


**Figure 4.2. AFM of digitonin treated membrane patches from *Synechocystis*.** Membrane patches purified from digitonin containing gradients were imaged at a resolution high enough to visualise single protein complexes. In **Figures a-f** the luminal protrusions of PSII and cytochrome *b<sub>6</sub>f* complexes can be seen in the membrane fragments. The sections through the membranes can be seen in **Figure 4.3**. All scale bars are 100 nm.

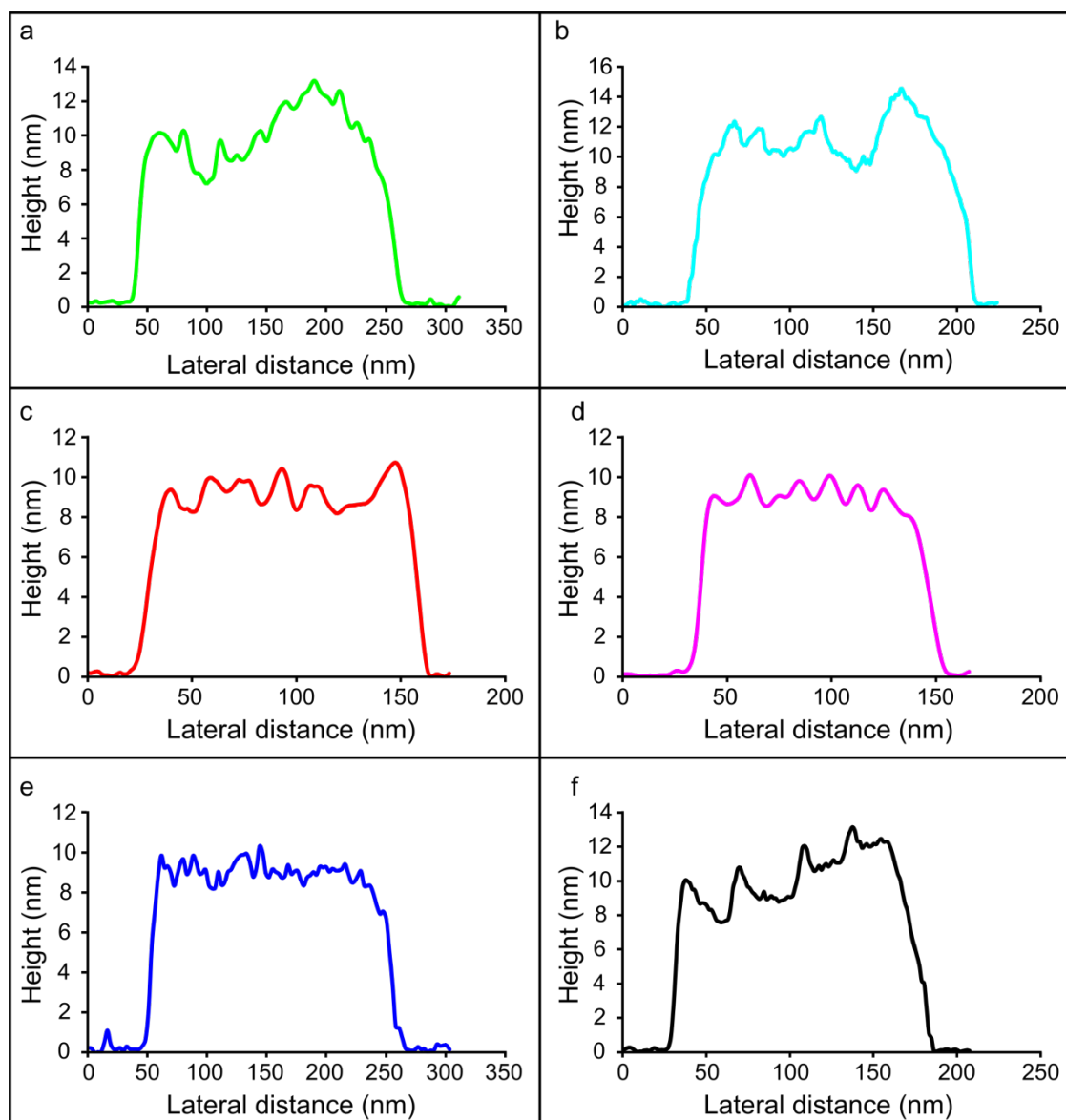


**Figure 4.3. Sections of membrane patches produced by digitonin treatment.** Sections in **a-f** correspond to sections of membrane patches shown in **Figure 4.2 a-f** respectively and are coloured accordingly. The heights shown in these sections of between approximately 8-14 nm would suggest the membrane patches in **4.2 a-f** are single layered protein-containing membrane patches. **Figures c, d and e** show membrane patches that are very flat with protein complexes protruding from a lipid bilayer. **Figures a, b and f** show membrane patches that are not flat due to membrane curvature although protein complexes can still be seen protruding from the lipid bilayer.

**Table 4.1. Measurements made on the membrane patches in Figure 4.2.** The features with topology are interpreted as arising from the major protein complexes which are PSI, PSII and the cytochrome *b<sub>6</sub>f* complex. A paired group of topological features is counted as two complexes for the purpose of this analysis.

Membrane Patch	Area (nm <sup>2</sup> )	Number of complexes	Number of complexes per μm <sup>2</sup>	Ratio of “high-topology” complexes: “low-topology” complexes
Figure 4.2a	33983	101	2972.1	NA
Figure 4.2b	33819	96	2838.6	NA
Figure 4.2c	18882	63	3336.5	26:15 (1.73)
Figure 4.2d	14573	50	3431	35:28 (1.25)
Figure 4.2e	33627	82	2438.5	33:17 (1.94)
Figure 4.2f	14897	46	3087.9	NA

### 4.3.3 Height measurements of protein complexes in membrane patches from *Synechocystis*

The height of protein complexes in patches from **Figures 4.2c, d and e** were measured and can be seen in **Figure 4.4**. The heights of complexes in patches from **Figures 4.2a, b and f** were not measured as there was slight membrane curvature throughout the patches which would have interfered with the measurements of protein topology; membranes need to be flat on the surface of the mica without any curvature for the heights of the protein complexes to be measured accurately. The best fit Gaussian distribution of the height data from each membrane patch showed two separate peaks that are likely to represent two complexes with different heights (**Figures 4.4b, d and f**).

The average height of the protein complexes with greater topology was measured to be 10.5 nm, 10.4 nm and 10.5 nm in **Figures 4.4a, c and e** respectively. These heights are consistent with the crystal structure of PSII (**Figure 4.5a**) which has a height of 10.5 nm and protrudes from the luminal side of the membrane by approximately 5 nm. The protein complexes with height of above 10 nm were assigned as either

dimeric or monomeric PSII and are numbered in yellow and red in **Figures 4.4a, c and e**. The AFM data agrees with the dimensions of the luminal protrusions of PSII which indicates that it is the luminal face of the membrane that is being imaged. The “high-topology” complexes were the most common feature in all of the membrane fragments however the ratio of “high-topology” complexes to “low-topology” complexes varies between patches (see **Table 4.1**).

The “low-topology” complexes had respective average heights of 9.6 nm, 9.1 nm and 9.7 nm in **Figures 4.4a, c and e**. Cytochrome  $b_6f$  has a height of 9.6 nm and protrudes by 4 nm from the luminal face of the membrane (**Figure 4.5b**), consistent with the average heights measured in **Figures 4.4a and e**; however the average height measured in **Figure 4.4c** is smaller than that expected for cytochrome  $b_6f$ . One possible explanation for this discrepancy might be the presence of partially disassembled PSII. Damage to the D1 subunit necessitates its removal and replacement at a relatively high rate which requires the partial disassembly of PSII (Nixon *et al.*, 2010). Removal of PSII subunits would reduce the height of the PSII complex so it closely resembled the cytochrome  $b_6f$  complex. The height of PSII without the PsbO, PsbU and PsbV subunits, which are believed to be removed during PSII repair (Nixon *et al.*, 2010), is 9.2 nm (**Figure 4.5c**). This is only 0.4 nm less than the cytochrome  $b_6f$  complex which would make it difficult to differentiate between the two complexes. It was therefore not possible to confidently assign individual cytochrome  $b_6f$  complexes; however the height data do support the presence of some of these complexes in PSII-enriched domains.

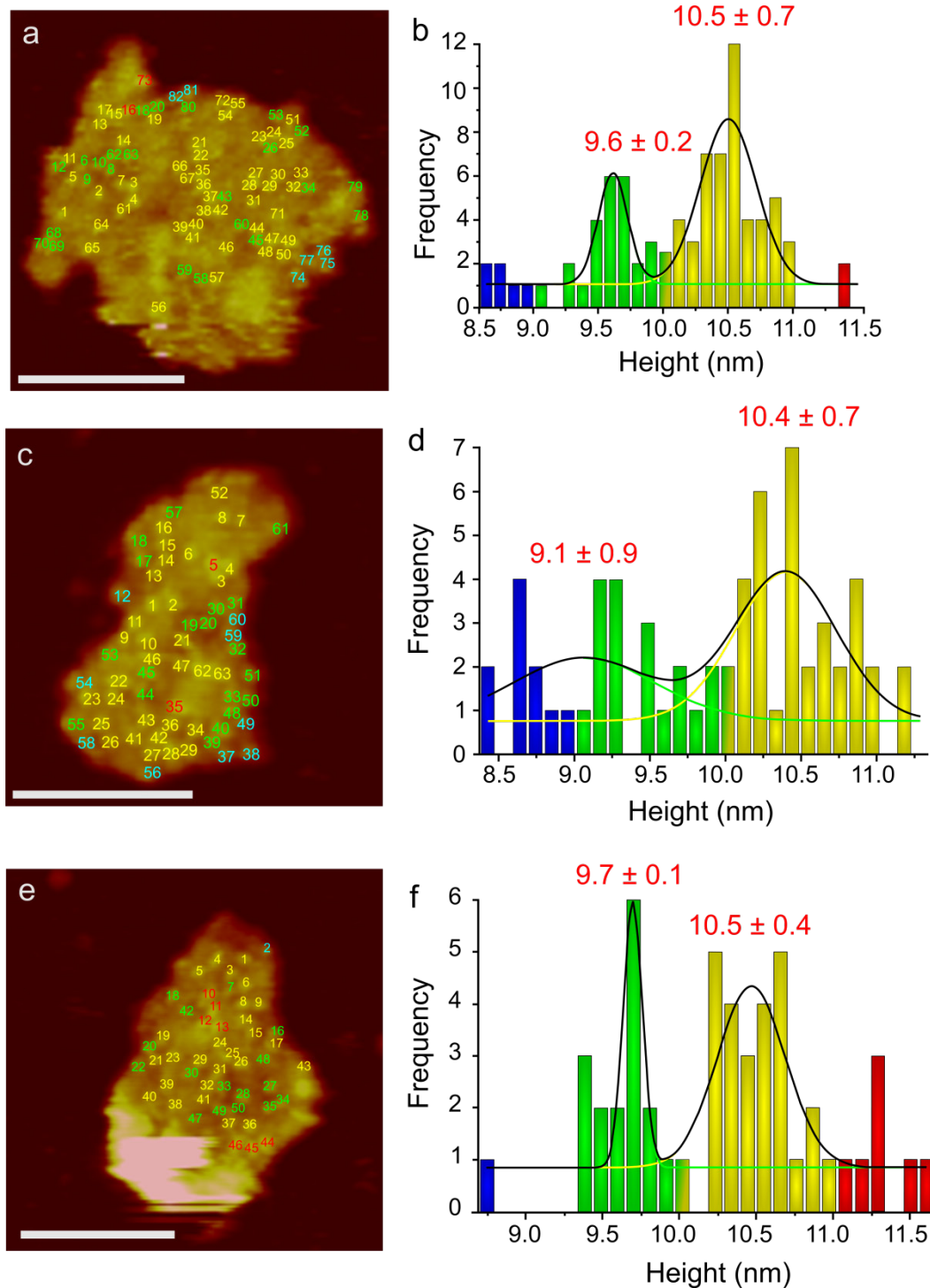


**Figure 4.4. Height measurements of protein complexes in flat membrane patches from *Synechocystis*.** The heights of protein complexes in flat membrane patches (**a, c and e**) were measured and fitted with a Gaussian distribution (**b, d and f**) which revealed the presence of two potential complexes. The “high-topology” complex was identified as PSII and the “low-topology” complex is believed to be either cytochrome *b<sub>6</sub>f* or partially disassembled PSII. Complexes were coloured according to their height; blue (< 9 nm), green (9-10 nm), yellow (10-11 nm) and red (> 11 nm). All scale bars are 100 nm.

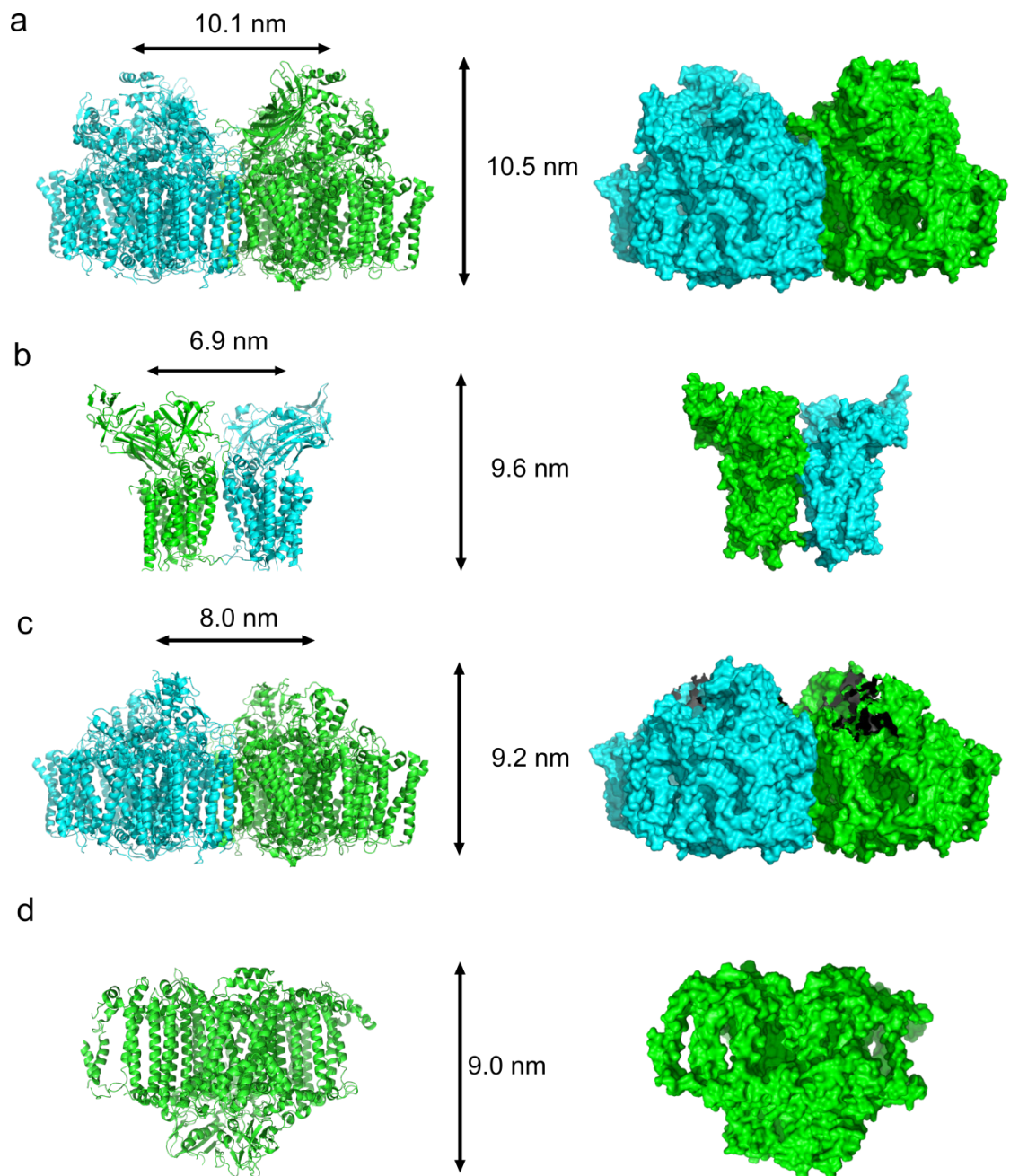


**Figure 4.5. Crystal structures of PSII, cytochrome  $b_6f$  and PSI.** (a) PSII has a height of 10.5 nm; (b) the cytochrome  $b_6f$  complex has a height of 9.6 nm; (c) PSII lacking the PsbO, PsbU and PsbV subunits has a height of 9.2 nm and (d) PSI had a height of 9.0 nm. PSII and the cytochrome  $b_6f$  complex form dimers; the distance between the centres of the protruding subunits is 10.1 nm in the PSII dimer, 6.9 nm in the cytochrome  $b_6f$  complex and 8.0 nm in the PSII complex lacking the PsbO, PsbU and PsbV subunits.

#### 4.3.4 Lateral measurements of protein complexes

Some of the protein complexes appeared to be in a dimeric configuration; this was expected as PSII exists as a dimer in the membrane (Komenda *et al.*, 2012). The distance between the luminal apices of the constituent PSII monomers was measured from the crystal structure to be 10.1 nm (**Figure 4.5a**). The lateral resolution of the AFM is not generally as accurate as the vertical resolution due to limitation by the “sharpness” of the probe; it was however possible to measure lateral distances in several putative dimeric PSII complexes (**Figure 4.6**). Some of the more distinct dimers were selected from a flat membrane patch (**Figure 4.6a**) and a membrane patch that had slight membrane curvature (**Figure 4.6b**). In both cases the distances between the constituent PSII monomers are consistent with the crystal structure of PSII.

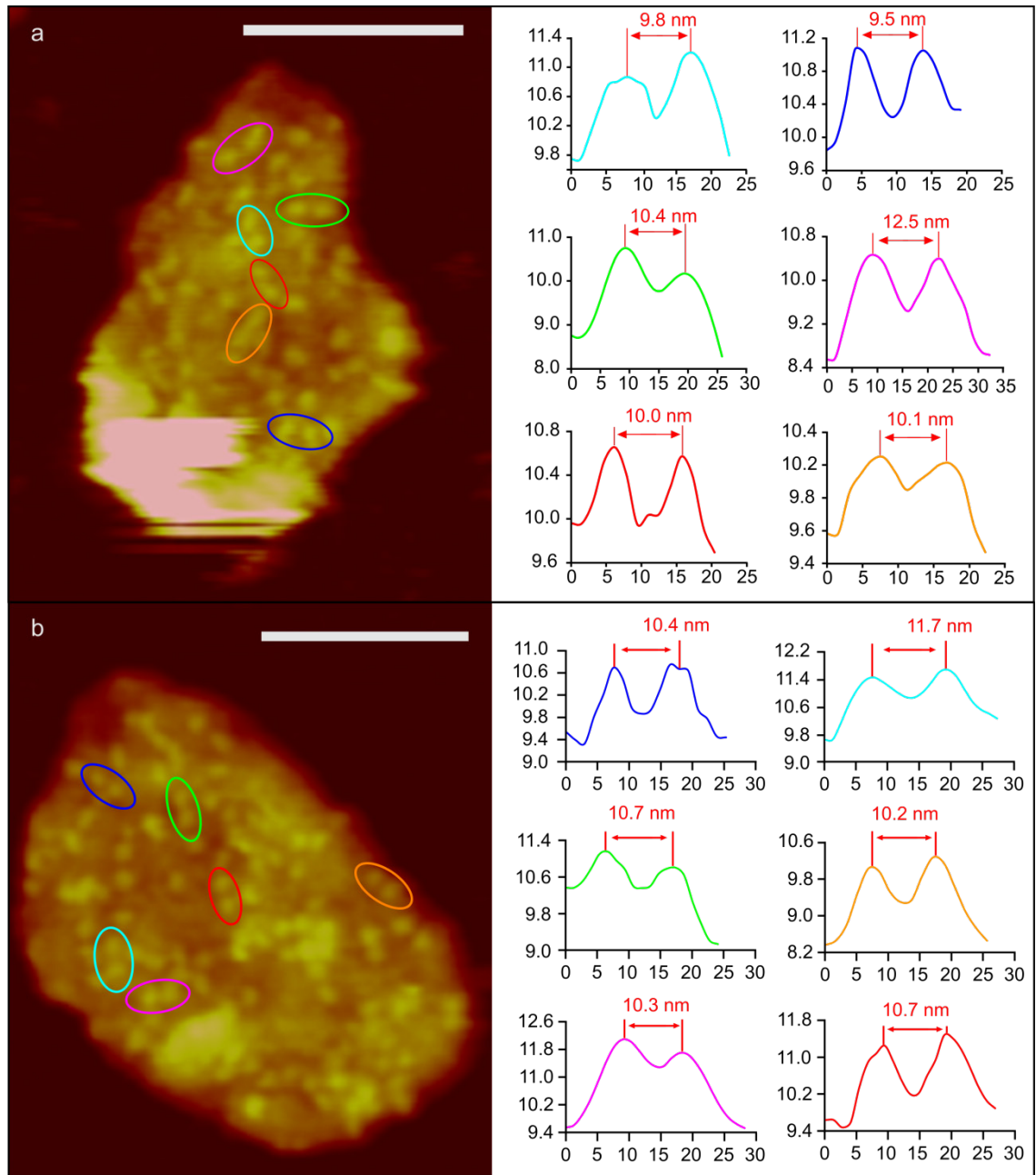


**Figure 4.6. Lateral measurements of putative PSII dimers.** The distances between complexes that appeared to be in a dimeric configuration were measured in **(a)** a flat membrane patch and **(b)** a membrane patch that had a small degree of curvature. In both cases the distances measured were consistent with PSII. All x-axes are the lateral distance in nm and all y-axes are the height in nm. All scale bars are 100 nm

#### 4.3.5 The organisation of protein complexes in membrane patches from *Synechocystis*

The organisation of protein complexes in the membrane appeared to be random in most cases although there were areas of the membrane in which complexes had formed into approximately parallel linear arrays (**Figures 4.7a and b**). These arrays are relatively small consisting of between 3 to 5 complexes with the majority of the complexes in these patches in an apparently random distribution. The membrane patches in **Figures 4.7c and d** could not be imaged to as high a resolution as **Figures 4.7a and b**; however there does appear to be large scale organisation of protein complexes in these membrane fragments. In **Figure 4.7c** several linear and approximately parallel structures can be observed in the membrane patch. These structures have similar dimensions to the rows of individual protein complexes seen in **Figures 4.7a and b** and are believed to be equivalent structures imaged to a lower resolution. **Figure 4.7d** is of slightly higher resolution and individual protein complexes can be observed in several membrane patches. These arrays have a similar appearance to the PSII domains seen in **Figure 4.1** and in Folea *et al.*, (2008a) with PSII being very tightly packed, as opposed to the appearance of less densely packed PSII rows seen in freeze fracture studies (Giddings *et al.*, 1983; Mörschel and Schatz, 1987; Olive *et al.*, 1986; Vernotte *et al.*, 1990; Olive *et al.*, 1997) and the majority of the AFM data in this study. It is important to note that all of the protein complexes in **Figures 4.7c and d** appear to form linear arrays as opposed to **Figures 4.7a and b** where the majority of protein complexes are in a random arrangement. The different organisation of protein complexes is possibly as result of the state transition. Freeze-fracture studies have reported PSII being organised into parallel rows in cyanobacteria that are in state 1; whereas an apparently random distribution of PSII was more common in cyanobacteria in state 2 (Olive *et al.*, 1986; Vernotte *et al.*, 1990). Although efforts were made to ensure consistent cell growth conditions it is possible that the membrane patches in **Figures 4.7a and b** were purified from bacteria that were in state 2 and the membrane patches in **Figures 4.7c and d** were purified from bacteria in state 1.

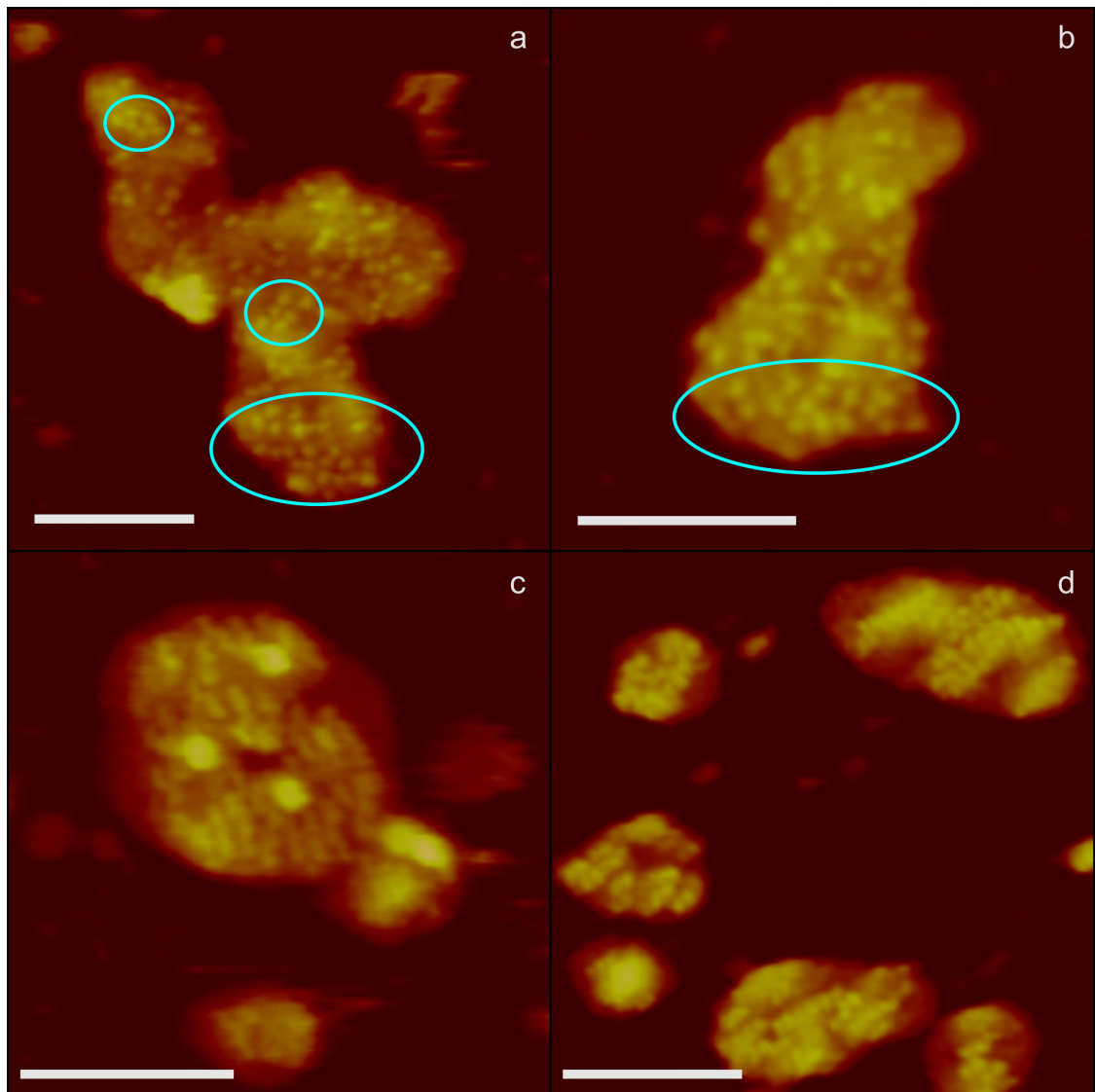


**Figure 4.7. Organisation of PSII complexes into linear arrays. (a and b)** High resolution AFM showing examples of linear arrays of PSII (circled in blue) in membranes where most of the complexes are in a seemingly random distribution. **(c and d)** Lower resolution AFM showing membrane patches in which all of the protein complexes appear to be in linear arrays. All scale bars are 100 nm.

#### 4.3.6 Possible topological features that correspond to PSI complexes in membrane patches from *Synechocystis*

Protein protrusions can be seen over most of the surface of the membrane patches but there are areas that appear to be relatively flat, which could house PSI, as this complex has minimal topology on luminal face of the membrane and would appear flat when imaged by AFM. Although it would be impossible to accurately assign PSI complexes in these regions the heights of these areas were measured to determine whether the dimensions of the membrane patch were compatible with the height of PSI, measured from the crystal structure to be 9.0 nm (**figure 4.9**). As with the heights of individual protein complexes, only membrane patches that did not have significant curvature were measured. **Figure 4.8** shows membrane patches with the flat areas outlined according to their height above the mica; areas less than 8 nm are highlighted in blue, areas that are between 8 nm and 10 nm are highlighted in green and areas with a height of greater than 10 nm are highlighted in red. The membrane patches in **Figures 4.8b and c** are densely packed with protein complexes and only have small areas that are compatible with the height of PSI. The membrane fragment in **Figure 4.8a** is less densely packed with protein complexes and there are several flat areas with heights between 8 and 10 nm. There are areas of membrane in **Figure 4.8a** have a height that is lower than 8 nm or greater than 10 nm but for the most part the heights of the flat areas of membrane are compatible with the height of PSI.

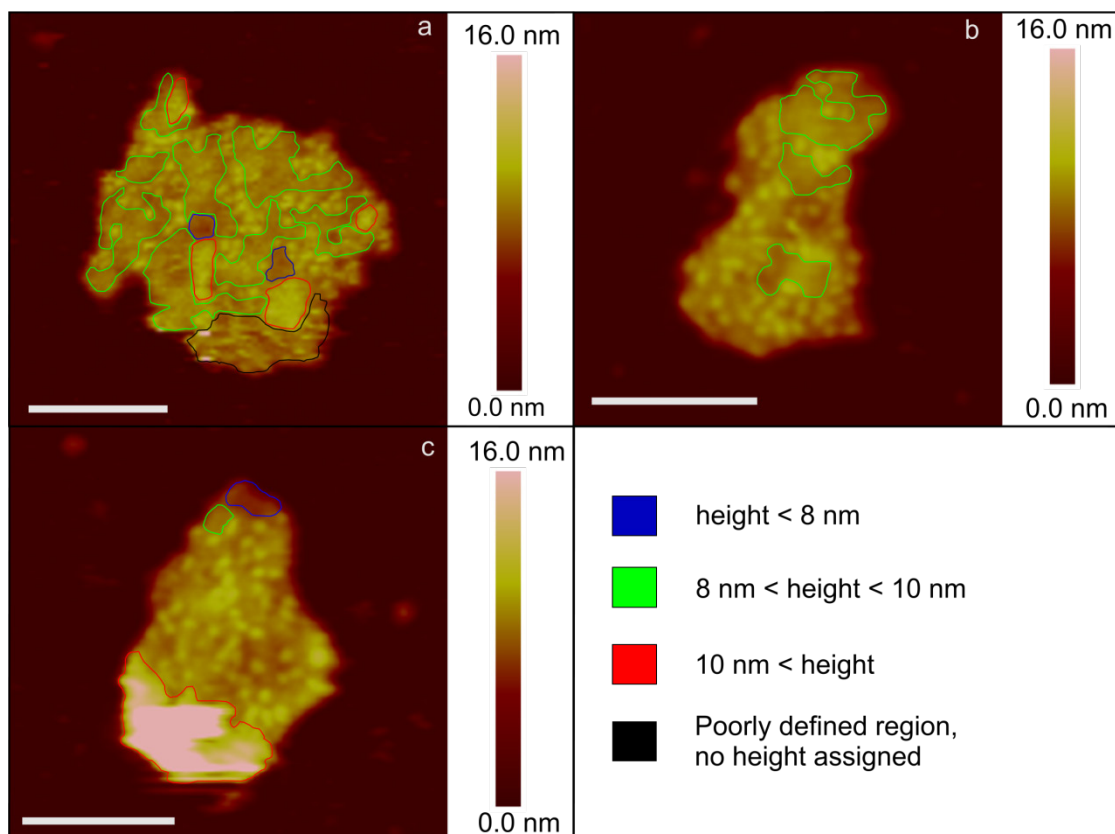


**Figure 4.8. PSI compatibility of membrane patches from *Synechocystis*.** Areas of the membrane in which protein complexes cannot be visualised have been outlined according to their height; blue (< 8 nm), green (8-10 nm) and red (> 10 nm). PSI has a height of 9.0 nm; therefore the areas of membrane outlined in green are compatible with PSI. All scale bars are 100 nm

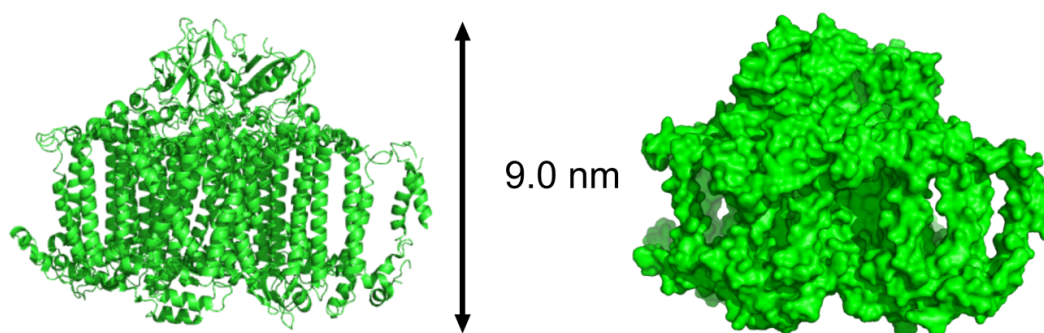


**Figure 4.9. Crystal structure of PSI.** The crystal structure of PSI showing a height of 9.0 nm (chlorophyll *a* molecules and electron transport co-factors are not shown).

#### 4.3.7 AFM of membrane patches from *Thermosynechococcus elongatus*

To see if membrane fragments could be purified from other cyanobacteria, thylakoid membranes from the cyanobacterium *Thermosynechococcus elongatus* were subjected to the digitonin treatment that was developed in 3.3.19. *T. elongatus* was chosen for AFM analysis as it is a different cyanobacterial model that has been extensively characterised and there are crystal structures for both PSI and PSII. This would mean that the topology of the any protein complexes that could be imaged in the membrane could be directly compared to the current crystal structures of cyanobacterial PSI and PSII. It would also be interesting to see if there any differences in membrane architecture between two cyanobacterial systems which have different levels of PSI, PSII and cytochrome *b<sub>6</sub>f*. Intact thylakoid membranes from *T. elongatus* were kindly provided by Dr. Karim Maghlaoui. Gradients produced a banding pattern similar to that seen in the centrifugation of *Synechocystis* membranes on digitonin-containing gradients, with a green smear spreading throughout the gradient. Membranes were harvested from the middle of the green smear and imaged by AFM.

Two flat protein-containing single layered membrane patches could be imaged to resolution of single protein complexes (**Figure 4.10**). These patches appeared to be similar to those from *Synechocystis* being of a comparable size to the membrane patches in **Figures 4.2a, b and e**. The topology of these membrane fragments is also similar to that of *Synechocystis* membrane patches with protein complexes clearly present and often appearing to be in a dimeric configuration. The major difference between the *Synechocystis* and *T. elongatus* membrane patches was the presence of large areas of featureless membrane in the latter. The *Synechocystis* membrane patches were dominated by protein complexes with protrusions that could be clearly identified however these complexes appear to be present at a lower density in membrane patches from *T. elongatus*. To identify the protein complexes in these membrane patches the height above the mica for each complex was measured; this was possible as neither patch had significant membrane curvature.

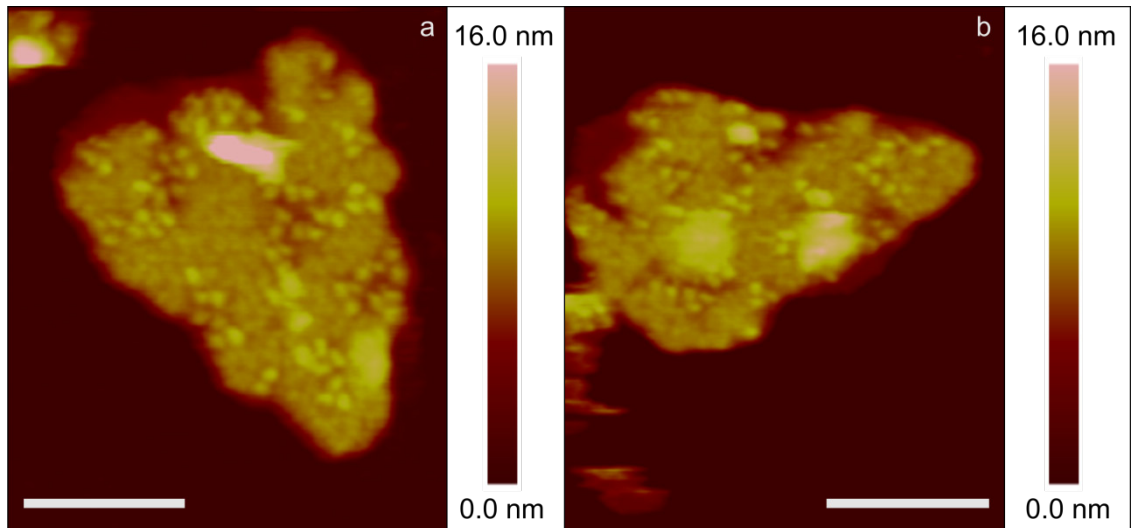


**Figure 4.10. AFM of digitonin treated membrane fragments from *T.elongatus*.** Membrane fragments from digitonin-containing gradients imaged at high resolution by AFM. Single protein complexes of high topology can be visualised in the membrane patches that have an appearance very similar to the membrane patches from *Synechocystis*. All scale bars are 100 nm.

**Table 4.2. The table shows measurements made on the membrane patches in figure 4.10**

Membrane Patch	Area (nm <sup>2</sup> )	Number of complexes	Number of complexes per μm <sup>2</sup>	Ratio of “high-topology” complexes: “low-topology” complexes
Figure 4.9a	40664	69	1697	40:29 (1.37)
Figure 4.9b	31130	48	1542	25:23 (1.09)

#### 4.3.8 Height measurements from *T. elongatus* membrane patches

As with *Synechocystis* membrane patches the heights of the protein complexes were measured and compared with crystal structures of PSII and cytochrome *b<sub>6</sub>f*. The height analysis (**Figure 4.11**) revealed two populations of complex in the membrane patches; the “high-topology” complex had average heights of 10.5 nm and 10.4 nm and the “low-topology” complex had average heights of 9.5 nm and 9.8 nm. These heights are consistent with those measured for complexes in *Synechocystis* membrane patches and as such the “high-topology” complexes were identified as PSII whereas the “low-topology” complexes are believed to be a mixture of cytochrome *b<sub>6</sub>f* and partially disassembled PSII. It is notable that there is no indication of PSII complexes forming parallel rows; however as this was a rare occurrence in *Synechocystis* membrane patches the existence of these PSII domains in *T.elongatus* should not be ruled out.

As previously mentioned large areas of membrane in which no complexes could be visualised were present in membrane patches from *T. elongatus*; the heights of these membrane patches were measured to see if they were compatible with the height of PSI. The areas of the membrane in which there are no identifiable complexes are highlighted according to their height in **Figure 4.12** using the same colour scale as for **Figure 4.8**. It can be clearly seen that the majority of the membrane patch is compatible with the height of PSI with smaller areas containing empty lipid and few regions that are taller than the rest of the membrane due to membrane curvature. The density of lumenally exposed complexes in these membrane patches is 1697 complexes per  $\mu\text{m}^2$  and 1542 complexes per  $\mu\text{m}^2$ . This is significantly lower than in membrane patches from *Synechocystis*; it is unknown if this is typical for *T.elongatus* or if these membrane patches are of particularly low density. A greater number of membrane patches will have to be imaged to get a more complete picture of the general density of PSII and cytochrome *b<sub>6</sub>f* in *T.elongatus* membranes.

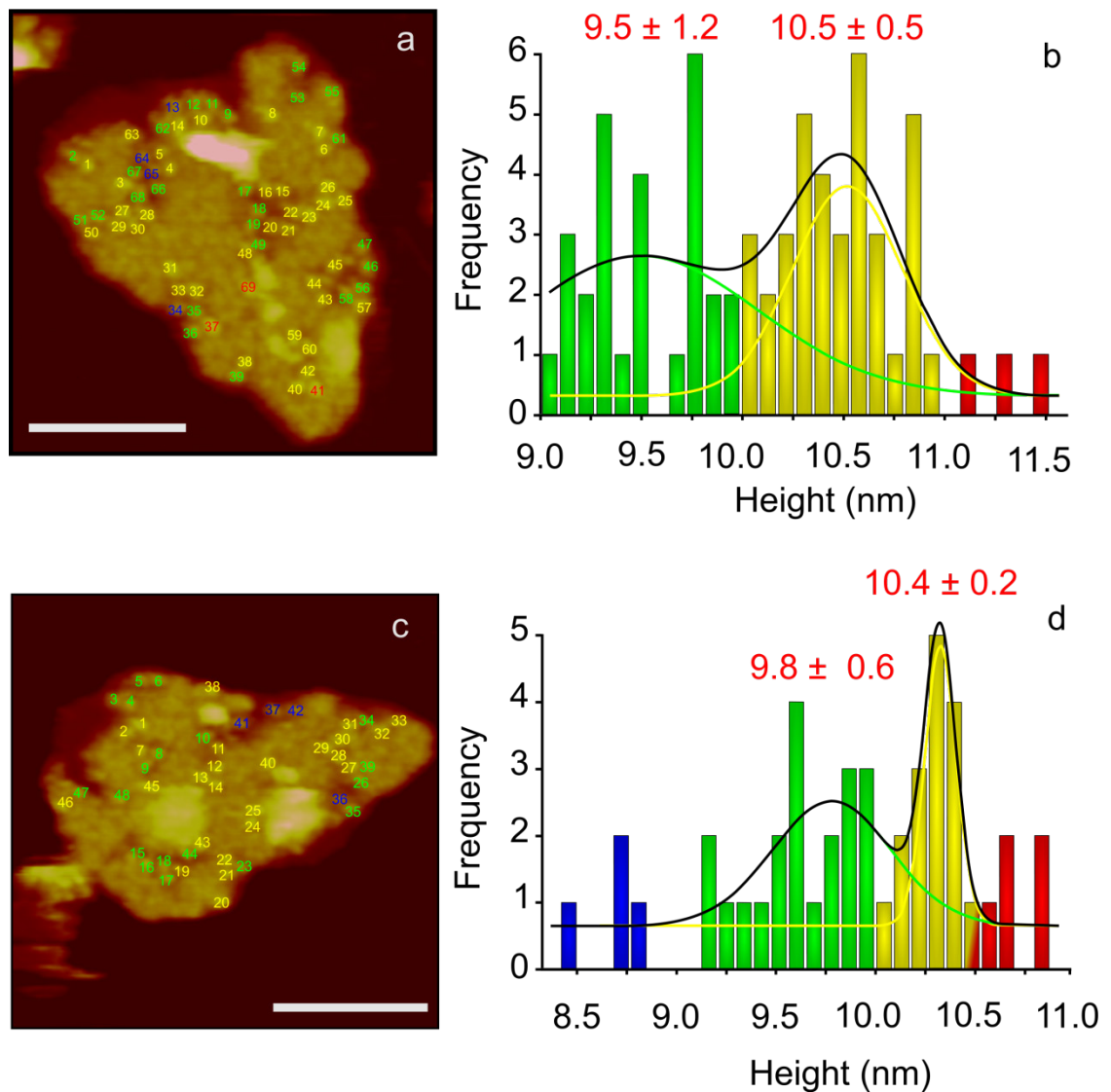


**Figure 4.11. Height measurements of protein complexes in flat membrane patches from *T. elongatus*.** The heights of protein complexes in flat membrane patches (**a** and **c**) were measured and fitted with a Gaussian distribution (**b** and **d**). This revealed the presence of two potential complexes; the “high-topology” complex was identified as PSII and the “low-topology” complex is believed to be either cytochrome  $b_6f$  or partially disassembled PSII. Complexes were coloured according to their height; blue (< 9 nm), green (9-10 nm), yellow (10-11 nm) and red (> 11 nm). All scale bars are 100 nm.

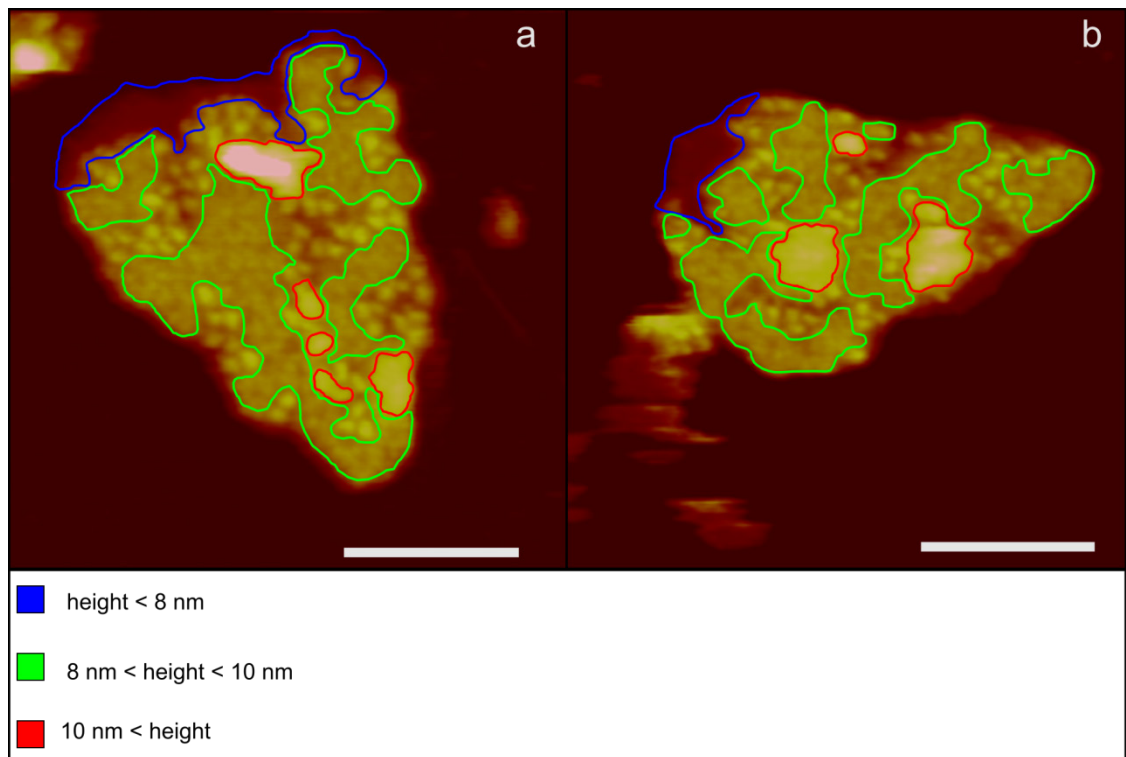


**Figure 4.12. PSI compatibility of membrane patches from *T. elongatus*.** Membrane regions where there are no visible protein complexes have been outlined according to their height; blue (< 8 nm), green (8-10 nm) red (> 10 nm). Areas of the membrane that are outlined in green are compatible with the height of PSI. All scale bars are 100 nm.

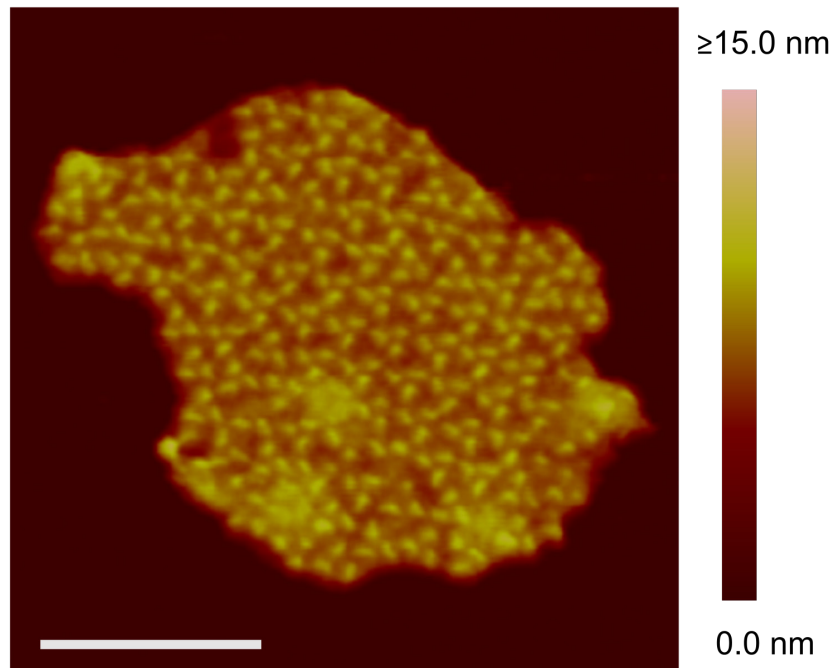
#### 4.3.9 AFM of trimeric complexes in *T. elongatus* membrane patches

One of the digitonin treated membrane patches from *T. elongatus* showed remarkably ordered arrays of a trimeric complex (**Figure 4.13**). As PSI can be purified from cyanobacterial thylakoid membranes as a trimer (Jordan *et al.*, 2001); the heights of the trimeric protein complexes above the mica were measured to see if they were consistent with the height of 9.1 nm from the crystal structure. The average height of individual protrusions was measured at  $9.3 \pm 0.36$  nm which fitted very well with the crystal structure of PSI (**Figure 4.13**). The distances between the protrusions in a number of the trimeric complexes were measured and found to be between 8-11 nm which also fits well with the distances between stromal protrusions of the trimeric PSI complex.

A second patch containing what appeared to be trimeric complexes was also imaged from digitonin treated thylakoid membranes in which trimeric complexes could be observed that were not in ordered arrays; but had a seemingly random distribution throughout the membrane patch (**Figure 4.14**). There were also areas in the membrane patch with minimal topology and no clear protein complexes could be identified. The heights of the protein complexes were measured and the average height was  $11.5 \pm 0.7$  nm which was much higher than expected for PSI. For this reason the seemingly flat areas surrounding the trimeric complexes were measured to see if they were consistent with the height of lipids surrounding protein complexes. The flat areas were seen to measure between 9.0 and 10.5 nm (**Figure 4.14d**) which is higher than the expected height for lipid surrounding protein complexes; which is around 5-7 nm. This height is however consistent with the height of the PSII complex and cytochrome *b<sub>6</sub>f* complex; it is our belief that these areas represent the stromal face of the PSII complex and the cytochrome *b<sub>6</sub>f* complex which have minimal topology. This would mean that the luminal projections of the PSII and the cytochrome *b<sub>6</sub>f* complexes would be in contact with the mica. The luminal protrusions of PSI and the cytochrome *b<sub>6</sub>f* complex extend by 3-5 nm from the surface of the lipid bilayer; it is therefore believed that these protrusions are responsible for the increase in the measured height of the trimeric complexes above the mica, which are believed to be PSI.

Finding PSI in linear arrays was a surprising discovery as such arrays have never before been reported in the literature and in previous models PSI was believed to be in a more random distribution (Folea *et al.*, 2008a). There are no reports of PSI segregation in *T.elongatus* of any kind whether in an ordered or disordered state; **Figure 4.13** therefore constitutes first evidence of PSI segregation in *T.elongatus*. **Figure 4.14** shows a membrane patch in which PSI does not appear to be segregated from other protein complexes but appears to be distributed somewhat randomly amongst other protein complexes; believed to be PSII and the cytochrome *b<sub>6</sub>f* complex. This organisation of PSI fits with what has previously been proposed, however this data suggests that both organisational states are present in native membranes.

a



b

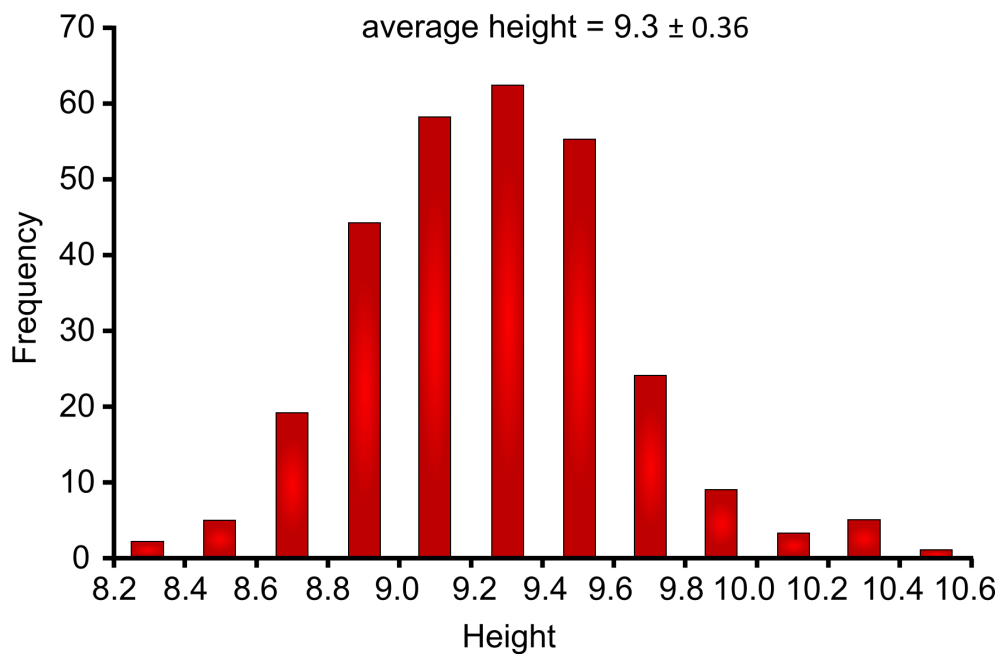


**Figure 4.13. AFM imaging and height analysis of a digitonin treated membrane patch from *T.elongatus* that contains trimeric complexes in ordered arrays.** Trimeric complexes believed to be PSI are seen to form parallel arrays in a membrane patch. The heights of the protein complexes were measured and had an average height of  $9.3 \pm 0.36$  nm which is consistent with the height of PSI measured from the crystal structure. Scale bar is 100 nm

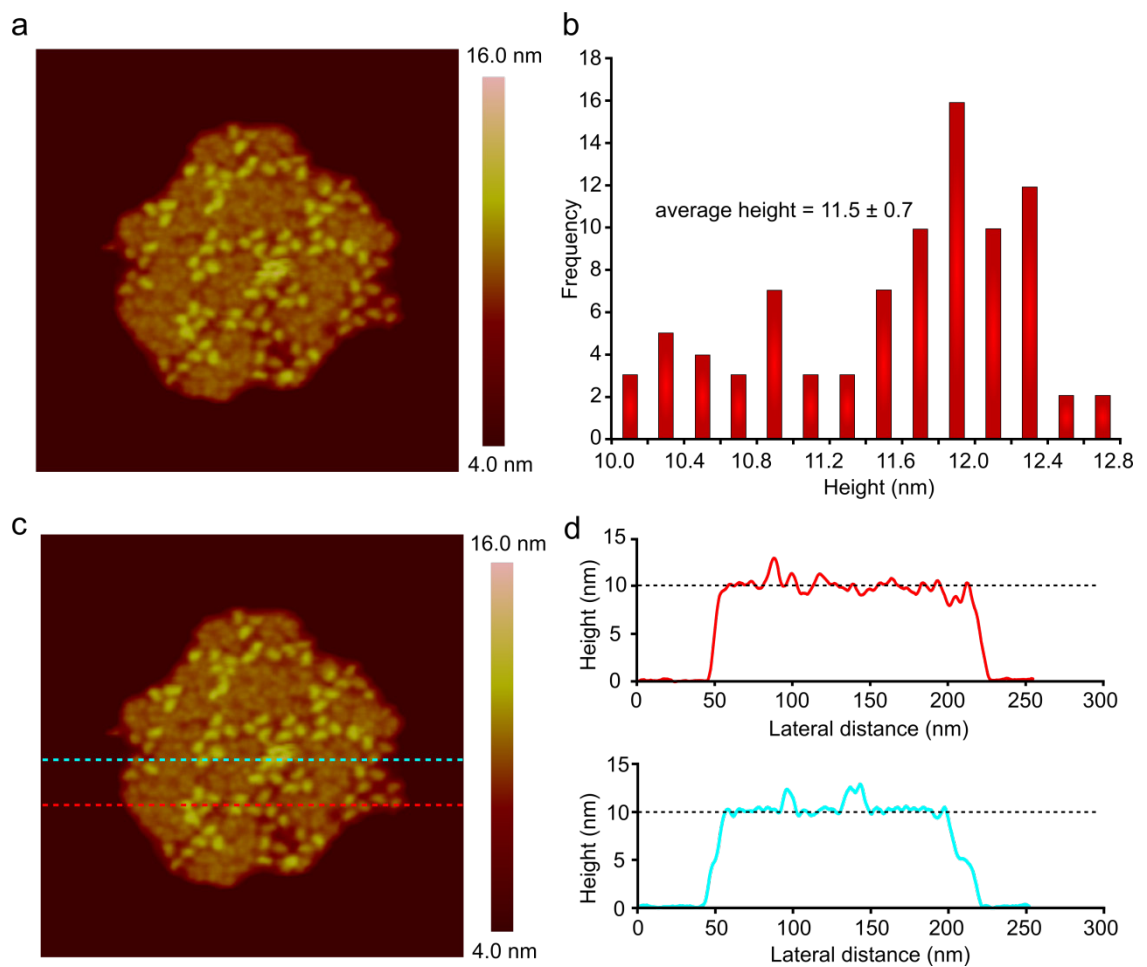


**Figure 4.14. AFM imaging and height analysis of a digitonin treated membrane patch from *T. elongatus* that contains trimeric complexes in a disordered arrangement. (a)** Trimeric complexes, believed to be PSI complexes, are seen in an apparently random distribution in the membrane. **(b)** The height measurement gives an average height of  $11.5 \pm 0.7$  nm which is significantly higher than expected for PSI. **(c)** Section were taken across the membrane patch and **(d)** revealed the areas of minimal topology had a height of 9.0-10.5 nm; a height consistent with the crystal structure of PSII and the cytochrome *b<sub>6</sub>f* complex.

#### 4.3.10 Room temperature absorption spectroscopy of digitonin treated thylakoid membranes from *Synechocystis* and *T.elongatus*

Room temperature absorption spectra were taken of thylakoid membranes from *Synechocystis* and *T.elongatus* before and after purification on standard sucrose gradients containing 0.1 % digitonin. A peak was present at 680 nm in the absorption spectrum of *Synechocystis* thylakoid membranes prior to detergent treatment (**Figure 4.15 a**); this peak was seen to shift slightly after detergent treatment to 678 nm (**Figure 4.15 b**). The absorption spectrum of thylakoid membranes from *T.elongatus* also had a peak at 680 nm (**Figure 4.15 c**) which was not seen to shift after digitonin treatment, remaining at 680 nm (**Figure 4.15 d**). The presence of the blue shifted peak in the absorption spectrum of thylakoid membranes from *Synechocystis* could be indicative of a greater abundance of PSII in the gradient fraction used for AFM analysis. The absorption spectrum of PSII has a maximum at 673 nm; therefore a greater abundance of PSII in the sample could be responsible for the 2 nm shift. The concentration of PSI and PSII was therefore investigated to determine the levels the two photosystems in the membrane patches produced by the digitonin treatment.

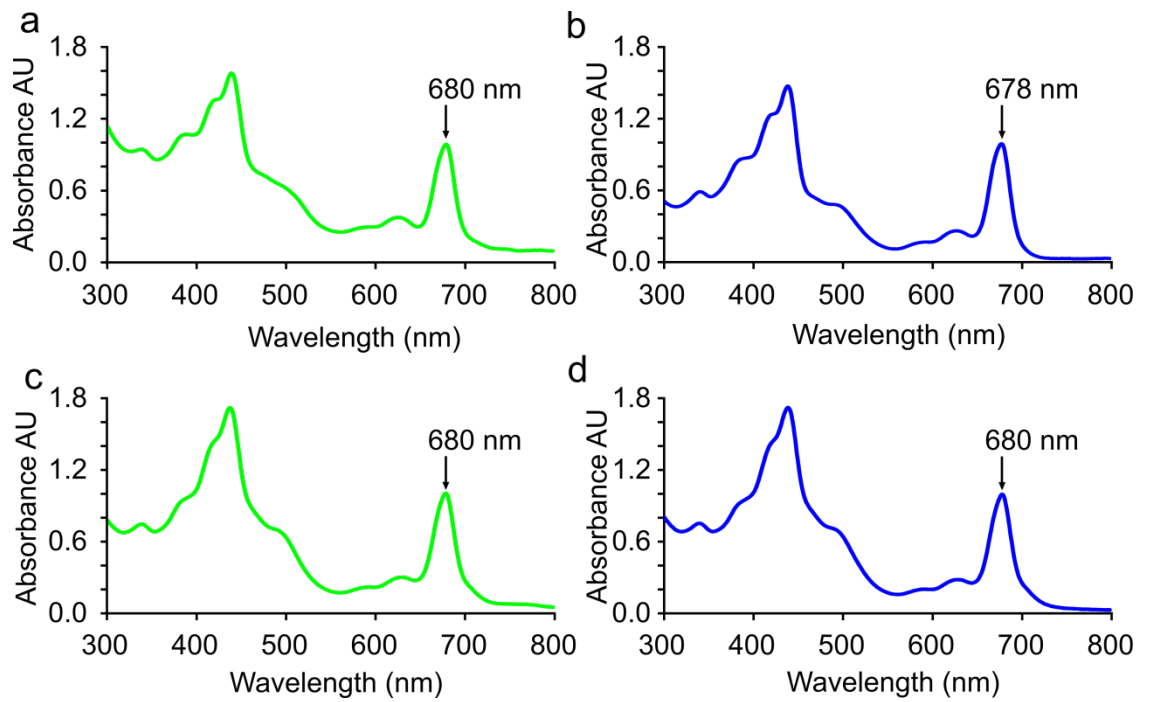


**Figure 4.15. Absorption spectra of thylakoid membranes from *Synechocystis* and *T. elongatus*.** Absorption spectrum of *Synechocystis* thylakoid membranes purified from; **(a)** digitonin-free sucrose gradients and **(b)** sucrose gradients containing 0.1 % digitonin. Absorption spectrum of *T. elongatus* thylakoid membranes purified from; **(c)** digitonin-free sucrose gradients and **(d)** sucrose gradients containing 0.1 % digitonin.

#### 4.3.11 Molar ratios of PSI and PSII in digitonin treated thylakoid membranes from *Synechocystis*

To determine the effect of digitonin on the PSI and PSII content of membrane patches from *Synechocystis*, it was decided to analyse membrane fractions by clear native (CN) PAGE. Typically, approximately 100 µl of sample at a concentration of around 0.2 mg/ml of chlorophyll is loaded per lane on a CN-PAGE. The concentration of chlorophyll in samples harvested from standard digitonin containing sucrose gradients is roughly 0.02-0.04 mg/ml. In order to produce a sample which was concentrated enough to load onto CN-PAGE gels 2 ml of lysed cells (broken according to **2.8**) were loaded onto 20-50 % continuous sucrose gradients that contained 0.01, 0.1, 0.5, 1.0 and 2.0 % digitonin in addition to a control gradient that contained no digitonin. The gradients can be seen in **Figure 4.16** after centrifugation at 40,000 rpm in an SW41 rotor for 2 hours. The upper band (outlined in blue in **Figure 4.16**) is the part of the gradient that is typically harvested for AFM analysis as it contains the greatest abundance of single layered protein-containing membrane patches in standard digitonin containing sucrose gradients. The upper band was harvested from the 0.1, 0.5, 1.0 and 2.0 % sucrose gradients in addition the lower band (outlined in red in **Figure 4.16**) from the control gradient for analysis by CN-PAGE.

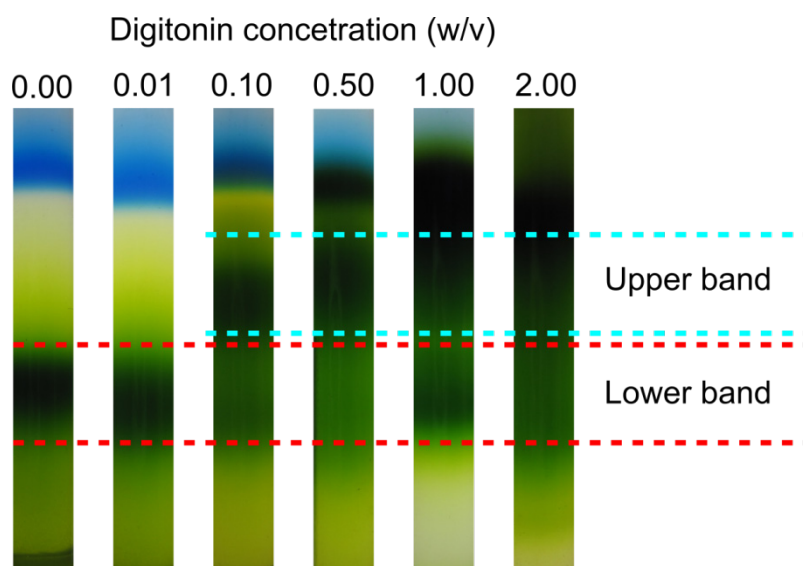


**Figure 4.16. Digitonin containing sucrose gradients.** Concentrated samples of *Synechocystis* thylakoid membranes were run on gradients containing different concentrations of digitonin. Samples were taken from the gradients for analysis by CN-PAGE.

The samples harvested from the sucrose gradients were solubilised in 2 %  $\beta$ -DDM before 100  $\mu$ l of the sample was loaded onto a clear native polyacrylamide gel. CN-PAGE of the samples showed clear separation between PSI trimers and PSII dimers (**Figure 4.17 a**); the more intense green band at the top of the gel contains PSI trimers and the less intense green band towards the bottom of the gel contained PSII dimers (Kopečná et al., 2012). The bands were cut out of the gel and absorption spectra were taken of the gel slices (**Figure 4.17 b and c**). A peak could be observed in the absorption spectra of the PSI band at 679 nm (**Figure 4.17 b**); in the PSII band the peak was observed at 673 nm (**Figure 4.17 c**). These spectra were consistent with the spectra for PSI and PSII confirming the presence of the complexes in the respective bands. In order to determine the PSI:PSII ratio of the samples, the photosystems were recovered from the gel slices via electroelution and the chlorophyll content was determined by methanol extraction. Based on PSI containing 96 bound chlorophyll *a* cofactors and PSII containing 35 bound chlorophyll *a* cofactors the PSI and PSII content was calculated (**Table 4.3**). The PSI:PSII ratio was higher in the lower band from the digitonin-free control gradient than in the upper bands from all the digitonin containing gradients. The general trend was for the PSI:PSII ratio to decrease as the

concentration of digitonin increases. This suggests that digitonin is preferentially producing membrane patches containing PSII that travel less distance through the sucrose gradient. It would also suggest that PSI is still present in the intact vesicular structures that are present in the lower band in the sucrose gradient.

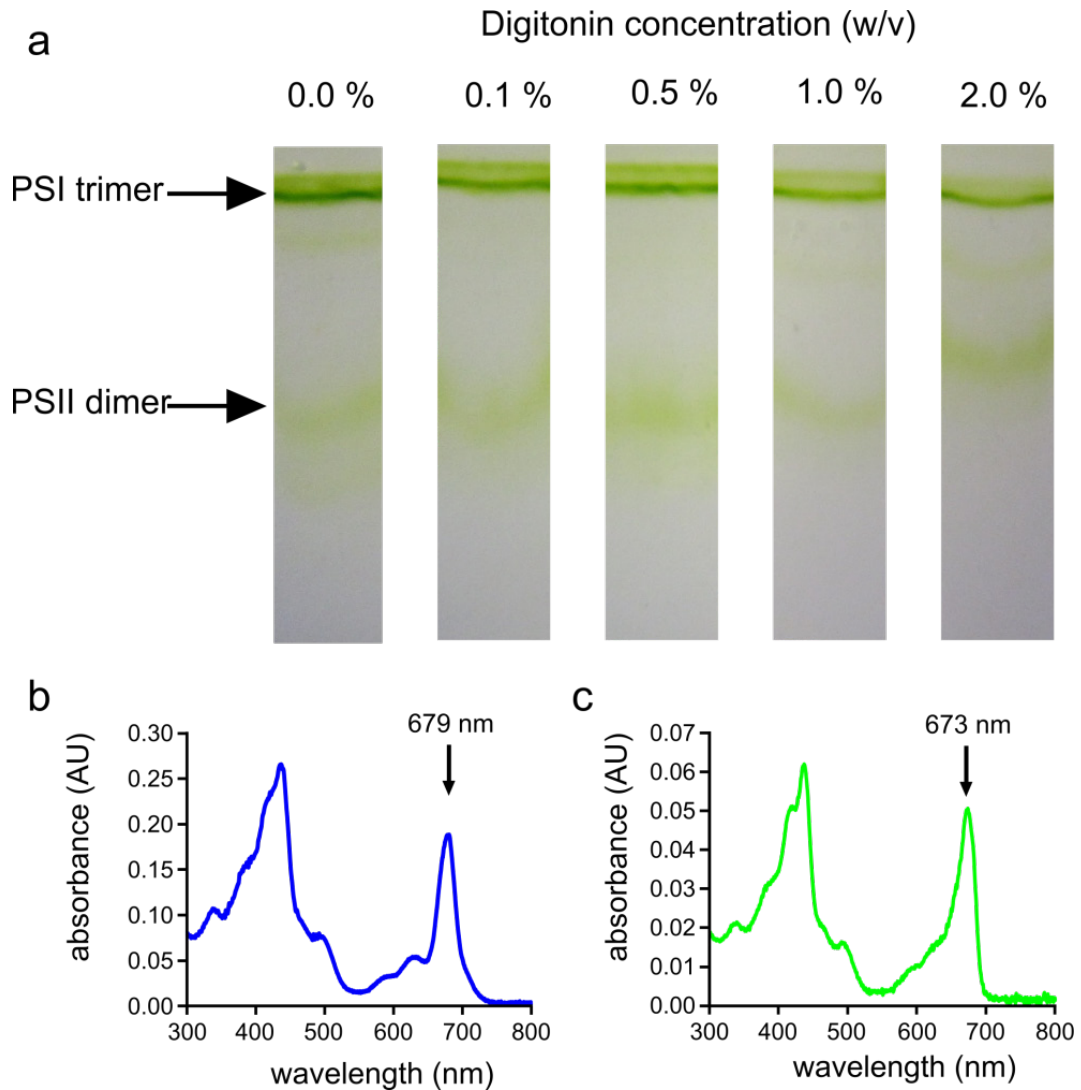


**Figure 4.17. CN-PAGE of solubilised *Synechocystis* thylakoid membranes from digitonin gradients. (a)** CN-PAGE of membrane samples taken from sucrose gradients used to prepare membranes for AFM analysis. In each gel lane two green bands can be observed; the intense green band at the top of the gel contains PSI trimers and the less intense green band towards the bottom of the gel contains PSII dimers. **(b)** Absorption spectrum of the upper band; the spectrum is typical for PSI with a peak at 679 nm. **(c)** Absorption spectrum of the lower band; the spectrum consistent with PSII with a peak at 673 nm.

**Table 4.3. PSI:PSII ratios for samples harvested from gradients in Figure 4.16.**

Digitonin concentration (w/v)	PSI:PSII ratio
0.00	2.73
0.10	1.38
0.50	1.56
1.00	1.26
2.00	1.06

#### **4.3.12 Molar ratios of PSI and PSII in digitonin treated thylakoid membranes from *T.elongatus***

The PSI and PSII content of thylakoid membranes from *T.elongatus* was determined in the same way as for thylakoid membranes from *Synechocystis*. As only a limited quantity of thylakoid membranes from *T.elongatus* had been supplied, it was only possible to run one digitonin-containing gradient and a digitonin-free control gradient. 2 ml of sample containing thylakoid membranes at a concentration of 1 mg/ml of chlorophyll was loaded onto a 20-50 continuous sucrose gradient that contained 1.0 % digitonin and an identical sucrose gradient that contained no digitonin. The gradients produced a banding pattern very similar to the gradients in **Figure 4.16** with a single band in the digitonin-free gradient and an upper band appearing in the 1.0 % digitonin gradient. The lower band from the digitonin-free gradient and the upper band from the 1 % digitonin gradient were harvested and analysed by CN-PAGE (**Figure 4.18 a**). A relatively intense PSI containing band and a barely visible PSII containing band could be identified in the clear native gel. The identity of the photosystem in each band was confirmed by taking absorption spectra of the bands after they were cut out from the gel (**Figure 4.18 b and c**). To determine the PSI:PSII ratio in the samples the complexes were recovered from the gel slices by electroelution and the chlorophyll content was measured by methanol extraction.

Based on PSI containing 96 chlorophyll *a* cofactors and PSII containing 35 chlorophyll *a* cofactors the PSI:PSII ratio was determined by the amount of chlorophyll recovered from each band (**Table 4.4**). The PSI:PSII ratio is relatively similar between the lower band from the digitonin-free gradient and the upper band from the 1.0 % digitonin gradient at approximately 4:1. This is higher than the PSI:PSII ratio in *Synechocystis* evidencing that PSI is present at a greater abundance in *T.elongatus* than in *Synechocystis*. In addition the fact that the PSI:PSII ratio is comparable between digitonin treated and untreated *T.elongatus* thylakoid membranes suggests that the digitonin is not preferentially producing membrane patches containing one type of photosystem; as is the case with *Synechocystis*.

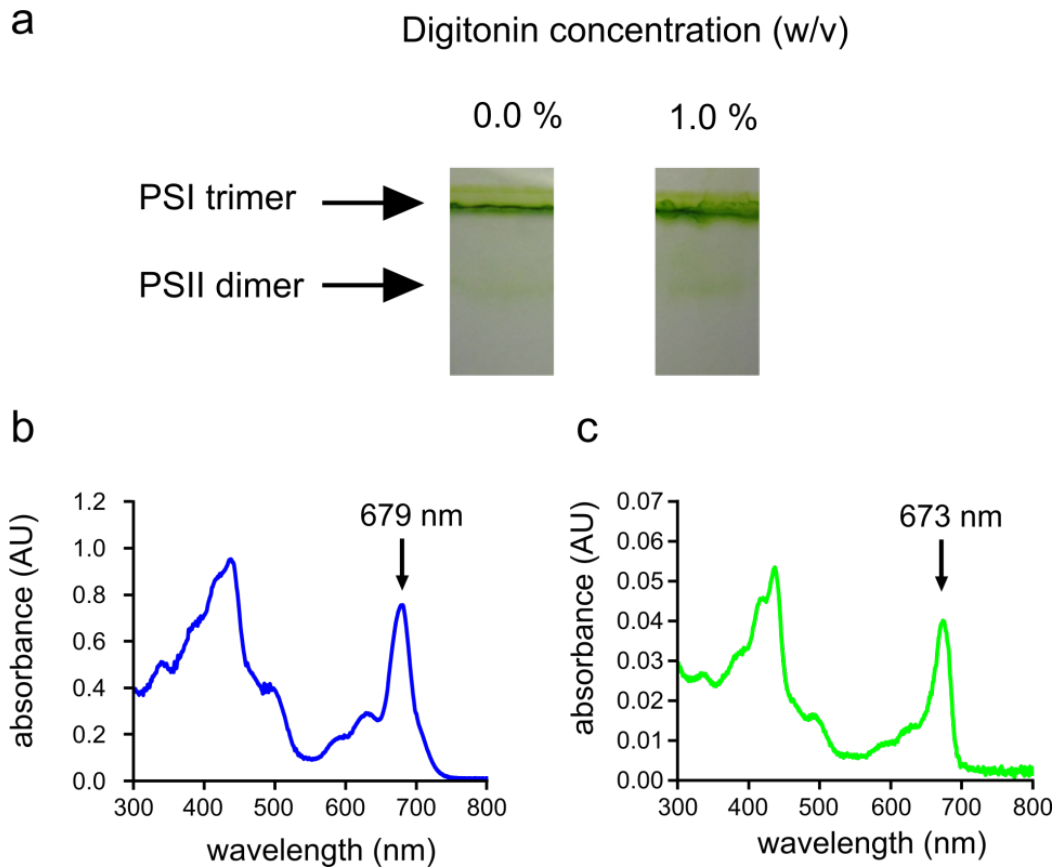


**Figure 4.18. CN-PAGE of solubilised *T.elongatus* thylakoid membranes from digitonin gradients.** (a) CN-PAGE of *T.elongatus* thylakoid membranes from a digitonin-containing and a digitonin-free sucrose gradient shows an intense green band containing PSI trimers and a barely visible green band containing PSII dimers. (b) An absorption spectrum confirms that the upper band contains PSI trimers. (c) The absorption band from the lower band confirms the presence of PSII.

**Table 4.3. PSI:PSII ratios for *T.elongatus* samples harvested from 0.0 % and 1.0 % digitonin sucrose gradients.**

Digitonin concentration (w/v)	PSI:PSII ratio
0.00	3.94
1.00	4.17

#### 4.3.13 Low temperature emission spectroscopy of thylakoid membranes from *Synechocystis* and *T.elongatus*

To further characterise the thylakoid membranes low temperature emission spectra were taken of thylakoid membranes from *Synechocystis* and *T.elongatus* prior to the digitonin treatment (**Figure 4.19**). The emission spectrum of *Synechocystis* thylakoid membranes had peaks at 685 and 695 nm (Andrizhiyevskaya *et al.*, 2005) from PSII fluorescence and a peak at 719 nm due to PSI fluorescence (Brecht *et al.*, 2009). The emission spectrum of *T.elongatus* thylakoid membranes had the 685 and 695 peaks from PSII fluorescence but the peak from PSI is red shifted from that of *Synechocystis* at 727 nm (Brecht *et al.*, 2009). The amplitudes of the PSII associated peaks relative to the PSI associated peak were greater in *Synechocystis* than in *T.elongatus* which is indicative of a smaller PSI:PSII ratio. This measurement agrees with the PSI:PSII ratios that were determined by CN-PAGE.

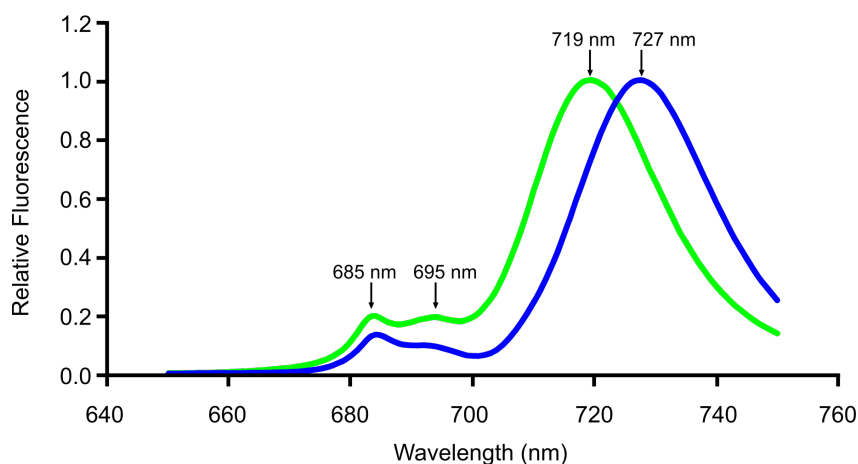


**Figure 4.19.** Low temperature emission spectra of thylakoid membranes from *Synechocystis* and *T.elongatus*. The emission spectrum from *Synechocystis* (green) has peaks at 685 nm and 695 nm from PSII and a peak at 719 nm from PSI. The emission spectrum from *T.elongatus* (blue) has peaks at 685 nm and 695 nm from PSII and a peak at 727 nm from PSI. The amplitudes of the PSII associated peaks are smaller relative to the PSI associated peak in the spectrum of *T.elongatus* membranes in comparison to the spectrum of *Synechocystis* membranes which is indicative of a higher PSI:PSII ratio. Spectra are normalised to the PSI associated peak.

## 4.4 Discussion

To get a better understanding of the light harvesting and electron transport processes of photosynthesis in cyanobacteria a more complete model of the native supramolecular organisation of photosynthetic protein complexes in thylakoid membranes has to be established. EM and AFM of photosynthetic membrane fragments from cyanobacteria has allowed the identification of photosynthetic complexes and in the latter case their supramolecular organisation under near-native buffer conditions.

### 4.4.1 EM of *Synechocystis* membranes

Domains in which PSII forms parallel linear arrays were identified in extracts of partially solubilised membranes by Folea *et al.*, (2008a). The identification of similar domains (**4.3.1**) in thylakoid membranes that have not been treated with high levels of detergent shows that this arrangement of PSII is likely to exist in the intact cyanobacterial thylakoid system. These domains are completely devoid of PSI and cytochrome *b<sub>6</sub>f* and are likely to play a role in the distribution of energy between the two photosystems as the reduced number of contacts with PSI would likely reduce the spill-over of excitation energy from PSII to PSI. It is also believed that PSII in this configuration would reduce the transfer of energy between the phycobilisomes and PSI as the phycobilisomes that are bound to PSII could only interact with PSI at the periphery of such domains (McConnell *et al.*, 2002). Nanodomains containing PSII and cytochrome *b<sub>6</sub>f* have been identified in granal thylakoid membranes from spinach which ensures rapid transport of quinone molecules between the two complexes (Johnson *et al.*, 2014). The transport of quinone molecules between cytochrome *b<sub>6</sub>f* and PSII in the large PSII enriched domains identified in **4.3.1** would require quinone molecules to migrate over greater distances. It would therefore be of great interest to investigate the relationship between cytochrome *b<sub>6</sub>f* and these densely packed PSII domains.

#### 4.4.2 Identification of complexes on the luminal face of the membrane

The most reliable measurement recorded by AFM is the height data which is typically accurate to 0.1 nm and is not dependent on the “sharpness” of the AFM probe. Therefore the first aspect of the AFM data that underwent analysis was the height measurements of individual protein complexes in the membrane. The existence of two populations of height measurement was unexpected as previous studies have reported membrane domains that were enriched in PSII with no indication of the presence of other protein complexes (Folea *et al.*, 2008a; Giddings *et al.*, 1983; Mörschel and Schatz, 1987; Olive *et al.*, 1986). EM of immunogold labelled *Synechococcus* cells showed that PSII and cytochrome *b<sub>6</sub>f* had similar distributions in the thylakoid membranes (Sherman *et al.*, 1994) so it would follow that domains containing both PSII and cytochrome *b<sub>6</sub>f* could be isolated and imaged. The measured heights of the “high-topology” complexes were relatively consistent between membrane patches with the average height ranging from 10.3 nm to 10.5 nm which fits well with the height of PSII. The distances between complexes that appear to form a dimer also fit well with the crystal structure of PSII. The fact that these complexes were occasionally seen to organise into linear arrays was also consistent with observations of PSII organisation made from freeze fracture and negative stain EM (Folea *et al.*, 2008a; Giddings *et al.*, 1983; Mörschel and Schatz, 1987; Olive *et al.*, 1986).

The crossover point between the Gaussian distributions for the height measurements from the two populations of complex in **Figures 4.4b, 4.4d, 4.4f, 4.11b and 4.11d** was close to 10 nm. From this measurement, complexes that had a height of greater than 10 nm could be assigned as PSII complexes with a high degree of certainty. Some of the PSII complexes have been measured with a height of greater than 11 nm. The presence of PsbQ and PsbP might explain why a small number of PSII complexes are have a measured height of greater than 11 nm. These subunits are believed to bind to the OEC but are not present in the crystal structure and have been shown to readily dissociate from the PSII complex. If a small number of PSII complexes still had PsbP and PsbQ bound, it could account for why occasionally the height of PSII complexes is measured to be greater than 11 nm

It is tempting to assign the “low-topology” complex as cytochrome  $b_6f$  owing to the height data agreeing somewhat with the crystal structure of the complex. In addition, PSII and cytochrome  $b_6f$  both protrude from the luminal surface of the membrane and it would be expected that areas of topology could be assigned to cytochrome  $b_6f$ . However during PSII repair there is partial disassembly of the PSII complex to allow the replacement of the D1 subunit (Nixon *et al.*, 2010). The removal of PSII subunits would cause a reduction in the height of the protein complex; if partially disassembled PSII complexes were present in the membrane fragments they could have heights that were similar to cytochrome  $b_6f$ . Additionally the PsbO, PsbU and PsbV subunits can dissociate from PSII when they are exposed to an aqueous environment (Papageorgiou and Murata, 1995) which would leave the PSII complex with a height of 9.2 nm. This complex would look very similar to cytochrome  $b_6f$  in the AFM data and as there is only 0.4 nm difference in the height of these two complexes it may not be possible to distinguish them on the basis of height alone. The peaks corresponding to cytochrome  $b_6f$  complexes in **Figures 4.4b, 4.4d, 4.4f, 4.11b and 4.11d** were quite variable, being sharp in some membrane patches and very broad in others. The average height of the “low-topology” complexes was also relatively variable ranging from 9.1 nm to 9.8 nm. If there were a variable number of PSII complexes that lacked the oxygen evolving complex or were in a state of partial disassembly in the different membrane fragments that were imaged, it might explain why the height measurements of the “low-topology” complexes varied significantly between membrane patches.

The ratio of PSII complexes to cytochrome  $b_6f$  complexes in cyanobacteria has previously been measured to be between 1.08-1.38 depending on growth conditions (Fujita and Murakami, 1987). The ratio of “high-topology” complexes to “low-topology” complexes in the *T. elongatus* was measured at 1.37 and 1.09 in the membrane patches in **Figures 4.10a** and **4.10b** respectively. The ratio of “high-topology” complexes to “low-topology” complexes in *Synechocystis* was somewhat higher measured at; 1.73, 1.25 and 1.94 in the membrane patches in **Figures 4.2c, 4.2d** and **4.2e** respectively. These values are relatively consistent with the expected PSII to cytochrome  $b_6f$  ratio, supporting the hypothesis that the identity

of the complexes with lower topology is cytochrome  $b_6f$  however they cannot be assigned on this basis alone.

One solution for distinguishing cytochrome  $b_6f$  complexes from the surrounding PSII complexes would be to use peak-force quantitative nanomechanical mapping (PF-QNM). This type of AFM measures the force between a functionalised AFM probe and the membrane sample allowing membrane topology to be correlated to specific probe-sample interactions. One study has used AFM probes that were functionalised with oxidised plastocyanin to identify cytochrome  $b_6f$  complexes in preparations of spinach thylakoid membranes (Johnson *et al.*, 2014). As the functionalised AFM probe scanned over the membrane patch, the oxidised plastocyanin that was conjugated to the apex of the AFM probe transiently interacted with the reduced cytochrome  $b_6f$  complexes that it encountered. The force of this interaction was measured by the AFM and allowed for accurate identification cytochrome  $b_6f$  (Johnson *et al.*, 2014). In principle the same method could be applied to membrane fragments from cyanobacterial thylakoids to identify which of the “low-topology” complexes are cytochrome  $b_6f$ .

In all the membrane fragments, domains that contained primarily PSII and potentially cytochrome  $b_6f$  could be identified. In some membrane patches the PSII containing domains were interspersed with large areas of membrane that are relatively flat and featureless. This was seen most prominently in membrane fragments from *T.elongatus* which had the lowest abundance of lumenally protruding complexes. The heights of these areas of flat membrane were too great for the areas to be empty lipid and must have some protein components. The obvious candidate for these areas of protein-containing membrane is PSI; however owing to the lack of luminal projections in the PSI structure it is not possible to image individual complexes. Despite this, the height data from these flat areas of membrane is compatible with the PSI crystal structure. Interestingly it may be possible to identify PSI using the same type of PF-QNM as was used to locate cytochrome  $b_6f$  complexes in Johnson *et al.*, (2014). Reduced plastocyanin interacts with the luminal face of PSI; therefore all that would be required is a change in buffer and illumination conditions to reduce plastocyanin enabling it to interact with photo-oxidised PSI.

#### 4.4.3 Identification of trimeric complexes in membrane patches from *T.elongatus*

The appearance of trimeric complexes in some of the membrane fragments from *T.elongatus* was unexpected as no obviously trimeric complexes had ever been imaged in membrane samples from *Synechocystis*. PSI was seen as the most likely candidate for the trimeric complex as it is known to form a trimer in cyanobacteria and is highly enriched in thylakoid membranes (Jordan *et al.*, 2001). The height measurement of the protein complexes again was primarily used for determining the identity of the complex as it is the most accurate measurement taken by the AFM. The average height of the protein complexes in **Figure 4.13** was  $9.3 \pm 0.4$  which is in agreement with the 9.1 nm measured from the crystal structure of the PSI complex. The lateral distances between complexes in a trimeric configuration were measured to be between 8-11 nm which was within the expected range for PSI. From these measurements and the fact the protein complexes have a trimeric structure; we have assigned each trimeric complex as trimeric PSI. The organisation of PSI into parallel linear arrays was very surprising as no such structure has ever been imaged before despite extensive analysis of cyanobacterial thylakoid membranes by freeze-fracture and negative stain EM. This could be an example of how the preparation and imaging conditions required for AFM, which are generally less damaging to biological structures than those required for EM, have been able to preserve the native structure of the thylakoid membrane.

#### 4.4.4 PSI and PSII content in membrane patches from *Synechocystis* and *T.elongatus*

For an accurate analysis of the PSI:PSII ratio in the membrane patches produced by the digitonin treatment; the membrane preparation had to be altered slightly. A more concentrated membrane sample had to be used so that the sample harvested from the sucrose gradient was of a high enough concentration to visualise the PSI and PSII bands on a clear native polyacrylamide gel. Using a higher concentration of membrane sample would however alter the lipid:detergent ratio in the gradient which could affect the type of membrane patch that was produced. For *Synechocystis*, it was decided to run sucrose gradients with a range of digitonin

concentrations and measure the PSI:PSII ratios of the membrane patches produced by each gradient. In the case of *T.elongatus* it was not possible to use a range of digitonin concentrations; as we had been supplied with a limited amount of material. It was therefore decided to use a sucrose gradient with a concentration of 1.0 (w/v) digitonin as this would give a lipid:detergent ratio that was similar to that of the standard sucrose gradient used throughout this study. The upper band (**Figure 4.16**) that was seen to appear in the digitonin-containing gradients was harvested for comparison with the lower band (**Figure 4.16**) in the control gradient. It was shown in **3.3.19** that the upper band in the sucrose gradient consists primarily of single layered protein-containing membrane patches. Using this fraction of the sucrose gradient allowed for a comparison of the PSI:PSII ratio between untreated membranes from the control gradient and the membrane patches that were imaged by AFM.

CN-PAGE of membranes that had not undergone any form of digitonin treatment revealed that there were significantly more PSI complexes present in the thylakoid membranes from both *Synechocystis* and *T.elongatus* than there were PSII complexes. The PSI:PSII ratio was 2.73 and 3.94 in *Synechocystis* and *T.elongatus* respectively. These numbers were consistent with low temperature fluorescence emission spectra taken of untreated thylakoid membranes. The PSII fluorescence was greater relative to the PSI fluorescence in *Synechocystis* than in *T.elongatus*; indicative of a lower PSI:PSII ratio in the former. CN-PAGE of membrane patches purified on sucrose gradients from *T.elongatus* showed that the PSI:PSII ratio was relatively similar to that of membranes that had not undergone digitonin treatment. This would suggest that the membrane patches have a similar protein architecture to the untreated membranes. The AFM data agrees with this somewhat in that large membrane patches that exclusively contain PSI can be imaged (**Figure 4.13**). Membrane patches containing relatively low levels of what are believed to be PSII and cytochrome *b<sub>6</sub>f* complexes can also be imaged (**Figure 4.10**).

In the case of *Synechocystis* membrane patches purified by digitonin-containing sucrose gradients; CN-PAGE revealed that the PSI:PSII ratio was significantly reduced in comparison to untreated membranes. In the membrane patches harvested from the sucrose gradient with a concentration of 0.1 % digitonin; the PSI:PSII ratio was

1.38, which was seen to decrease to 1.06 in membrane patches purified from the sucrose gradient containing 2 % digitonin. This would suggest that the digitonin containing sucrose gradients are preferentially producing membrane patches that are enriched in PSII; agreeing with the absorption spectrum taken of digitonin treated membrane patches which shows a blue shifted peak at 678 nm. An increased level of PSII in the samples would account for the 2 nm shift from 680 nm to 678 nm as PSII has a peak at 673 nm in its absorption spectrum. When using AFM to image membrane patches purified on digitonin-containing sucrose gradients; it was only possible to image membrane patches that had a high abundance of complexes that were believed be PSII and cytochrome *b<sub>6</sub>f* complexes. The fact it was not possible to image PSI complexes in the membrane patches from *Synechocystis* in addition to the increased level of PSII present in the sample indicated that the digitonin-containing gradients are preferentially producing membrane patches that are enriched in PSII.

There is still a significant amount of PSI in the sample that is used for AFM analysis and there are a number of reasons why it might not possible to image the complex in the membrane. Whilst the major membrane structures found in the digitonin treated sample are single layered protein-containing membrane patches; there is still a significant number of large vesicular membranes (as described in **3.3.14**). It is possible that PSI is present in these structures which cannot be imaged to the level of single protein complexes due to their high degree of curvature. It is also a possibility that single layered protein-containing membrane patches that are enriched in PSI are not able to bind securely to the surface of the mica; although this seems unlikely as PSI enriched membrane patches from *T.elongatus* are capable of attachment to the mica. It is still however unclear why it is possible to image both PSI and PSII complexes in membrane patches from *T.elongatus* whereas it is only possible to image PSII complexes in membrane patches from *Synechocystis*. Both organisms have relatively similar protein and lipid contents so it would be expected that the digitonin treatment would produce similar types of membrane patch.

#### 4.4.5 Supramolecular organisation of cyanobacterial thylakoid membranes

PSII complexes apparently either form parallel linear arrays or adopt a seemingly random arrangement; a mixture of the two organisations is also observed with smaller linear arrays punctuating an otherwise disordered membrane system. It has been shown by freeze fracture EM that the organisation of PSII is dependent on state transition. In state 1 parallel rows of PSII are observed with increased frequency, whereas in state 2 the organisation of PSII is seen to randomise (Olive *et al.*, 1986; Vernotte *et al.*, 1990). It is also interesting to note that the spacing between parallel arrays of PSII was observed to vary significantly in freeze fracture studies (Olive *et al.*, 1997); such a high degree of variation is not seen in the AFM data with parallel rows having a maximal spacing of less than 15 nm.

Whether in an ordered or disordered arrangement, PSII complexes in *Synechocystis* membrane patches typically clustered in relatively large densely packed domains. The height data from **Figures 4.4** and **4.11** suggests that cytochrome *b<sub>6</sub>f* is also present throughout these PSII enriched domains. This would be consistent with Johnson *et al.*, (2014) which found cytochrome *b<sub>6</sub>f* complexes throughout the PSII enriched regions of the granal lamellae. This co-localisation would allow for fast exchange of plastoquinone molecules between the two complexes enabling efficient electron transport from PSII to cytochrome *b<sub>6</sub>f*.

Owing to the dense packing of these domains, PSI cannot be present due to steric hindrance. Segregation of PSI and PSII has been observed in chloroplasts so it is not surprising that there is spatial separation of photosystems in cyanobacterial thylakoid membranes. PSII is also seen in smaller domains that are surrounded by featureless areas of flat membrane that are compatible with the height of PSI (**Figures 4.8a** and **4.12**). These smaller PSII domains are more prominent in *T.elongatus* membrane patches and may suggest that PSII generally clusters into smaller domains in this cyanobacterium. These domains may represent areas where the supramolecular organisation favours the spill-over of excitation energy from PSII to PSI as the bacteria regulate the distribution of the absorbed light energy between the two photosystems.

No efforts were made to induce either state 1 or state 2 in bacteria during growth. It would be interesting to see the frequency with which the different organisations of PSII can be imaged in bacteria grown under conditions that induce either state. It would be expected that in state 1 the parallel linear arrays of PSII would be more prevalent whereas bacteria in state 2 would have a more disordered arrangement of PSII.

A model of the membrane organisation of PSI, PSII, the cytochrome *b<sub>6</sub>f* complex and ATP synthase is suggested in **Figure 4.20** based the AFM data from *Synechocystis* membrane patches. We suggest that there are areas of the membrane that are enriched in PSII and the cytochrome *b<sub>6</sub>f* complex. There are also areas that consist exclusively of PSII which is organised into parallel linear arrays. In this model PSI is present in a disordered arrangement between the areas that are enriched in PSII and the cytochrome *b<sub>6</sub>f* complex. It has been shown by CN-PAGE that PSI is much more abundant than PSII in *Synechocystis* thylakoid membranes and the PSI:PSII ratio in the membrane model (**Figure 4.20**) is representative of the PSI:PSII ratio that was measured. It should be made clear that due to a lack of AFM data of PSI complexes in membrane patches from *Synechocystis*; the organisation of PSI in this model is largely speculative. It is possible that PSI can form large ordered arrays like those seen in membrane patches from *T.elongatus*. Further research in the form of AFM or EM will be required to produce a more definitive model of PSI organisation in thylakoid membranes from *Synechocystis*. The organisation of the ATP synthase in cyanobacterial thylakoid membranes is still very unclear; there have not been any conclusive studies locating its position in relation to the protein complexes that make up the photosynthetic unit. It is included in this model as it is known to be relatively abundant in *Synechocystis* thylakoid membranes (Srivastava *et al.*, 2005). We can conclude that ATP synthase is not present in the highly ordered arrays of PSII due to steric hindrance. However, as it was not possible to image the ATP synthase in any of the membrane patches that were analysed by AFM; its organisation in the membrane model is largely speculative.

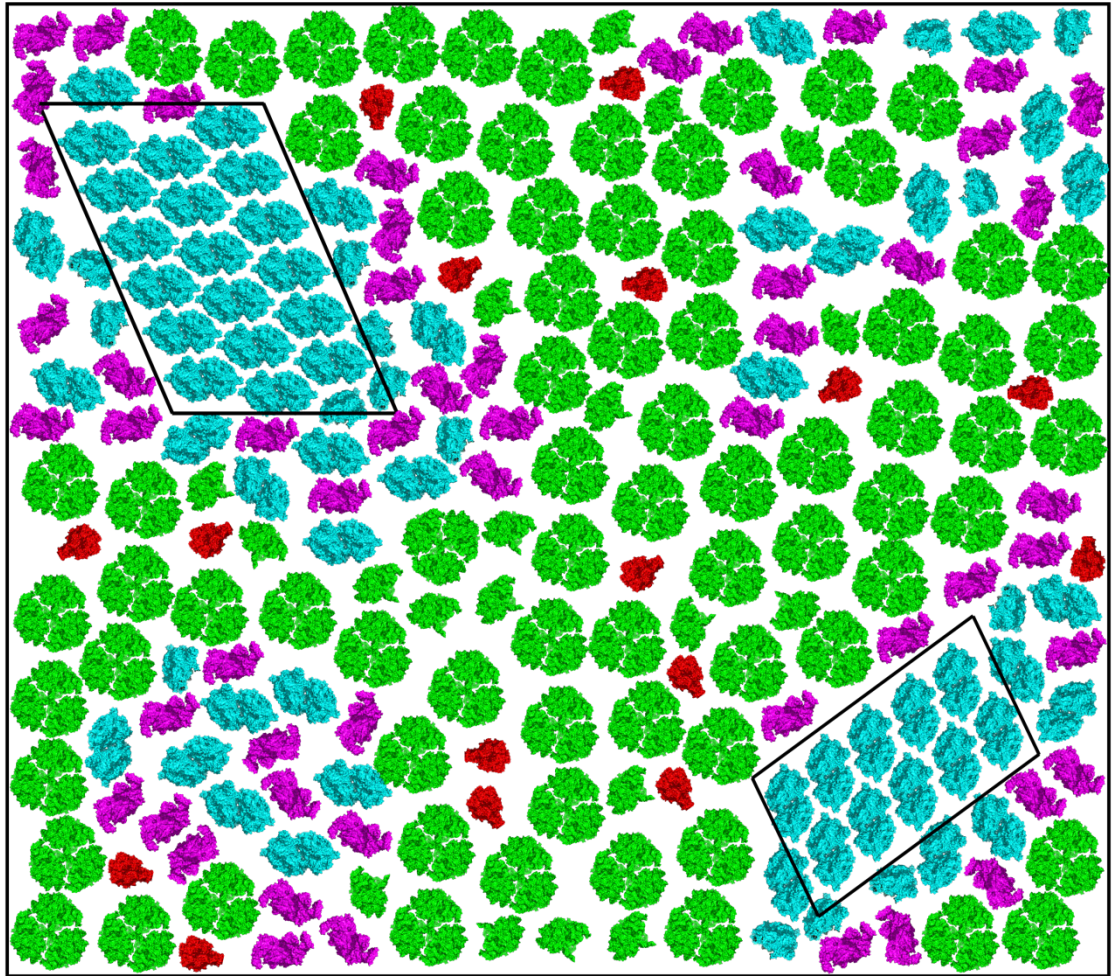


**Figure 4.20. Model for the organisation of PSI, PSII, the cytochrome  $b_6f$  complex and ATP synthase in *Synechocystis* thylakoid membranes based on AFM data.** PSI (green), PSII (blue), the cytochrome  $b_6f$  complex (pink) and ATP synthase (red) are presented in a suggested model for the protein architecture of the *Synechocystis* thylakoid membrane. There are regions of the membrane that exclusively contain PSII and the cytochrome  $b_6f$  complex in a disordered arrangement. There are also areas where PSII forms into parallel linear rows that exclude cytochrome  $b_6f$  (outlined by the black quadrilateral). PSI is believed to be present in between the areas of that are enriched in PSII and the cytochrome  $b_6f$  complex. The PSI:PSII ratio is 2.7 as shown by CN-PAGE of untreated thylakoid membranes; the PSII:cytochrome  $b_6f$  complex ratio is 0.8 as shown by Fujita and Murakami., (1987).

The organisation of PSI in membrane patches from *T.elongatus* was similar to that of PSII in *Synechocystis*, in that PSI trimers can form highly ordered arrays (**Figure 4.13**) or have an apparently random distribution (**Figure 4.14**). One possible explanation for finding PSI in a highly ordered organisational state is that it allows the cyanobacterium to alter the activities of PSI and PSII depending on the redox state of the quinone pool. When PSI and PSII are in close proximity, excitation energy can “spill-over” from PSII to PSI meaning that PSI activity increases while PSII activity decreases; this leads to the quinone pool becoming more oxidised. Much in the same way PSII arrays are believed to reduce the spill-over of excitation energy; the formation of PSI arrays would reduce the number of contacts between PSI and PSII and allow for an increase in PSII activity in response to an oxidised quinone pool. By contrast the membrane patch in **Figure 4.14** has a much more disordered arrangement of PSI with complexes spread throughout the membrane patch amongst other proteins believed to be PSII and the cytochrome *b<sub>6</sub>f* complex. It is not possible to positively identify PSII and the cytochrome *b<sub>6</sub>f* complex in these areas of the membrane without using a form of PF-QNM similar to that discussed in **4.4.2** due to the minimal topology of the protein complexes. The height measurements taken of these areas agree with the heights of PSII and the cytochrome *b<sub>6</sub>f* complex and the presence of these complexes would explain the increase in the measured height of the PSI trimers in **Figure 4.14**. If these areas of the membrane do contain PSII and the cytochrome *b<sub>6</sub>f* complex, this constitutes a membrane organisation similar to that which has been previously suggested, with PSI distributed throughout the membrane system (Folea *et al.*, 2008a) and not in segregated domains seen in **Figure 4.13**. This organisation of PSI and PSII has important implications for the spill-over of excitation of energy from PSII to PSI. In the disordered arrangement seen in **Figure 4.14** the number of contacts between PSI and PSII will increase; this will allow for increased levels of spill-over from PSII to PSI resulting in an increase in PSI function and a decrease in PSII function. The ability to segregate PSI complexes from PSII complexes by incorporating them into these large arrays provides an effective method for the *T.elongatus* to control the spill-over of excitation energy from PSII to PSI. This in turn allows *T.elongatus* to regulate the activity of its reaction centres in accordance to the redox state of the quinone pool.

Interestingly cytochrome  $b_{6f}$  complexes are not present in these large PSI arrays which would mean that plastocyanin would have to diffuse greater distances to transport electrons from cytochrome  $b_{6f}$ . When PSI is incorporated into these large arrays it would therefore appear to be in an organisation that would be inefficient for electron transport from cytochrome  $b_{6f}$ . It should be noted however that if the reason for the formation of these ordered arrays of PSI is to increase PSII activity at the expense of PSI activity; the greater distance the plastocyanin molecules have to travel would be consistent with a reduced level of PSI activity. In the more disordered arrangement seen in **Figure 4.14** there are areas in the membrane in which cytochrome  $b_{6f}$  complex could occupy. In this organisational state plastocyanin would only have to diffuse over very short distances to reduce PSI. This would be important as it is believed that the excitation of PSI is favoured over PSII in this organisational state; requiring plastocyanin to be readily available to PSI in order to donate an electron to P700<sup>+</sup>.

A model for the organisation of PSI, PSII, the cytochrome  $b_{6f}$  complex and ATP synthase in *T.elongatus* is presented in **Figure 4.21**. In this model, PSI can exist as part of an ordered array which excludes both PSII and the cytochrome  $b_{6f}$  complex or in a more disordered arrangement where it is amongst PSII and the cytochrome  $b_{6f}$  complex. In this model PSII and the cytochrome  $b_{6f}$  complex are distributed randomly in small clusters as this is how they appeared in the AFM data (**Figure 4.9**). The presence of ordered PSII arrays in *T.elongatus* cannot be disregarded despite the fact it was not possible to image such arrays. There is significant similarity in the structures of PSI, PSII and the cytochrome  $b_{6f}$  complex between *Synechocystis* and *T.elongatus*. In addition, the need for cyanobacteria to alter the organisation of these protein complexes in response to the redox state of the quinone pool would suggest it is possible that the segregation of both PSI and PSII into ordered arrays can occur in both *Synechocystis* and *T.elongatus*. As was the case with *Synechocystis* membrane patches; it was not possible to directly image ATP synthase; although it is possible to discount its presence in the ordered arrays of PSI due to steric hindrance. It is included in this model as it has been shown to be a major protein component of *T.elongatus* thylakoid membranes (Folea *et al.*, 2008b); although its suggested organisation is largely speculative.

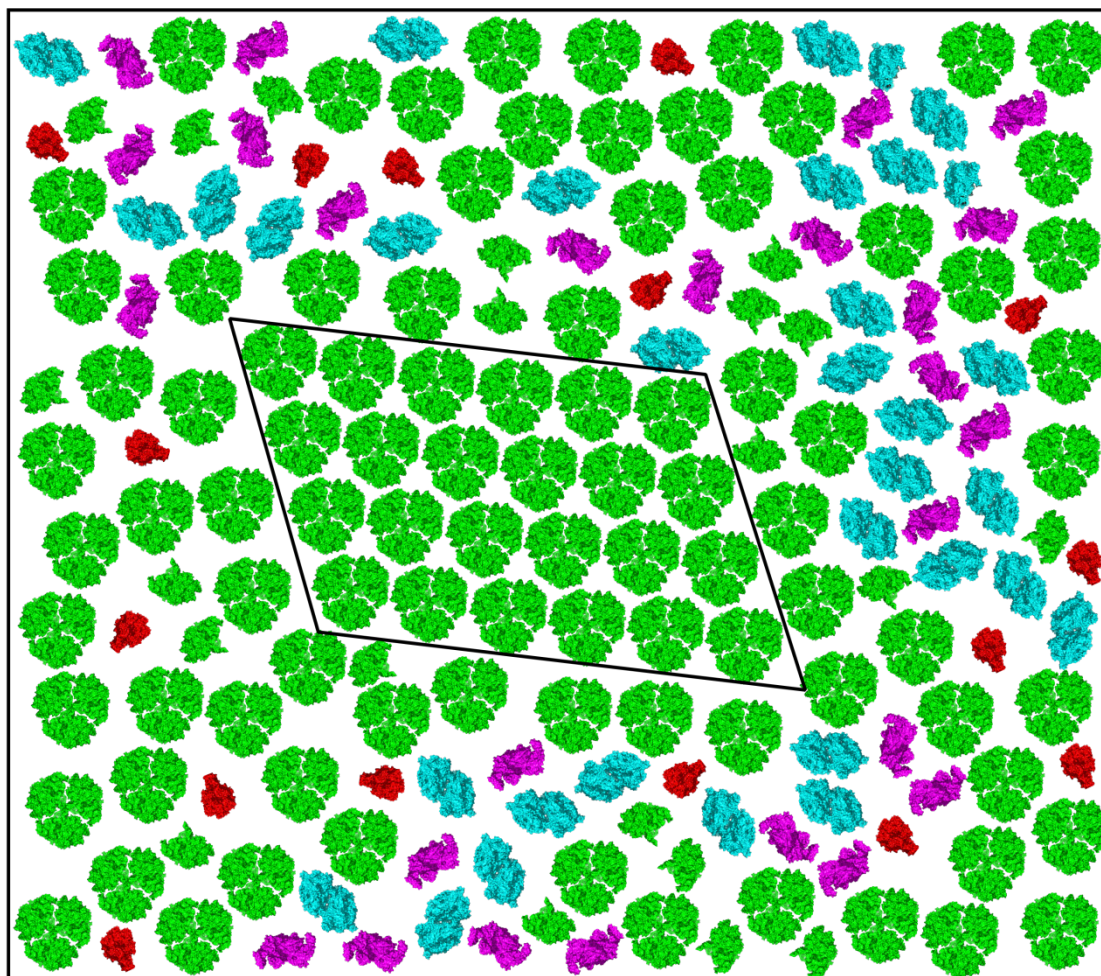


**Figure 4.21. Model for the organisation of PSI, PSII, the cytochrome  $b_6f$  complex and ATP synthase in *T.elongatus* membranes based on AFM data.** In this model, arrays that exclusively contain trimeric PSI (green) are present in the membrane (outlined by the black quadrilateral). Other areas of the membrane are disordered and contain PSI, PSII (blue), the cytochrome  $b_6f$  complex (pink) and the ATP synthase. The PSI:PSII ratio is 4.0 as shown by CN-PAGE of untreated thylakoid membranes; the PSII:cytochrome  $b_6f$  complex ratio is 0.8 as shown by Fujita and Murakami., (1987).

# Chapter 5: Purification and imaging of the IsiA-PSI supercomplex and nanopatterning of cyanobacterial photosystems

## 5.1 Summary

*Synechocystis* was grown under low iron conditions to promote the synthesis of the IsiA-PSI supercomplex. The cell lysate was applied to continuous sucrose gradients which were subsequently centrifuged to purify bulk amounts of the IsiA-PSI supercomplex. Samples harvested from sucrose gradients were not of high purity and were further purified by anion exchange and gel filtration. Samples containing the IsiA-PSI supercomplex were analysed by negative stain TEM and AFM in conjunction with SDS-PAGE to assess their purity. Samples harvested from sucrose gradients that had undergone gel filtration in addition to anion exchange were of high enough purity to be used for nanopatterning.

Single particle reconstruction using TEM images of the purified IsiA-PSI supercomplex made it possible to resolve the PSI trimer and the 18 membered ring that surrounds it. AFM analysis of the purified IsiA-PSI supercomplexes was used to measure the height the supercomplex. The average measured height was consistent with the 3D model proposed in (Nield *et al.*, 2003)

Reverse nanoimprint lithography (RNIL) was used to direct the formation of self-assembled monolayers (SAMs) to construct nanopatterns of cyanobacterial photosystem complexes. The nanopatterns consisted of a (3-mercaptopropyl)trimethoxysilane (MPTMS) monolayer for immobilising protein complexes and a 2-[methoxy(polyethyleneoxy)propyl]trimethoxysilane monolayer (referred to as PEG-silane throughout the text) that resisted protein adhesion.

IsiA-PSI supercomplexes were immobilised on the MPTMS nano-lines and imaged with AFM, which resolved individual supercomplexes. The AFM data showed that

IsiA-PSI supercomplexes were highly enriched on the MPTMS nano-lines and had a minimal presence on the PEG-silane monolayer. Fluorescence microscopy was used to image large sections of the nanopatterns showing that the pattern extends over an area of the order of millimetres. The fluorescent properties of immobilised IsiA-PSI supercomplexes were measured to determine if the supercomplex was still functional. The room temperature fluorescent emission spectrum of immobilised supercomplexes was consistent with the room temperature emission spectrum for supercomplexes in solution. Fluorescence lifetime imaging was used to determine the fluorescence lifetime of the immobilised IsiA-PSI supercomplex which was found to be longer than the characteristic lifetime of IsiA-PSI complexes in solution.

Purified PSII complexes were incorporated into nanopatterns; AFM revealed the presence of PSII complexes on the MPTMS nano-lines with minimal levels of the protein complex on PEG-silane monolayers. The width of the MPTMS nano-lines was larger than expected, however single particles could be imaged that had dimensions consistent with the PSII dimer. Fluorescence microscopy was used to image the PSII nanopatterns, which extended over a millimetre length scale, showing nano-lines that were highly enriched in PSII. Fluorescence microscopy also showed that the PEG-silane monolayer was relatively free of fluorescence indicating that PSII complexes were not present in significant numbers. The room temperature emission spectrum of immobilised PSII complexes agreed with the room temperature emission spectrum from PSII complexes in solution indicating the complexes had retained their fluorescence properties. The fluorescence lifetime of the PSII complexes was measured and found to be consistent with the characteristic lifetime of PSII complexes in solution.

## 5.2 Introduction

Controlling the distribution of pigment-containing protein complexes is one of the fundamental goals for creating bio-inspired devices that can utilise the extremely efficient energy transport properties of biological arrays of light harvesting protein complexes. Towards this end highly purified samples of pigment-containing protein complexes have to be produced that are stable and retain their spectroscopic properties.

PSI is the photosystem found at the highest abundance in cyanobacterial thylakoid membranes and contains 96 molecules of chlorophyll *a* (Jordan *et al.*, 2001). This is significantly more than PSII which has 35 (Umena *et al.*, 2011); PSII is more closely associated with phycobilisome antenna complexes than PSI which utilises its own large chlorophyll antenna system to harvest light. PSI typically forms a trimer under normal growth conditions; however, when *Synechocystis* is grown under low iron conditions it synthesizes a supercomplex in which the PSI trimer is surrounded by an 18 membered ring of the IsiA protein (Bibby *et al.*, 2001a; Boekema *et al.*, 2001). IsiA contains approximately 16-17 molecules of chlorophyll *a* (Andrizhiyevskaya *et al.*, 2002) which has been shown to efficiently channel energy to the PSI core of the supercomplex (Melkozernov *et al.*, 2003). The chlorophylls present in the IsiA proteins increase the antenna size by 100 % relative to the PSI trimer (Andrizhiyevskaya *et al.*, 2002). The transcription of PSII and phycobilisome genes is reduced under low iron growth conditions (Singh *et al.*, 2003) and it is believed that the increased antenna size of PSI compensates for the reduced light harvesting capacity of cyanobacteria grown under low iron conditions.

The IsiA-PSI supercomplex is an ideal protein complex for nanopatterning as it contains a reaction centre surrounded by an extensive antenna system which is relatively stable (Melkozernov *et al.*, 2003). Its large size is also a useful property as it will allow for the supercomplex to be readily identified by TEM and AFM. In addition the line-widths of nanopatterns produced by NIL are approaching the size of the

diameter of the IsiA-PSI supercomplex which could allow for the production of linear arrays, one supercomplex wide.

Photosynthetic chlorophyll-protein complexes are able to absorb and transfer energy with close to 100 % quantum efficiency to drive charge separation in reaction centres; the exploitation of this characteristic is a major goal in producing bio-inspired solar cells. Developing procedures for controlling the nanoscale distribution of reaction centres that remain functionally active is an important step towards this goal.

In previous studies reaction centres have been immobilised on gold surfaces for the purposes of measuring the photocurrent produced when these complexes are exposed to light (Tan *et al.*, 2012; Kamran *et al.*, 2014). The cyanobacterial PSI complex has been a target for such studies and it has been shown that this complex generates a photocurrent in response to illumination (Frolov *et al.*, 2005; Gerster *et al.*, 2012). In the aforementioned studies monolayers of the respective proteins were assembled on gold substrates, but no efforts were made to influence their surface arrangement or distribution. With the recent advances in lithographic techniques such as nanoimprint lithography (Falconnet *et al.*, 2004; Escalante *et al.*, 2008) and photolithography (Reynolds *et al.*, 2007) it is possible to direct the distribution of protein complexes on the nanoscale.

Most of the efforts in nanopatterning of photosynthetic protein complexes have focused on light harvesting antenna complexes such as LH2 and LHCII which have been incorporated into nanopatterns created with the previously mentioned techniques (Escalante *et al.*, 2008; Reynolds *et al.*, 2007; Vasilev *et al.*, 2014). Relatively little work has been performed on the nanopatterning of reaction centres; in particular there are no reports of using photosystems from cyanobacteria for nanopatterning, despite their attractive properties in terms of structural and functional characterisation, thermostability and amenability to protein engineering.

In standard NIL a thermoplastic polymer is spin coated onto the surface of a substrate such as silicon. A mould of the desired nanopattern (master pattern) is then pressed

into the polymer under pressure and heated to allow the polymer to mould to the contours of the master pattern. After cooling the mould is removed and the thinner areas where the nanopattern has pressed into the polymer are removed by an etch process such as reactive ion etching to allow access to the surface of the substrate. A SAM can then be formed on the areas of the substrate that are exposed. The remaining polymer can then be removed and a SAM can be formed on the newly exposed substrate. By selecting compounds that form SAMs suitable for immobilising protein complexes or compounds that are resistant to the adherence of protein complexes, it is possible to direct the distribution of proteins, photosynthetic reaction centres in this case, on the surface of the substrate.

A variant of NIL is reverse nanoimprint lithography (RNIL) where a polymer such as polystyrene is spin coated directly onto the master pattern that has the required dimensions before being floated off the master pattern and adsorbed to a suitable substrate such as glass or silicon. The polystyrene film has a complementary shape to the master pattern and can be used to direct the formation of SAMs. The distribution of protein complexes can be directed by the selection of the correct compounds for the formation of SAMs in the same way as for standard NIL. This technique does not require the use of high temperatures and pressures or the additional etching process used in standard NIL; therefore RNIL was used for producing nanopatterns in this work. (See **Figure 5.11** for a detailed description of RNIL)

The functionality of immobilised photosynthetic protein complexes is typically determined by measuring their *in situ* fluorescent properties. Fluorescence-lifetime imaging is one method used to assess the functionality of photosynthetic protein complexes that have been immobilised on nanopatterns. In this technique a population of immobilised protein complexes is excited by light; decay of excited chlorophylls back to the ground state gives rise to the emission of photons which are detected and counted using a photomultiplier tube (PMT). The amount of time that has elapsed between the excitation of the protein complexes and the detection of the emitted photons is also measured (typically of the order of picoseconds to nanoseconds). Using a pulsed laser source, protein complexes can be excited millions of times per second with the time taken for the detection of the emitted photon

recorded after each pulse. The values for the elapsed time are grouped into bins of user defined size and the value for each bin is then plotted. The time data are subsequently fitted with an exponential decay function with the formula in **Formula 5.1**. The rate of decay in this function is dependent on the value of the  $\tau$  term. The  $\tau$  term is the value for the lifetime of the protein complex which corresponds to the average amount of time that elapses between the excitation of the protein complexes and the detection of the emitted photons. Often the decay curve that is fitted to the time data will have more than one exponential component, each with a separate lifetime value corresponding to a different route of fluorescence in the protein complex. Each fluorescent protein complex has a characteristic value for its average lifetime which is the amplitude averaged value of all the component lifetimes. If the measured value from the immobilised complex is consistent with the value of the protein complex in solution it can be inferred that immobilisation is not having a significant effect on the function of the protein complex.

$$N(t) = N_0 e^{-t/\tau}$$

**Formula 5.1** this equation describes the decay curve of a population fluorophores after excitation by suitable wavelength of light.

## 5.3 Results

### 5.3.1 Growth conditions

Growth conditions had to be modified to induce the formation of the IsiA-PSI supercomplex in *Synechocystis*. 80 ml cultures of BG-11 medium were inoculated with a loop of cells and grown to an OD<sub>750</sub> of approximately 1.0. A 720 ml culture of BG-11, in which no iron-containing compounds were present, was inoculated with the entire 80 ml culture giving a 1 in 10 dilution of the iron-containing compounds in the BG-11 medium of the original culture. The 800 ml culture was allowed to grow to an OD<sub>750</sub> of approximately 1.0 before it was used to inoculate a flask containing 7.2 litres of iron-free BG-11. The final concentration of ammonium ferric citrate (the iron containing compound in BG-11 medium) in the culture was 210 nM. Cultures were grown for a period of three days prior to harvesting; the OD<sub>750</sub> of these cultures was relatively low with no cultures achieving an OD<sub>750</sub> of greater than 0.6. This approach of diluting the iron concentration was found to be the most effective at producing large volumes of low iron adapted cells, as directly inoculating low iron medium with cells from a plate required extended growth periods and produced cultures of very low OD<sub>750</sub>.

Room temperature absorption spectra of normal iron and low iron cell cultures (**Figure 5.1**) revealed that the PSI-associated peak was blue shifted. This indicated that the growth conditions were inducing the formation of the IsiA-PSI supercomplex which is known to cause a blue shift in the absorption properties of PSI. The peaks associated with pigments were still visible above the cell scatter although they were significantly less prominent than the peaks seen in the absorption spectra from cultures grown with normal iron levels. This indicated a reduced number of photosystems per cell which is consistent with the findings that transcription of certain PSI and PSII subunits is reduced in low iron adapted cells (Singh *et al.*, 2003).

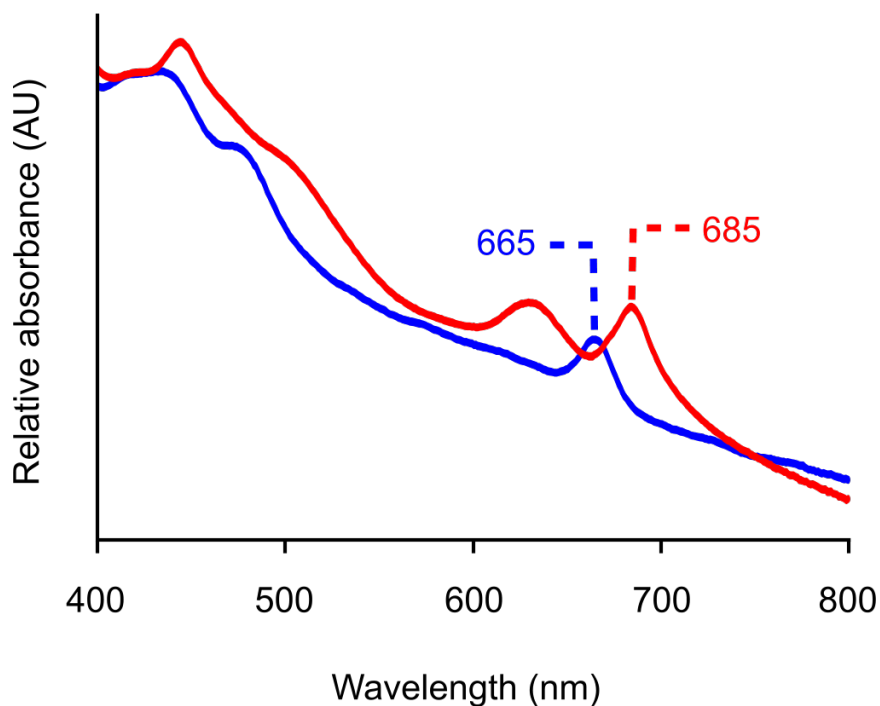


**Figure 5.1. Room temperature absorption spectra.** *Synechocystis* cells grown under normal iron conditions (red) had a PSI-associated peak at 685 nm. Cells grown under low iron conditions (blue) had a PSI-associated peak at 665 nm. The shift is due to the formation of the IsiA-PSI supercomplex in the low iron culture. Spectra are normalised 750 nm.

### 5.3.2 Purification of the IsiA-PSI supercomplex on sucrose gradients

Samples of the IsiA-PSI supercomplex have previously been prepared on sucrose gradients (Bibby *et al.*, 2001a) and the same approach was repeated here for the preparation of bulk quantities of the supercomplex. Solubilised membranes from cells grown in low iron conditions and normal iron conditions were applied to continuous sucrose gradients (prepared as in **2.14**) and centrifuged for 16 hours at 100,000 x g. The post centrifugation gradients (**Figure 5.2a**) contain several bands, with one present towards the bottom of the low iron gradient (outlined in blue) that is not present in the gradient for the normal iron sample. The lowest band in the normal iron gradient (outlined in red) is also absent in the low iron gradient. In the normal

iron gradient only the PSI trimer is present and as it is the largest chlorophyll-containing protein complex it migrates the furthest through the gradient. In the low iron gradient PSI has been incorporated into the IsiA-PSI supercomplex which increases its size from 900 kDa to 1,700 kDa and results in the complexes migrating further through the gradient, hence the absence of the PSI band from the low iron gradient and presence of the IsiA-PSI supercomplex towards the bottom of the gradient. The PSI containing bands were harvested from the low iron and normal iron gradients and room temperature absorption spectra were taken for the two samples. In the absorption spectra from the normal iron sample, the peak associated with PSI can be seen at 680 nm whereas in the low iron sample it is blue shifted to 673 nm (**Figure 5.2b**). This observation confirmed the presence of the IsiA-PSI supercomplex which has previously been measured to be blue shifted relative to the PSI trimer by several nanometres (Bibby *et al.*, 2001b).

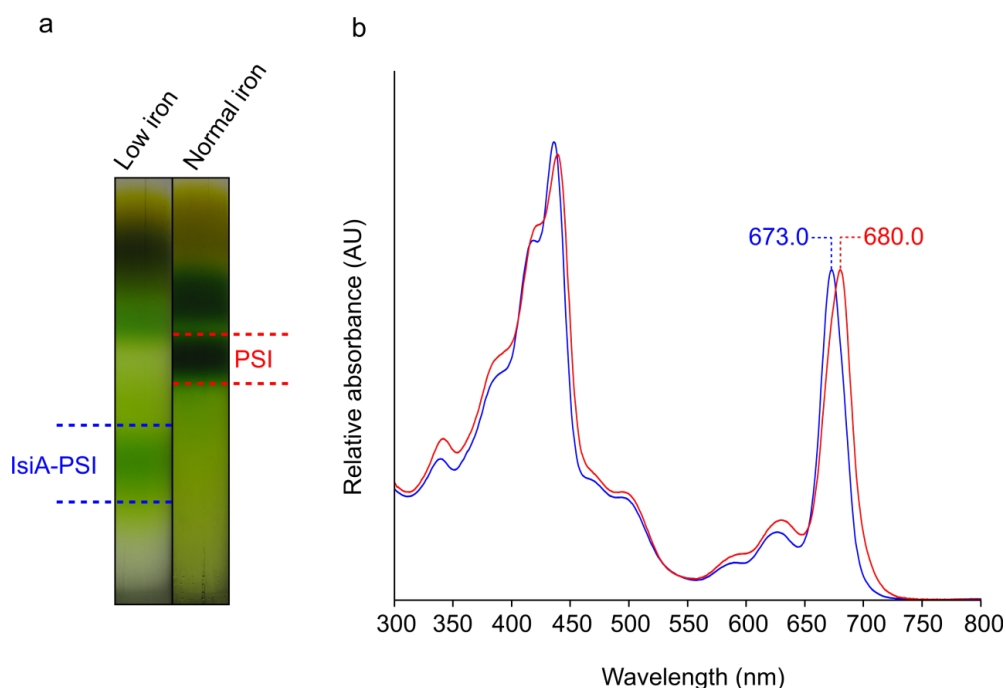


**Figure 5.2. (a) Sucrose gradients and (b) room temperature absorption spectra. (a)** The IsiA-PSI supercomplex can be purified from *Synechocystis* cells grown under low iron conditions; the supercomplex travels further through the sucrose gradient than the PSI trimer. **(b)** Room temperature spectra of the purified PSI trimer (red) shows a peak at 680 nm; in the absorption spectra of the purified IsiA-PSI supercomplex (blue) the peak is shifted to 673 nm. Spectra are normalised at the PSI-associated peak.

### 5.3.3 Anion exchange of the IsiA-PSI supercomplex

Sucrose gradients generally do not produce samples of protein complexes that are of high enough purity for nanopatterning; therefore the samples harvested from the gradients were further purified by anion exchange. Samples harvested from the continuous sucrose gradients were concentrated to a volume of 5 ml before being loaded onto an anion exchange column (prepared as in **2.14**). A NaCl gradient from 100 mM to 500mM was run over the course of 60 minutes. Absorbance at 280 nm was detected at a concentration of approximately 260 mM NaCl indicating that protein was starting to elute at this concentration of NaCl (**Figure 5.3**). Fractions of 1 ml were collected throughout the entirety of the NaCl gradient.

Room temperature spectra were taken of every 5th fraction starting with the 25th fraction as this was the first fraction for which a protein peak was detected. The room temperature spectra of fractions; 25, 30, 35, 40 and 45 (**Figure 5.4**, note: spectra for fractions 30 and 40 are not shown) were very similar, with the PSI-associated peak maxima at 673 nm indicating the presence of the IsiA-PSI supercomplex; in addition the  $OD_{673}:OD_{280}$  ratio was similar in these fractions (**Table 5.1**). The absorption spectrum of fraction 50 (**Figure 5.4d**) was noticeably different from the previous spectra. Whilst the PSI-associated peak was still present at 673 nm, the  $OD_{673}:OD_{280}$  ratio was significantly lower indicating the presence of other non-pigment containing proteins in the fraction (**Table 5.1**). Room temperature spectra were taken of the next two fractions which revealed that the PSI-associated peak was red shifted to 676 nm and 680 nm in fractions 51 and 52 respectively. This red shift indicated that the PSI trimer was still present in the sample harvested from the sucrose gradient and eluted from the anion exchange column at a higher concentration of NaCl. Fractions 25 to 45 were pooled and concentrated.

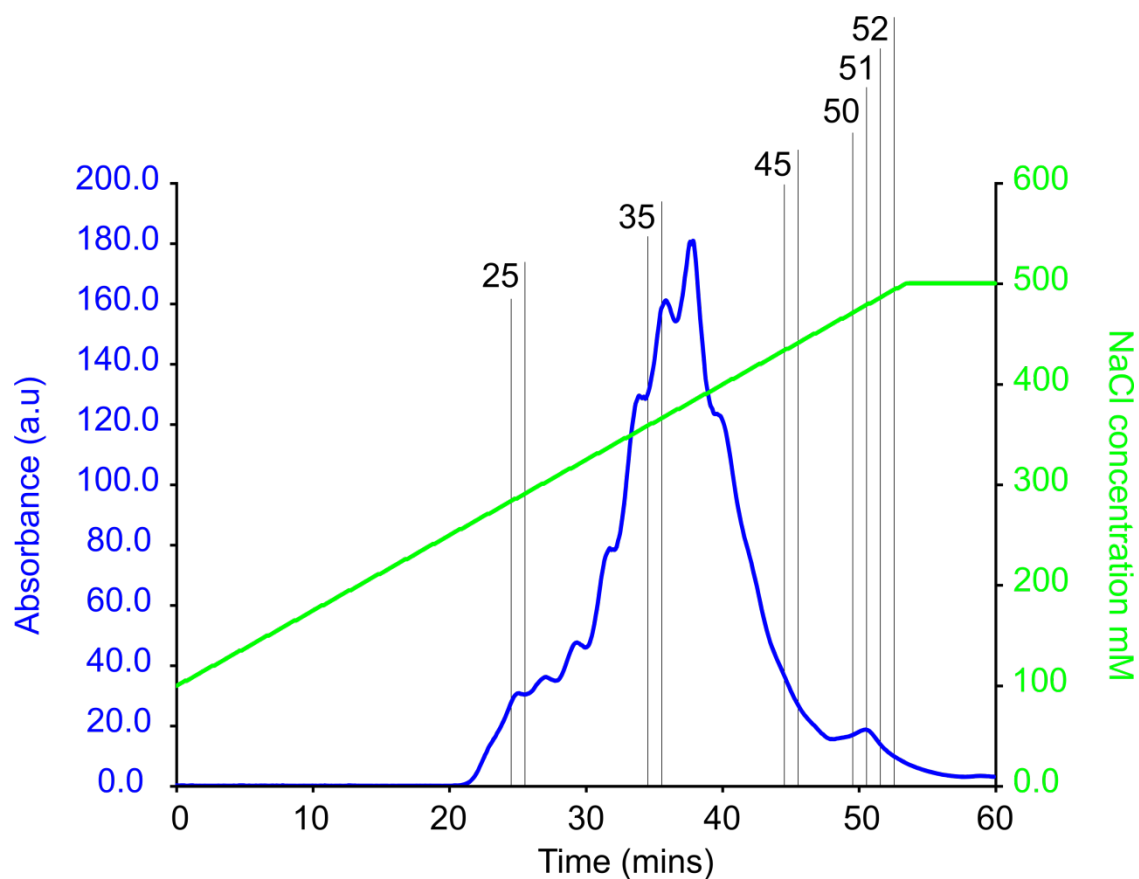


**Figure 5.3. Anion exchange of IsiA-PSI supercomplex.** A continuous NaCl gradient was run from 100 mM to 500 mM to elute protein from the anion exchange column with the eluate being collected in 1 ml fractions. Protein was detected eluting from the anion exchange column at a concentration of 260 mM NaCl and continued to elute until the end of the gradient. The time at which fractions; 25, 35, 45, 50, 51 and 52 were collected are shown.

**Table 5.1. Spectroscopic properties of anion exchange fractions.**

Fraction	Wavelength of PSI associated peak	$OD_{\text{PSI peak}} : OD_{280}$
25	673.0	2.37
30	673.0	2.72
35	673.0	2.72
40	673.0	2.61
45	673.0	2.57
50	673.0	0.91
51	676.0	1.14
52	680.0	2.52

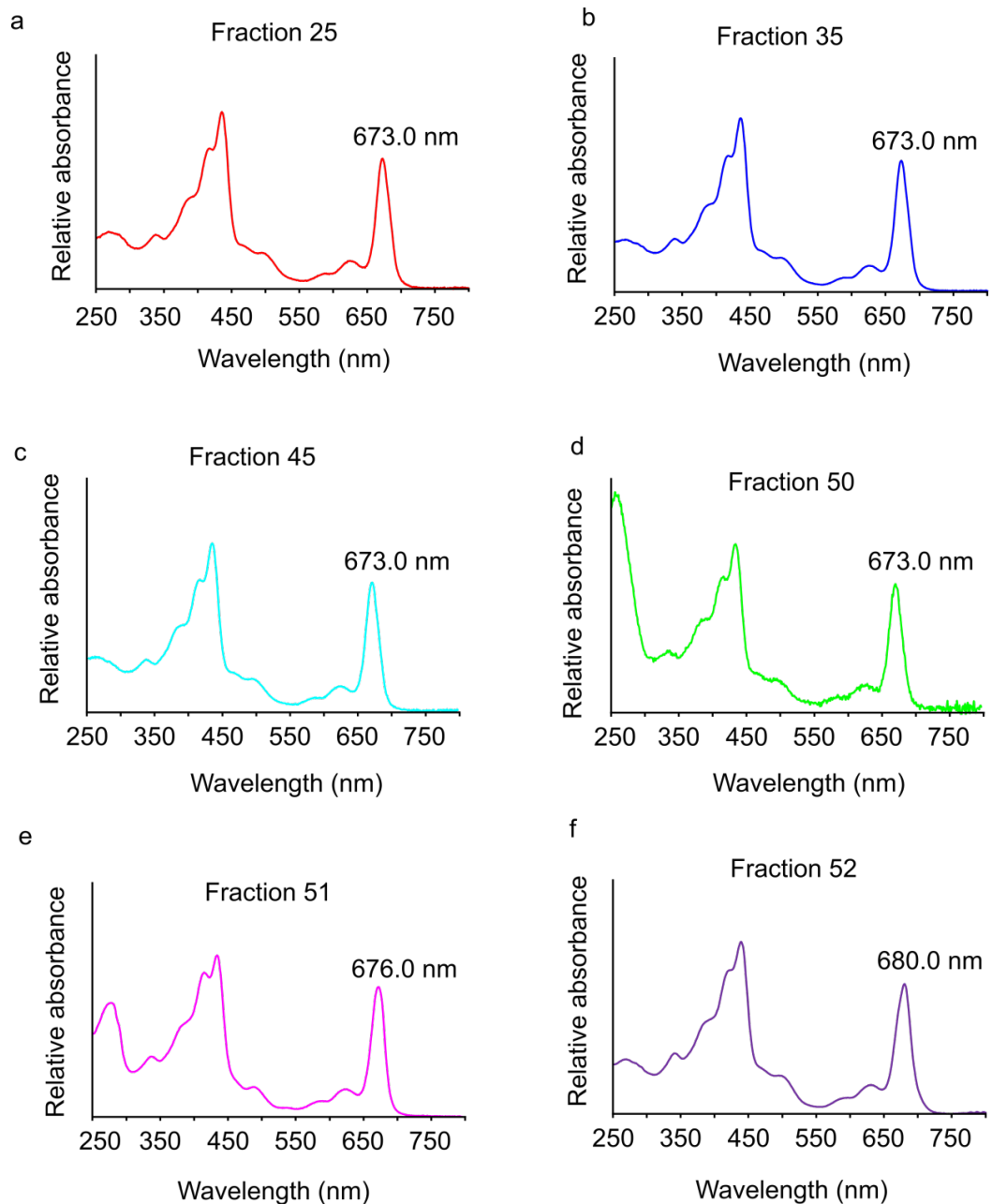


**Figure 5.4. Room temperature absorption spectra of anion exchange fractions. (a)** Fraction 25; **(b)**, fraction 35; **(c)**, fraction 45; **(d)**, fraction 50; **(e)**, fraction 51; **(f)**, fraction 52; The PSI-associated peak shifts from 673 nm to 680 nm in the last few fractions of the anion exchange purification. This indicates that the IsiA-PSI supercomplex is eluting prior to any PSI that was still present in the sample after the sucrose gradient purification. Spectra are normalised at the PSI-associated peak.

#### 5.3.4 Negative stain TEM and AFM of the anion exchange eluate

Negative stain TEM and AFM were used to approximate the abundance of the IsiA-PSI supercomplex in the pooled fractions from the anion exchange purification and also to determine if there was a significant level of contamination. Both negative stain TEM (**Figure 5.5a**) and AFM (**Figure 5.5b**) were able to identify the IsiA-PSI supercomplex from its size and in both cases significant background contamination could be imaged. The observed diameter of supercomplexes in the negative stain TEM data varied between 30 nm and 40 nm which is consistent with the diameter of 33.0 nm that was measured for the supercomplex in Bibby *et al.*, (2001a). The diameter of complexes in the AFM data was larger than expected with most complexes measuring between 40 nm and 50 nm although this increase in size can be attributed to tip convolution from probes that were not particularly “sharp”.

The contamination was believed to be protein as contaminating lipid structures such as membrane patches and micelles tend to have a diameter of greater than 50 nm and no such structures could be identified in TEM or AFM. It was clear that further purification of the IsiA-PSI supercomplex was required. As the IsiA-PSI supercomplex was by far the largest structure that could be identified, gel filtration was selected as the next purification step.

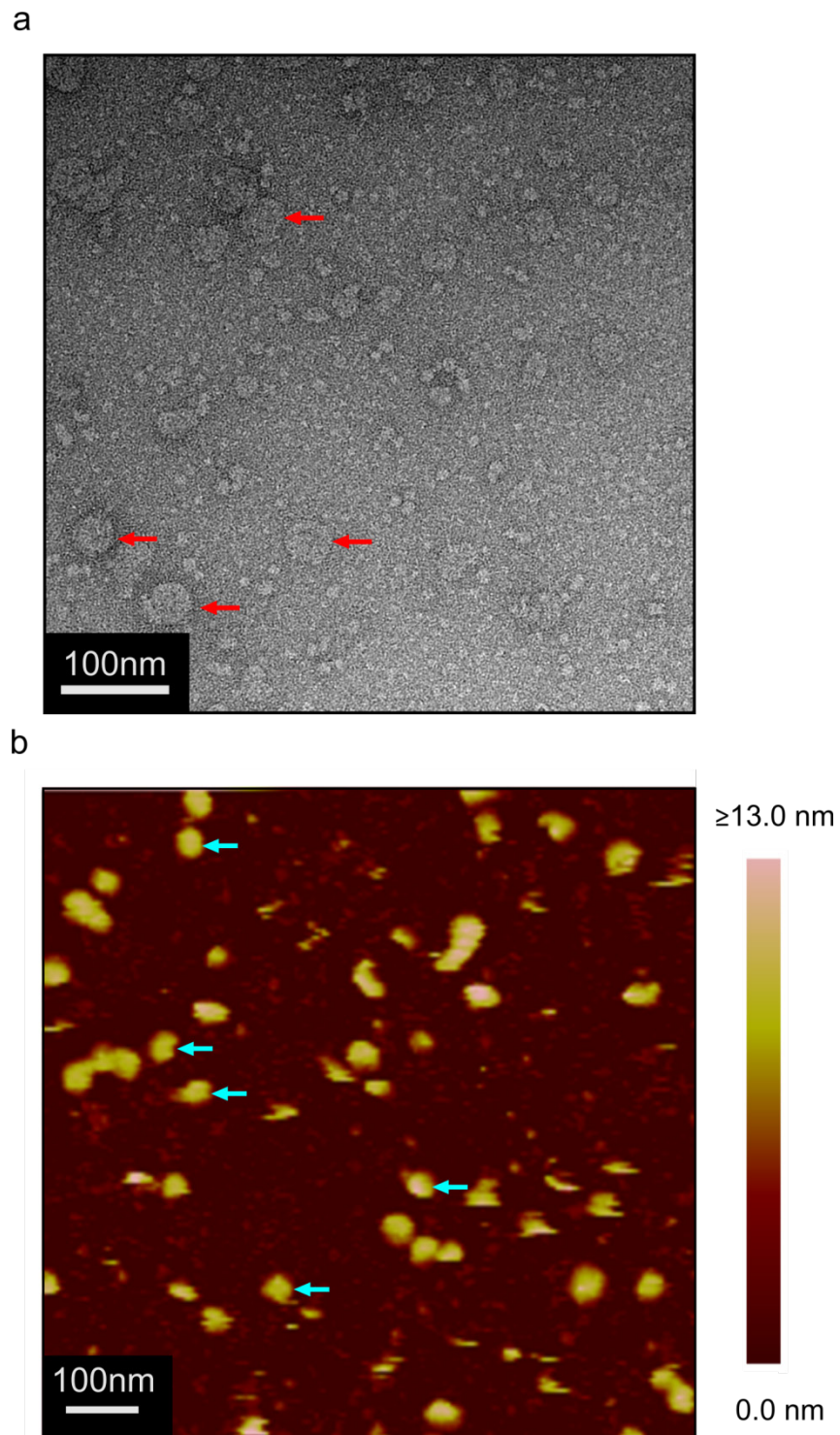


**Figure 5.5. AFM and negative stain TEM of IsiA-PSI complexes after anion exchange. (a)** IsiA-PSI supercomplexes (red arrows) can be visualised by TEM after purification by anion exchange. **(b)** Supercomplexes were also imaged by AFM (blue arrows) after anion exchange; a significant amount of contamination by what are believed to be smaller proteins can be observed in both images.

### 5.3.5 Gel filtration of the IsiA-PSI supercomplex

The IsiA-PSI supercomplex has a diameter of 33.0 nm (Bibby *et al.*, 2001a) which is very large for a protein complex and larger than any of the contamination that was observed in the TEM and AFM data. The eluate from the anion exchange column was further purified by gel filtration through the use of a BioSep SEC-s3000 column; this column was selected as it has a pore size of 29.0 nm. It was believed that the IsiA-PSI supercomplex would not be able to enter the beads in the column and instead it would pass straight through the column. The smaller contaminating protein would enter the gel filtration beads and its passage through the column would be retarded; this process should provide good separation between the IsiA-PSI supercomplex and the contaminating protein.

The concentrated anion exchange eluate was run on the gel filtration column which was set up as in **2.14.4** and 1 ml fractions were collected from 0 minutes to 30 minutes. The absorbance at 280 nm was measured and a large peak was detected eluting from the column after 10 minutes (**Figure 5.6a**) followed by three much smaller protein peaks (**Figure 5.6b**). The first peak was believed to represent the IsiA-PSI supercomplex which was confirmed by room temperature absorption spectra. The three later peaks had significantly lower absorbance at 280 nm than the first peak indicating that there was much less protein in these eluting from the column at this time. This could indicate that the gel filtration had not been very successful at purifying the IsiA-PSI supercomplex and that the majority of the contaminating protein had co-eluted with the IsiA-PSI supercomplex.

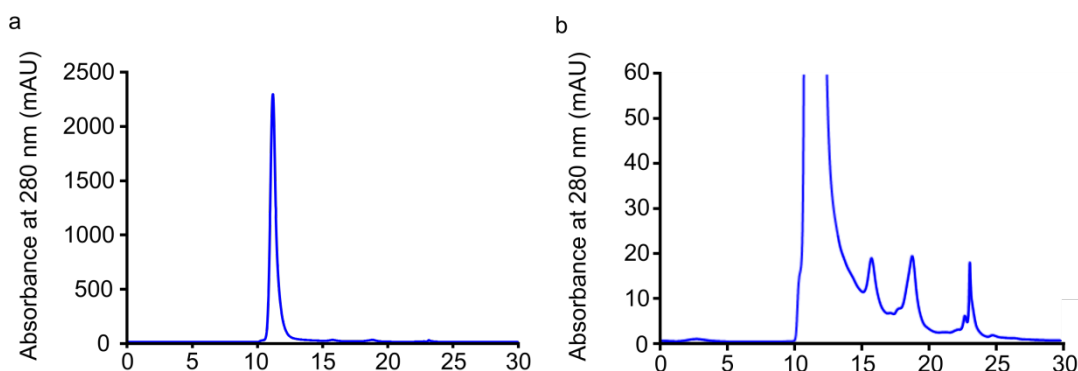


**Figure 5.6. Gel filtration of the IsiA-PSI supercomplex. (a)** Proteins with high molecular weight were seen to elute after 10 minutes which were believed to be the IsiA-PSI supercomplex. **(b)** By reducing the scale of the y-axis three much smaller peaks can be seen which were believed to represent the protein contamination seen in **Figure 5.5a** and **b**.

### 5.3.6 Negative stain TEM and AFM of the gel filtration eluate

Negative stain TEM and AFM were used to image the gel filtration eluate to determine the level to which gel filtration had removed the contaminating protein that was present after anion exchange. Negative stain TEM (**Figure 5.7**) showed a large reduction in the level of background contamination and the IsiA-PSI supercomplex can be seen clearly in **Figures 5.7a**. The staining of IsiA-PSI supercomplexes was of high quality and the trimeric PSI core can be observed in several particles in **Figure 5.7b**. In some cases individual IsiA proteins can be visualised in the ring surrounding the PSI core (**Figure 5.7c**). Particles were selected from the TEM images for single particle analysis to visualise the individual subunits of the IsiA-PSI supercomplex. In the averaged structure (**Figure 5.7d**) the trimeric PSI core is clearly visible; the 18 membered IsiA-PSI ring can also be seen in this image surrounding the PSI core.

The AFM data agreed with the TEM data showing a large reduction in the levels of background contamination (**Figure 5.8a**). The cross section of one of the particles (**Figure 5.8b**) gives a height of 9.4 nm which agrees with the predicted height for the IsiA-PSI supercomplex (Bibby *et al.*, 2001b). These data show that using gel filtration

as a purification step produces samples that are highly enriched in the IsiA-PSI supercomplex with minimal contamination. The heights of 50 particles were recorded and the average height of the supercomplex was found to be  $9.3 \pm 0.6$  nm; this value is consistent with the 3D cryo-EM map of the IsiA-PSI supercomplex described in Nield *et al.*, (2003)

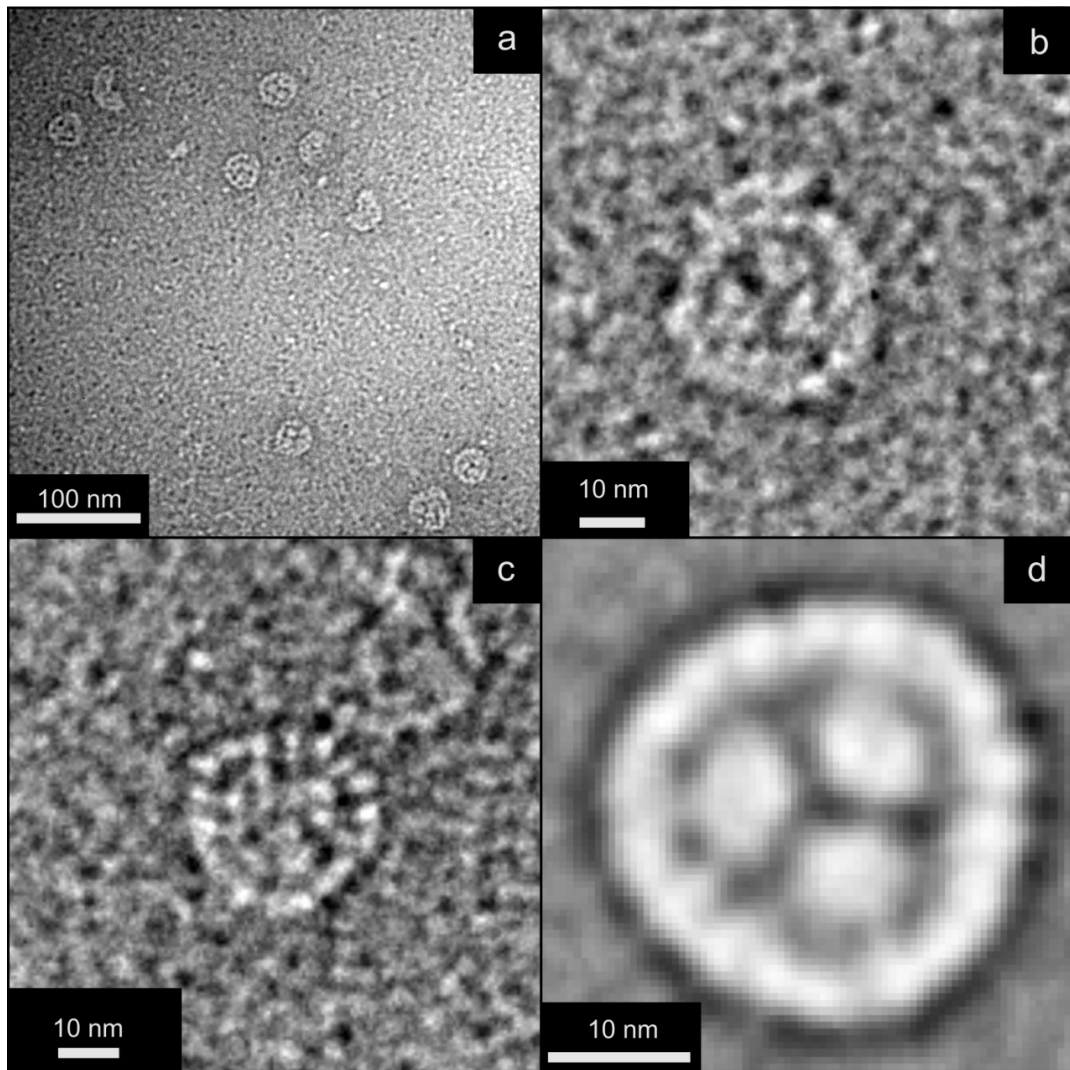


**Figure 5.7. Negative stain TEM of IsiA-PSI complexes after gel filtration. (a)** A field containing IsiA-PSI supercomplexes which have been purified by gel filtration is shown; the level of background contamination is greatly reduced relative to **Figure 5.5a**. **(b)** The trimeric PSI core can be clearly seen in some particles, **(c)** the IsiA proteins can be seen the ring surrounding the PSI core. **(d)** Single particle averaged image of the IsiA-PSI supercomplex; 52 particles were used for the image processing.

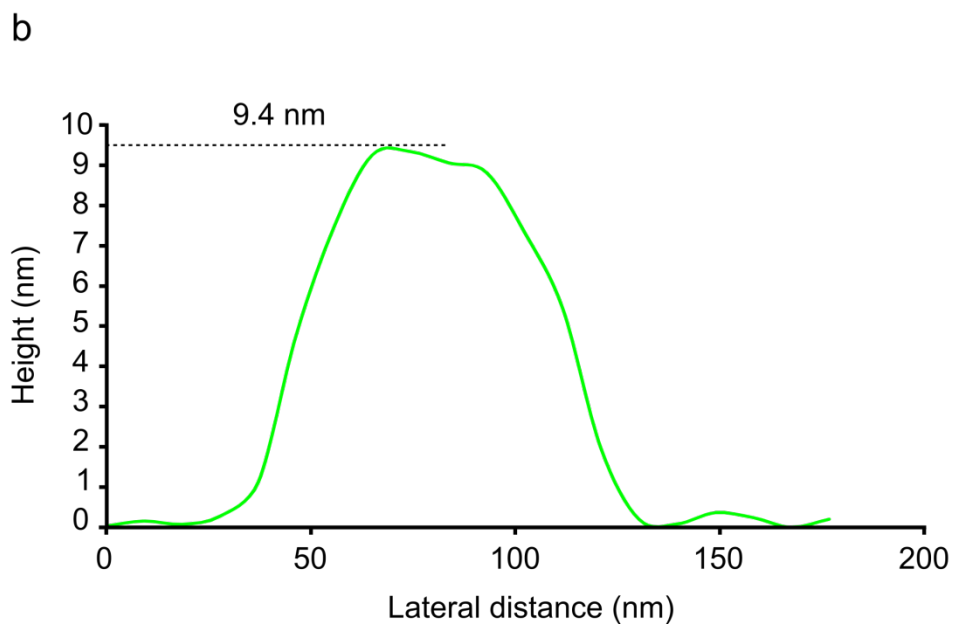
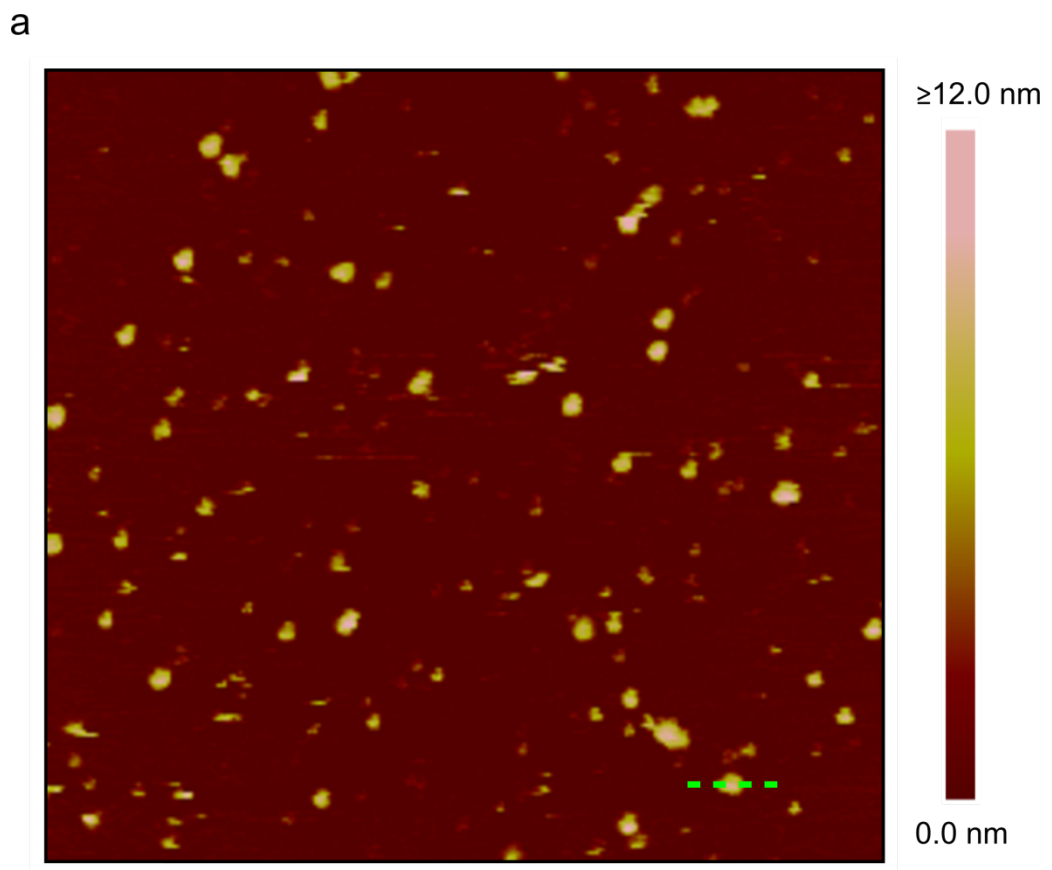


**Figure 5.8. AFM of IsiA-PSI complexes after gel filtration. (a)** IsiA-PSI supercomplexes purified by gel filtration imaged by AFM; the background contamination is significantly reduced relative to **Figure 5.5b**. **(b)** The measured height of 9.4 nm is consistent with the current structural model of the IsiA-PSI supercomplex (Nield *et al.*, 2003).

### 5.3.7 SDS-PAGE of IsiA-PSI samples

SDS-PAGE of samples from every step of the purification show how the IsiA-PSI supercomplex is purified for at each stage. The bands corresponding to the IsiA protein and the PsaA and PsaB subunits of PSI can be seen to become clearer after each purification step (**Figure 5.9**). The number of bands corresponding to contaminating protein is seen to decrease with each purification step (**Figure 5.9**) which validates their use.

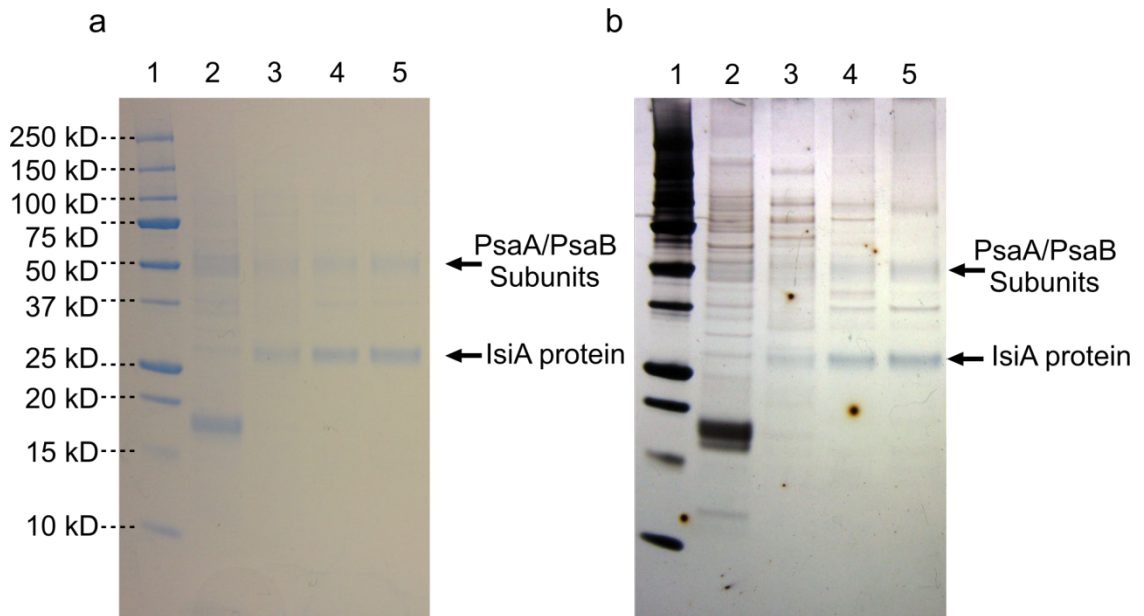


**Figure 5.9. (a) Coomassie stained and (b) silver stained SDS-PAGE of samples from all purification steps.** Lane 1, markers; lane 2, solubilised thylakoid membranes; lane 3, lower band from sucrose gradient; lane 4, pooled anion exchange eluate; lane 5, gel filtration eluate. The PsaA/PsaB band and the IsiA band become stronger with each purification step. 15  $\mu$ l of 1.0 OD<sub>280</sub> of each sample were loaded per lane.

### 5.3.8 Production of functionalised surfaces using RNIL

Master patterns with a line width of 150 nm and a period of 4  $\mu\text{m}$  (see **Figure 5.10**) were spin coated with a solution of polystyrene in toluene to produce masks that had a complementary shape to the master pattern. The mask was then floated off the surface of the master pattern and transferred to a piranha cleaned silicon wafer before being dried in a desiccator under vacuum. The polystyrene mask was split in the axis perpendicular to the direction of channels; this left the ends of the channels open in order to allow access to the compounds used to make the SAM. The split polystyrene mask was then transferred from the silicon wafer to a piranha cleaned glass substrate and dried in a desiccator overnight to allow the polystyrene mask to adhere to the surface of the glass. The channels in the mask left areas of the glass substrate exposed; this allowed the formation of a SAM in these areas of the substrate for the attachment of protein complexes by cross linking. The mask and glass substrate were then placed into a desiccator with 25  $\mu\text{l}$  of MPTMS and left under vacuum overnight to allow for the formation of a SAM of MPTMS through chemical vapour deposition. The polystyrene mask was then floated off the glass substrate which was then dried under a stream of nitrogen and placed into a solution of 15 mg/ml PEG-silane in toluene for 90 minutes. This allowed the formation of a SAM of PEG-silane between the MPTMS monolayers in order to minimise the adherence of protein complexes to these areas of the glass substrate (see **Figure 5.11**).

Glass was used as the substrate to produce nano-lines because photosystems were analysed using optical techniques (discussed later in this chapter); using opaque substrates, for example silicon, would make such analysis difficult as it does not transmit light and can quench the native fluorescence of photosynthetic protein complexes.

### 5.3.9 Immobilisation of IsiA-PSI supercomplexes on MPTMS nano-lines

The nanopatterns were treated with a solution of sulfosuccinimidyl 4-(*N*-maleimidomethyl)cyclohexane-1-carboxylate (sulfo-SMCC) in dry DMSO. Sulfo-SMCC is a crosslinker which can covalently link the amine groups of lysine residues in the protein complexes to the sulfhydryl groups exposed on the MPTMS SAM. A solution of the IsiA-PSI complex was applied to the nanopattern to bind the supercomplex to the sulfo-SMCC crosslinker. There are lysine residues present at both the luminal and stromal faces of the PSI complex meaning that the orientation of the IsiA-PSI supercomplex could not be controlled by this type of crosslinking. The nanopatterns of the IsiA-PSI supercomplex were then analysed by AFM.

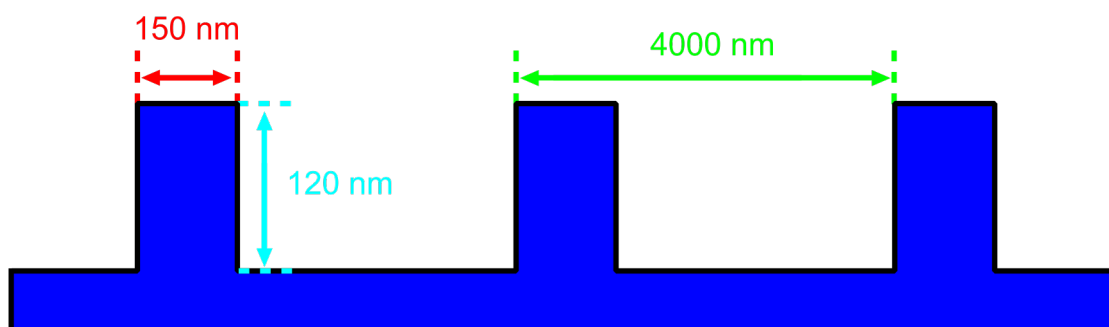


**Figure 5.10. Dimensions of the master pattern.** The master patterns were made by electron beam lithography on silicon substrates. The master pattern had a line width of 150 nm (red) and a period of 4000 nm (green). The nano-lines protruded from the silicon surface by 120 nm (light blue).

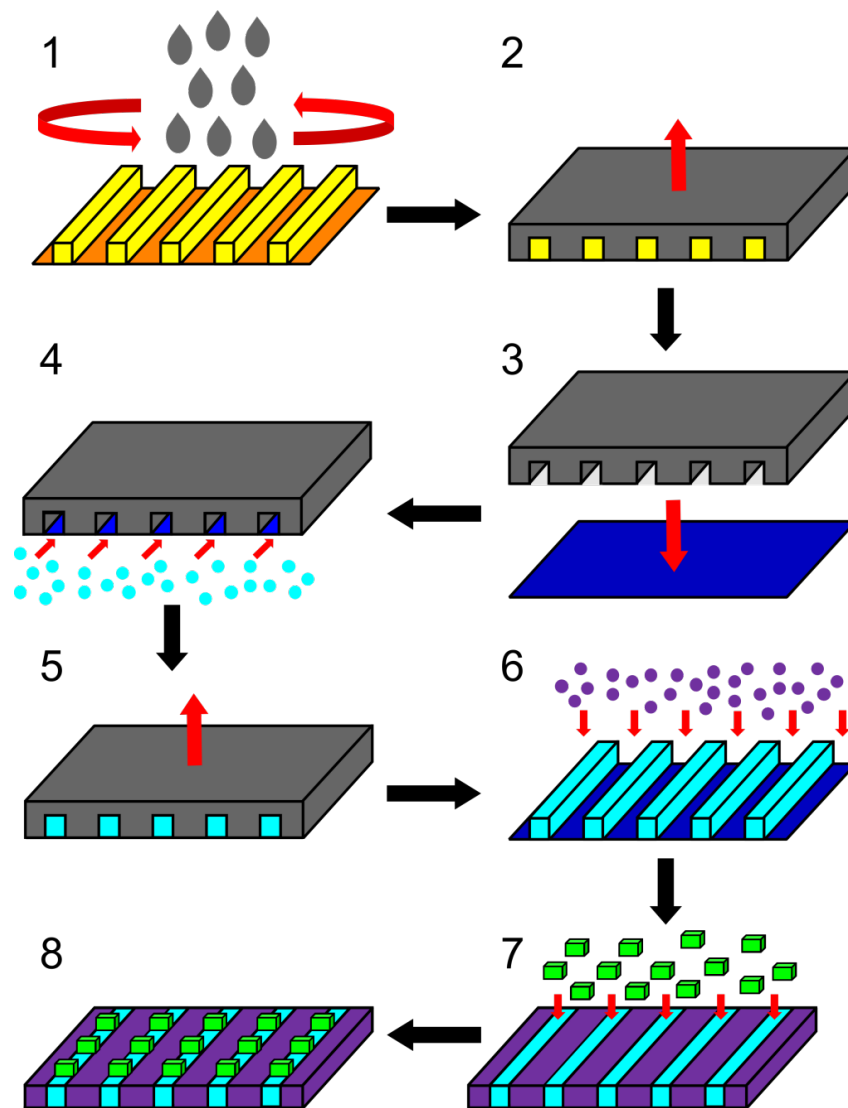


**Figure 5.11. Schematic for producing nano-lines of immobilised protein complexes using RNIL.** (1) The master pattern (orange and yellow) is spin-coated with a thin layer  $\approx 300$  nm thick) of polystyrene (grey) to make a polystyrene mask; (2) the polystyrene mask is then floated off the surface of the master pattern. (3) The polystyrene mask is then adsorbed to a glass substrate (dark blue) and dried under vacuum. (4) Once dry the mask and glass substrate are placed in a desiccator with MPTMS (light blue) which is left under vacuum overnight allowing the formation of an MPTMS SAM. (5) The polystyrene mask is then floated off the surface of the glass substrate. (6) The glass substrate is then placed in a solution of PEG-silane (purple) in toluene to allow for a SAM of PEG-silane to form in the areas of the glass which were previously in contact with the polystyrene mask. The glass substrate is then incubated with a solution of sulfo-SMCC (not shown) which forms a covalent linkage with the MPTMS SAM before (7) being incubated with a solution of protein complexes (green) (8) which are immobilised to the MPTMS SAM via the sulfo-SMCC crosslinker.

### 5.3.10 AFM of IsiA-PSI nanopatterns

IsiA-PSI supercomplexes were prepared as detailed in Chapter 5. Following immobilisation, AFM was used to image IsiA-PSI supercomplexes to assess the degree to which they had attached specifically to the MPTMS nano-lines and also to determine whether the supercomplex had adhered to the PEG-silane monolayers between the nano-lines. The biggest drawback to this form of imaging is that the maximum scan size for the instrument used is 15 x 15  $\mu\text{m}$  allowing only small areas of the total nanopattern to be imaged. It was possible to image several nano-lines and to demonstrate that protein complexes were immobilised, shown by the height data in **Figure 5.12b**. It was also clear that significantly lower levels of protein complexes were present on the PEG-silane monolayers between the nano-lines (**Figure 5.13**). The width of the nano-lines was 120-180 nm, consistent with the dimensions of the master pattern which has a line width of 150 nm (see **Figure 5.10**). This indicated the structure of the polystyrene mask was not being significantly damaged or deformed during the production of the nano-lines.

In some of the less densely packed areas of the nano-lines individual IsiA-PSI supercomplexes could be identified by their height above the MPTMS monolayer and the diameter of the particles (**Figure 5.13**). The heights of the supercomplexes in the nano-lines, measured by AFM, varied between 8.9 and 9.8 nm consistent with the previously measured height for the supercomplex in **5.3.6** which gave a height of between 9.0 and 10.5 nm (**Table 5.2**). The diameters of the supercomplexes in the nano-lines were measured to be between 35 and 45 nm (**Table 5.2**); these diameters are consistent with the diameters measured in **5.3.6** indicating that the IsiA-PSI supercomplexes were stable under imaging conditions.

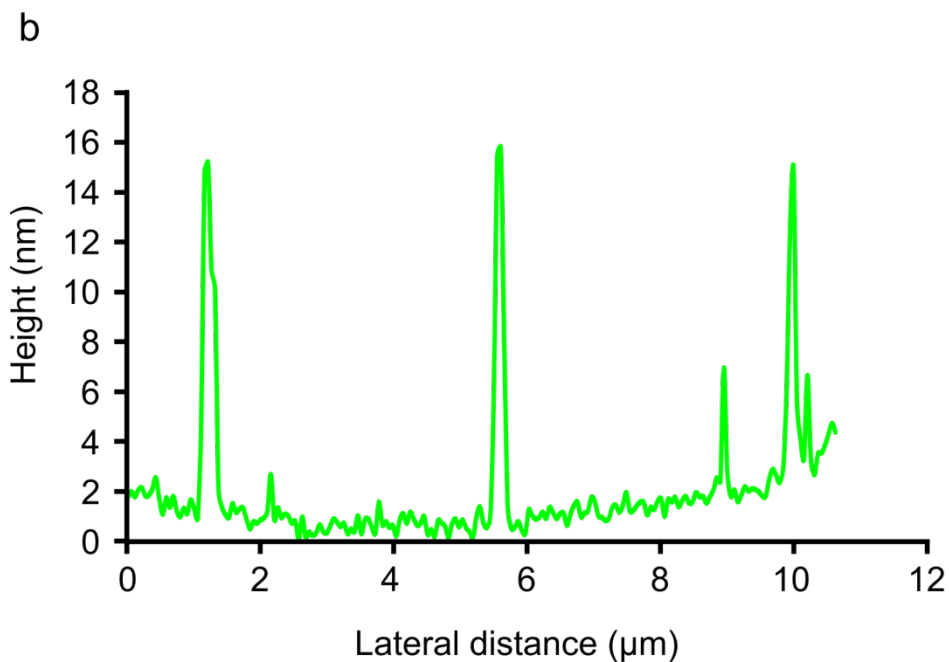
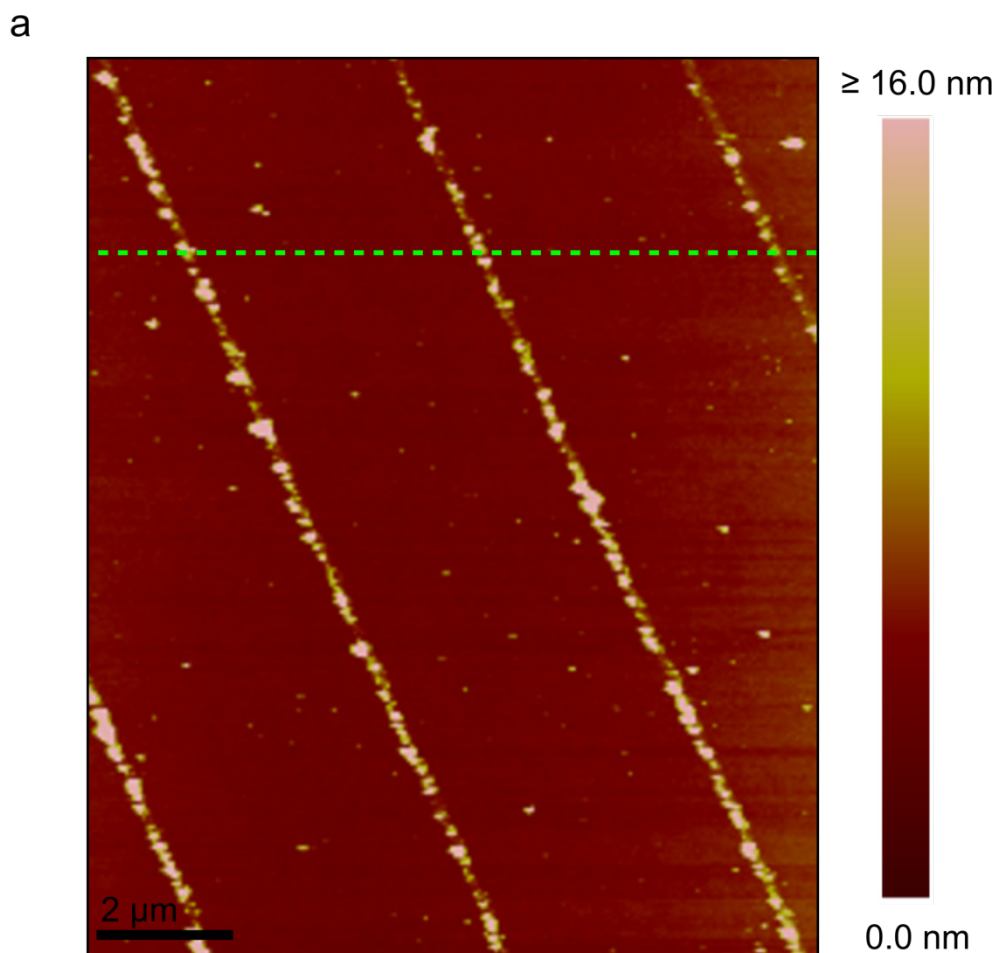


**Figure 5.12. AFM of IsiA-PSI nano-lines.** (a) Nanopatterns of IsiA-PSI supercomplexes were imaged with AFM showing an enrichment of protein complexes on the MPTMS nano-lines and very low levels of protein complexes on the PEG-silane monolayer. (b) The cross section gives the heights of the IsiA-PSI nano-lines.

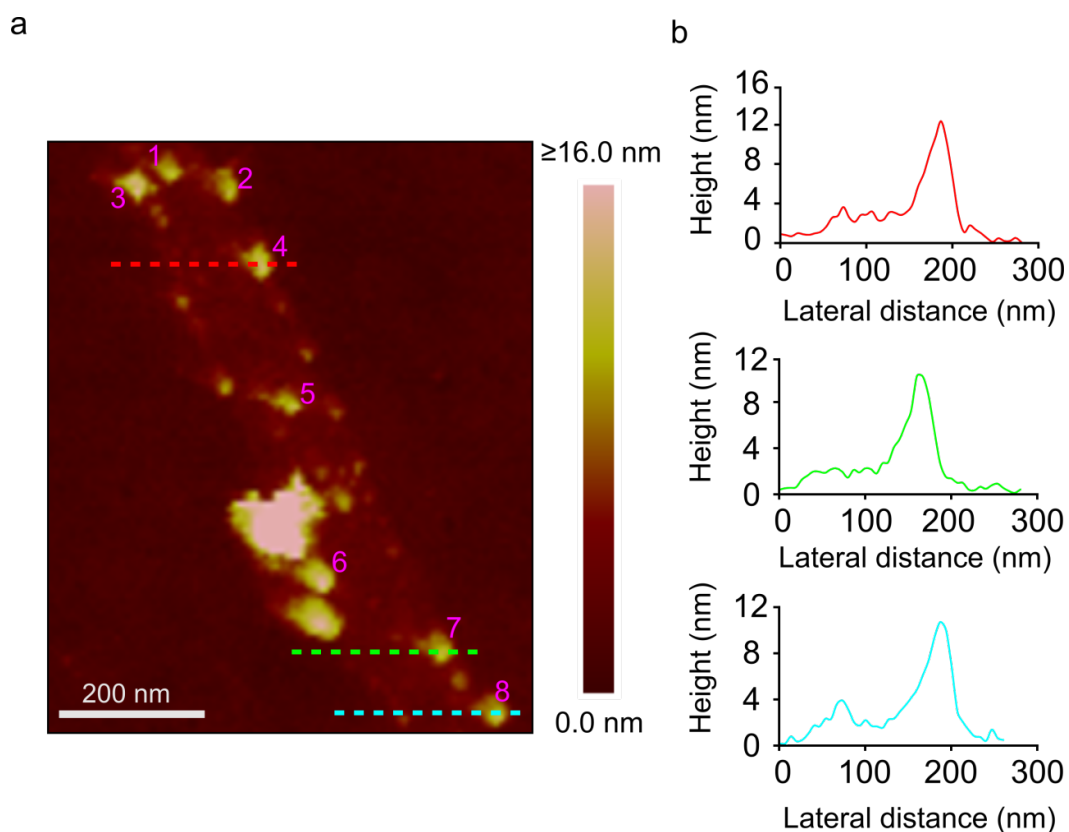


**Figure 5.13. AFM of individual IsiA-PSI supercomplexes on MPTMS nano-lines.**(a) AFM has been used to identify individual IsiA-PSI supercomplexes (numbered in pink); (b) the cross sections of complexes 4 (red), 7 (green) and 8 (blue) are shown.

**Table 5.2. Dimensions of IsiA-PSI supercomplexes.** The heights and diameters of the IsiA-PSI supercomplexes identified by AFM are presented here.

Complex number	Complex height (nm)	Complex diameter (nm)
1	9.3	39.0
2	10.0	36.6
3	10.4	38.5
4	9.8	41.4
5	9.6	36.6
6	10.3	43.9
7	8.9	41.0
8	9.3	39.2

### 5.3.11 Fluorescence imaging of IsiA-PSI nanopatterns

The IsiA-PSI supercomplex has a requirement to absorb light energy to drive charge separation; it is therefore important to determine if the supercomplex retains its spectroscopic properties after it has been immobilised on the MPTMS nano-lines. A home-built fluorescence microscope was used to image the IsiA-PSI supercomplex nano-lines; in addition the microscope was used to record spectral and time-resolved fluorescence data. Fluorescence microscopy revealed patterns over a distance of millimetres with the length of individual nano-lines in excess of 1 mm. The MPTMS nano-lines were highly enriched in IsiA-PSI supercomplexes with the PEG-silane monolayers having relatively little complex adhered to the surface (**Figure 5.14**).

Room temperature emission spectra of a solution of IsiA-PSI supercomplexes showed a peak at 680 nm (**Figure 5.14b**). To see if the IsiA-PSI supercomplexes had retained their fluorescent properties after immobilisation *in situ* room temperature emission spectra were recorded. Two regions on the nanopattern were selected; an IsiA-PSI nano-line and an area of PEG-silane monolayer (**Figure 5.14a**). The signal from the nano-line was significantly greater than that of the PEG-silane monolayer and there was a peak at 680 nm confirming the presence of the IsiA-PSI supercomplex and showing that it had retained its spectroscopic properties. The PEG-silane monolayer had no recognisable peak and a very low signal indicating that there were very low levels of IsiA-PSI supercomplexes present between the nano-lines.

The IsiA-PSI supercomplex nanopatterns were analysed using fluorescence-lifetime imaging to assess the functionality of the immobilised supercomplexes. The fluorescence-lifetime data were fitted with a single exponential decay curve which has an amplitude averaged lifetime of  $856 \pm 123$  ps (**Figure 5.14c**), significantly longer than the amplitude averaged lifetime of 40 ps for IsiA-PSI supercomplex in solution (Melkozernov *et al.*, 2003). This difference in the lifetimes indicates that immobilisation of IsiA-PSI supercomplexes is affecting their functionality, although the noise in the data precludes any identification of a fast component in the decay curves.

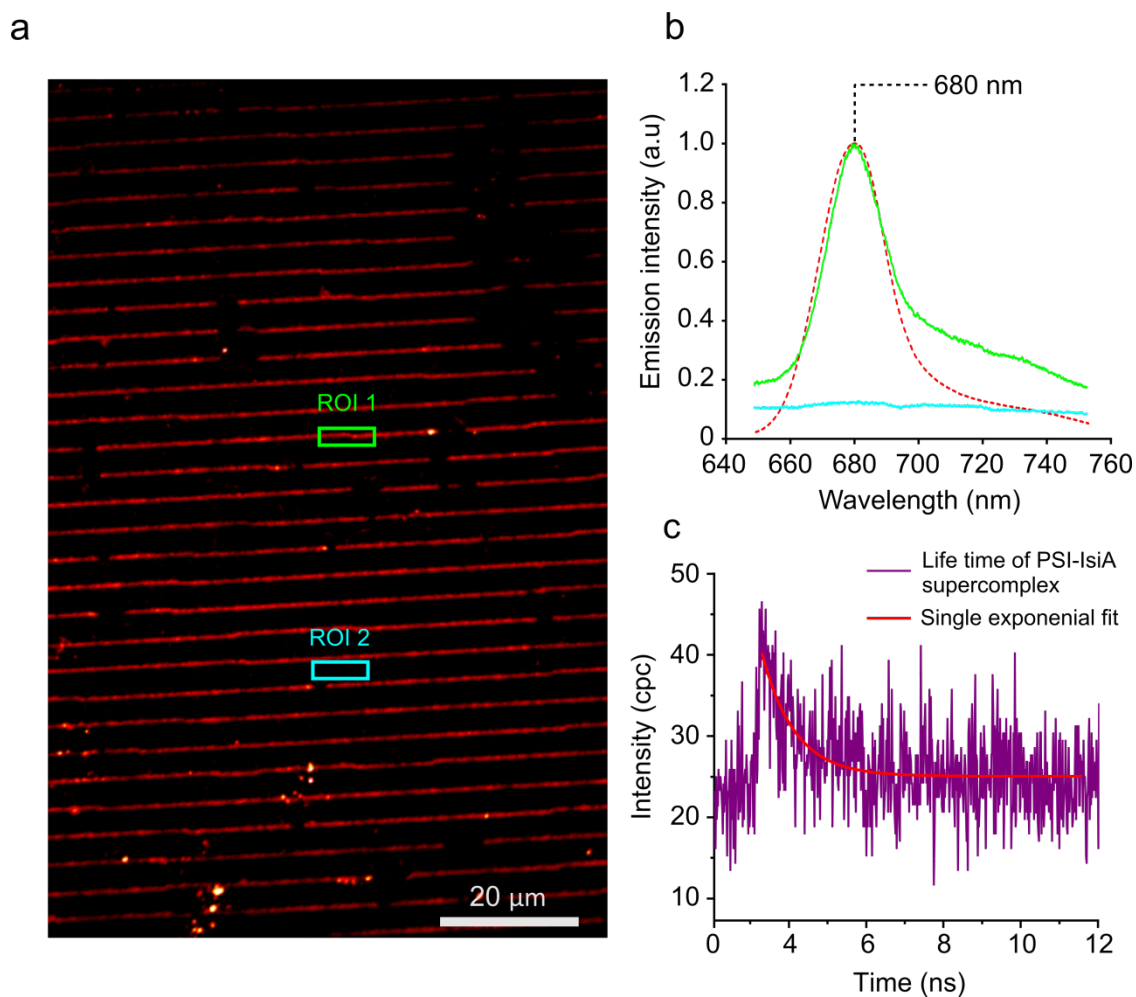


**Figure 5.14. Fluorescence microscopy, room temperature emission spectra and fluorescence lifetime imaging of IsiA-PSI nanopatterns.** (a) Fluorescence microscopy of IsiA-PSI nanopatterns shows nano-lines of the immobilised complexes extending over a large area. (b) *In situ* emission spectra were taken in two areas of the nanopattern; in region of interest 1 (ROI1) (green rectangle in a) an emission spectrum was taken for IsiA-PSI supercomplexes immobilised on an MTPMS nano-line. The spectrum from ROI1 (green spectrum) was very similar to the room temperature emission spectrum taken of IsiA-PSI supercomplexes in solution (dotted red spectrum) both of which have a peak at 680 nm. As a control an emission spectrum was taken for ROI2 (blue rectangle in a) which was an area of PEG-silane monolayer between two nano-lines. The spectrum (blue spectrum) had a relatively low signal with no discernible peaks. (c) Fluorescence-lifetime data of the nano-lines in ROI1 were fitted with a single exponential decay curve that, giving amplitude averaged lifetime of  $856 \pm 123$  ps. The excitation wavelength was selected with a 470/40 nm bandpass filter; the detection wavelength was selected with a monochromator centred at 680 nm with exit slits set to 15 nm.

### 5.3.12 Immobilisation of PSII complexes on MPTMS nano-lines

Samples of PSII complexes from *Thermosynechococcus elongatus* of the purity required to routinely produce 3D crystals for structure determination (Ferreira *et al.*, 2004) were kindly provided by Dr. Karim Maghlaoui. PSII complexes were purified from thylakoid membranes through hydrophobic interaction chromatography followed by anion exchange chromatography. Purified PSII complexes were analysed by SDS-PAGE to show the purity of the sample (**Figure 5.15**). Bands from several PSII subunits can be visualised in the gel with no clear bands present from contamination. PSII complexes were immobilised on nanopatterns made using the same method as in **5.3.9**, using sulfo-SMCC as a crosslinker between the lysine residues in the PSII complex and the sulfhydryl groups on the MPTMS SAM. Owing to the presence of lysine residues on both the stromal and luminal faces of the PSII complex, their surface orientation cannot be controlled using this method of crosslinking.

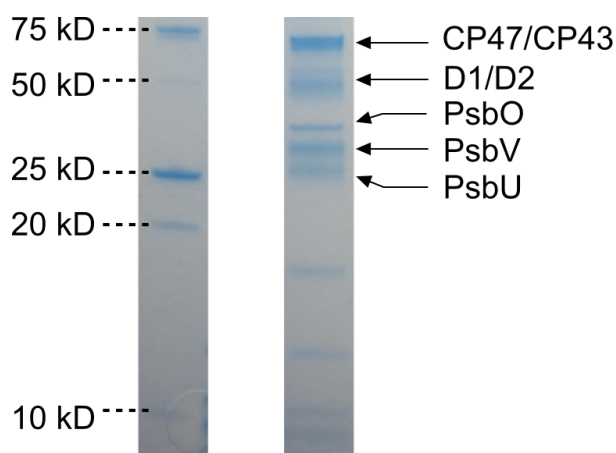


**Figure 5.15. Coomassie stained SDS-PAGE of purified PSII complexes.** Bands from several subunits of the PSII complex can be identified their comparison with the marker lane.

### 5.3.13 AFM of PSII nanopatterns

As with the IsiA-PSI supercomplex nano-lines could be imaged using AFM showing PSII complexes immobilised on the MPTMS nano-lines and relatively low levels of protein complexes bound to the PEG-silane monolayer regions **Figure 5.16**. Interestingly the width of the nano-lines was significantly larger than expected, at 150 nm; the maximum and minimum widths measured were 500 nm and 450 nm respectively. The distance between the nano-lines was measured to be between 3.50 and 3.55  $\mu\text{M}$ , less than the 3.85  $\mu\text{M}$  period of the master pattern. These measurements indicated that the polystyrene mask did not accurately reflect the dimensions of the master pattern; however the mask did have channels that were of consistent width and spacing. The packing of complexes on the nano-lines is relatively dense but it is still possible to image individual protein complexes (**Figure 5.17**). Some structures had lateral and vertical dimensions similar to those of the PSII dimers; cross sections were taken of 3 particles in **Figure 5.18**. The measured heights of the three particles above the surface of the MPTMS monolayer varied from 9.0 to 12.3 nm which was slightly different to the height of 10.5 nm expected from the crystal structure (Umena *et al.*, 2011). The glass substrate and the MPTMS monolayer are not atomically flat and protein complexes have to be measured from the area of the MPTMS monolayer that is directly adjacent to them. This area may not be of the same height as the area of the monolayer that the complexes are attached to. This variation in the height of the surface is believed to be responsible for the measured heights of the protein complexes not matching the crystal structure, rather than breakdown of the PSII protein complex.

The dimeric PSII complex has lateral dimensions of 20.5 x 11 nm giving a length:width ratio of 1.86; the length and width measurements for the particles in **Figure 5.18** can be seen in **Table 5.3**. The length:width ratio of the selected particles varies from 1.70 to 1.84, which is consistent with the length:width ratio of PSII. Although the absolute values for the length and width are somewhat larger than expected for PSII, these increased values are believed to be the result of imaging the complexes with a relatively blunt AFM probe, and these particles are therefore assigned as PSII dimers.

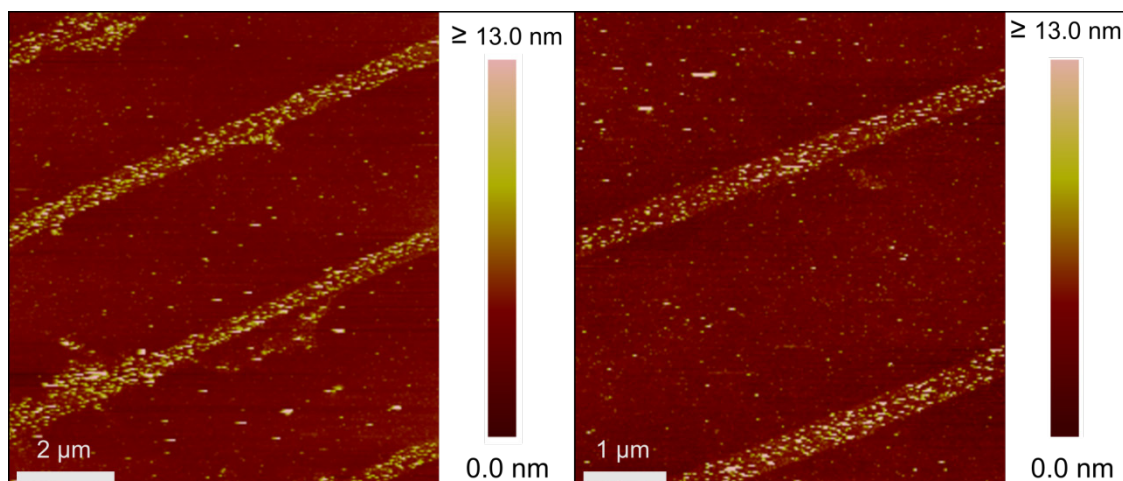
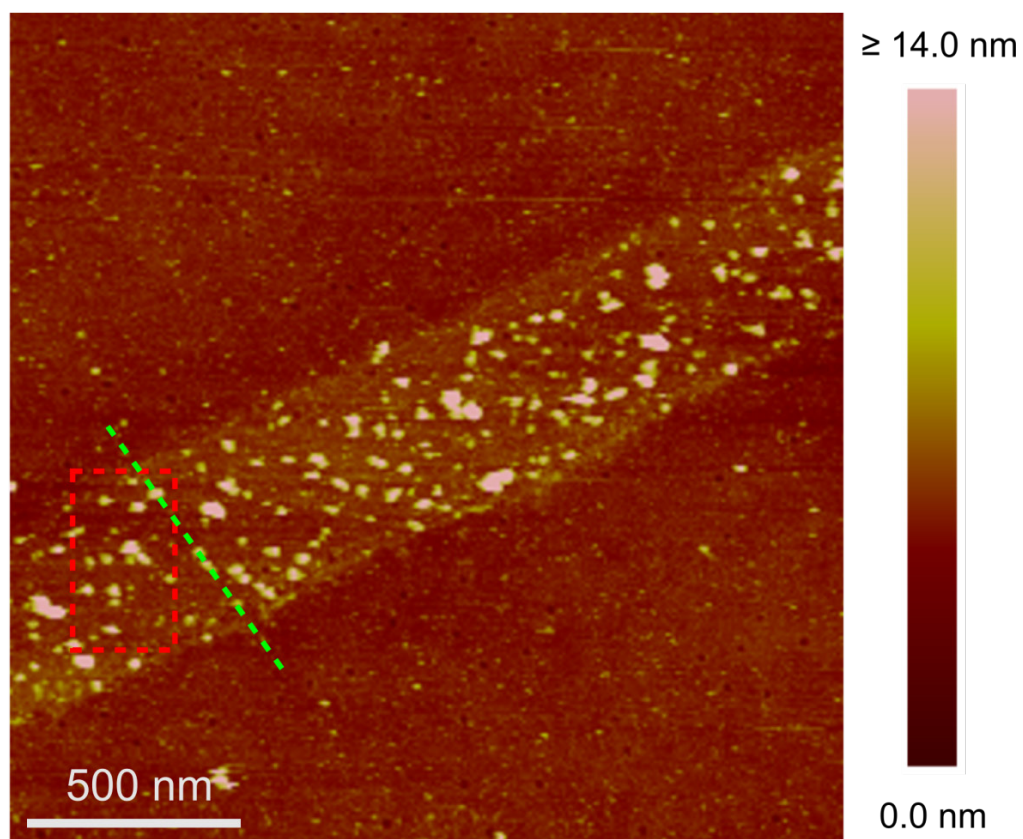


**Figure 5.16. AFM of PSII nano-lines.** Several MPTMS nano-lines on which PSII complexes had been immobilised could be imaged with AFM. The nano-lines were highly enriched in PSII complexes with relatively little contamination of the PEG-silane monolayer.

a



b

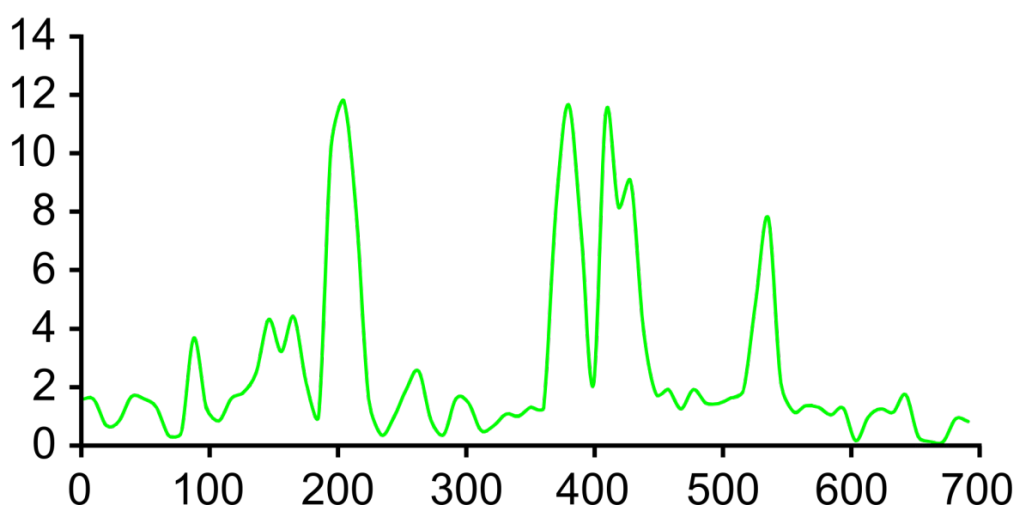


**Figure 5.17. AFM of a single PSII nano-line. (a)** Higher resolution AFM revealed the presence of individual particles on the nano-lines; the nano-line itself was thicker than expected with a line width of 450-500 nm. **(b)** The cross section of the nano-line (shown in green in **a**) revealed the heights of the particles to be consistent with PSII complexes. The area highlighted in red is shown in **Figure 5.18** at higher magnification.

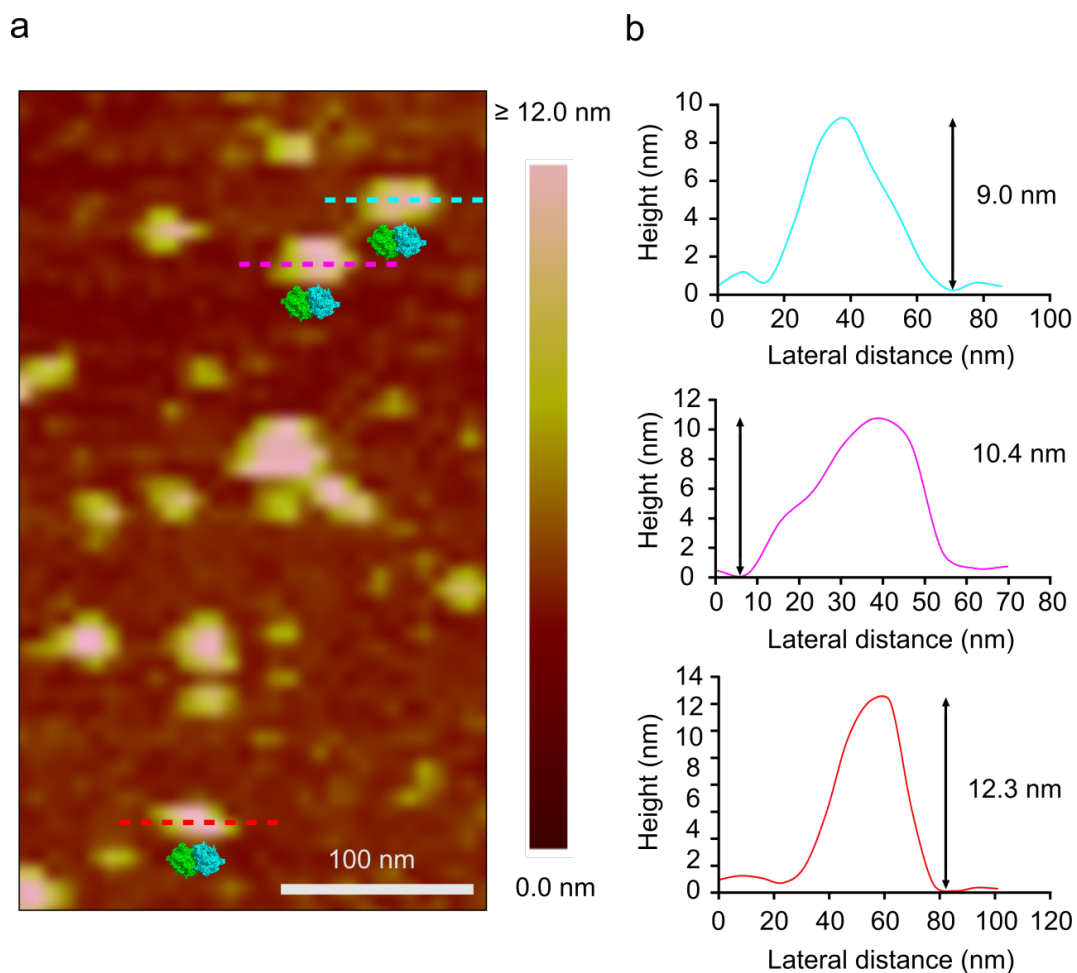


**Figure 5.18. AFM of potential PSII dimers immobilised on MPTMS nano-lines. (a)** Individual particles could be imaged that had dimensions similar to that of the PSII dimer; a scaled version of the dimeric PSII crystal structure is shown next to the putative PSII complexes for reference. **(b)** Cross sections of three particles revealed the height of the particles to be consistent with that of the PSII complex which is 10.5 nm.

**Table 5.3. Measurements of complexes in Figure 5.18.** The lengths and widths of three particles from Figure 5.18 and their respective length:width ratio.

Complex	Complex length (nm)	Complex width (nm)	length:width ratio
Blue	35.4	20.0	1.77
Pink	38.0	22.4	1.70
Red	34.5	18.8	1.84

### 5.3.14 Fluorescence imaging of PSII nanopatterns

Fluorescence microscopy of the PSII nanopatterns (**Figure 5.19a**) has shown that the nanopatterns extend over an area of millimetres and individual lines can have a length of over a millimetre. As with the IsiA-PSI supercomplex, PSII absorbs light to drive charge separation and it was therefore important to see if PSII complexes retained their spectral properties after immobilisation on the MPTMS monolayer. Room temperature emission spectra of the PSII complexes in solution revealed the presence of a peak at 681 nm (**Figure 5.19b**). An *in situ* room temperature emission spectrum was taken of a PSII nano-line to determine if the spectral properties of the complexes were unchanged; an emission spectrum was also recorded for an area of PEG-silane monolayer as a control (**Figure 5.19b**). In the emission spectrum from the PSII nano-line a peak was present at 681 nm, consistent with the emission spectrum taken of complexes in solution and indicates that PSII complexes had retained their spectroscopic characteristics after immobilisation. Additionally the emission spectrum of the PEG-silane monolayer had a relatively low signal with no discernible peaks indicating that there were very low levels of PSII in these areas of the nanopattern.

The PSII nanopatterns were analysed via fluorescence-lifetime imaging to determine whether the lifetime of the immobilised complex was comparable to that of PSII complexes in solution (**Figure 5.19c**). Fluorescence-lifetime data of the PSII nanopatterns were fitted with a single exponential decay curve which gave an amplitude averaged lifetime of  $199 \pm 10$  ps. This time is slightly longer than the amplitude averaged lifetime of PSII in solution which has been measured at 176 ps (Schatz *et al.*, 1988) however it shows that the PSII complex has retained its spectroscopic properties after it has been immobilised.

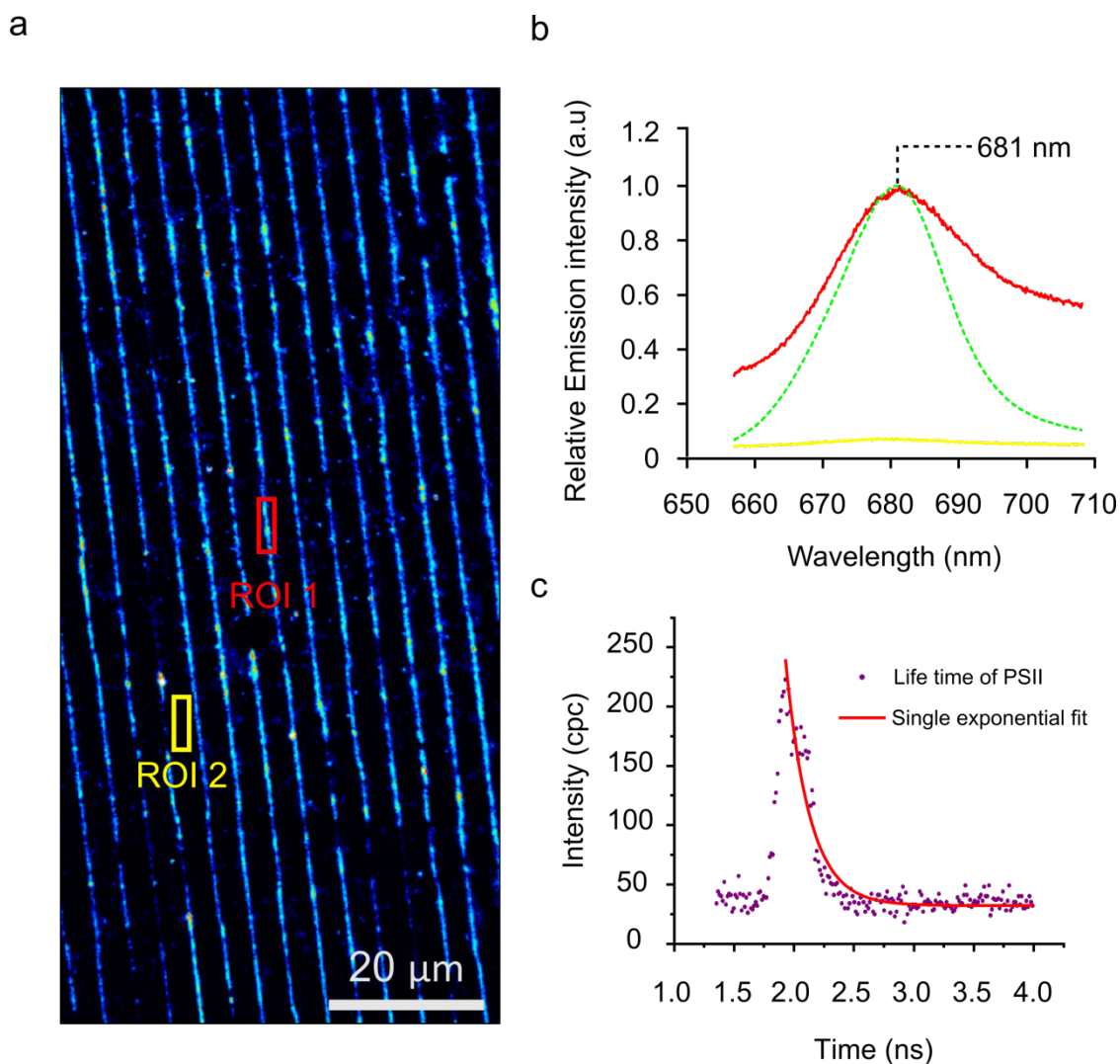


**Figure 5.19. Fluorescence microscopy, room temperature emission spectra and fluorescence lifetime imaging of PSII nanopatterns.** (a) PSII nanopatterns imaged by fluorescence microscopy revealed a relatively large area where PSII complexes had been immobilised on MPTMS nano-lines with minimal contamination of the PEG-silane monolayer. (b) *In situ* emission spectra were taken in two areas in the nanopattern; in region of interest 1 (ROI1) (red rectangle in a) an emission spectrum was taken for PSII complexes immobilised on an MPTMS nano-line (red spectrum). The spectrum from ROI1 was very similar to a room temperature emission spectrum taken of PSII complexes in solution (green dotted spectrum), both having a peak at 681 nm. As a control an emission spectrum was recorded for ROI2 (yellow rectangle a) which was an area of PEG-silane monolayer between two nano-lines. The spectrum (yellow spectrum) had relatively low signal with no discernible peaks. (c) The fluorescence-lifetime data of PSII nano-lines in ROI1 were fitted with a single exponential decay curve, showing an amplitude averaged lifetime of  $199 \pm 10$  ps. The excitation wavelength was selected with a 470/40 nm bandpass filter; the detection wavelength was selected with a monochromator centred at 680 nm with exit slits set to 15 nm.

## 5.4 Discussion

Sucrose gradients were useful in producing large volumes of the IsiA-PSI supercomplex and as an initial purification step. SDS-PAGE of supercomplexes purified on sucrose gradients and the solubilised membrane loading material show significantly fewer protein bands in the former; however there was still significant contamination indicating that further purification was required.

Purifying the sample harvested from the sucrose gradients on an anion exchange column appeared to allow for the removal of residual PSI trimers that the sucrose gradient had not removed. This was evidenced by the shift in the PSI-associated peak from 673.0 nm to 680.0 nm in the later fractions indicating that the PSI trimer eluted from the anion exchange column at a higher NaCl concentration than the IsiA-PSI supercomplex. The purity of the sample had also improved with the IsiA protein band being the strongest in the SDS-PAGE of the anion exchange eluate. The absence of many of the bands representing contaminating protein in the SDS-PAGE also evidenced the increased purity of the anion exchange eluate relative to the sample harvested from sucrose gradient. The TEM and AFM data (**Figure 5.5**) revealed the presence of what were believed to be small protein contaminants in the fractions of the anion exchange eluate that contained the IsiA-PSI supercomplex. The contamination was believed to be great enough to require a further purification step before IsiA-PSI supercomplexes could be used for the purposes of nanopatterning.

The IsiA-PSI supercomplex was by far the largest structure that could be observed by either AFM or TEM; therefore using a purification technique that discriminated by size such as gel filtration was the next logical step for purifying the supercomplex. The elution of a large amount of protein about 10 minutes after the sample was loaded onto the gel filtration column was expected as the IsiA-PSI supercomplex should not enter the gel filtration beads and instead elute in the void volume. The presence of three peaks in the elution trace that were very small in relation to the initial peak was unexpected as the amount of contaminating protein seen in the TEM and AFM data appeared to similar to the level of the IsiA-PSI supercomplex. It would therefore

follow that if the gel filtration column was separating the smaller contaminating protein from the IsiA-PSI supercomplex the peaks corresponding to the contaminating protein would be of comparable size to the peak corresponding to the supercomplex. The absence of such peaks was initially believed to show that the gel filtration had been unsuccessful in removing the smaller contaminating proteins. TEM and AFM analysis of the gel filtration eluate revealed that the majority of the small contaminating protein had in fact been removed from the sample. SDS-PAGE of the gel filtration fractions containing the IsiA-PSI supercomplex agreed with the AFM and TEM data, showing a reduced number of bands corresponding to contaminating protein and an enrichment of the IsiA protein and PsaA/PsaB bands. One possible explanation for the lack of peaks representing contaminating protein in the gel filtration elution trace is that the smaller protein simply did not elute from the gel filtration column. After gel filtration the sample was believed to be pure enough for the purposes of nanopatterning the IsiA-PSI supercomplex.

The staining of the IsiA-PSI supercomplexes purified by gel filtration was of high quality; through TEM imaging the PSI trimer could be observed in many particles and occasionally individual IsiA subunits could be observed in the ring surrounding the PSI trimer. Through single particle reconstruction using selected particles from TEM images it was possible to resolve the PSI trimer and the 18 membered IsiA ring; the structure was consistent with that described in Bibby *et al.*, (2001a) and Boekema *et al.*, (2001).

There are no reports of the IsiA-PSI supercomplex being imaged by AFM; previous studies have used single particle reconstruction of TEM and cryo-TEM data to resolve the structure of the IsiA-PSI supercomplex. The IsiA-PSI supercomplex has a tendency to adhere to the carbons grids used to mount samples in TEM analysis with the luminal face of the supercomplex in contact with the grid and the stromal face exposed. This property makes it challenging to get accurate height data for the supercomplex using TEM. The height data is the most reliable measurement recorded by the AFM making it an ideal tool for assessing the height of the IsiA-PSI supercomplex. AFM imaging also has the advantage that the supercomplex is in buffer conditions close to that of its native environment and at room temperature.

The average height of  $9.3 \pm 0.6$  nm is consistent with the 3D cryo-EM model described in Nield *et al.*, (2003) and supports the accuracy of this model. These data also indicate that the low temperatures used for imaging the IsiA-PSI supercomplex in constructing the 3D model had a negligible effect on the height of the supercomplex.

RNIL was very successful at producing nanopatterns of SAMs that could be used to direct the immobilisation of cyanobacterial photosystems. AFM of the IsiA-PSI supercomplex nanopatterns revealed nano-lines with dimensions consistent with those of the master patterns with a line width of approximately 150 nm and a period of 4  $\mu$ m. The AFM data of PSII nanopatterns showed line widths of approximately 500 nm, much larger than the master pattern. One possible explanation for this is that the method used to produce the master patterns, electron beam lithography, does not always produce patterns that are consistent over their entire area. Some protrusions can be significantly thicker or thinner than the desired width which will correspond to variations in the thickness of nano-lines that are imaged. Another possible explanation for the difference in line width is that the master patterns are damaged during cleaning. Piranha solution was used to remove any contamination from the surface of the master patterns prior to spin coating with polystyrene. Whilst piranha solution has only a very slightly corrosive effect on silicon, repeated cleaning could have resulted in degradation and widening of the ridges in the master pattern.

Using sulfo-SMCC as a crosslinker for covalently attaching protein complexes to the MPTMS monolayer proved to be very effective. The occupancy of the MPTMS nano-lines appeared to be very high in both the IsiA-PSI and the PSII nanopatterns when imaged by fluorescence microscopy. High resolution AFM revealed that areas in the IsiA-PSI nanopatterns were of low occupancy where individual complexes could be visualised. Imaging the PSII nanopatterns at high resolution with AFM showed they were not as highly occupied as might be assumed from the fluorescence data. Whilst there are a significant number of PSII complexes present on the nano-line there are also relatively large gaps between complexes where the MPTMS monolayer can be imaged. The use of PEG-silane as a protein resistant monolayer was sufficient to

prevent significant adherence of protein complexes to the areas between the nano-lines. AFM was the best tool for investigating the level of protein complexes adhered to the PEG-silane monolayer as any protein present on the surface was large enough for even a relatively “blunt” AFM probe to register a height profile. Topological features, presumably protein, could still be imaged in the PEG-silane areas of both the IsiA-PSI and PSII nanopatterns, but relative to the MPTMS nano-lines these regions of the pattern were effectively devoid of complexes.

Fluorescence microscopy of the nanopatterns was consistent with the AFM data, showing nano-lines that had high fluorescence and the areas of PEG-silane monolayer that had a much lower fluorescence. This was seen over the majority of the nanopattern indicating that the AFM data was representative of the entire nanopattern with protein complexes being enriched on the MPTMS nano-lines and having relatively little presence on the PEG-silane monolayer.

One of the main goals when patterning photosynthetic protein complexes is to ensure they retain their spectroscopic activity. The room temperature fluorescence emission spectrum of IsiA-PSI nano-lines was consistent with the fluorescence emission spectrum of IsiA-PSI supercomplexes in solution with a peak at 680 nm. Nanopatterned PSII complexes also had a similar room temperature emission spectrum to complexes in solution with a peak at 681 nm. This data was encouraging as it suggested that the two photosystems had not been damaged or inactivated by the cross linking reaction and were stable at room temperature.

Previous studies of PSII complexes in solution have shown that their fluorescence decay is biexponential; the lifetimes of the two decay curves are  $80 \pm 20$  ps and  $520 \pm 120$  ps (Schatz *et al.*, 1987) indicating that there is more than one route for absorbed energy to be emitted as fluorescence. The amplitude averaged fluorescence lifetime of PSII complexes in solution has been measured to be 177 ps (Schatz *et al.*, 1988). Whilst the data in the present study were not of sufficient quality to resolve the two exponential components of the decay curve, the amplitude averaged fluorescence lifetime was measured at  $199 \pm 10$  ps. The slight difference in the value of the lifetime measurement is not significant and could reflect different methods of

preparation, or conformational changes in the structure of the PSII complex induced by its immobilisation on the MTPMS monolayer. Taken together, the time-resolved and fluorescence emission data show that the immobilised PSII complexes retain their spectroscopic properties following surface immobilisation.

In the case of the IsiA-PSI supercomplex nano-lines, the measured value of the fluorescence lifetime of  $856 \pm 123$  ps was much larger than anticipated. Previous work on IsiA-PSI complexes from *Synechocystis* has shown the fluorescence decay has a number of exponential components (Melkozernov *et al.*, 2003), with a dominant  $43 \pm 4$  ps component having a relative amplitude of 94-96 %; this decay is attributed to the overall loss of excitation in the antenna chlorophylls of the IsiA-PSI supercomplex due to charge separation. One possible reason for the measured value of the lifetime being significantly higher than expected is that the complex is unable to perform charge separation. This seems unlikely as the PSI trimer has been shown to generate photocurrent after immobilisation (Frolov *et al.*, 2005; Gerster *et al.*, 2012). A more likely explanation would be that the level of uncoupled pigment is greater in the immobilised supercomplex than when in solution. It has been shown that the exponential components that correspond to uncoupled pigments in the PSI trimer and the IsiA-PSI supercomplex have relatively long lifetimes, typically in the region of 3-5 ns (Turconi *et al.*, 1996; Melkozernov *et al.*, 2003). For complexes in solution the amplitudes of these components are relatively low (typically less than 5 %) and thus do not have a much of an effect on the amplitude averaged lifetime of the IsiA-PSI supercomplex (Melkozernov *et al.*, 2003). A small increase in the number of uncoupled pigment molecules would cause a large increase in the amplitude averaged lifetime which would explain why the lifetime measured for immobilised IsiA-PSI supercomplexes is larger than expected. Better quality data will have to be obtained before any conclusions can be drawn regarding amplitudes and lifetimes.

To confirm the immobilised IsiA-PSI supercomplexes are functionally active, the capacity for nanopatterned supercomplexes to generate photocurrent in response to illumination could be investigated using a method such as conductive AFM. As individual IsiA-PSI supercomplexes could be imaged by AFM in the nanopatterns it would be possible to measure the photocurrent produced by a single supercomplex. It

would also be interesting to see if PSII could generate photocurrent in response to light using the same technique.

Another possible direction for this work would be to co-pattern antenna complexes such as phycobilisomes with the reaction centres using a similar method as (Vasilev *et al.*, 2014) to see if it is possible to transfer energy between the two immobilised complexes. This would be particularly interesting in the case of PSII as it relies on phycobilisomes to provide to the majority of the energy to drive charge separation *in vivo*. By using master patterns with different dimensions it would be possible to alter the ratio of immobilised reaction centres to antenna complexes and see what effect this has on energy transfer between the two complexes and whether it affects the production of photocurrent.

## References

- Acharya, K., Zazubovich, V., Reppert, M., Jankowiak, R., (2012). Primary electron donor(s) in isolated reaction center of photosystem II from *Chlamydomonas reinhardtii*. *J. Phys. Chem. B* **116**, 4860–4870.
- Adams, P.G., Hunter, C.N., (2012). Adaptation of intracytoplasmic membranes to altered light intensity in *Rhodobacter sphaeroides*. *Biochimica et Biophysica Acta (BBA)-Bioenergetics*. **1817**, 1616–1627.
- Addlesee, H.A., Hunter, C.N., (1999). Physical mapping and functional assignment of the geranylgeranyl-bacteriochlorophyll reductase gene, *bchP*, of *Rhodobacter sphaeroides*. *J. Bacteriol.* **181**, 7248–7255.
- Albertsson, P.-Å., (2001). A quantitative model of the domain structure of the photosynthetic membrane. *Trends Plant Sci.* **6**, 349–354.
- Anderson, S.L., McIntosh, L., (1991). Light-activated heterotrophic growth of the cyanobacterium *Synechocystis* sp. strain PCC 6803: a blue-light-requiring process. *J. Bacteriol.* **173**, 2761–2767.
- Andrizhiyevskaya, E.G., Schwabe, T.M., Germano, M., D’Haene, S., Kruij, J., van Grondelle, R., Dekker, J.P., (2002). Spectroscopic properties of PSI–IsiA supercomplexes from the cyanobacterium *Synechococcus* PCC 7942. *Biochim. Biophys. Acta BBA-Bioenerg.* **1556**, 265–272.
- Andrizhiyevskaya, E.G., Chojnicka, A., Bautista, J.A., Diner, B.A., van Grondelle, R., Dekker, J.P., (2005) Origin of the F685 and F695 fluorescence in photosystem II. *Photosynth. Res.* **84**, 173–180
- Armstrong, G.A., (1994). Eubacteria show their true colors: genetics of carotenoid pigment biosynthesis from microbes to plants. *J. Bacteriol.* **176**, 4795–4802.

Armstrong, G.A., (1997). Genetics of eubacterial carotenoid biosynthesis: a colorful tale. *Annu. Rev. Microbiol.* **51**, 629–659.

Arteni, A.A., Ajlani, G., Boekema, E.J., (2009). Structural organisation of phycobilisomes from *Synechocystis* sp. strain PCC6803 and their interaction with the membrane. *Biochimica et Biophysica Acta (BBA)-Bioenergetics.* **1787**, 272–279.

Bahatyrova, S., Frese, R.N., Siebert, C.A., Olsen, J.D., van der Werf, K.O., van Grondelle, R., Niederman, R.A., Bullough, P.A., Otto, C., Hunter, C.N., (2004). The native architecture of a photosynthetic membrane. *Nature* **430**, 1058–1062.

Battersby, A.R., Fookes, C.J., Matcham, G.W., McDonald, E., Hollenstein, R., (1983). Biosynthesis of porphyrins and related macrocycles. Part 20. Purification of deaminase and studies on its mode of action. *J Chem Soc Perkin Trans* **1** 3031–3040.

Beale, S.I., (1993). Biosynthesis of phycobilins. *Chem. Rev.* **93**, 785–802.

Bibby, T.S., Nield, J., Barber, J., (2001a). Iron deficiency induces the formation of an antenna ring around trimeric photosystem I in cyanobacteria. *Nature* **412**, 743–745.

Bibby, T.S., Nield, J., Barber, J., (2001b). Three-dimensional model and characterization of the iron stress-induced CP43-photosystem I supercomplex isolated from the cyanobacterium *Synechocystis* PCC 6803. *J. Biol. Chem.* **276**, 43246–43252.

Blankenship, R.E., (2002). Molecular mechanisms of photosynthesis,. Blackwell Publishing: Oxford.

Boehm, M., Romero, E., Reisinger, V., Yu, J., Komenda, J., Eichacker, L.A., Dekker, J.P., Nixon, P.J., (2011). Investigating the Early Stages of Photosystem II Assembly in *Synechocystis* sp. PCC 6803 ISOLATION OF CP47 AND CP43 COMPLEXES. *J. Biol. Chem.* **286**, 14812–14819.

Boekema, E.J., Hifney, A., Yakushevskaya, A.E., Piotrowski, M., Keegstra, W., Berry, S., Michel, K.-P., Pistorius, E.K., Kruijff, J., (2001). A giant chlorophyll–protein complex induced by iron deficiency in cyanobacteria. *Nature* **412**, 745–748.

Bollivar, D.W., Wang, S., Allen, J.P., Bauer, C.E., (1994). Molecular genetic analysis of terminal steps in bacteriochlorophyll *a* biosynthesis: characterization of a *Rhodobacter capsulatus* strain that synthesizes geranylgeraniol-esterified bacteriochlorophyll *a*. *Biochemistry (Mosc.)* **33**, 12763–12768.

Brecht, M., Radics, V., Nieder, J.B., Bittl, R., (2009). Protein dynamics-induced variation of excitation energy transfer pathways. *Proc. Natl. Acad. Sci.* **106**, 11857–11861.

Brown, S.B., Houghton, J.D., Vernon, D.I., (1990). New trends in photobiology biosynthesis of phycobilins. Formation of the chromophore of phytochrome, phycocyanin and phycoerythrin. *J. Photochem. Photobiol. B* **5**, 3–23.

Cardona, T., Sedoud, A., Cox, N., Rutherford, A.W., (2012). Charge separation in photosystem II: a comparative and evolutionary overview. *Biochimica et Biophysica Acta (BBA)-Bioenergetics.* **1817**, 26–43.

Cartron, M.L., Olsen, J.D., Sener, M., Jackson, P.J., Brindley, A.A., Qian, P., Dickman, M.J., Leggett, G.J., Schulten, K., Neil Hunter, C., (2014). Integration of energy and electron transfer processes in the photosynthetic membrane of *Rhodobacter sphaeroides*. *Biochimica et Biophysica Acta (BBA)-Bioenergetics.*

Chen, M., Schliep, M., Willows, R.D., Cai, Z.-L., Neilan, B.A., Scheer, H., (2010). A red-shifted chlorophyll. *Science* **329**, 1318–1319.

Chitnis, V.P., Chitnis, P.R., (1993). PsaL subunit is required for the formation of photosystem I trimers in the cyanobacterium *Synechocystis* sp. PCC 6803. *FEBS Lett.* **336**, 330–334.

Cogdell, R.J., Frank, H.A., (1987). How carotenoids function in photosynthetic bacteria. *Biochim. Biophys. Acta BBA-Rev. Bioenerg.* **895**, 63–79.

Crockett, N., Alefounder, P.R., Battersby, A.R., Abell, C., (1991). Uroporphyrinogen III synthase: studies on its mechanism of action, molecular biology and biochemistry. *Tetrahedron* **47**, 6003–6014.

Dammeyer, T., Frankenberg-Dinkel, N., (2006). Insights into phycoerythrobilin biosynthesis point toward metabolic channeling. *J. Biol. Chem.* **281**, 27081–27089.

Dobáková, M., Tichý, M., Komenda, J., (2007). Role of the Psbl protein in photosystem II assembly and repair in the cyanobacterium *Synechocystis* sp. PCC 6803. *Plant Physiol.* **145**, 1681–1691.

Dühring, U., Irrgang, K.-D., Lünser, K., Kehr, J., Wilde, A., (2006). Analysis of photosynthetic complexes from a cyanobacterial *ycf37* mutant. *Biochimica et Biophysica Acta (BBA)-Bioenergetics.* **1757**, 3–11.

Dühring, U., Ossenbühl, F., Wilde, A., (2007). Late assembly steps and dynamics of the cyanobacterial photosystem I. *J. Biol. Chem.* **282**, 10915–10921.

Escalante, M., Maury, P., Bruinink, C.M., van der Werf, K., Olsen, J.D., Timney, J.A., Huskens, J., Hunter, C.N., Subramaniam, V., Otto, C., (2008). Directed assembly of functional light harvesting antenna complexes onto chemically patterned surfaces. *Nanotechnology* **19**, 025101.

Falconnet, D., Pasqui, D., Park, S., Eckert, R., Schiff, H., Gobrecht, J., Barbucci, R., Textor, M., (2004). A novel approach to produce protein nanopatterns by combining nanoimprint lithography and molecular self-assembly. *Nano Lett.* **4**, 1909–1914.

Farah, J., Rappaport, F., Choquet, Y., Joliot, P., Rochaix, J.D., (1995). Isolation of a *psaF*-deficient mutant of *Chlamydomonas reinhardtii*: efficient interaction of

plastocyanin with the photosystem I reaction center is mediated by the PsaF subunit. *EMBO J.* **14**, 4976.

Ferreira, K.N., Iverson, T.M., Maghlaoui, K., Barber, J., Iwata, S., (2004). Architecture of the photosynthetic oxygen-evolving center. *Science* **303**, 1831–1838.

Folea, I.M., Zhang, P., Aro, E.-M., Boekema, E.J., (2008a). Domain organization of photosystem II in membranes of the cyanobacterium *Synechocystis* PCC6803 investigated by electron microscopy. *FEBS Lett.* **582**, 1749–1754.

Folea, I.M., Zhang, P., Nowaczyk, M.M., Ogawa, T., Aro, E.-M., Boekema, E.J., (2008b). Single particle analysis of thylakoid proteins from *Thermosynechococcus elongatus* and *Synechocystis* 6803: localization of the CupA subunit of NDH-1. *FEBS Lett.* **582**, 249–254

Foote, C.S., 1976. Photosensitized oxidation and singlet oxygen: consequences in biological systems. *Free Radic. Biol.* **2**, 85–133.

Fotiadis, D., Qian, P., Philippsen, A., Bullough, P.A., Engel, A., Hunter, C.N., (2004). Structural analysis of the reaction center light-harvesting complex I photosynthetic core complex of *Rhodospirillum rubrum* using atomic force microscopy. *J. Biol. Chem.* **279**, 2063–2068.

Frolov, L., Rosenwaks, Y., Carmeli, C., Carmeli, I., (2005). Fabrication of a photoelectronic device by direct chemical binding of the photosynthetic reaction center protein to metal surfaces. *Adv. Mater.* **17**, 2434–2437.

Fujita, Y., Murakami, A., (1987). Regulation of electron transport composition in cyanobacterial photosynthetic system: stoichiometry among photosystem I and II complexes and their light-harvesting antennae and cytochrome *b<sub>6</sub>f* complex. *Plant Cell Physiol.* **28**, 1547–1553.

Gerster, D., Reichert, J., Bi, H., Barth, J.V., Kaniber, S.M., Holleitner, A.W., Visoly-Fisher, I., Sergani, S., Carmeli, I., (2012). Photocurrent of a single photosynthetic protein. *Nat. Nanotechnol.* **7**, 673–676.

Giddings, T.H., Wasmann, C., Staehelin, L.A., (1983). Structure of the thylakoids and envelope membranes of the cyanelles of *Cyanophora paradoxa*. *Plant Physiol.* **71**, 409–419.

Grigorieva, G., Shestakov, S., (1982). Transformation in the cyanobacterium *Synechocystis* sp. 6803. *FEMS Microbiol. Lett.* **13**, 367–370.

Hagiwara, Y., Sugishima, M., Takahashi, Y., Fukuyama, K., (2006). Crystal structure of phycocyanobilin: ferredoxin oxidoreductase in complex with biliverdin IX $\alpha$ , a key enzyme in the biosynthesis of phycocyanobilin. *Proc. Natl. Acad. Sci. U. S. A.* **103**, 27–32.

Hermoso, J.A., Mayoral, T., Faro, M., Gómez-Moreno, C., Sanz-Aparicio, J., Medina, M., (2002). Mechanism of Coenzyme Recognition and Binding Revealed by Crystal Structure Analysis of Ferredoxin–NADP<sup>+</sup> Reductase Complexed with NADP<sup>+</sup>. *J. Mol. Biol.* **319**, 1133–1142.

Horton, P., Ruban, A.V., Walters, R.G., (1996). Regulation of light harvesting in green plants. *Annu. Rev. Plant Biol.* **47**, 655–684.

Johnson, M.P., Vasilev, C., Olsen, J.D., Hunter, C.N., (2014). Nanodomains of Cytochrome *b<sub>6</sub>f* and Photosystem II Complexes in Spinach Grana Thylakoid Membranes. *Plant Cell Online* tpc.114.127233. doi:10.1105/tpc.114.127233

Jordan, P., Fromme, P., Witt, H.T., Klukas, O., Saenger, W., Krauss, N., (2001). Three-dimensional structure of cyanobacterial photosystem I at 2.5 Å resolution. *Nature* **411**, 909–917.

Jordan, P.M., (1991). The biosynthesis of 5-aminolaevulinic acid and its transformation into uroporphyrinogen III. Biosynth. *Tetrapyrroles* 1–66.

Kamran, M., Delgado, J.D., Friebe, V., Aartsma, T.J., Frese, R.N., (2014). Photosynthetic Protein Complexes as Bio-photovoltaic Building Blocks Retaining a High Internal Quantum Efficiency. *Biomacromolecules* **15**, 2833–2838.

Kaneko, T., Tabata, S., (1997). Complete genome structure of the unicellular cyanobacterium *Synechocystis* sp. PCC6803. *Plant Cell Physiol.* **38**, 1171–1176.

Karapetyan, N.V., Holzwarth, A.R., Rögner, M., (1999). The photosystem I trimer of cyanobacteria: molecular organization, excitation dynamics and physiological significance. *FEBS Lett.* **460**, 395–400.

Kato, K., Tanaka, R., Sano, S., Tanaka, A., Hosaka, H., (2010). Identification of a gene essential for protoporphyrinogen IX oxidase activity in the cyanobacterium *Synechocystis* sp. PCC6803. *Proc. Natl. Acad. Sci.* **107**, 16649–16654.

Komenda, J., Knoppová, J., Kopečná, J., Sobotka, R., Halada, P., Yu, J., Nickelsen, J., Boehm, M., Nixon, P.J., (2012a). The Psb27 assembly factor binds to the CP43 complex of photosystem II in the cyanobacterium *Synechocystis* sp. PCC 6803. *Plant Physiol.* **158**, 476–486.

Komenda, J., Nickelsen, J., Tichý, M., Prášil, O., Eichacker, L.A., Nixon, P.J., (2008). The cyanobacterial homologue of HCF136/YCF48 is a component of an early photosystem II assembly complex and is important for both the efficient assembly and repair of photosystem II in *Synechocystis* sp. PCC 6803. *J. Biol. Chem.* **283**, 22390–22399.

Komenda, J., Reisinger, V., Müller, B.C., Dobáková, M., Granvogl, B., Eichacker, L.A., (2004). Accumulation of the D2 protein is a key regulatory step for assembly of the photosystem II reaction center complex in *Synechocystis* PCC 6803. *J. Biol. Chem.* **279**, 48620–48629.

Komenda, J., Sobotka, R., Nixon, P.J., (2012b). Assembling and maintaining the Photosystem II complex in chloroplasts and cyanobacteria. *Curr. Opin. Plant Biol.* **15**, 245–251.

Kopečná, J., Komenda, J., Bučinská, L., Sobotka, R., (2012). Long-term acclimation of the cyanobacterium *Synechocystis* sp. PCC 6803 to high light is accompanied by an enhanced production of chlorophyll that is preferentially channeled to trimeric photosystem I. *Plant Physiol.* **160**, 2239–2250.

Kroll, D., Meierhoff, K., Bechtold, N., Kinoshita, M., Westphal, S., Vothknecht, U.C., Soll, J., Westhoff, P., (2001). VIPP1, a nuclear gene of *Arabidopsis thaliana* essential for thylakoid membrane formation. *Proc. Natl. Acad. Sci.* **98**, 4238–4242.

Kurisu, G., Zhang, H., Smith, J.L., Cramer, W.A., (2003). Structure of the cytochrome *b<sub>6</sub>f* complex of oxygenic photosynthesis: tuning the cavity. *Science* **302**, 1009–1014.

Ihalainen, J.A., D’Haene, S., Yeremenko, N., van Roon, H., Arteni, A.A., Boekema, E.J., van Grondelle, R., Matthijs, H.C., Dekker, J.P., (2005). Aggregates of the chlorophyll-binding protein IsiA (CP43’) dissipate energy in cyanobacteria. *Biochemistry (Mosc.)* **44**, 10846–10853

Laemmli, U.K., (1970). Cleavage of structural proteins during the assembly of the head of bacteriophage T4. *Nature* **227**, 680–685.

Lavergne, J., (1982). Mode of action of 3-(3, 4-dichlorophenyl)-1, 1-dimethylurea. Evidence that the inhibitor competes with plastoquinone for binding to a common site on the acceptor side of photosystem II. *Biochim. Biophys. Acta BBA-Bioenerg.* **682**, 345–353.

Lehmann, M., Wöber, G., (1976). Accumulation, mobilization and turn-over of glycogen in the blue-green bacterium *Anacystis nidulans*. *Arch. Microbiol.* **111**, 93–97.

Li, H., Kaneko, Y., Keegstra, K., 1994. Molecular cloning of a chloroplastic protein associated with both the envelope and thylakoid membranes. *Plant Mol. Biol.* **25**, 619–632.

Liu, L.-N., Chen, X.-L., Zhang, Y.-Z., Zhou, B.-C., (2005). Characterization, structure and function of linker polypeptides in phycobilisomes of cyanobacteria and red algae: an overview. *Biochim. Biophys. Acta BBA-Bioenerg.* **1708**, 133–142.

Loll, B., Kern, J., Saenger, W., Zouni, A., Biesiadka, J., (2005). Towards complete cofactor arrangement in the 3.0 Å resolution structure of photosystem II. *Nature* **438**, 1040–1044.

Luo, J., Lim, C.K., (1993). Order of uroporphyrinogen III decarboxylation on incubation of porphobilinogen and uroporphyrinogen III with erythrocyte uroporphyrinogen decarboxylase. *Biochem J* **289**, 529–532.

MacColl, R., (1998). Cyanobacterial phycobilisomes. *J. Struct. Biol.* **124**, 311–334.

Maslova, I.P., Mouradyan, E.A., Lapina, S.S., Klyachko-Gurvich, G.L., Los, D.A., (2004). Lipid fatty acid composition and thermophilicity of cyanobacteria. *Russ. J. Plant Physiol.* **51**, 353–360.

McConnell, M.D., Koop, R., Vasil'ev, S., Bruce, D., (2002). Regulation of the distribution of chlorophyll and phycobilin-absorbed excitation energy in cyanobacteria. A structure-based model for the light state transition. *Plant Physiol.* **130**, 1201–1212.

Melkozernov, A.N., Barber, J., Blankenship, R.E., (2006). Light harvesting in photosystem I supercomplexes. *Biochemistry (Mosc.)* **45**, 331–345.

Melkozernov, A.N., Bibby, T.S., Lin, S., Barber, J., Blankenship, R.E., (2003a). Time-resolved absorption and emission show that the CP43'antenna ring of iron-stressed *Synechocystis* sp. PCC6803 is efficiently coupled to the photosystem I reaction center core. *Biochemistry (Mosc.)* **42**, 3893–3903.

Miyashita, H., Ikemoto, H., Kurano, N., Miyachi, S., Chihara, M., (2003). ACARYOCHLORIS MARINA GEN. ET SP. NOV.(CYANOBACTERIA), AN OXYGENIC PHOTOSYNTHETIC PROKARYOTE CONTAINING CHL D AS A MAJOR PIGMENT1. *J. Phycol.* **39**, 1247–1253.

Möller, C., Allen, M., Elings, V., Engel, A., Müller, D.J., (1999). Tapping-mode atomic force microscopy produces faithful high-resolution images of protein surfaces. *Biophys. J.* **77**, 1150–1158.

Morais, F., Kühn, K., Stewart, D.H., Barber, J., Brudvig, G.W., Nixon, P.J., (2001). Photosynthetic Water Oxidation in Cytochrome b 559 Mutants Containing a Disrupted Heme-binding Pocket. *J. Biol. Chem.* **276**, 31986–31993.

Mörschel, E., Schatz, G.H., (1987). Correlation of photosystem-II complexes with exoplasmatic freeze-fracture particles of thylakoids of the cyanobacterium *Synechococcus* sp. *Planta* **172**, 145–154.

Müller, B., Eichacker, L.A., (1999). Assembly of the D1 precursor in monomeric photosystem II reaction center precomplexes precedes chlorophyll *a*-triggered accumulation of reaction center II in barley etioplasts. *Plant Cell Online* **11**, 2365–2377.

Mullineaux, C.W., (1999). The thylakoid membranes of cyanobacteria: structure, dynamics and function. *Funct. Plant Biol.* **26**, 671–677.

Mullineaux, C.W., (2008). Phycobilisome-reaction centre interaction in cyanobacteria. *Photosynth. Res.* **95**, 175–182.

Naithani, S., Hou, J.-M., Chitnis, P.R., (2000). Targeted inactivation of the *psaK1*, *psaK2* and *psaM* genes encoding subunits of Photosystem I in the cyanobacterium *Synechocystis* sp. PCC 6803. *Photosynth. Res.* **63**, 225–236.

Nelson, N., Ben-Shem, A., (2004). The complex architecture of oxygenic photosynthesis. *Nat. Rev. Mol. Cell Biol.* **5**, 971–982.

Nickelsen, J., Rengstl, B., Stengel, A., Schottkowski, M., Soll, J., Ankele, E., (2011). Biogenesis of the cyanobacterial thylakoid membrane system—an update. *FEMS Microbiol. Lett.* **315**, 1–5.

Nield, J., Morris, E.P., Bibby, T.S., Barber, J., (2003). Structural analysis of the photosystem I supercomplex of cyanobacteria induced by iron deficiency. *Biochemistry (Mosc.)* **42**, 3180–3188.

Nixon, P.J., Michoux, F., Yu, J., Boehm, M., Komenda, J., (2010). Recent advances in understanding the assembly and repair of photosystem II. *Ann. Bot. mcq059*.

Olive, J., Ajlani, G., Astier, C., Recouvreur, M., Vernotte, C., (1997). Ultrastructure and light adaptation of phycobilisome mutants of *Synechocystis* PCC 6803. *Biochim. Biophys. Acta BBA-Bioenerg.* **1319**, 275–282.

Olive, J., M'bina, I., Vernotte, C., Astier, C., Wollman, F.A., (1986). Randomization of the EF particles in thylakoid membranes of *Synechocystis* 6714 upon transition from state I to state II. *FEBS Lett.* **208**, 308–312.

Olsen, J.D., Tucker, J.D., Timney, J.A., Qian, P., Vassilev, C., Hunter, C.N., (2008). The organization of LH2 complexes in membranes from *Rhodobacter sphaeroides*. *J. Biol. Chem.* **283**, 30772–30779.

Papageorgiou, G.C., Murata, N., (1995). The unusually strong stabilizing effects of glycine betaine on the structure and function of the oxygen-evolving photosystem II complex. *Photosynth. Res.* **44**, 243–252.

Partensky, F., Hess, W.R., Vaulot, D., (1999). *Prochlorococcus*, a marine photosynthetic prokaryote of global significance. *Microbiol. Mol. Biol. Rev.* **63**, 106–127.

Pogoryelov, D., Yu, J., Meier, T., Vonck, J., Dimroth, P., Muller, D.J., (2005). The c15 ring of the *Spirulina platensis* F-ATP synthase: F1/F0 symmetry mismatch is not obligatory. *EMBO Rep.* **6**, 1040–1044.

Popelkova, H., Yocum, C.F., (2011). PsbO, the manganese-stabilizing protein: Analysis of the structure–function relations that provide insights into its role in photosystem II. *J. Photochem. Photobiol. B* **104**, 179–190.

Preiss, J., (1984). Bacterial glycogen synthesis and its regulation. *Annu. Rev. Microbiol.* **38**, 419–458.

Reid, J.D., Hunter, C.N., (2004). Magnesium-dependent ATPase activity and cooperativity of magnesium chelatase from *Synechocystis* sp. PCC6803. *J. Biol. Chem.* **279**, 26893–26899.

Renger, T., Schlodder, E., (2011). Optical properties, excitation energy and primary charge transfer in photosystem II: Theory meets experiment. *J. Photochem. Photobiol. B* **104**, 126–141.

Reynolds, N.P., Janusz, S., Escalante-Marun, M., Timney, J., Ducker, R.E., Olsen, J.D., Otto, C., Subramaniam, V., Leggett, G.J., Hunter, C.N., (2007a). Directed formation of micro-and nanoscale patterns of functional light-harvesting LH2 complexes. *J. Am. Chem. Soc.* **129**, 14625–14631.

Reynolds, N.P., Janusz, S., Escalante-Marun, M., Timney, J., Ducker, R.E., Olsen, J.D., Otto, C., Subramaniam, V., Leggett, G.J., Hunter, C.N., (2007b). Directed formation of micro-and nanoscale patterns of functional light-harvesting LH2 complexes. *J. Am. Chem. Soc.* **129**, 14625–14631.

Rieble, S., Beale, S.I., (1991). Purification of glutamyl-tRNA reductase from *Synechocystis* sp. PCC 6803. *J. Biol. Chem.* **266**, 9740–9745.

Roose, J.L., Kashino, Y., Pakrasi, H.B., (2007). The PsbQ protein defines cyanobacterial photosystem II complexes with highest activity and stability. *Proc. Natl. Acad. Sci.* **104**, 2548–2553.

Schabert, F.A., Henn, C., Engel, A., (1995). Native *Escherichia coli* OmpF porin surfaces probed by atomic force microscopy. *Science* **268**, 92–94.

Schatz, G.H., Brock, H., Holzwarth, A.R., (1987). Picosecond kinetics of fluorescence and absorbance changes in photosystem II particles excited at low photon density. *Proc. Natl. Acad. Sci.* **84**, 8414–8418.

Schatz, G.H., Brock, H., Holzwarth, A.R., (1988). Kinetic and energetic model for the primary processes in photosystem II. *Biophys. J.* **54**, 397–405.

Scheuring, S., (2006). AFM studies of the supramolecular assembly of bacterial photosynthetic core-complexes. *Curr. Opin. Chem. Biol.* **10**, 387–393.

Scheuring, S., Müller, D.J., Stahlberg, H., Engel, H.-A., Engel, A., (2002). Sampling the conformational space of membrane protein surfaces with the AFM. *Eur. Biophys. J.* **31**, 172–178.

Schluchter, W.M., Shen, G., Zhao, J., Bryant, D.A., (1996). Characterization of *psaL* and *psaL* mutants of *Synechococcus* sp. strain PCC 7002: a new model for state transitions in cyanobacteria. *Photochem. Photobiol.* **64**, 53–66.

Schotchkowski, M., Gkalypoudis, S., Tzekova, N., Stelljes, C., Schünemann, D., Ankele, E., Nickelsen, J., (2009) *The Journal of Biological Chemistry*, **284**, 1813-1819.

Seelert, H., Poetsch, A., Dencher, N.A., Engel, A., Stahlberg, H., Müller, D.J., (2000). Structural biology: proton-powered turbine of a plant motor. *Nature* **405**, 418–419.

Şener, M.K., Olsen, J.D., Hunter, C.N., Schulten, K., (2007). Atomic-level structural and functional model of a bacterial photosynthetic membrane vesicle. *Proc. Natl. Acad. Sci.* **104**, 15723–15728.

Sétif, P., Fischer, N., Lagoutte, B., Bottin, H., Rochaix, J.-D., (2002). The ferredoxin docking site of photosystem I. *Biochim. Biophys. Acta BBA-Bioenerg.* **1555**, 204–209.

Sherman, D.M., Sherman, L.A., (1983). Effect of iron deficiency and iron restoration on ultrastructure of *Anacystis nidulans*. *J. Bacteriol.* **156**, 393–401.

Sherman, D.M., Troyan, T.A., Sherman, L.A., (1994). Localization of membrane proteins in the cyanobacterium *Synechococcus* sp. PCC7942 (radial asymmetry in the photosynthetic complexes). *Plant Physiol.* **106**, 251–262.

Singh, A.K., McIntyre, L.M., Sherman, L.A., (2003). Microarray analysis of the genome-wide response to iron deficiency and iron reconstitution in the cyanobacterium *Synechocystis* sp. PCC 6803. *Plant Physiol.* **132**, 1825–1839.

Smith, A.G., Marsh, O., Elder, G.H., (1993). Investigation of the subcellular location of the tetrapyrrole-biosynthesis enzyme coproporphyrinogen oxidase in higher plants. *Biochem J* **292**, 503–508.

Srivastava, R., Pisareva, T., Norling, B., (2005). Proteomic studies of the thylakoid membrane of *Synechocystis* sp. PCC 6803. *Proteomics* **5**, 4905–4916.

Stanier, R.Y., Bazine, G.C., (1977). Phototrophic prokaryotes: the cyanobacteria. *Annu. Rev. Microbiol.* **31**, 225–274.

Stroebel, D., Choquet, Y., Popot, J.-L., Picot, D., (2003). An atypical haem in the cytochrome *b<sub>6</sub>f* complex. *Nature* **426**, 413–418.

Sznee, K., Dekker, J.P., Dame, R.T., van Roon, H., Wuite, G.J., Frese, R.N., (2011). Jumping mode atomic force microscopy on grana membranes from spinach. *J. Biol. Chem.* **286**, 39164–39171.

Tan, S.C., Crouch, L.I., Mahajan, S., Jones, M.R., Welland, M.E., (2012). Increasing the open-circuit voltage of photoprotein-based photoelectrochemical cells by manipulation of the vacuum potential of the electrolytes. *ACS Nano* **6**, 9103–9109.

Turconi, S., Kruij, J., Schweitzer, G., Rögner, M., Holzwarth, A.R., (1996). A comparative fluorescence kinetics study of Photosystem I monomers and trimers from *Synechocystis* PCC 6803. *Photosynth. Res.* **49**, 263–268.

Umena, Y., Kawakami, K., Shen, J.-R., Kamiya, N., (2011). Crystal structure of oxygen-evolving photosystem II at a resolution of 1.9 Å. *Nature* **473**, 55–60.

Van de Meene, A.M., Hohmann-Marriott, M.F., Vermaas, W.F., Roberson, R.W., (2006). The three-dimensional structure of the cyanobacterium *Synechocystis* sp. PCC 6803. *Arch. Microbiol.* **184**, 259–270.

Van Niel, C.B., (2006). The Bacterial Photosyntheses and Their Importance for the General Problem of Photosynthesis, in: Nord, F.F., Werkman, C.H. (Eds.), *Advances in Enzymology and Related Areas of Molecular Biology. John Wiley & Sons, Inc.*, pp. 263–328.

Vasilev, C., Johnson, M.P., Gonzales, E., Wang, L., Ruban, A.V., Montano, G., Cadby, A.J., Hunter, C.N., (2014). Reversible Switching between Nonquenched and Quenched States in Nanoscale Linear Arrays of Plant Light-Harvesting Antenna Complexes. *Langmuir* **30**, 8481–8490.

Vermaas, W.F., Timlin, J.A., Jones, H.D., Sinclair, M.B., Nieman, L.T., Hamad, S.W., Melgaard, D.K., Haaland, D.M., (2008). In vivo hyperspectral confocal fluorescence imaging to determine pigment localization and distribution in cyanobacterial cells. *Proc. Natl. Acad. Sci.* **105**, 4050–4055.

Vernotte, C., Astier, C., Olive, J., (1990). State 1-state 2 adaptation in the cyanobacteria *Synechocystis* PCC 6714 wild type and *Synechocystis* PCC 6803 wild type and phycocyanin-less mutant. *Photosynth. Res.* **26**, 203–212.

Vittadello, M., Gorbunov, M.Y., Mastrogiovanni, D.T., Wielunski, L.S., Garfunkel, E.L., Guerrero, F., Kirilovsky, D., Sugiura, M., Rutherford, A.W., Safari, A., (2010). Photoelectron generation by photosystem II core complexes tethered to gold surfaces. *ChemSusChem* **3**, 471–475.

Wada, H., Murata, N., (1990). Temperature-induced changes in the fatty acid composition of the cyanobacterium, *Synechocystis* PCC6803. *Plant Physiol.* **92**, 1062–1069.

Wada, H., Murata, N., (2007). The essential role of phosphatidylglycerol in photosynthesis. *Photosynth. Res.* **92**, 205–215

Westphal, S., Heins, L., Soll, J., Vothknecht, U.C., (2001). Vipp1 deletion mutant of *Synechocystis*: a connection between bacterial phage shock and thylakoid biogenesis? *Proc. Natl. Acad. Sci.* **98**, 4243–4248.

Wilde, A., Härtel, H., Hübschmann, T., Hoffmann, P., Shestakov, S.V., Börner, T., (1995). Inactivation of a *Synechocystis* sp strain PCC 6803 gene with homology to conserved chloroplast open reading frame 184 increases the photosystem II-to-photosystem I ratio. *Plant Cell Online* **7**, 649–658.

Wittig, I., Karas, M., Schägger, H., 2007. High resolution clear native electrophoresis for in-gel functional assays and fluorescence studies of membrane protein complexes. *Mol. Cell. Proteomics* **6**, 1215–1225.

Xu, Q., Yu, L., Chitnis, V.P., Chitnis, P.R., (1994). Function and organization of photosystem I in a cyanobacterial mutant strain that lacks PsaF and PsaJ subunits. *J. Biol. Chem.* **269**, 3205–3211.

Xu, W., Tang, H., Wang, Y., Chitnis, P.R., (2001). Proteins of the cyanobacterial photosystem I. *Biochim. Biophys. Acta BBA-Bioenerg.* **1507**, 32–40.

Yoshida, M., Muneyuki, E., Hisabori, T., (2001). ATP synthase—a marvellous rotary engine of the cell. *Nat. Rev. Mol. Cell Biol.* **2**, 669–677.

Zhong, Q., Inniss, D., Kjoller, K., Elings, V.B., (1993). Fractured polymer/silica fiber surface studied by tapping mode atomic force microscopy. *Surf. Sci. Lett.* **290**, L688–L692.

Zouni, A., Witt, H.-T., Kern, J., Fromme, P., Krauss, N., Saenger, W., Orth, P., (2001). Crystal structure of photosystem II from *Synechococcus elongatus* at 3.8 Å resolution. *Nature* **409**, 739–743.